Exploring many-body physics with ultracold atoms

Lindsay J. Leblanc

Exploring many-body physics with ultracold atoms

by

Lindsay Jane LeBlanc

A thesis submitted in conformity with the requirements
for the degree of Doctor of Philosophy
Graduate Department of Physics
University of Toronto

Abstract

Exploring many-body physics with ultracold atoms

Lindsay Jane LeBlanc, Doctor of Philosophy, 2011

Graduate Department of Physics, University of Toronto

The emergence of many-body physical phenomena from the quantum mechanical properties of atoms can be studied using ultracold alkali gases. The ability to manipulate both Bose-Einstein condensates (BECs) and degenerate Fermi gases (DFGs) with designer potential energy landscapes, variable interaction strengths and out-of-equilibrium initial conditions provides the opportunity to investigate collective behaviour under diverse conditions.

With an appropriately chosen wavelength, optical standing waves provide a lattice potential for one target species while ignoring another spectator species. A "tune-in" scheme provides an especially strong potential for the target and works best for Li-Na, Li-K, and K-Na mixtures, while a "tune-out" scheme zeros the potential for the spectator, and is preferred for Li-Cs, K-Rb, Rb-Cs, K-Cs, and ^{39}K-^{40}K mixtures. Species-selective lattices provide unique environments for studying many-body behaviour by allowing for a phonon-like background, providing for effective mass tuning, and presenting opportunities for increasing the phase-space density of one species.

Ferromagnetism is manifest in a two-component DFG when the energetically preferred many-body configuration segregates components. Within the local density approximation (LDA), the characteristic energies and the three-body loss rate of the system all give an observable signature of the crossover to this ferromagnetic state in a trapped DFG when interactions are increased beyond $k_F a(0) = 1.84$. Numerical simulations of an extension

to the LDA that account for magnetization gradients show that a hedgehog spin texture emerges as the lowest energy configuration in the ferromagnetic regime. Explorations of strong interactions in ^{40}K constitute the first steps towards the realization of ferromagnetism in a trapped ^{40}K gas.

The many-body dynamics of a ^{87}Rb BEC in a double well potential are driven by spatial phase gradients and depend on the character of the junction. The amplitude and frequency characteristics of the transport across a tunable barrier show a crossover between two paradigms of superfluidity: Josephson plasma oscillations emerge for high barriers, where transport is via tunnelling, while hydrodynamic behaviour dominates for lower barriers. The phase dependence of the many-body dynamics is also evident in the observation of macroscopic quantum self trapping. Gross-Pitaevskii calculations facilitate the interpretation of system dynamics, but do not describe the observed damping.

Acknowledgements

I was rather delighted the day I found the analogy between the emergence of many-body physics and the working of a community – a general description that says the individual particles of a physical system are better off when they cooperate and work together. While such anthropomorphization may not help solve any physics problems, this analogy provided me a kinship with my atoms, in the knowledge that I, too, benefit from the communities that surround me. In particular, the work presented in this thesis was made possible through the support of my many teachers, colleagues, family and friends.

More than anyone else, I owe my thanks to Joseph Thywissen for his support in all of the work that is presented in this thesis. In his role as my thesis supervisor, his mentorship has meant much to me. For the early years and our weekly meetings where I was free to ask my naïve questions, for listening to me and challenging me, for many pieces of good advice, for the spirit of compromise, discussion, and consensus that was always applied to the decisions made in the lab, for the broader picture at the times when I was lost in the details, for an awareness of the impact personality has on the physics, and for confidence in me as I presented work to the wider world that would eventually lead to my moving on from his group, my thanks.

Without the labmates who have walked alongside me throughout my PhD, this thesis could not have happened. The spirit of cooperation and friendship that permeates our lab not only makes it a pleasant place to work, but contributes to our success. I owe special thanks to Seth Aubin for teaching me much of what I know about running an experiment, and to postdocs Stefan Myrskog, Thorsten Schumm, and Jason McKeever, for their generosity of time and knowledge. To my fellow "Chip Experiment" students, Marcius Extavour and Alma Bardon, my thanks for the time, effort, and insight that have contributed to many of the results in this thesis, to the labmates next door, Dylan Jervis and Dave MacKay, my thanks for thoughtful questions and helpful advice, and to Alan Stummer, my thanks for a certain wizardry with the electronics.

Both at the University of Toronto and through interactions with fellow physicists at

various international conferences and workshops, I have appreciated the sense of collaboration and helpfulness that characterizes my physics community. I owe much thanks to Arun Paramekanti for his interest in the work on ferromagnetism, and patiently helping to develop my early calculations into something more serious. Regular interactions with Aephraim Steinberg, Daniel James, and their groups have helped me to broaden my outlook. With Arun and Aephraim, I thank the other members of my examination committee Allan Griffin and Chris Westbrook for their helpful advice on this thesis. Many thanks are due to our collaborators at the University of Trento, Augusto Smerzi and Francesco Piazza, for their simulations of and insight into the double well BEC work. I would also like to thank the Innsbruck Ultracold Atoms group for their hospitality during May 2009.

To the many friends who have made the years of graduate school some of the best in my life, my thanks. To Cheryl, for inspiring the move to Toronto and remaining my friend once I got here; to Asya, for giving me a life outside the lab; to Chris, for being a wonderful housemate. To physics-friends, Jean-Michel, Etienne, , Julien, Susanne, Nir, Cristen, Brendan, Lisa, Sarah, and others, for being more social than the stereotypes and bringing both serious conversation and laughter into my life. To Loretta, Celia, Dana, Nikki and the many others from across my life, for friendships that have endured the tests of time and distance. To the Wednesday crew at the Redeemer Lunch Program and the SGS womens' basketball teams through the years, for making Wednesday mornings and Monday nights something to look forward to.

Though graduate school took me farther from them, my family's never-ending support has followed me across the country. For always fostering and facilitating my curiosity, I thank my parents Bill and Avril. For becoming some of my closest friends, I thank my sisters Katie and Valerie, and for making our family a bigger and better place through marriage and birth, Brad and Jackson.

And though it seems silly to say, I would like to thank the City of Toronto, for being the kind of place where you are free to become the person you are meant to be, and for providing the kind of environment in which the coming together of people from all backgrounds benefits us all.

Preface

The work presented in this thesis is the culmination of six years of experimental and theoretical work performed at the Toronto Ultracold Atoms Lab. I have had the opportunity to work with many different people on a variety of projects. The following specifies the specific publications arising from the work discussed in each chapter, and acknowledges the contributions of my collaborators to work presented in this thesis.

Chapter 2: A versatile BEC-DFG machine

Chapter 2 discusses the apparatus used for the experiments in this thesis. Much of the original work building the apparatus was done by Seth Aubin, Stefan Myrskog and Marcius Extavour. Thorsten Schumm and Marcius Extavour were responsible for the construction of the electronics used to produce the radio-frequency dressed potentials. Publications describing this work, as well as the early results from this apparatus, include:

- S. Aubin *et al.*, *Trapping Fermionic* ^{40}K *and Bosonic* ^{87}Rb *on a Chip*, J. Low Temp. Phys. **140**, 377 (2005).

- S. Aubin, S. Myrskog, M. Extavour, L. LeBlanc, D. McKay, A. Stummer, and J. H. Thywissen, *Rapid sympathetic cooling to Fermi degeneracy on a chip*, Nat. Phys. **2**, 384 (2006).

- M. H. T. Extavour, L. J. LeBlanc, T. Schumm, B. Cieslak, S. Myrskog, A. Stummer, S. Aubin, and J. H. Thywissen, *Dual-species quantum degeneracy of* ^{40}K *and* ^{87}Rb *on an atom chip*, At. Phys. **20**, 241 (2006).

Chapter 3: Species-specific optical lattices

Chapter 3 was work done in collaboration with Joseph Thywissen, who is especially responsible for the discussion of effective mass tuning. This chapter is primarily a reprint of work published in *Physical Review A*. Modifications to this work include some notation changes to conform with other chapters in this thesis (e.g., all potential energies $U \to V$), and the addition of references to work that has been published in the interim. The section

"III.D Lattice confinement effects" (following what is §3.3.3 in this Chapter) has been omitted. In that section, we neglected the effects of dipole fluctuations, which can contribute significantly to the heating of ultracold atoms in a lattice [1]. A recent publication discusses the "blue-detuned advantage" we were considering in the context of the quantum motions of the atoms [2], and we refer to this work for a better understanding of the effects. Section 3.2.2 has also been revised to include the counter-rotating terms in the heating rate, which in turn modifies the calculated heating rates for those cases where the laser wavelength is far-detuned from the atomic transition in question.

- L. J. LeBlanc and J. H. Thywissen, *Species-specific optical lattices*, Phys. Rev. A **75**, 053612 (2007).

Chapter 4: Ultracold ferromagnetism

The theoretical work described in Chapter 4 arose from discussions with Arun Paramekanti and Joseph Thywissen regarding possible observable signatures of itinerant ferromagnetism in a trapped ultracold Fermi gas. The analytics discussed in this chapter were originally derived by Arun Paramekanti. The work presented was §4.2 and §4.3 published in *Physical Review A*. Some of the notation has been changed from this previous publication to conform to the notations established in this thesis.

- L. J. LeBlanc, J. H. Thywissen, A. A. Burkov, and A. Paramekanti, *Repulsive Fermi gas in a harmonic trap: Ferromagnetism and spin textures*, Phys. Rev. A **80**, 013607 (2009).

Chapter 5: BEC dynamics in a double well

The experiments of Chapter 5 would not have met with same success without the groundwork laid by Marcius Extavour and Jason McKeever in understanding the process of creating a double well potential with our atom chip. The data presented in this chapter was collected with the help of Alma Bardon. The formulation and calculation of the hydrodynamic "spring constant" approximation was done by Joseph Thywissen. The code for the numerical calculations of the GPE in §5.3 used to determine the trap parameters and to set the V_b/μ axes was written by Joseph Thywissen, the first calculations determining the beyond-rotating wave approximation and the decaying MQXT state were done by Jason McKeever, and the three-dimensional GPE simulations and interpretations in §5.4 was performed by Francesco Piazza and Augusto Smerzi of the University of Trento. The calculation using a WKB-type approximation for the tunnelling was suggested by Eugene Demler. The work

described in §5.4 has been submitted for publication.

- L. J. LeBlanc, A. B. Bardon, J. McKeever, M. H. T. Extavour, D. Jervis, J. H. Thywissen, F. Piazza, and A. Smerzi, *Dynamics of a tunable superfluid junction*, ArXiv:1006.3550 (2010) (submitted to *Phys. Rev. Lett.*).

Contents

List of Figures

List of Tables

Chapter 1

Introduction

In pursuit of the unknown, physics finds itself exploring ever deeper into length and energy scales extending away from those of human experience. As an understanding of the behaviour of matter at these extremes is developed, it can be a challenge to connect the principles responsible for behaviour on one scale with those on the next. These connections, however, increase our understanding of the fundamental properties of the universe and bring closer to human understanding those phenomena which seem to defy common sense.

The field of atomic physics has proven itself valuable in the exploration of physical phenomena on many scales. In the infancy of this field, the emerging understanding of atomic structure was coupled to the development of quantum mechanics, such that the understanding of one informed the other, and principles such as the quantization of energy and the existence of spin angular momentum emerged from the partnership. Measurements of the distinct spectral features of an atom can be carried out for atoms over many length scales – from exploring the details of atomic structure in the laboratory, to using absorption characteristics of the Earth's atmosphere to determine its composition, to ascertaining the behaviour of astronomical objects through the shifts of well-known spectral features.

In recent years, atomic physics has proven itself an ideal venue in which to probe the smallest known energy scales. Upon establishing techniques to render temperature-driven motion negligible [3, 4], the quantum statistics and indistiguishability inherent to an atom become evident as an ultracold gas attains quantum degeneracy as a Bose-Einstein condensate (BEC) [5] or a degenerate Fermi gas (DFG) [6] for bosons or fermions, respectively. With the freezing-out of thermal degrees of freedom, the direct and exchange interactions of the atoms set the dominant energy scales, and the atoms no longer act as individuals. By studying the transitions from individual to collective behaviour, these atomic systems re-

veal connections between the quantum mechanics of individual particles and the many-body behaviour of macroscopic systems.

The study of many-body physics provides insight into the emergence of macroscopic phenomena ranging from familiar examples like the structure of solids and origins of magnetism, to more exotic examples like superconductivity. In general, the microscopic degrees of freedom (the individual motions or state of atoms, for example) can be ignored and a new macroscopic "order parameter" emerges as the important degree of freedom for the problem. The identification of this order parameter can be made through experimental observation of a system without knowledge of its microscopics, as is the case in systems like high-temperature superconductors where superconductivity is clearly observed, but the underlying macroscopic description of its origin remains an open question. While it is not necessary to understand the origin of such behaviour before exploiting it as a technology, one can imagine that identifying the required microscopic properties leading to this behaviour would enable much broader applications of such technologies.

The precision and versatility of atomic experiments provide many advantages for studying many-body phenomena. Well known internal transitions of the atom permit selective addressability and detection, interactions with electromagnetic fields make possible designer potential energy landscapes, Bose or Fermi statistics dictate their relationships with their neighbours, tunable interactions allow an exploration of various coupling regimes, and weak interactions with external decoherence mechanisms allow for long-lived quantum mechanical integrity. Atoms can be used as a set of versatile building blocks, and experiments can be designed to mimic other physical systems whose behaviour is governed by the same fundamental principles.

A variety of analogues to condensed-matter systems have been explored by introducing quantum degenerate gases into customized environments, including, for example, the Mott-insulator transition [7], the Tonks-Giradeau gas [8], superfluidity of fermionic pairs [9, 10], and Anderson localization [11]. By demonstrating a correspondence between atomic and condensed matter systems, these experiments lay the foundations for the use of ultracold gases to explore many-body physics. Increasing the complexity of the interactions and environments experienced by the atoms will allow these experiments to approach a regime in which the underlying physics is incalculable. In particular, systems of fermionic atoms could be arranged to mimic systems in which Fermi statistics, and their requirement of antisymmetrization of the wavefunction, render insufficient the computational resources needed to model systems of reasonable particle number. The atomic system could then be

thought of as a "quantum simulator" [12] – a calculating machine that comes to its results by taking a quantum mechanical system, allowing it evolve in a controlled environment, and reaping the results from measurements of the final state. Several proposals have been developed suggesting models that could be implemented by ultracold gases as analogues to condensed matter problems, including, for example, the emergence of high-temperature d-wave superconductivity from a Fermi-Hubbard model [13] or exotic forms of magnetism [14].

This thesis discusses three main advances in the development of the use of ultracold gases for the study of many-body physics. First, a technique for creating customized and selective potential energy landscapes for mixtures of two or more species of atom. This type of potential would could provide a means to tune the effect mass of one species, provide a phonon-like background to atoms trapped in an optical lattice, or allow a mechanism for a isothermal phase-space increase. Second, a proposal for the study of itinerant ferromagnetism among ultracold fermions is discussed, and the first steps towards its implementation in fermionic ^{40}K are described. The microscopic origins of this many-body behaviour are not well understood, and these experiments may provide insight into this problem. Third, the collective transport behaviour of bosonic ^{87}Rb in a double well potential is explored. The character of the transport is explored as a function of the coupling between wells, and both perfect-fluid hydrodynamics and Josephson-junction behaviour are found, indicating the limits in which the macroscopic description associated with each of these is appropriate for the system.

Outline

◇ **Chapter 2** describes the apparatus for which techniques are developed and on which the experiments are performed. This versatile machine produces quantum degenerate samples of both bosons and fermions using the efficiency and flexibility of an atom chip. Two methods for manipulation the potential energy landscape are discussed. Optical fields are used as external forces and confinement potentials, and radio-frequency fields are used to manipulate the potential energy surfaces into double-well potentials through internal state manipulations of the atoms.

◇ **Chapter 3** describes a technique that allows for the creation of a lattice-like environment

for one species of atom while inducing no external potential on another species. This technique exploits the differences in atomic structure between species to customize an environment in which to study the many-body properties of a mixture of atomic species. This method could prove useful as a means to tune the effective mass of one species, to provide a phonon background to atoms trapped in a lattice potential, or to implement a mechanism for isothermal phase-space increase.

◇ **Chapter 4** describes the emergence of many-body collective behaviour of ultracold fermions under the influence of strong repulsive interactions, and how this behaviour mimics itinerant ferromagnetism among electrons in metals. Mean-field calculations suggest that measurements of the total energy will indicate the crossover to ferromagnetism for trapped gases, and extensions to a local-density approximation indicate that configurations displaying spin textures could reduce the total energy of the system. The first steps towards the experimental realization of this system in ^{40}K are reported here.

◇ **Chapter 5** describes the quantum mechanical transport of a ultracold bosons in a double well potential. Using a tunable barrier, the character of the transport is studied as the density in the region connecting the wells is varied from finite to vanishingly small values, where the classical density is zero and tunnelling is responsible for transport. We study both the population and phase evolution of this system under various initial conditions and find that the many-body behaviour can be described as hydrodynamic in the strong-coupling limit and as a Josephson junction for weak coupling.

Chapter 2

A versatile BEC-DFG machine

One of the primary advantages to studying many-body physics in ultracold gases is the versatility with which atomic systems can be controlled. Well established methods to address an atom's internal and external degrees of freedom are used to cool a system to the quantum degenerate regime, to manipulate it upon arrival there, and to measure its final state upon completion of an experiment.

The "Chip Experiment" apparatus at the University of Toronto Ultracold Atoms Lab serves as either the real or presumed setting for the experimental and theoretical work described in this thesis. This experimental apparatus was designed as general-purpose BEC-DFG machine, using an atom chip for efficiently cooling ^{87}Rb and ^{40}K to quantum degeneracy. It has been used to pursue a variety of scientific questions throughout its young life, and will continue to do so as it matures.

This chapter describes the general operation of this machine in §2.1, deferring a recent thesis [15] for most details. Sections 2.2 and 2.3 describe two of the newer tools used to manipulate the ultracold gases created by this apparatus: optical traps and radio-frequency dressed potentials, respectively. Details regarding the construction and operation of these tools are discussed in those sections.

2.1 A versatile BEC-DFG machine: basic principles

The design of this apparatus was carefully planned to provide a versatile platform from which to launch experiments using a ^{87}Rb Bose-Einstein condensate (BEC), a ^{40}K degenerate Fermi gas (DFG), or both. Using an atom chip for fast and efficient evaporation,

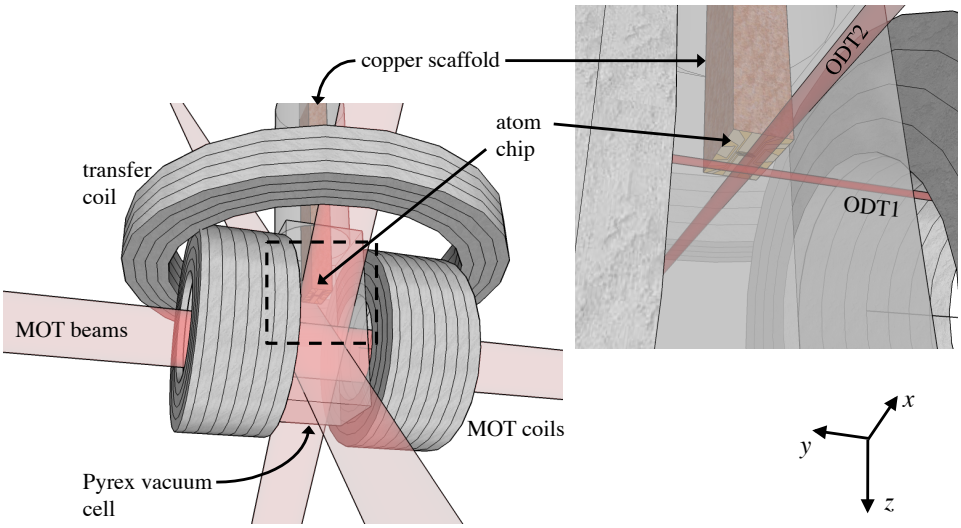

FIGURE 2.1: Apparatus schematics. Left: Experimental apparatus from afar. Red MOT beams, 5 cm in diameter intersect in the middle of the glass-box vacuum chamber. Parallel external magnetic coils provide the quadrupole field for MOT and magnetic trapping, while the large top coil is used for magnetic transport of the atoms to the atom chip, seen inside the glass vacuum chamber. Right: Close up of atom chip, inside vacuum chamber. Also shown is the crossed ODT, skimming the surface of the atom chip. MOT beams have been turned off in this view.

this simple one-chamber experiment provides fast cycle times and reasonable atom numbers with a minimum of technical complication. Details of the operation of the apparatus are presented elsewhere (see Refs. [16–18] and especially [15]), but a brief description of the machine is given here.

The main elements of the apparatus are sketched in Fig. 2.1. A Pyrex box acts as the single vacuum chamber, in which the six magneto-optical trap (MOT) beams intersect. The atom chip is suspended by a copper scaffold 5 cm above the MOT beam intersection point. External magnetic coils provide the magnetic field gradients needed for the MOT, magnetic trap, and magnetic transport.

2.1.1 GENERIC SEQUENCE FOR BEC/DFG

The standard route to quantum degeneracy, either as a BEC of ^{87}Rb or a DFG of ^{40}K , proceeds as follows:

◇ **MOT.** The magneto-optical trap (MOT) is formed at the intersection of six counterpropagating beams, with 5 cm diameter and ≈ -26 MHz detuning from the $|F = 2, m_F =$

$2\rangle \rightarrow |F' = 3, m_{F'} = 3\rangle$ and $|F = 9/2, m_F = 9/2\rangle \rightarrow |F' = 11/2, m_{F'} = 11/2\rangle$ cycling transition resonances in ^{87}Rb and ^{40}K , respectively. For a ^{87}Rb BEC alone, the ^{87}Rb MOT time ranges from 1 to 5 s. For a DFG or a mixture, the ^{40}K MOT is started first, and is run for up to 20 s, after which the ^{87}Rb MOT light is turned on together with ^{40}K light, and the overlapping beams generate simultaneous MOTs. Due to excited-state collisional loss, we minimize the time during which both MOTs run at the same time. Typical atom numbers at the conclusion of this step are, for ^{87}Rb and ^{40}K respectively, $N_{\mathrm{Rb,MOT}} = 2 \times 10^9$ and $N_{\mathrm{K,MOT}} = 4 \times 10^7$.

◇ **Optical molasses.** An "optical molasses" step is used to further cool the ^{87}Rb , exploiting sub-Doppler cooling mechanisms in the absence of magnetic fields. The ^{87}Rb temperature is reduced from $T_{\mathrm{Rb,MOT}} \approx 130$ µK to $T_{\mathrm{Rb,molasses}} \approx 30$ µK.

◇ **Optical pumping.** To optimize the magnetic trapping in subsequent steps, the atoms are spin-polarized into the low-field-seeking stretched states of the ground states $|F = 2, m_F = 2\rangle$ for ^{87}Rb and $|F = 9/2, m_F = 9/2\rangle$ for ^{40}K . We use σ^+ polarized light on the $F = 2 \rightarrow F' = 2$ ($F = 9/2 \rightarrow F' = 9/2$) transition for ^{87}Rb (^{40}K) to promote then shelve the atoms in these dark states.

◇ **Magnetic trapping and transfer.** Using the same coils as were used for the MOT, a quadrupole magnetic field is turned on suddenly with a gradient that will trap only the stretched-state atoms against the force of gravity. After compressing the gas by increasing the confinement of the trap, the magnetic field minimum is shifted 5 cm vertically toward the chip surface by changing the current of the "transfer coil." We find a transfer efficiency to the magnetic trap (measured for ^{87}Rb) of $N_{\mathrm{Rb,Btrap}}/N_{\mathrm{Rb,MOT}} \gtrsim 40\%$.

◇ **Atom chip trapping.** Once the atoms are near the surface of the chip, the "chip trap" is activated, by flowing current through both the "Z-wire" on the chip and external bias coils providing uniform magnetic fields. The atoms are trapped in a highly elongated cigar-shaped trap. The transfer efficiency from the magnetic trap to the chip trap is $N_{\mathrm{Rb,chip}}/N_{\mathrm{Rb,Btrap}} \sim 4\%$. We believe that free evaporation is responsible for some of the loss in this process, resulting in the colder atoms being preferentially transferred, which is to our advantage. The compression of the chip trap increases the temperature, which we estimate to be $T_{\mathrm{Rb,\ chip}} \approx 300$ µK.

◇ **Evaporative and sympathetic cooling.** A radio-frequency (rf) current is fed through an auxillary chip wire, parallel to the long axis of the cloud, providing near-field rf radiation which couples adjacent m_F states in the magnetic trap. Sweeping the frequency from high to low, the hottest atoms ^{87}Rb are ejected from the trap and those left behind rethermalize to lower temperatures. If ^{40}K is present, collisions between species bring them to an equal temperature, allowing the ^{40}K to be sympathetically cooled as ^{87}Rb is evaporated. With appropriate sweep rates, the phase space densities increase and quantum degeneracy is achieved. Typical atom numbers are $N_{\mathrm{Rb,BEC}} = 2 \times 10^5$ for a quasi-pure ^{87}Rb BEC (when produced alone), and $N_{\mathrm{K,DFG}} = 4 \times 10^4$ for $T_{\mathrm{K}}/T_{\mathrm{F}} = 0.09 \pm 0.04$ for ^{40}K DFGs, where T_{F} is the Fermi temperature.

◇ **Experiment.** At this point in the sequence, either a BEC or DFG is available to be manipulated in whatever way will answer the question of the day.

◇ **Imaging.** Absorption imaging is used to determine both the number and momentum distribution of the cold atoms. Typically, the atoms are released from their trapping potential and allowed some time of flight (TOF) before imaging. A 100 µs pulse of light resonant to the cycling transition is incident on the atoms, whose intensity is chosen such that the absorption of the light by the atoms remains in the low-saturation-parameter limit (See Appendix B). The resulting shadow image is recorded on a CCD camera after passing through imaging optics. After the atoms are removed from the field of view, either by letting them fall farther or shelving them in a dark state, a second reference image is recorded on the CCD. The amount of light absorbed and its position on the camera give information about both the total number and momentum distribution of the atom clouds.

A quantum gas for everyone

At the "Experiment" point in the sequence, either a BEC, DFG, or a mixture of the two is available for study. In most cases, additional steps are taken to create a more interesting or exotic environment for the quantum gas. In the work presented here, we consider a number of situations: Chapter 3 considers (theoretically) the case of applying optical lattices to a mixture of atomic species, taking into special consideration the ^{40}K -^{87}Rb mixture available in this experiment; Chapter 4 considers transferring a DFG of ^{40}K to an all-optical trap, applying strong magnetic field to access a Feshbach resonance, where strong repulsive

interactions can lead to collective behaviour; and Chapter 5 considers deformations of the magnetic trap via rf dressing fields, to study the dynamics of a ^{87}Rb BEC in a double well. The apparatus is constructed to allow switching between these configurations with a change of commands from the sequencing computer, lending it a high degree of versatility.

2.2 Optical forces: traps and levitation

The use of optical forces is a standard tool for the manipulation of ultracold atomic gases [19]. Laser light whose intensity is spatially dependent, often as focussed beams or standing waves, will create a potential energy surface for the gas. In addition to the unique geometries these potentials make available, schemes using all-optical trapping permit the trapping of weak-field seeking states and tunability of magnetic field, which are unavailable in magnetic trapping schemes. With this freedom, the tunability of interaction strength enters as an additional control parameter, as the Feshbach resonance [20] can be exploited.

In this apparatus, we combine the advantages of the atom chip technology with those offered by all-optical traps. The potential energy for the far-detuned traps we use is discussed in §2.2.1, the limitations associated with combining an optical trap with an atom chip are discussed in §2.2.2 and the application of this optical force as a levitation field is discussed in §2.2.3.

2.2.1 Optical trapping potential

The origin of the optical forces we consider here is the ac-Stark shift, the second-order perturbative energy shift due arising from the interaction of an oscillating electric field with an atom, through the dipole operator. With spatially-varying optical fields, atoms will experience spatially-dependent optical forces, which can be used to trap the atoms in what are sometimes called optical dipole traps (ODTs). For optical frequencies far detuned from any optical transitions, the far-off-resonant trap (FORT) provides a potential energy [19]

$$V_{\mathrm{opt}}(\mathbf{r}) \approx \frac{3\pi c^2 \Gamma}{2\omega_0^3}\left(\frac{1}{\Delta} - \frac{1}{\Delta_+}\right) I(\mathbf{r}), \tag{2.1}$$

where Γ is the natural linewidth of the atomic transition, $I(\mathbf{r})$ is the local intensity, $\omega_0 = 2\pi c/\lambda$ is the frequency of the dominant transition, λ is the wavelength, $\Delta = \omega_L - \omega_0$ is the detuning of the laser light from the dominant optical transition, $\Delta_+ = \omega_L + \omega_0$ is the

counter-rotating term (which becomes important only at large detunings), and ω_L is the frequency of the optical field used for trapping.

In this work, we use single focussed beams to effect the optical potentials that manipulate the atoms. With the assumption of Gaussian beam optics, we consider generic coordinates $\mathbf{r} = (r_1, r_2, r_3)$. We take the direction of propagation along r_3 and assume cylindrical symmetry where the radial coordinate $\varrho_{12} = \sqrt{r_1^2 + r_2^2}$ is valid. In this case, the intensity is Gaussian

$$I(\varrho_{12}, r_3) = \frac{2P}{\pi w^2(r_3)} \exp\left(-\frac{2(\varrho_{12} - \varrho_{12}^0)^2}{w_0^2}\right), \tag{2.2}$$

where P is the total power in the beam, $(\varrho_{12}^0, 0)$ is the location of the beam focus, w_0 is the beam waist at $r_3 = 0$, where the waist is, in general, $w(r_3) = w_0\sqrt{1 + (r_3/r_\mathrm{R})^2}$, and $r_\mathrm{R} = \pi w_0^2/\lambda$ is the Rayleigh range of the beam. The combination of Eqs. 2.1 and 2.2 gives a full expression for the potential in terms of measurable quantities P and w.

The Gaussian shape of the potential is approximately harmonic at the trap centre, and effective trap frequencies can be related to the beam waist and power [19]. The two trap frequencies are

$$\omega_{12} = \sqrt{\frac{4V_\mathrm{opt}(\mathbf{0})}{mw_0^2}} \tag{2.3a}$$

$$\omega_3 = \sqrt{\frac{2V_\mathrm{opt}(\mathbf{0})}{mr_R^2}}. \tag{2.3b}$$

The optical potentials used in this apparatus are generated from 1064 nm laser light, from either the 500 mW solid state (Nd:YAG & Nd:YVO4) CrystaLaser (CL-1064-500) or a 10 W ytterbium fibre laser from IPG (YLR-10-1064-LP). At this wavelength, the detuning is sufficiently far off-resonance to avoid large heating rates, and to make valid the far-detuned approximations discussed above for both ^{87}Rb ($\lambda = 780$ nm) and ^{40}K ($\lambda = 767$ nm). Both lasers pass through power-controlling AOMs before entering fibre optics that act both as spatial filters and means to transport the light from one location to the next. The output power from the fibre is actively stabilized via feedback to the AOM.

2.2.2 Crossed-beam optical trap near an atom chip

To bring a trapping beam near the surface of an atom chip, the size of the focus will be limited by the clipping of the beam at the edges of the chip. For a beam of a given spot size, w_0, the distance from the chip surface, z_trap will be restricted depending on the width

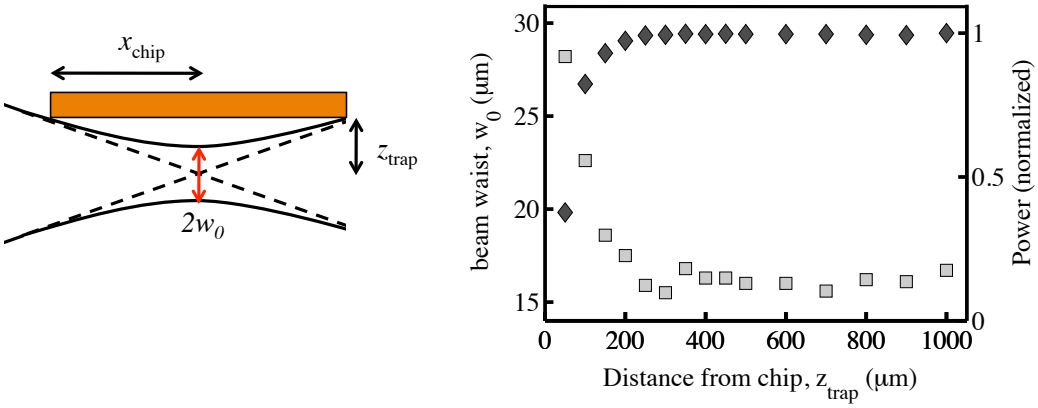

FIGURE 2.2: Optical trapping near a surface. The schematic shows the geometry of a focussed beam skimming the surface of an atom chip. The beam waist w_0 is limited by the distance from the chip z_{trap} and the horizontal length from the edge of the trap to the trap position, x_{chip}. The plot shows a measurement of the waist size (light squares, left axis) and power throughput (dark diamonds, right axis) for a 1064 nm beam focussed at various distances z_{trap} from the surface of a 16 mm long surface. The beam is degraded as the beam approaches closer than 200 μm to the chip.

of the chip, x_{chip}. Figure 2.2 shows the geometry of this situation. A rough estimate for the minimum distance from the chip, $z_{\text{trap}}^{\text{min}}$ can be found by assuming that the beam must at all times allow one beam waist to be transmitted past the edge of the chip. In this case,

$$z_{\text{trap}} \geq z_{\text{trap}}^{\text{min}} = w_0 \left(1 + \left(\frac{\lambda x_{\text{chip}}}{\pi w_0^2}\right)^2\right)^{1/2} \tag{2.4}$$

where λ is the wavelength of the trapping light. In this experiment, where $\lambda = 1064$ nm, $x_{\text{chip}} = 8$ mm, and $w_0 \approx 16$ μm, this expression gives $z_{\text{trap}} \geq 170$ μm. Figure 2.2 shows a measurement of the spot size and through-power of a beam focussed at various distances from a 16 mm long surface. The spot size begins to increase at $z_{\text{trap}} \approx 200$ μm from the chip, which is close to the estimate. This degradation of the beam is due to the high-momentum wavevectors being removed at the edge of the chip.

In this apparatus, we trap the atoms ~ 200 μm from the surface of the chip. At this distance, we can use beams with $w_0 \gtrsim 16$ μm. We use two focussed 1064 nm beams to manipulate the atoms, alone or separately. These are shown schematically in Fig. 2.1 (inset); Fig. 2.3 shows the layout of the optical elements used to create these traps. The two beams, known as "ODT1" and "ODT2" cross at the location of that atoms, ODT1 (along y) with a waist of $w_0 \approx 18$ μm and ODT2 (along x) with $w_0 \approx 35$ μm.

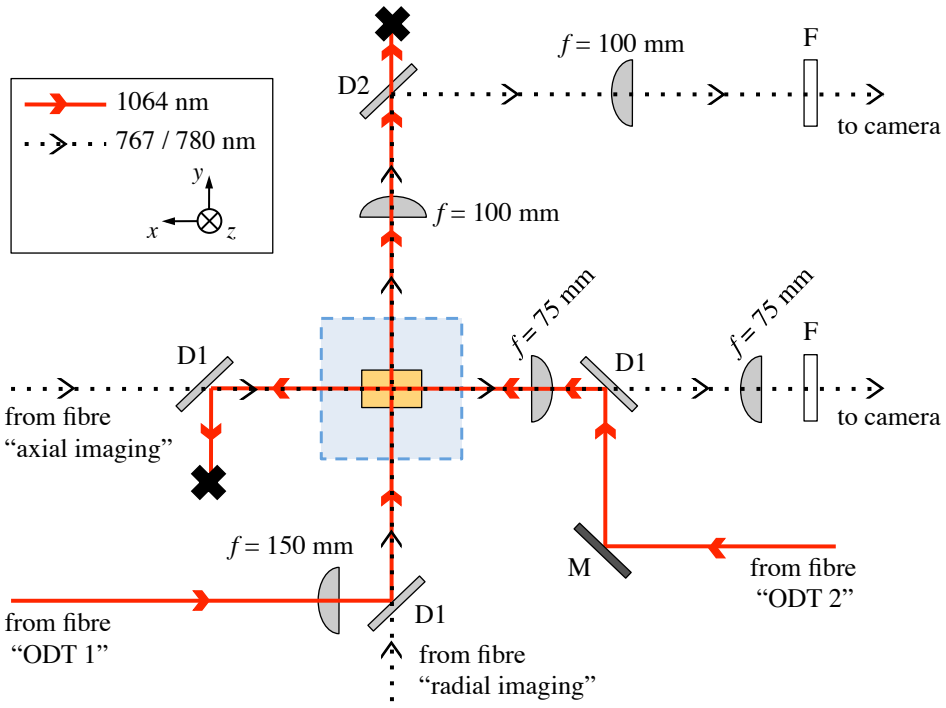

Figure 2.3: Crossed-beam ODT layout, including imaging axes (view from above). Blue box shows vacuum cell, with yellow atom chip inside. Mirror (M), lenses (f), 1064 nm notch filters (F), dichroic mirrors (D1: transmits 767/780 nm, reflects 1064 nm) and (D2: transmits 1064 nm, reflects 767/780 nm), and beam dumps (black X) shown. Solid red lines show the two paths for the ODTs: ODT1 is the more-tightly focussed beam, passing through the atoms in the y-direction; ODT2 is the broader beam, passing through the atoms in the x-direction. Dashed black lines show the paths of the imaging beams: "radial imaging" copropagating with ODT1 along the y-direction and "axial imaging" counterpropagating with ODT2 along x. Note that the lens used for focussing ODT2 ($f = 75$ mm, closest to vacuum cell) is also used for imaging.

Atoms can be transferred with near-unity efficiency from the magnetic trap to either trap individually, or to a crossed ODT1+ODT2 trap. The general procedure for transfer is to turn on the ODTs slowly (~ 100 ms) while the magnetic trap is present, turning off the magnetic traps with an equivalent time-scale once the ODT is fully on.

2.2.3 Optical levitation forces for cancelling gravity

In some circumstances, we find that the potential energy gradient due to gravity negatively affects the shape of the trapping potential. While this is usually not a problem in

the tightly-confined atom chip traps used in our experiments, we found that the shapes of rf-dressed adiabatic potentials were more sensitive (see §2.3 for more details). To counteract this effect, we position the weakly-focussed ODT2 above the location of the atoms, in order to place the linear slope of the potential at the position of the atoms. By adjusting the power of this beam, we can exactly cancel the effect of gravity.

To determine the positioning of the beam that will best cancel gravity, we employ a procedure that exerts a pulsed force on the atoms. The position of greatest linearity in a Gaussian beam, where $\varrho_{12} - \varrho_{12}^0 = w_0/2$, is also the point of largest gradient in the potential. Since the force exerted by this potential ($F(\mathbf{r}) = -\nabla V(\mathbf{r})$) is greatest at this point, we seek the position of the beam where we can exert the greatest force on the atoms. After creating a small BEC in the atom chip trap, we turn off the magnetic trap and immediately pulse on the optical beam ODT2 for a short time, before the atoms have moved significantly. The position of ODT2 is scanned vertically (in z), and upon measuring the average distance of the atoms after some time of flight, we can find the position of the ODT at which the the atoms have fallen the least, corresponding to the position of greatest upward force. Figure 2.4 shows one such measurement.

After calibrating the position, we position ODT2 at the optimal location, and determine the minimum power required for levitation of the atoms upon release from the magnetic trap. We employ ODT2 at this power and position to mitigate the effects of gravity.

2.3 Chip-based rf double-well potentials

The use of radio frequency (rf) radiation to deform magnetic potential energy surfaces began in earnest as a tool for forced evaporative cooling. The effective potential seen by the atoms is modified by the coupling between the oscillating rf magnetic fields and the static potential of the magnetic trap, which can be used more generally to deform the geometry of magnetic potentials [21, 22].

The proximity of the atoms to the rf antennae on a atom chip allows for strong coupling between the rf radiation and the atoms, which, with polarization considerations, can be used to create double well potentials [23]. Like the work described in Refs. [23–25], we use this technique to deform a single well into a double well, carefully controlling the barrier height and distance between the minima of the two wells with the frequency and amplitude of the rf fields.

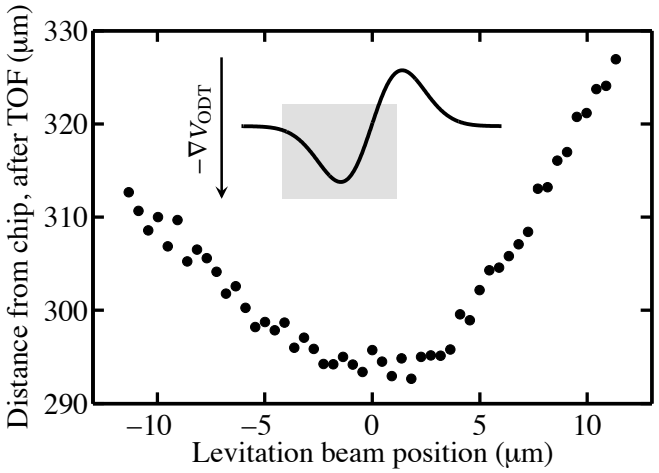

Figure 2.4: Optical levitation calibration. The inset shows the force profile expected for a Gaussian beam, with the grey region highlighting the regime for the data in this plot. Upon being released from a trap, an atom cloud is subjected to a force from the optical beam, whose magnitude depends on the position of the atoms in the beam. The magnitude of the force is scanned by moving the beam through the cloud. After the force is applied, the position of the atom cloud is recorded after some time of flight. The greater the upward force, the less the atoms fall. The minimum in the atom cloud position indicates the levitation beam position which exerts a maximum force on the atoms, corresponding to the position of greatest linearity in the optical potential. The zero in the beam position is arbitrary, and increasing values of position move away from the chip.

The geometry of the atom chip used in this experiment, and the magnetic and rf-dressed potentials available from it, are described extensively in Ref. [15]. Since the completion of that thesis, we have worked to further modify the geometry of the traps through the use of different antennae and optical forces. Section 2.3.1 gives an analytic form for the potetnials used in this work, and §2.3.2 discusses the necessary corrections needed to compensate for the approximations made. Section 2.3.3 discusses the details of the three-dimensional geometry of the double well and describes modifications to the potential using the optical forces described in §2.2.

2.3.1 Rotating-wave approximation of potential

The double-well potential is created through a coupling between static and rf magnetic fields. In the dressed state picture, these combine to form the effective potential [24]

$$V_{\mathrm{RWA}}(\mathbf{r}) = m'_{\mathrm{F}}\sqrt{\left[\hbar\omega_{\mathrm{rf}} - g_{\mathrm{F}}\mu_{\mathrm{B}}B_{\mathrm{S}}(\mathbf{r})\right]^2 + \left[\frac{g_{\mathrm{F}}\mu_{\mathrm{B}}B_{\mathrm{rf},\perp}(\mathbf{r})}{2}\right]^2} \tag{2.5}$$

where m'_F is the adiabatic magnetic quantum number, g_F is the g-factor, μ_B is the Bohr magneton, $B_{\mathrm{S}}(\mathbf{r})$ is the static magnetic field, described by an Ioffe-Pritchard potential, and $B_{\mathrm{rf},\perp}(\mathbf{r}) = |\mathbf{B}_{\mathrm{S}}(\mathbf{r})\times\mathbf{B}_{\mathrm{rf}}(\mathbf{r})|/|\mathbf{B}_{\mathrm{S}}(\mathbf{r})|$ is the component of the oscillating magnetic field locally perpendicular to the static field at each point, $\mathbf{r}$.

The static magnetic trap arises a result of the combination of current flowing through the "Z"-wire on the chip, an external bias field, and an external Ioffe field. In combination, these create an Ioffe-Pritchard style trap, a static magnetic field $\mathbf{B}_{\mathrm{S}} = B_1\hat{\mathbf{r_1}} + B_2\hat{\mathbf{r_2}} + B_3\hat{\mathbf{r_3}}$, whose components are described by [26]

$$B_1(r_1, r_3) = B'r_1 - \frac{B''}{2}r_1r_3 \tag{2.6}$$

$$B_2(r_2, r_3) = -B'r_2 - \frac{B''}{2}r_2r_3 \tag{2.7}$$

$$B_3(r_1, r_2, r_3) = B_{\mathrm{S}}(\mathbf{0}) + \frac{B''}{2}\left(r_3^2 - \tfrac{1}{2}(r_1^2 + r_2^2)\right) \tag{2.8}$$

with a magnitude of

$$B_{\mathrm{S}}(r_1, r_2, r_3) = \sqrt{B_1^2(r_1, r_3) + B_2^2(r_2, r_3) + B_3^2(r_1, r_2, r_3)}. \tag{2.9}$$

In the limit of a small cloud, the static potential is well-approximated by a harmonic trap, characterized by radial and axial trapping frequencies ω_{12} and ω_3. In terms of these measurable values, the static trap-bottom term, the gradient term, and the curvature term are given by

$$B_{\mathrm{S}}(\mathbf{0}) = \frac{2\hbar\omega_{\mathrm{TB}}}{m'_{\mathrm{F}}g_{\mathrm{F}}\mu_{\mathrm{B}}} \tag{2.10}$$

$$B' = \sqrt{\frac{mB_{\mathrm{S}}(\mathbf{0})}{m'_{\mathrm{F}}g_{\mathrm{F}}\mu_{\mathrm{B}}}\left(\omega_{12}^2 + \frac{\omega_3^2}{2}\right)} \tag{2.11}$$

$$B'' = \frac{m\omega_3^2}{m'_{\mathrm{F}}g_{\mathrm{F}}\mu_{\mathrm{B}}}, \tag{2.12}$$

respectively, where we define $\omega_{\mathrm{TB}} = \mu_{\mathrm{B}}g_{\mathrm{F}}B_{\mathrm{S}}(\mathbf{0})/\hbar$ as the "trap bottom" frequency. In the coordinate system of this apparatus, $r_1 \to x$, $r_2 \to z$, and $r_3 \to y$ such that $\omega_{12} = \omega_{x,z}$ and $\omega_3 = \omega_y$.

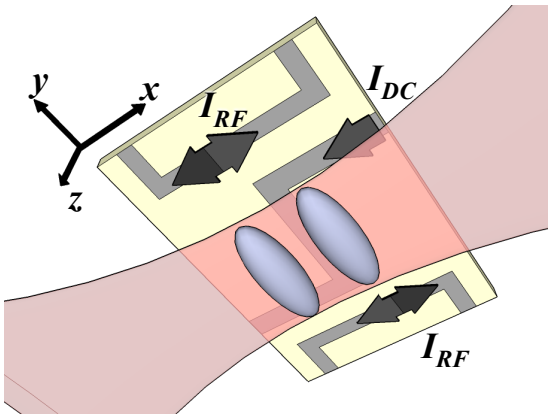

Figure 2.5: Geometry of the chip-based rf-dressed adiabatic double well potential. Purple clouds represent the atom clouds, red beam shows the gravity-compensating levitation beam.

As discussed in §2.2.3, we can use an optical force to compensate for the effects of gravity. This additionally compresses the trap along the weak, y. If we characterize this force through an effective harmonic trapping frequency $\omega_{y,0}$, the total effective potential becomes

$$V_{\mathrm{RWA}}(\mathbf{r}) = m'_F \mathrm{sgn}(g_F)\hbar\sqrt{\delta(\mathbf{r})^2 + \Omega_\perp^2(\mathbf{r})} + \tfrac{1}{2}m\omega_{y,0}^2 y^2, \tag{2.13}$$

where $\delta(\mathbf{r}) = \omega_{\mathrm{rf}} - |\mu_{\mathrm{B}} g_F B_{\mathrm{S}}(\mathbf{r})/\hbar|$ is the detuning, $\Omega_\perp(\mathbf{r}) = \mu_{\mathrm{B}} g_F B_{\mathrm{rf},\perp}(\mathbf{r})/2\hbar$ is the rf Rabi frequency,

Typical values for the parameters in Eqs. 2.12 and 2.13 are: $\omega_{(r,y)} = 2\pi \times (1310, 10)$ Hz, $\omega_{\mathrm{TB}} = 2\pi \times 787$ kHz, $B_{\mathrm{rf},\perp} = 240$ mG, $\omega_{y,0} = 2\pi \times 95$ Hz, and in the $|F = 2, m'_{\mathrm{F}} = 2\rangle$ state of ^{87}Rb we use, $m'_{\mathrm{F}} g_{\mathrm{F}} = 1$.

In Eq. 2.13, the first term under the square root defines a shell of resonance upon which the potential is minimized. The second term indicates the effect of the polarization on the coupling; the vertically (in the z-direction) polarized rf radiation used in this experiment leads to symmetric absolute minima on the shell that are the minima of the double well potential. Figure 2.6 shows the calculated potentials for various values of the detuning, $\delta_0 \equiv \delta(\mathbf{r} = 0)$. Figure 2.5a shows a schematic of the two elongated clouds below the surface of the atom chip with the gravity-compensating laser beam.

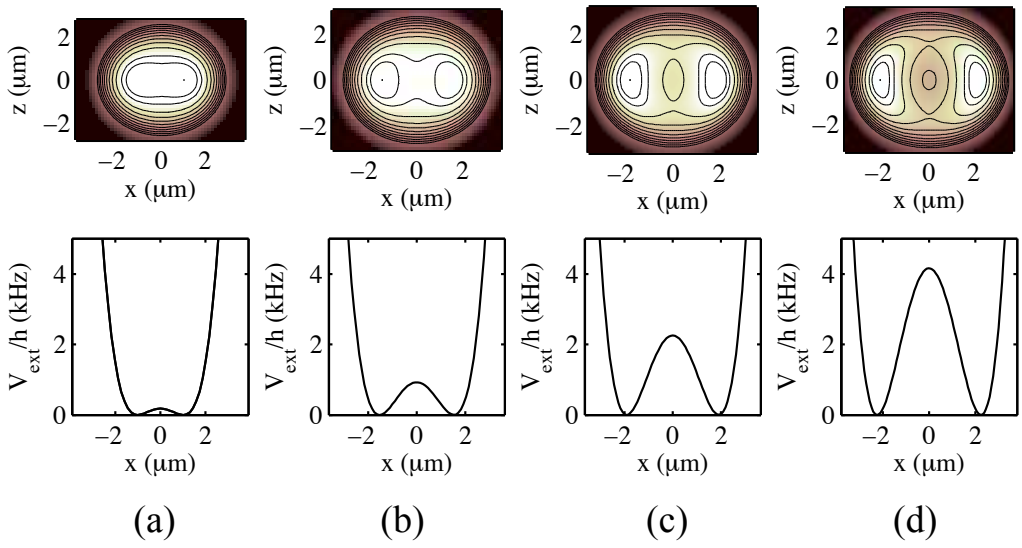

Figure 2.6: Calculated RWA potential energies. Top row shows contours in the $x-z$ plane for $y=0$, with contours at $\Delta V(\mathbf{r})/\hbar = 2\pi\times 1$ kHz from 0 to 10 kHz, with one additional contour at $V(\mathbf{r})/\hbar = 2\pi\times 0.5$ kHz. Bottom row shows cuts through potential at $y=z=0$ for various detunings. (a) $\delta_0 = -2\pi\times 5$ kHz, (b) $\delta_0 = 2\pi\times 0$ kHz, (c) $\delta_0 = +2\pi\times 5$ kHz, and (d) $\delta_0 = +2\pi\times 10$ kHz.

2.3.2 Beyond-rotating-wave corrections

In using Eq. 2.13 to calculate our adiabatically dressed potential, we invoke the rotating-wave approximation (RWA). However, in this experiment, like others [25], the coupling strength is sufficiently strong as to render the approximation invalid. To account for the corrections to the RWA, we calculate the full potential and compare it to the RWA results. We obtain a small correction factor used in all subsequent analyses.

The full expression for the energies of the dressed eigenstates for atoms in a magnetic trap coupled to a strong rf field can be found be diagonalizing the full Hamiltonian describing this system. Following Ref. [25], we consider atoms with total spin $\mathbf{F}$ in a static potential $\mathbf{B}_{\rm S}(\mathbf{r})$ coupled to an oscillating field $\mathbf{B}_{\rm rf}(\mathbf{r})\exp(i\omega_{\rm rf}t)$, leading to the Hamiltonian

$$H_{\rm BRWA}(\mathbf{r}) = g_F\mu_{\rm B}|\mathbf{B}_{\rm S}(\mathbf{r})|F_z + \hbar\omega_{\rm rf}a^\dagger a + \mathcal{G}\left[B_{\rm rf,\perp}(\mathbf{r})a^\dagger + h.c.\right]F_x + \mathcal{G}\left[B_{\rm rf,||}(\mathbf{r})a^\dagger + h.c.\right]F_z \qquad (2.14)$$

where $\mathcal{G} = g_F\mu_{\rm B}/\sqrt{2\langle N_{\rm ph}\rangle}$, $\langle N_{\rm ph}\rangle$ is the average photon number in the rf field, $a^\dagger$(a) is the creation (annihilation) operator of the rf field, and $B_{\rm rf,\perp}(B_{\rm rf,||})$ is the complex amplitude of

the component of $\mathbf{B}_{\rm rf}(\mathbf{r})$ perpendicular (parallel) to the static field $\mathbf{B}_{\rm S}(\mathbf{r})$, for each spatial point $\mathbf{r}$, and *h.c.* denotes the hermitian conjugate.

To diagonalize the Hamiltonian, we use the basis states $\{|m_F;\Delta N_{\rm ph}\rangle\}$ for $F=2$, and we choose a large photon number basis, $\Delta N_{\rm ph} = N_{\rm ph} - \langle N_{\rm ph}\rangle = -12,\ldots,12$. We assume $\langle N_{\rm ph}\rangle \gg 1$ such that $\sqrt{N_{\rm ph}+1} \approx \sqrt{N_{\rm ph}}$. We solve for the energies $E(\mathbf{r})$ from $H(\mathbf{r})\psi_0 = E(\mathbf{r})\psi_0$ and select the eigenvalue which connects to the $|\psi_0\rangle = |F_z = 2, \Delta N_{\rm ph} = 0\rangle$ state. After subtracting off any offset at the trap minimum, we compare this potential energy $E(\mathbf{r})$ to the RWA calculation $V_{\rm RWA}(\mathbf{r})$ for the same values of $\omega_{\rm rf}$ and $\mathbf{B}_{\rm S}(\mathbf{r})$.

To perform the comparison, we choose a single plane at $y=0$. After calculating $E(x,0,z)$ at some δ_0, we perform a two-dimensional fit of $V(x,0,z)$, where $\delta_0 \to \delta_0 + \delta_{\rm shift}$, to this potential energy surface, using $\delta_{\rm shift}$ as the fit parameter. In so doing, we determine a systematic shift by which we adjust the RWA-calculated potentials to account for the beyond-RWA effects. Figure 2.7(a) shows the differences between the two methods of calculaton, while Fig. 2.7(b) shows the necessary shift as a function of the detuning parameter, δ_0.

2.3.3 Potential energy gradients and the double-well potential

As is discussed in Ref. [15] (§6.3.1), gradients in the rf field, $B_{{\rm rf},\perp}(\mathbf{r})$ can lead to the "banana" effect, wherein the potential energy is minimized not at two points opposite each other on the shell of resonance for which $\hbar\omega_{\rm rf} = g_{\rm F}\mu_{\rm B}B_{\rm S}(\mathbf{r})$, but along a "drooping" path between these points. This can be mitigated by reducing the Ioffe bias field and increasing the gradients of the static trap, $B_S(\mathbf{r})$, such that the relative gradient of the rf field is smaller. However, we find these measures are not sufficient to completely eliminate banana effects.

To reduce the effects of gradients in $B_{{\rm rf},\perp}(\mathbf{r})$, we move from antennae close to the atoms to those farther away. Figure 2.8 shows the layout of the atom chip, and panel (b) shows the main wires used in these configurations. The central blue 'Z'-wire provides the main static trapping gradients that lead to $B_{\rm S}(\mathbf{r})$. The original rf adiabatic potentials implemented the red 'U'-shaped wires [15], which are only 100 µm from the centre of the trap (while atoms are trapped $\approx$ 190 µm from the surface of the chip). The magnetic field gradients of the rf field at the position of the atoms are reduced by using the green "end" wires, at 1580 µm from the trap position. The RWA potentials calculated for these two scenarios are compared in Figs. 2.9(a) and (b), where (a) uses the former configuration and (b) the latter. Two main differences are seen: first, the drooping "banana" effect is reduced, and

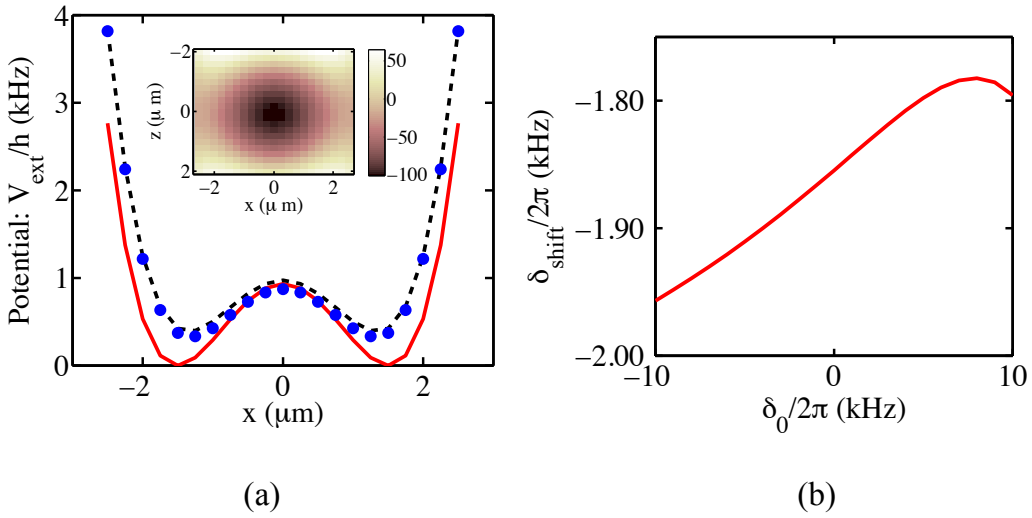

Figure 2.7: Comparisons between RWA and full potential calculations. (a) Potential energy curve through $y = z = 0$ with $\delta_0/2\pi = 0$, calculated using full expression Eq. 2.14 (blue dots), RWA approximation Eq. 2.13 (red solid line), and RWA approximation with fitted shift of $\delta_{\text{shift}}/2\pi = -1.85$ kHz (black dashed line). Inset: difference between full potential and RWA potential with shift over entire 2D plane at $y = 0$ used for fit. Color bar indicates in Hz the difference between the corrected RWA potential and the full calculation. (b) Fitted detuning shift as a function of detuning, i.e., the number one should add to the detuning in the RWA expression to obtain the best estimate of the potential.

second and more drastically, the separation of the clouds looking along the z-axis (bottom panel) is much improved with the far wires. The centres of the traps in the y direction are much closer when the end wires are used.

Despite the improvements seen in Fig. 2.9(b), two problems remain. The drooping effect persists due to the potential gradient of gravity, and a significant twisting of the potentials away from the y-axis arises from the 'Z'-shaped geometry of the trapping wire. The twisting separates the well centres along y to distances on the order of 50 μm. For experiments hoping to study the coupling and tunnelling between BECs in the double well, this prevents significant overlap of the condensate wavefunctions between the wells, and reduces the chance of observing the effects related to that overlap.

To address both the twisting and the drooping, we apply an optical force to the atoms in this trap to levitate and compress the atoms against gravity, as discussed in §2.2.3. We use a focussed Gaussian beam, propagating along x and focussed above the atoms in z to levitate the atoms. The auxillary effect of this optical force is a confinement along y, which

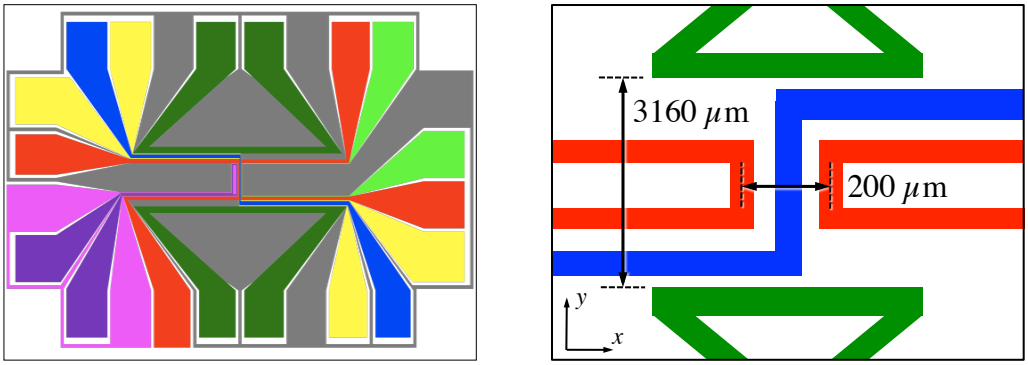

(a) (b)

Figure 2.8: Atom chip schematics. (a) Full layout of the Toronto atom chip. Refer to Ref. [15] for detailed explanation of each wire. (b) Simplified schematic of atom chip, showing the wires relevant to rf dressing in these experiments. Not to scale. Blue 'Z'-wire provides static field, and either the red U-wires or green bar-wires act as rf antennae for the dressed potentials.

brings the trap centres to the same position in y, allowing for good wavefunction overlap. This configuration is shown schematically Fig. 2.5 and the calculation of the RWA potetnial is found in Fig. 2.9(c).

The optical levitation and compression were found to significantly improve the performance of the double well potential for the applications discussed in Chapter 5. These results show that all potential energy gradients must be accounted for when describing the potential of chip-based adiabatic rf potentials.

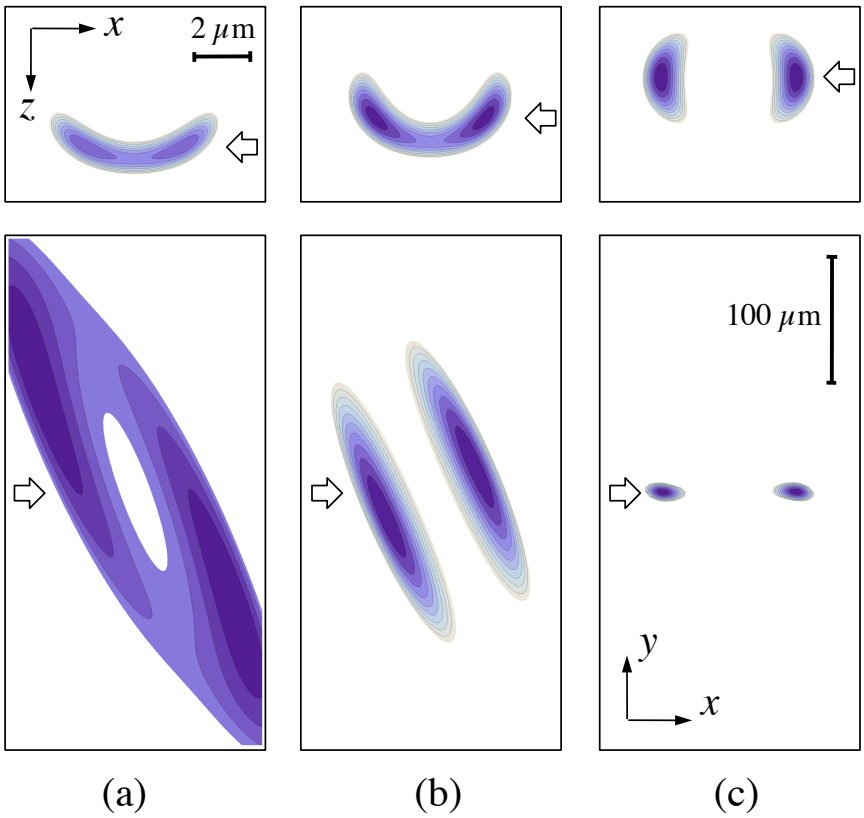

Figure 2.9: Effects of gravity on adiabatic double well potentials. Upper row are cuts at $y = 0$, with a aspect ratio equal in both directions. Bottom row are cuts at $z = z_{\min}$, that is, the vertical position at which the potential is minimized. White arrows show the position of the plane for the corresponding views. Dark regions show small potential energies, with regular spaced contours indicating increasing potential energy. Aspect ratio in upper row is 1:1; horizontal dimensions are equal in top and bottom rows, though the vertical scale is compressed, as indicated by the size bar in (c). (a) Original configuration, U-wire rf source. (b) New configuration, end-wire rf source. (c) New configuration, end-wire rf source, with optical levitation/compression

Chapter 3

Species-specific optical lattices

The ability to design the potential energy landscape for an ultracold gas permits the study many-body phenomena in a variety of environments. Using the forces provided by oscillating electromagnetic fields, optical potentials can be created in single or multiple well configurations, the latter often realized as one-, two-, or three-dimensional lattices. The well-known optical resonances characteristic of each atomic species can be exploited to create differential optical forces for different atomic species or internal states by choosing carefully the wavelength used for these potentials. Several such schemes have been implemented: a "magic wavelength" scheme was used to cancel the differential energy shift between ground and excited states [27], spin-dependent lattices have addressed individually two internal states of an atom [28–31], and species specific dipole potential has been used to separately address the species in a mixture [32].

This chapter discusses two techniques by which an optical trap can be used to selectively address an atomic species while having little or no effect on a second species. The necessary experimental parameters and several applications of this scheme are discussed. The background for this technique is discussed in §3.1 and the description of the effects of optical fields on alkali atoms is found in §3.2. Quantitative measures for evaluating the feasibility of a species-specific potential are defined in §3.3 and applied to two different techniques. These two methods, the "tune-in" and "tune-out" methods are compared for various mixtures of alkali atoms. Section 3.4 discusses the interactions between different atomic species in the selective lattice, including the emergence of a mean-field potential and the thermalization between species. Applications of a species specific lattice, including phase-space increase, phonon inclusion in ultracold gases, and effective mass tuning are discussed in §3.5 before concluding in §3.6.

3.1 Background

As the field of ultracold atoms research enters its adolescence, experiments are increasingly including more than one element or isotope. Dual-species experiments offer possibilities for creating heteronuclear polar molecules [33], sympathetic cooling [34–37], and investigating Bose-Fermi mixtures [35–38] which may provide opportunities for studying boson-mediated superfluid states [39, 40]. More recently, experiments involving up to three atomic species have been implemented for sympathetic cooling of two fermionic species [41, 42].

Dually degenerate experiments have so far used external trapping potentials common to both atomic species. A species-specific trapping potential would add a degree of freedom to improve sympathetic cooling [43], to tune effective mass, or to create a lattice for one species in the presence of a background reservoir. Though careful selection of internal atomic states can provide differential magnetic trapping, optical far-off resonant traps (FORTs) and magnetostatic traps are not species-specific.

Species-selective adiabatic potentials have been proposed [44] and demonstrated [18] in the case of ^{87}Rb -^{40}K, where the Landé factors $|g_F|$ are distinct. A radio-frequency transverse field can be resonant with only one of the two species, selectively deforming its dressed potential. Onofrio and co-workers [43, 45] propose using two overlapping FORTs at frequency detunings far above and below the dominant ground state transitions of both species in a two-species mixture. The confinement of each species can be chosen independently by individually adjusting the intensity of the two beams used to create the trap. Unfortunately, none of these schemes lends itself to a uniform three-dimensional lattice potential for atoms: the radio-frequency scheme fails because it is limited to one-dimensional periodic potentials and the two-frequency balancing because lattice periodicity depends on wavelength. Recently, two schemes for two-dimensional lattices of fixed spacing with arbitrary wavelength have been created using diffractive optics and high-resolution imaging [46, 47].

In this chapter we discuss the generation and application of species-specific optical lattice potentials. Our motivation is the strong analogy between atoms in optical lattices and electrons in crystalline solids. Cold bosons in lattice potentials can be used to explore strongly interacting many-body physics, such as the superfluid-insulator transition [7, 48]. At sufficiently low temperatures, cold fermions in lattices [49, 50] might be able to address open questions about the ground state of the Hubbard Model [13]. Unlike crystal lattices, optical lattices do not support the lattice vibrations responsible for many physical

phenomena. However, phonon mediation between neutral atomic fermions could arise in the presence of a condensed bosonic species capable of sustaining phonon-like excitations [39, 40, 51, 52]. Although Bose-Fermi mixtures were recently loaded into optical lattices [53, 54], the lattices confined bosons as well as fermions. Using a lattice to tune the effective mass of the bosonic background allows a tailoring of the speed of sound in the condensate, and with it, the spectrum of phonon excitations allowed. To couple phonons to the fermions at the edge of the Fermi sea, for instance, requires that the speed of sound in the condensate exceeds the Fermi velocity [55].

We discuss two approaches to species-specific optical potentials, both of which involve only a single frequency of laser light. The first approach is to tune the laser wavelength close to the atomic resonance of one species, making its induced dipole moment much stronger than that of any other atomic species present. We refer to this strategy as the "tune-in" (TI) scheme. A second approach exists for atoms, such as alkalis, with an excited-state fine structure splitting. Between the resonances of the doublet, a wavelength can be chosen such that the induced dipole moment is strictly zero. We refer to this strategy as the "tune-out" (TO) scheme. Both approaches allow for the creation of a species-specific optical lattice with a tunable relative potential strength between species.

In the following sections we consider the relative merits of the TI and TO schemes. We focus our attention on Bose-Fermi combinations throughout, paying special attention to mixtures including ^{87}Rb [17, 49, 56–60].

3.2 Optical potentials for alkali atoms

We consider the light-atom interaction in the limit of a small excited-state fraction. An electromagnetic field induces an electric dipole potential on a neutral atom, which can be used as a trapping potential for ultracold atomic samples. We consider the residual effect of spontaneous emission in §3.2.2.

3.2.1 Dipole potential

An atom in a ground state $|g\rangle$ will experience a potential shift due to coupling by the light field to the excited states $|e\rangle$. We calculate the sum of these shifts on each state $|g\rangle$,

including the counter-rotating term, using second-order perturbation theory:

$$V_g(\mathbf{r}) = \frac{1}{2\epsilon_0 c}\sum_e \left[\frac{|\langle e|\mathbf{d}\cdot\hat{\epsilon}|g\rangle|^2}{\hbar(\omega_\mathrm{L}-\omega_\mathrm{eg})} - \frac{|\langle e|\mathbf{d}\cdot\hat{\epsilon}|g\rangle|^2}{\hbar(\omega_\mathrm{L}+\omega_\mathrm{eg})}\right] I(\mathbf{r}), \tag{3.1}$$

where ω_L is the laser frequency, $\hbar\omega_\mathrm{eg}$ is the energy difference between $|e\rangle$ and $|g\rangle$, $\mathbf{d}$ is the dipole operator, $\hat{\epsilon}$ is the polarization of the light, and $I(\mathbf{r})$ is the spatially-dependent light intensity. In the case of atoms in a weak magnetic field, we use the matrix elements defined in the $|F, m_F\rangle$ basis, where F is the total angular momentum and m_F is the magnetic quantum number.

We will consider only alkali atoms, which have two dominant $n\,\mathrm{s} \to n\,\mathrm{p}$ transitions due to the fine structure splitting. Using nomenclature established by Fraunhofer for the $3^2\mathrm{S}_{1/2} \to 3^2\mathrm{P}_{1/2}$ and $3^2\mathrm{S}_{1/2} \to 3^2\mathrm{P}_{3/2}$ transitions in sodium, we label the corresponding lines in each of the alkalis D_1 and D_2, respectively. Spin-orbit coupling splits each excited state by a frequency $\Delta_\mathrm{FS} = \omega_{D_2} - \omega_{D_1}$, while each ground and excited state is further split by the hyperfine interaction Δ_HFS and Δ'_HFS, respectively. The atomic data used for Eq. (3.1) are the measured linewidths and line centres of the D_1 and D_2 lines, and the ground and excited state hyperfine splittings [61–66].

Transitions to higher excited states $n\,\mathrm{s} \to (n{+}1)\,\mathrm{p}$ are neglected by our treatment. When detuned within Δ_{FS} of the $n\,\mathrm{s} \to n\,\mathrm{p}$ transition, the relative magnitude of the $n\,\mathrm{s} \to (n{+}1)\,\mathrm{p}$ shift is less than 2×10^{-5} for Cs and 7×10^{-8} for Li.

As Eq. (3.1) requires a sum over several states and knowledge of individual matrix elements, it is useful to have an approximate but simpler expression for V_g. If the detunings $\Delta_\mathrm{eg} = \omega_\mathrm{L} - \omega_\mathrm{eg}$ are small compared to Δ_FS, but large compared to the excited state hyperfine splitting Δ'_HFS, an approximate expression for the dipole shift is [19]

$$V_g(\mathbf{r}) \approx \frac{\pi c^2\Gamma}{2\omega_0^3}\left(\frac{1-\mathscr{P}g_F m_F}{\Delta_1} + \frac{2+\mathscr{P}g_F m_F}{\Delta_2}\right) I(\mathbf{r}), \tag{3.2}$$

where $\mathscr{P} = 0, \pm1$ for π, $\sigma^\pm$ polarization, respectively, g_F is the Landé factor, $\Delta_{1(2)}$ is the detuning from the $\mathrm{D}_{1(2)}$ line, $\omega_0 = (\omega_{\mathrm{D}_1} + 2\omega_{\mathrm{D}_2})/3$ is the line centre weighted by line strength, and $\Gamma = (\Gamma_{\mathrm{D}_1} + \Gamma_{\mathrm{D}_2})/2$ is the average of the D_1 and D_2 linewidths. Since $\Gamma_{\mathrm{D}_2}/\Gamma_{\mathrm{D}_1} \approx 1 + 3\Delta_\mathrm{FS}/\omega_0$, one can expect an accuracy between $\pm7\%$ for Cs and $\pm0.003\%$ for Li. At small detunings, we empirically find that Eq. (3.2) deviates from Eq. (3.1) by $\approx1\%$ for detunings $\min\{|\Delta_1|, |\Delta_2|\}/2\pi \lesssim 1.5\sqrt{\widetilde{m}}$ GHz, where $\widetilde{m}$ is the mass in atomic units.

As an approximate form, Eq. (3.2) neglects the counter-rotating terms. For $|\Delta| < \Delta_\mathrm{FS}$, the strength of the counter-rotating contribution is at most $\Delta_\mathrm{FS}/2\omega_\mathrm{L}$ relative to the

contribution of one near-resonant dipole transition. Thus the neglected shift is at most -2% for Cs, and -0.001% for Li for estimates of the TO wavelength. Scenarios involving larger detunings require the full expression Eq. (3.1); for consistency, this expression is used in the following sections unless otherwise specified.

3.2.2 Heating rates

Detuning and intensity of optical traps must be chosen with consideration of the incoherently scattered trapping light that heats the atoms. For each state $|g\rangle$, we quantify the rate of scattering in the low saturation limit,

$$\gamma_{\rm sc} = \frac{I(\mathbf{r})}{2\epsilon_0 c}\sum_e \frac{\Gamma_e |\langle e|\mathbf{d}\cdot\hat{\epsilon}|g\rangle|^2}{\hbar^2}\left[\frac{1}{(\omega_{\rm L}-\omega_{\rm eg})^2}+\frac{1}{(\omega_{\rm L}+\omega_{\rm eg})^2}\right] \tag{3.3}$$

where $\Gamma_{\rm e}$ is the natural linewidth of the $g \to e$ transition, and $\Delta_{\rm eg} = \omega_{\rm L} - \omega_{\rm eg}$. The rate of scattering of photons can be converted to an average heating rate, $H_g = \frac{2}{3}E_{\rm R}\gamma_{sc}$, where $E_{\rm R} = \hbar^2k^2/2m$ is the recoil energy, $k = \omega_{\rm L}/c$, and c is the speed of light. The factor of 2/3 arises due to the partition of energy $E = \frac{3}{2}k_{\rm B}T$.

This estimate of the heating rate is derived from the product of the spontaneous decay rate and the excited state population. In semiclassical treatments of the heating rate, absorption and induced emission effects were also found to be important [1]. For a standing wave potential, the three contributions to the heating rate are found to add in such a way as to render the heating rate independent of position in the lattice, at a value that is given by $H_g(I_{\rm max})$, where $I_{\rm max}$ is the maximum intensity in the standing wave.

Recent calculations of heating in a lattice accounting for the quantum mechanical motion of the atoms confirms this position independence, if atoms can access multiple bands within the lattice [2]. The heating rate for the ground band is less than the above value, and is smaller for blue-detuned lattices than for red. The heating rate, therefore, will depend on the configuration used in a particular experiment, and must be adjusted accordingly. For the purposes of the calculations in this chapter, we consider $H_g(I_{\rm max})$, which can be modified as the experimental consideration dictates according to some factor as found, for example, in Ref. [2].

3.3 Species selection

It is not surprising that optical traps can be species-specific given that optical resonances are unique to atomic elements and isotopes. However, most species-specific optical traps, such as magneto-optical traps, are tuned to within a few linewidths of resonance, which is incompatible with quantum degenerate ensembles. At low temperatures and high density, any gain in trap depth close to resonance must be balanced against the heating due to unwanted light scattering (§3.2.2).

In the subsections below we consider two-species mixtures. The goal is to apply a dipole force to the "target" species while inducing as little potential as possible on the second species, which we will call the "spectator". We define the "selectivity" as

$$\mathbb{S} = \left| \frac{V_\mathrm{t}}{V_\mathrm{s}} \right|, \tag{3.4}$$

where $V_{\mathrm{t,(s)}}$ is the potential induced on the target (spectator).

As discussed in §3.2, in the low saturation limit, both the induced dipole potential and the heating rate are proportional to intensity. We define the intensity-independent ratio

$$\mathsf{s} = \frac{V_\mathrm{t}}{H_\mathrm{t} + H_\mathrm{s}} \tag{3.5}$$

to be the "sustainability", where $H_{\mathrm{t(s)}}$ is the heating rate of the target (spectator). The absolute value of s sets the scale for possible trapping time[1]. The laser frequency will be chosen to maximize both $\mathbb{S}$ and $|\mathsf{s}|$.

3.3.1 Tune-out method: cancelling the Stark shift

The tune-out wavelength scheme exploits the characteristic doublet structure of the alkali atoms. By choosing a wavelength that lies between the two strongest transitions, the large negative energy shift of the D_2 line is balanced against the large positive energy shift of the D_1 line (see Fig. 3.1). This atom becomes a spectator, while any other species feels the shift induced by the laser and becomes a target. Since the potential shift on the spectator can be zero, the selectivity of the tune-out approach is infinite.

The laser frequency, ω_TO, at which $V_\mathrm{s} = 0$, is determined numerically using Eq. (3.1) with all $|F, m_\mathrm{F}\rangle$ excited states in the D_1 and D_2 manifolds. Table 3.1 shows the tune-out

[1]The sustainability, s, has units of seconds and gives the approximate time it would take to heat the atoms out of the trap

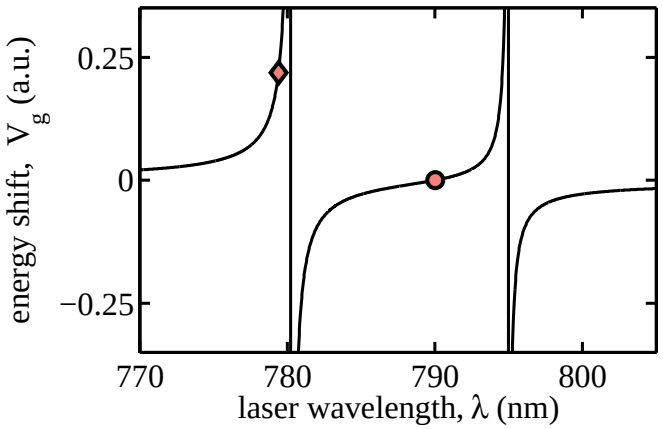

Figure 3.1: Energy shift as a function of wavelength for ^{87}Rb in the $|F, m_F\rangle = |2, 2\rangle$ state, under linear polarization, for 1 mW/cm^2. This general structure will arise for each of the alkali elements, with the divergences located at the D_1 and D_2 lines. The tune-in scheme for a ^{87}Rb target is indicated by the diamond marker on the blue-detuned branch of the potential energy curve. The round marker indicates the position of the tune-out wavelength, where the energy shift is zero. Here, ^{87}Rb is the spectator.

wavelength for all ^{87}Rb ground states with π, x, σ^+, and σ^- polarizations[2]. An approximate expression for this wavelength can be derived from Eq. (3.2), giving

$$\omega_{\mathrm{TO}} = \omega_0 - \frac{1 + P g_{\mathrm{F}} m_F}{3} \Delta_{\mathrm{FS}}. \tag{3.6}$$

For ^{87}Rb , Eq. (3.6) predicts tune-out wavelengths of 785.10 nm, 787.54 nm, 790.01 nm, and 792.49 nm for $P g_{\mathrm{F}} m_F$ = -1, -0.5, 0, and 0.5, respectively. Comparing these values to the results of Table 3.1, we see the that approximations are accurate to 0.04 nm or better. Equation (3.6) also gives $\omega_{\mathrm{TO}} = \omega_{\mathrm{D}_1}$ for the case of $P g_{\mathrm{F}} m_F = 1$, which is inconsistent with the assumption that $|\Delta_1| \gg \Delta_{\mathrm{HFS}}$. In fact, since $P g_{\mathrm{F}} m_F = 1$ corresponds to a dark state with respect to the D_1 excitation, there is no tune-out wavelength for this case.

We note that in Table 3.1 the tune-out wavelengths for linear (π and x) polarizations are nearly independent of the choice of ground state, in contrast to σ^+ or σ^- polarizations. Given this independence, we calculate the tune-out wavelengths using Eq. (3.1) for several of the common alkali isotopes in their stretched ground states under x polarization (Table 3.2)[3].

[2]By x polarization, we refer to an equal superposition of σ^+, and σ^- polarizations.

[3]Unlike for σ^+, σ^-, geometric considerations allow that linear (either x or π) polarization can be chosen for all directions of a 3D optical lattice when a weak quantizing magnetic field is present along one of the

Polarization	$\|F, m_F\rangle$	λ_{TO} (nm)	γ_{sc}/I ($\mathrm{cm}^2/\mathrm{mJ}$)
π	$\|2, \pm 2\rangle$	790.04	
	$\|2, \pm 1\rangle$	790.04	
	$\|2, 0\rangle$	790.04	9.0×10^{-6}
	$\|1, \pm 1\rangle$	790.04	
	$\|1, 0\rangle$	790.03	
x	$\|2, \pm 2\rangle$	790.04	
	$\|2, \pm 1\rangle$	790.04	
	$\|2, 0\rangle$	790.03	9.1×10^{-6}
	$\|1, \pm 1\rangle$	790.03	
	$\|1, 0\rangle$	790.04	
σ^-	$\|2, 2\rangle$	785.13	9.1×10^{-6}
	$\|2, 1\rangle$	787.58	8.1×10^{-6}
	$\|2, 0\rangle$	790.03	9.1×10^{-6}
	$\|2, -1\rangle$	792.53	14.5×10^{-6}
	$\|2, -2\rangle$	(none)	-
	$\|1, 1\rangle$	792.51	14.5×10^{-6}
	$\|1, 0\rangle$	790.03	9.1×10^{-6}
	$\|1, -1\rangle$	787.57	8.1×10^{-6}
σ^+	$\|2, 2\rangle$	(none)	-
	$\|2, 1\rangle$	792.50	14.4×10^{-6}
	$\|2, 0\rangle$	790.03	9.1×10^{-6}
	$\|2, -1\rangle$	787.59	8.1×10^{-6}
	$\|2, -2\rangle$	785.13	9.1×10^{-6}
	$\|1, 1\rangle$	787.58	8.1×10^{-6}
	$\|1, 0\rangle$	790.03	9.1×10^{-6}
	$\|1, -1\rangle$	792.51	14.5×10^{-6}

Table 3.1: Tune-out wavelengths and scattering rates in ^{87}Rb, for select polarizations and all ground states. Two states have no tune-out wavelength, because the D_1 line has no $F = 3$ excited state.

Tables 3.1 and 3.2 also give the scattering rates per unit intensity (scattering cross-

coordinate axes.

Element	$\lvert F, m_F\rangle$	λ_{TO} (nm)		γ_{sc}/I
		Eq. (3.1)	Eq. (3.2)	($\mathrm{cm}^2/\mathrm{mJ}$)
^{6}Li	$\lvert\frac{3}{2},\frac{3}{2}\rangle$	670.99	670.99	2.8
^{7}Li	$\lvert 2,2\rangle$	670.97	670.97	2.4
^{23}Na	$\lvert 2,2\rangle$	589.56	589.56	2.0×10^{-3}
^{39}K	$\lvert 2,2\rangle$	768.95	768.95	1.4×10^{-4}
^{40}K	$\lvert\frac{9}{2},\frac{9}{2}\rangle$	768.80	768.80	1.7×10^{-4}
^{87}Rb	$\lvert 2,2\rangle$	790.04	790.01	9.1×10^{-6}
^{133}Cs	$\lvert 4,4\rangle$	880.29	880.06	1.5×10^{-6}

Table 3.2: Tune-out wavelengths and scattering rates for various elements. We have assumed x-polarization and stretched states, and show a comparison of Eqs. (3.1) and (3.2).

section) for the spectator species at the tune-out wavelength. Due to the large dispersion of fine splitting among the alkalis, scattering cross-sections vary by over 6 orders of magnitude. To understand the implications for trapping, we need to consider the sustainability, s, of various pairs of atomic species. Table 3.3 shows s_{TO} in the same mixtures for which s_{TI} is calculated. Spectators with larger scattering cross-sections at λ_{TO} have lower sustainability. In addition to these data, we note that the ^{133}Cs-^{87}Rb spectator-target combination gives the highest possible sustainability among alkalis in the tune-out scheme: $\mathsf{s} = 34$ s at a tune-out wavelength of $\lambda_{\mathrm{TO}} = 880.29$ nm (not shown in tables).

As an example, consider making a linearly-polarized lattice for ^{40}K ($\lvert F = 9/2, m_F = 9/2\rangle$) only, leaving ^{87}Rb ($\lvert F = 2, m_F = 2\rangle$) unaffected by the lattice and confined only by a background magnetic trap or FORT. If we consider the mixture in a three-dimensional lattice of arbitrary depth, the ^{40}K potential shift is 1.54×10^{-5} μK×$[I(\mathrm{mW/cm^2})]$; with beams of 100 μm waist, the potential shift is 98 nK/mW. If we require the target to experience a lattice that is $8E_{\mathrm{R}}$ deep[4] where E_{R} is the recoil energy, we find a ^{87}Rb heating rate of 210 nK/s.

3.3.2 Tune-in method: differential optical forces

The simplest selective potential is one in which the laser is tuned close to a resonance of the target (see Fig. 3.1). Since scattering rate is inversely proportional to the square of the detuning, we consider only heating of the target such that $\mathsf{s}_{\mathrm{TI}} \to V_{\mathrm{t}}/H_{\mathrm{t}}$. Considering

[4] In a 3-dimensional optical lattice, the first band is fully confined for lattice depths $\geq 7.4\ E_{\mathrm{R}}$.

Target		Spectator				
	$\mathbb{S}$	^{7}Li	^{23}Na	^{39}K	^{87}Rb	^{133}Cs
^{6}Li	∞	0.00134	7.77×10^{-4}	-0.0381	-1.19	-8.26
	100	1.37×10^{-8}	0.217	0.290	0.332	0.601
	10	2.70×10^{-6}	2.03	3.11	3.55	6.42
^{40}K	∞	4.28×10^{-7}	5.77×10^{-4}	0.188	-8.99	-25.4
	100	2.35	3.45	1.04×10^{-5}	0.267	1.83
	10	23.3	34.1	4.68×10^{-4}	3.49	25.6

Table 3.3: Sustainabilities, s, of two-species mixtures for tune-out and tune-in schemes, in units of seconds, using Eq. (3.5). The second column indicates the selectivity. Rows with $\mathbb{S} = \infty$ are calculated using the TO scheme while rows with $\mathbb{S} = 100$ and $\mathbb{S} = 10$ use the TI scheme. For the lighter spectators, the TI scheme has higher $|\mathsf{s}|$. The heaviest elements and isotope mixtures favor the TO scheme.

Eq. (3.2) in the limit $|\Delta_t| \ll |\Delta_s|$, a simple estimate is

$$\mathsf{s}_{\mathrm{TI}} \approx \left(\frac{3\hbar}{2E_{\mathrm{R,t}}\Gamma_{\mathrm{t}}}\right)\Delta_{\mathrm{t}}. \tag{3.7}$$

The choice of detuning Δ_{t} will depend upon the desired selectivity. Assuming the wavelength is chosen near the D2 line of the target and the spectator is far-detuned, $\Delta_{\mathrm{s}} \approx (\omega_{0,\mathrm{t}} - \omega_{0,\mathrm{s}})$ and

$$\mathbb{S}_{\mathrm{TI}} \approx \left(\frac{2\Gamma_{\mathrm{t}}}{3\Gamma_{\mathrm{s}}}\frac{\omega_{0,\mathrm{s}}^3|\omega_{0,\mathrm{t}} - \omega_{0,\mathrm{s}}|}{\omega_{0,\mathrm{t}}^3}\right)\frac{1}{|\Delta_{\mathrm{t}}|}. \tag{3.8}$$

Together, Eqs. (3.7) and (3.8) explicitly show the opposing dependence on Δ_{t} and the necessary trade-off between selectivity and sustainability.

Table 3.3 shows the sustainability for bosonic species as spectators and fermionic species as targets, calculated using Eqs. (3.1) and (3.3) for tune-in selectivities of 100 and 10. The inverse scaling predicted by Eqs. (3.7) and (3.8) is observed: s_{TI} drops by approximately a factor of ten when $\mathbb{S}_{\mathrm{TI}}$ is increased by a factor of ten. The product of s_{TI} and $\mathbb{S}_{\mathrm{TI}}$ in Table 3.3 varies between 22 s and 36 s for ^{6}Li mixtures and between 26 s and 530 s for ^{40}K mixtures, whereas Eqs. (3.7) and (3.8) would predict a ranges of 8 s to 21 s and 64 s to 132 s, respectively, excluding isotope mixtures from the comparison. Finally, we note that ^{23}Na-^{40}K is the optimal tune-in mixture.

3.3.3 Discussion: tune-in vs. tune-out

With the data of Table 3.3, we can evaluate the practicality of both the tune-in and tune-out schemes for Bose-Fermi mixtures of neutral alkali atoms. Since the scattering rate in the tune-out scheme can be smaller for elements with larger fine structure splittings, this approach is better suited to more massive elements[5]. In particular, the tune-in scheme is preferable for Li-Na, Li-K, and K-Na mixtures, and for applications requiring selectivity of less than 10:1. The tune-out scheme is preferable for Li-Cs, K-Rb, and K-Cs mixtures when the selectivity required is greater than 10:1, and for Li-Rb mixtures at selectivity of greater than 20:1.

An isotope mixture of potassium could be compatible with the tune-out scheme, where $\mathsf{s} > 100$ ms. Isotope-specific manipulation within a lithium mixture is less practical due to sustainabilities of 1 ms or less.

Other factors may also influence whether the tune-in or tune-out approach is preferred. For experiments with time scales that are slow compared to the thermalization rate (discussed further in §3.4.2), it may be preferable to heat the minority species and allow for sympathetic cooling. If the reservoir of spectator atoms is large, the tune-in scheme might be preferred since extra energy due to near-resonant heating would be transferred to the reservoir. For experiments on time scales fast compared to the thermalization rate, the tune-out scheme might be preferred even if s is smaller, since spectator heating will not affect the target.

Finally, we note that if a third species is included, it will play a spectator role in the tune-in scheme and a target role in the tune-out scheme.

3.4 Interspecies interactions

3.4.1 Mean field interactions

Interactions between elements may couple the environment felt by the target to the spectator, spoiling the species-specific potential shaping of both schemes. If target atoms are trapped in a lattice in the presence of a background spectator species, a periodic interaction potential could arise for the spectator due to its interaction with the periodically modulated

[5]The fine structure splitting increases approximately as the third power of mass.

density of the target. A mean-field approach is used to make a simple estimate of the magnitude of this effect. The interaction potential of the spectator due to the target is given by

$$V_{\mathrm{int,s}} = \frac{4\pi\hbar^2|a_{\mathrm{st}}|n_t}{m_{\mathrm{st}}}, \tag{3.9}$$

where a_{st} is the scattering length between species, n_{t} is the density of the target, and $m_{\mathrm{st}} = 2m_{\mathrm{s}}m_{\mathrm{t}}/(m_{\mathrm{s}} + m_{\mathrm{t}})$ is the reduced mass. For a lattice potential

$$V_{\mathrm{t}}(x, y, z) = \eta E_{\mathrm{R}} \cos^2(4\pi x/\lambda) \cos^2(4\pi y/\lambda) \cos^2(4\pi z/\lambda), \tag{3.10}$$

where $\eta = V_{\mathrm{t}}^{\mathrm{pk}}/E_{\mathrm{R}}$, the trap is approximately harmonic near the centre of a lattice site with a characteristic frequency $\omega_{\mathrm{latt}} = (4\pi/\lambda)\sqrt{\eta E_{\mathrm{R}}/m_{\mathrm{t}}}$. Assuming a single atom per site, the standard harmonic oscillator ground state in such a trap gives a density

$$n_{\mathrm{t}}(\mathbf{0}) = \left(\frac{m_{\mathbf{t}}\omega_{\mathrm{latt}}}{\pi\hbar}\right)^{3/2}. \tag{3.11}$$

The minimum potential seen by the spectator atoms will be dominated by the interactions with the target. The selectivity is limited to a maximum value

$$\mathbb{S}_{\mathrm{max}} \equiv \left|\frac{V_{\mathrm{t}}}{V_{\mathrm{int,s}}}\right| = \frac{\hbar m_{\mathrm{st}}\eta^{1/4}}{32\pi|a_{\mathrm{st}}|m_{\mathrm{t}}^{3/2}E_{\mathrm{R}}^{1/2}}. \tag{3.12}$$

In the case of the ^{6}Li-^{87}Rb stretched state target-spectator mixture, the interaction-limited selectivity is $\mathbb{S}_{\mathrm{max}} = 3.1\eta^{1/4}$ [60], while for the ^{40}K-^{87}Rb stretched-state target-spectator mixture, it is $\mathbb{S}_{\mathrm{max}} = 0.22\eta^{1/4}$. To be in a regime where interaction effects might be ignored, we require $\mathbb{S}_{\mathrm{max}} \gg 1$ which gives $\eta \gg 0.01$ for ^{6}Li-^{87}Rb and $\eta \gg 400$ for ^{40}K-^{87}Rb . While for the lithium target, this condition is quite reasonable, the large lattice depths required for potassium would completely localize the atoms to individual sites and prevent the exploration of interesting tunneling-driven physics. Overcoming this interaction limitation and achieving the high selectivity discussed in §3.3 may be possible by tuning a magnetic field to a value where $a_{\mathrm{RbK}} \approx 0$ near a Feshbach resonance [67]. For instance, with depth $\eta = 8$ and $\mathbb{S}_{\mathrm{max}} \geq 10$, the scattering length between species is limited to $|a_{\mathrm{st}}| \leq 7.5a_0$, where a_0 is the Bohr radius.

Where species selectivity is not the goal, this interaction-induced periodic potential for a second species could be used to generate alternative lattice potentials. Such potentials are non-sinusoidal, do not involve a Stark shift, and may have a dynamic structure if target atoms are mobile. The strength of this induced potential could be controlled through the interaction strength, such as at a Feshbach resonance, as described above.

3.4.2 Thermalization

An understanding of the thermalization between species is important when considering heating or cooling in the trap. The rate at which energy is transferred between the species will be relevant in setting the time scales on which adiabatic experiments can take place. Thermometry is also possible if there is good thermalization between species; a high density target could be confined within a species-specific lattice while the spectator remains extremely dilute and thus at lower quantum degeneracy, where temperature is more easily measured. Conversely, thermal isolation could be useful in shielding one species from the spontaneous heating in the other.

In the classical limit, the thermalization rate is proportional to the collision rate of the atoms in the trap, given by $\gamma_{\text{coll}} = n\sigma v$, where n is the overlap density, σ the scattering cross-section, and v the relative velocity between species. Random collisions act to equilibrate the system and the rate of rethermalization is $\gamma_{\text{therm}} = \mathcal{C}\gamma_{\text{coll}}$, where $\mathcal{C}$ is a coefficient that depends on the geometry of the system. For non-degenerate atoms in a three-dimensional harmonic trap, $\mathcal{C} \approx 1/2.7$ [68], but may be modified by, for instance, Pauli blocking where in one experiment $\mathcal{C} \approx 1/0.75$ [69], or by reducing the dimensionality, where, for instance, thermalization is not completed after thousands of collisions [70].

For a degenerate mixture of bosons and fermions, the classical picture of scattering breaks down and the rate of thermalization decreases as the fermionic system becomes more degenerate. An estimate of the sympathetic cooling of a uniform system in the degenerate regime using the quantum Boltzmann equations gives the rate of change in the degeneracy [71]:

$$\frac{d}{dt}\left(\frac{T}{T_F}\right) = -\frac{6\zeta(3)}{\pi^2}\gamma'_{\text{coll}}\left(\frac{T}{T_F}\right)^2, \tag{3.13}$$

where $\gamma'_{\text{coll}} = (3/8)n_{\text{B}}\sigma v_{\text{F}}$ is the collision rate between species, with the scattering cross-section $\sigma = 4\pi a_{\text{BF}}^2$, Fermi velocity, $v_{\text{F}} = \hbar(6\pi n_{\text{F}})^{1/3}/m_{\text{F}}$, $\zeta(3) \approx 1.20206$ is the Riemann zeta function and T_{F} is the Fermi temperature. Though other assumptions[6] of this treatment are not valid for the systems we consider in this paper, we use this expression to determine an order of magnitude for the thermalization rate.

Taking boson density $n_B = 1 \times 10^{14}$ cm^{-3}, fermion density $n_F = 1 \times 10^{13}$ cm^{-3}, and using the mass for ^{40}K, we calculate that $d/dt(T/T_{\text{F}}) \approx -350s^{-1}(T/T_{\text{F}})^2$ using the three-dimensional thermalization coefficient, which gives a temperature relaxation time of ≈ 30 ms

[6] We assume that the species are of equal mass, that the system is highly degenerate ($T/T_{\text{F}} \ll 1$), and that the bosons are either in the condensate or removed immediately from the system when excited.

at $T = 0.1T_F$. This is an order of magnitude larger than the the classical expectation for the rethermalization time of ≈ 2 ms for particles moving at the Fermi velocity. Thus for rapid experiments in the deeply degenerate regime, thermal contact is essentially broken, allowing, for instance, the target to be unaffected by the heating of the reservoir in the tune-out scheme.

In addition to the reduction in thermalization due to Fermi statistics, recent experiments [31] have found that thermalization between two spin states in a state-dependent lattice is suppressed, indicating that the confinement of the lattice may also play a role.

3.5 Applications of species specificity

3.5.1 Isothermal phase space increase

Two-species mixtures can be used to realize various cooling schemes. For example, dark state cooling by superfluid immersion is discussed in Ref. [72]. We present two simple cooling scenarios in which the presence of an uncompressed spectator allows the target species to be compressed with negligible temperature increase but significant improvement in phase space density. In both cases, target atoms are first compressed isothermally, spectator atoms are then removed from the trap, and finally, the target atoms are decompressed adiabatically.

We consider a species-selective single well dipole trap and a species-selective lattice. A closed cycle is described for both scenarios with atoms beginning and ending in a FORT. We assume that the heat capacity ratio between spectator and target is infinitely large and that thermalization in the spectator and between the spectator and target species is faster than any other time scale considered. The latter assumption may restrict fermion cooling to the non-degenerate regime (see §3.4.2).

In the first scenario, schematically represented in Fig. 3.2, a single species-specific beam crosses a FORT. Adiabatic cooling reduces temperature in proportion to the ratio of average trapping frequencies, that is, $T_i/T_f = \overline{\omega_i}/\overline{\omega_f}$, where i, f indicate "initial" and "final". As an example, consider ^{40}K-^{87}Rb and ^{6}Li-^{87}Rb mixtures, confined by a 1064 nm, 500 mW single-beam FORT with a $1/e^2$ radius of 20 µm and a corresponding trap-averaged harmonic oscillator frequency $\overline{\omega_i} = 2\pi \times 540$ Hz for ^{40}K and $\overline{\omega_i} = 2\pi \times 950$ Hz for ^{6}Li. A 500 mW, 50 µm waist beam at λ_{TO} (see Table 3.2) is turned on perpendicular to the FORT to compress the fermions in a trap with frequency $\overline{\omega_f} = 2\pi \times 3040$ Hz for ^{40}K and $\overline{\omega_f} = 2\pi \times 3810$ Hz for

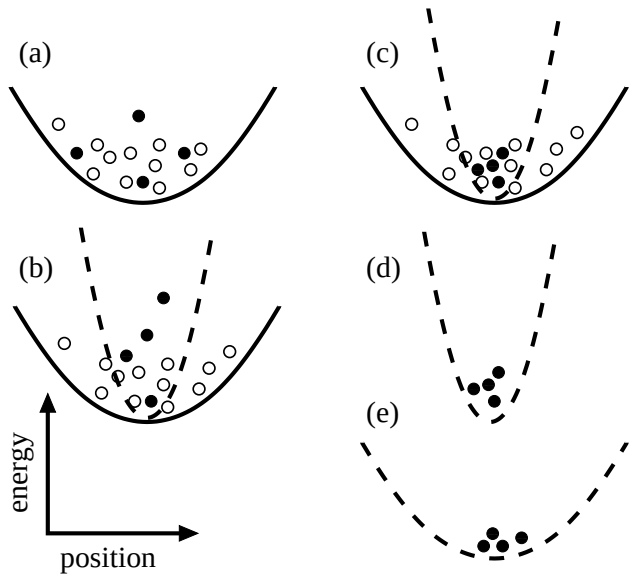

Figure 3.2: A cooling procedure using species-specific trapping; one-dimensional trap shape represents three-dimensional trap-averaged shape. The solid line represents a FORT, the dashed line the species-specific trap; open circles are the spectator species and closed circles are the target. (a) Two species are trapped in a FORT; (b) the species-selective beam is turned on, compressing and heating the target species; (c) the target species rethermalizes with the spectator; (d) the spectator is removed; (e) the target is adiabatically decompressed to a lower temperature and transferred to a FORT.

lithium. After providing sympathetic cooling during the compression of the target atoms, the rubidium is ejected from the trap by temporarily removing the FORT or by using a resonant pulse of light. The species-specific trap is then adiabatically ramped down and turned off, leaving the fermions in the FORT at a temperature approximately 5.7 (4.0) times colder than when they began for potassium (lithium). Though this is a modest change in temperature, the phase space density in a harmonic trap is proportional to the inverse cube of the temperature, indicating a factor of 180 increase in phase space density for potassium and a factor of 60 for lithium.

In the second scenario, we consider a 3D lattice created by the tune-out wavelength[7]. The target-specific lattice is ramped on until peak lattice intensity is reached. The spectator is evaporatively cooled and ejected by reducing the spectator trap depth. The lattice is then ramped back down isentropically, leaving the target in the initial trap with an entropy and

[7] 1D and 2D lattices may be a way to increase confinement strength of the first scheme. Assuming high per-site occupancy, the cooling attained will be governed by single-site physics.

temperature limited by the "plateau entropy" discussed in [73]. As shown there, a target of fermions with unity filling has an entropy plateau of zero, which would suggest no lower limit to the achievable temperature.

An important limitation of these schemes will be the competition between adiabaticity and heating. For an ideal gas, the condition of adiabaticity requires any changes to take place in times longer than the inverse of the smallest trap frequency. Using the numbers given in the ^{40}K-^{87}Rb example of the crossed dipole trap in the tune-out scheme, we find that adiabaticity requires a relaxation time of 35 ms, at an intensity of 3.5×10^7 mW/cm^2, yielding a heating of 1.3 μK during this time, which sets a lower bound for the temperature attainable in this scheme. Another possible limitation of the cooling schemes is the interspecies thermalization, which limits the speed of the isothermal step (see discussion in §3.4.2).

3.5.2 Phonons

Unlike crystal lattices of solids, optical lattices do not support phonons. Since these quasiparticles play a leading role in the physics of condensed matter, it is of interest to introduce phonon-like excitations into a system of ultracold atoms in an optical lattice. The boson-mediated interaction between fermions has been studied in both uniform [39, 40, 51, 52] and lattice systems [55, 74, 75]. Little theoretical work has been done on a system in which only the fermions are confined to the lattice [76]. Here, the background bosons are free to interact with the fermions and with one another. If the bosons are degenerate, the condensate can sustain phonon-like excitations and allow for boson-mediated interactions between fermions on spatially separated lattice sites.

For the phonons in the condensate to play a role in mediating interactions, their spatial extent must exceed the lattice spacing. The healing length of a uniform Bose condensate, $\xi = (8\rho a_{st})^{-1/2}$ where ρ is the condensate density and a_{st} is the scattering length between species, sets the relevant length scale. Species-specific trapping allows the superfluid bosons to remain at low density while fermions are tightly bound in the lattice, thereby maximizing the range of the mediated interaction. A finite selectivity does not prevent mediation of interactions, since the bosons remain superfluid at depths less than the Mott-insulator superfluid transition [7], permitting both tune-in and tune-out schemes to be used for this application.

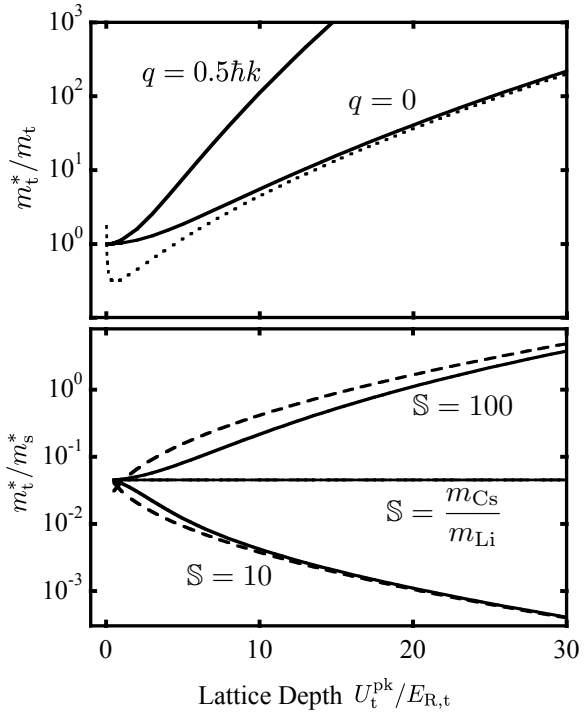

FIGURE 3.3: **(a)** The ratio of the effective mass to bare mass of the target species is shown as a function of trap depth η_t, for both $q = 0$ and $q_c = 0.5\hbar k$, as labeled. The tight binding approximation (dashed line) approaches the exact calculation for $\eta_t \gg 1$. **(b)** The effective mass ratio is shown for the case of a ^{6}Li target and a ^{133}Cs spectator. Whether the ratio increase or decreases depends on the selectivity $\mathbb{S}$ of the lattice. The critical point is when $\mathbb{S} = m_s/m_t$ (= 22.2 in this case), as explained in the text. The tight binding approximation of the effective mass ratio is also shown (dashed line).

3.5.3 Effective mass tuning

An optical lattice can be used to change the effective mass of the atoms in it, allowing for the tuning of experimental parameters including interaction strength [77] and tunneling rate [78], which can be used, for example, to explore different regimes of collective dynamics [79]. The effective mass of a wave packet centered at quasi-momentum q_c is

$$m^*(q_c) = \left[\frac{d^2E}{dq^2}\right]^{-1}_{q_c}, \tag{3.14}$$

where $E(q)$ is the band energy. Figure 3.3(a) shows the effective mass for $q_c = 0$ and $q_c = 0.5\hbar k_L$ in a one-dimensional optical lattice potential $V_{latt}(x) = V_{latt}^{pk} \sin^2(k_L x)$.

For deep lattices, an approximate form for the $q_c = 0$ case is $m^* = \hbar^2 k^2 / 2\pi^2 J$, where J is the tunnelling energy [80], giving an effective mass enhancement

$$\frac{m^*}{m} \approx \frac{e^{2\sqrt{\eta}}}{4\pi^{3/2}\eta^{3/4}}. \tag{3.15}$$

The ratio of effective masses for the target and spectator can be estimated from Eq. (3.15):

$$\frac{m_{\mathrm{t}}^*}{m_{\mathrm{s}}^*} \approx \frac{\exp\left\{2\sqrt{\eta_{\mathrm{t}}}\left(1-\sqrt{m_{\mathrm{s}}/\mathbb{S}m_{\mathrm{t}}}\right)\right\}}{\mathbb{S}^{3/4}}\left(\frac{m_{\mathrm{t}}}{m_{\mathrm{s}}}\right)^{1/4}. \tag{3.16}$$

Figure 3.3(b) shows the effective mass ratio for the case of a ^{6}Li target and a ^{133}Cs spectator. In particular, it is striking that for $\mathbb{S} = 10$, the ratio decreases with lattice depth, while for $\mathbb{S} = 100$, the ratio increases with lattice depth. The critical selectivity is well predicted by Eq. (3.16); at $\mathbb{S} = m_{\mathrm{s}}/m_{\mathrm{t}}$, the effective mass ratio is independent of lattice depth.

Both the tune-out and tune-in schemes provide the means of choosing selectivity. Several tune-in selectivities are shown in Table 3.3; the tune-out selectivity can be chosen simply by choosing a wavelength slightly different from λ_{TO}. In the example used here, the sustainability for $\mathbb{S} = 10$ is better for the tune-in scheme, but tuning to $m_{\mathrm{Li}}^* > m_{\mathrm{Cs}}^*$ at moderate lattice depths requires a $\mathbb{S} = 100$, for which the tune-out scheme has higher sustainability.

3.6 Species selective conclusions

We have discussed how the choice of wavelength used to create an optical lattice can tune its selectivity between elements or isotopes. This control should increase the range of parameters that can be explored in multispecies ultracold atom experiments. The tune-out wavelength scheme allows for the complete cancellation of the trapping potential for one species while providing a confining or lattice potential for any other species in the system. This scheme will work best using the heavier alkali atoms, Rb and Cs, as the spectator elements, and is most successful for the ^{40}K-^{133}Cs fermion-boson mixture. The alternative tune-in scheme uses a near-detuned optical potential, creating a much stronger potential for one element than the others, without the ability to strictly cancel the potential for one element. Mixtures involving the Li, Na, and K as spectators are most compatible with this approach, where the ^{40}K-^{23}Na is the most promising fermion-boson mixture.

The power of species selection is in its use to engineer specific lattice environments for the atoms, including adding a bosonic background to mimic the phonons present in solids, and tuning the relative effective mass of two species. Applications for which experiments are rapid compared to the sustainabilities calculated in §3.3 are especially promising. Species selection enables cooling in a two-species mixture, and in the case of fermions trapped in a lattice, reduces the temperature of fermions as they are loaded into a lattice, in contrast to

current experimental realizations [73, 81]. Though questions regarding the thermalization in a lattice remain open [2, 31, 82], species-specific lattices may help to resolve this issue with their ability to differentially address the components of the system, whose path back to equilibrium can be measured.

Chapter 4

Ultracold ferromagnetism

In the decade following the realization of the first ultracold degenerate Fermi gas [6], much of the scientific focus in this field has been fixed on the physics of strong interactions [83–86]. In this pursuit, the manipulation of the interactions between different components of a cold Fermi gas became a standard technique, and most studies focussed on attractive interactions between the fermionic constituents to induce BCS- and BEC-like superfluidity [10, 87].

Despite the prevalence and success of experiments using strongly attractive interactions between fermions, the equally-accessible repulsive interactions were not completely ignored. Collective behaviours that emerge with attractive interactions do so as a consequence of the pairing of fermions into molecular or Cooper pair bosons, and these statistics allow for the condensation of the pairs. In the regime of strong repulsive interactions, the collective response is more directly inherited from the fermionic statistics of the particles. The canon of such behaviours is diverse and includes one of the most familiar and yet mysterious of physical phenomena – magnetism.

This chapter begins by discussing the development of a quantum-mechanical understanding of magnetism in metals, and the subsequent realization of its possible emergence in ultracold gases in §4.1. Section 4.2 establishes a mean-field description of a trapped degenerate Fermi gas and applies this to the regime of strong repulsive interactions. The emergence of spin segregation and the macroscopic energetic signatures of this crossover are calculated. In an extension to the local density approximation, a term is added to the previous approximation in §4.3 to account for the energetic cost of magnetization gradients, and is used to calculate the optimal spin texture among trial ansatzes. Details of the numerical calculations are given in §4.4 and recent developments related to these calculations

are discussed in relation to these results in §4.5. Section 4.6 discusses the first steps towards the realization of ultracold ferromagnetism in a ^{40}K system, with explorations of the strong interactions near a Feshbach resonance.

4.1 Ferromagnetism in metals and quantum gases

Magnetism in metals

One of the inherent characteristics of an atom or molecule is its magnetic moment – the tendency to align itself with a magnetic field. At the microscopic level, this moment originates from the intrinsic spin of the components of the atom or molecule and the orbital motion of any charged particles within it. From a macroscopic point of view, magnetism arises when these individual components cooperate to form an ordered arrangement, where many or all of the magnetic moments are aligned.

A metal becomes ferromagnetic when the energy of the system is minimal in the configuration where all or most magnetic moments are aligned in the same direction. Due to their relative mobility in a metal compared to the other constituent particles, electrons acts as the agents of magnetism, and their spins are the magnetic moments of interest. The Pauli exclusion principle and its demand for antisymmetrized wavefunctions among these fermions dictates the behaviour of the electron system. A ferromagnetic state will have all magnetic moments in a symmetric spin state and requires a fully antisymmetric spatial state. The increased separation of electrons in the antisymmetric spatial state results in a reduction of Coulomb interactions, and this energy savings will, in some circumstances, be sufficient to induce a ferromagnetic ground state.

It is perhaps surprising that the interactions driving the system towards ferromagnetic order are not predominantly magnetic. The electrostatic Coulomb interaction between the charged particles far exceeds the strength of magnetic dipole-dipole or spin-orbit interactions between particles [88] and is responsible for the magnetism. The spatial wavefunction dependence of the interactions can be described in terms of various possible exchange interactions.

The nature of these exchange interactions can take different forms, which will in turn affect the mechanisms behind a transition to magnetic ordering. “Direct exchange” describes independent magnetic moments localized to individual lattice sites coupled via the

Coulomb interaction, which was used by Heisenberg to formulate one of the first models of ferromagnetism [89]. Through a very different mechanism, Bloch developed a model for ferromagnetism with "itinerant exchange" in which delocalized electrons interact in a conduction band [90]. Experimental evidence suggests that rare earth metal ferromagnetism is better described by a localized model while that in the transition metals like iron, cobalt and nickel is primarily itinerant [91].

Heisenberg's direct exchange ferromagnetism arises from the minimization of total energy for the antisymmetric spatial state. For atoms at fixed separation, the antisymmetric wavefunction will include nodes between the atoms, such that the wavefunction overlap, and thus the Coulomb interaction, is reduced. The correspondence between this wavefunction and the symmetric spin state leads to the system's preference for ferromagnetism.

Itinerant ferromagnetism was initially proposed to account for the non-integral values of the magnetic moment per atom found in nickel, cobalt, iron, and other metals [92], and allowed for conductivity while the material was ferromagnetic. Assuming that antiparallel spins may approach more closely that parallel, due to Pauli exclusion, the energetic cost of the Coulomb repulsion is greater for the unmagnetized (antiparallel) configuration. If this energetic cost exceeds the increase in kinetic energy due to filling the single-spin-state band to higher energies, the parallel spin configuration is preferred and ferromagnetism emerges.

In an attempt to reconcile the two pictures, Hubbard introduced his now-famous model, in part, to explain the origins of ferromagnetism [93]. Citing that the d-bands responsible for ferromagnetism display both atomic- and band-like characteristics, he developed a model to allow for correlations between electrons associated with separated atoms while maintaining the band structure for the conduction electrons. For certain model wavefunctions, ferromagnetism emerges in this model.

The spatial correlations between all electrons are an important consideration in these models, especially for the itinerant-like cases. While parallel spins will avoid each other due to Pauli exclusion, antiparallel spins also avoid each other due to Coulomb repulsion. The subsequent reduction in the potential energy, known as correlation energy, needs to be properly accounted for by a correct choice of many-body wavefunction. Gutzwiller presented one among the first such solutions [94], where he constructed a wavefunction in which opposite spins avoided existing on the same lattice sites. By doing so, he reduced the large repulsive interaction term and was able, within his approximations, to eliminate the ferromagnetic configuration as a ground state, though it was closest to his calculated state for filling factors near one-half.

While many models have been constructed to understand the basis of ferromagnetism, it remains that many-body fermion problems are computationally challenging and calculable microscopic models can only begin to approximate reality. The examples discussed here, along with many more throughout the literature, show that there is a strong model-dependence to many of the conclusions.

Quantum gas magnetism

The realization of ultracold degenerate Fermi gases provided a new vehicle for studies of collective behaviour among fermions. The discovery of Feshbach resonances for the fermionic isotopes of the alkali metal atoms gave experimentalists the tool they needed to arbitrarily control the interaction strength between fermions. While much excitement centred on the attractive nature of the interactions and the ensuing superfluidity of these systems, observations of repulsive interactions were more quietly reported.

In theoretical quarters, discussions of magnetism in these ultracold gases slowly emerged. To mimic the binary spin degree of freedom of the electron, the study of magnetism in neutral fermion gases considers a two-component mixture, where the "pseudospin" components are, for example, two Zeeman sublevels within a ground-state hyperfine manifold of an atom. Contact interactions between these pseudospin components play the role of the Coulomb interaction. Early papers [95–97] describing the effects of interactions in a two-component Fermi gas discuss the phase separation of these spin[1] components for large particle numbers or interaction strengths.

Sogo and Yabu [98] study the energetics of an interacting two-component harmonically trapped Fermi gas, and develop analytic solutions for the density profiles as a function of interaction strength and particle number. By increasing the number in one component or spatially separating the two, the total interaction energy of the system decreases at the expense of an increased total Fermi energy. Above a critical interaction strength, the imbalanced and separated solutions are energetically favourable, and a transition from a paramagnetic to a ferromagnetic state is recognized.

While electrons in a metal can flip their spins, through the spin-orbit interaction, there is no energetically-allowed mechanism by which ultracold atoms can change their pseudospin and flip from one to the other. In assuming that the particle number can be exchanged between components, Sogo and Yabu's results remain outside the realm of experimental

[1] In the remainder of this chapter, we generally refer to the "pseudospin" simply as "spin."

realization for alkali atoms. At the same time, they lend intuition to the analogy between itinerant metallic magnetism and magnetic-like order in ultracold gases by recognizing the competition between interaction and kinetic plus potential energy that allows for a transition between magnetic and non-magnetic states.

In work more closely addressing experimental possibilities, Duine and MacDonald [99] use a beyond-mean-field approach to explore possibilities for itinerant ferromagnetism in ultracold Fermi gases. Due to the conservation of pseudospin required by experiment, they propose initializing the system in a special ferromagnetic state, where each atom is in an equal superposition of the two component states. There is no possibility of interactions in this initial state given the Pauli exclusion principle and the indistinguishability of each atom.

In this situation, two atoms might interact if they become distinguishable via dephasing, which might, for example, arise due to a spatial dependence of the energetic splitting of the two components in the superposition. If the two components, when in a mixed state, are strongly interacting, this interaction will cost energy as the atoms dephase. Duine and MacDonald's results suggest that in the presence of sufficiently strong interactions, the cost of the interaction energy would suppress the dephasing and the lifetime of the ferromagnetic state would increase. The strength of the required interaction is mapped out for various temperatures and a phase diagram shows regions of first and second order transitions between magnetized and unmagnetized states. In this scheme, measures of expansion energy reveal both the amount of interaction energy and the degree to which the system is in a ferromagnetic state.

Further work was done by Berdnikov, Coleman and Simon exploring the ferromagnetic transition of a quantum gas in a trap [100]. Using a Landau-Ginzberg free energy functional, they studied various topological possibilities for the ground state of the system in both two- and three-dimensions and found that geometries with gradual spatial variations in the magnetization were preferred ground states.

Recent quantum Monte Carlo (QMC) studies have confirmed that a ferromagnetic state exists in a gas of ultracold fermions [101]. In this work, the magnetic susceptibility is calculated as a function of interaction strength, and is found to diverge for sufficiently strong interaction strengths. Using these results, a phase diagram for the magnetization vs. interaction strength is mapped out. These results demonstrate that a ferromagnetic state does exist in these gases, and that further study in ascertaining its character is justified.

With particular inspiration from both Refs. [99] and [100], this chapter describes the

critical transition strength for ferromagnetic-like behaviour in a trap and the experimentally observable signatures of this behaviour. In a trapped environment, we use a modified local-density approximation (LDA) to calculate the density profiles for the two components in the system, and use an energy functional approach to calculate the energies of various magnetization configurations.

4.2 Mean-field description of strongly interacting trapped fermions

The initial goals of this theoretical work were to understand the density profiles of a two-spin-component trapped ultracold Fermi gas and their dependence upon the interaction strength between the two spin components. In maintaining the restriction that pseudospin is conserved in this system, we aim to attain results in the vein of Sogo and Yabu [98] and determine a criterion for phase separation and thus ferromagnetism.

We use standard mean-field techniques to accomplish this goal. Though we expect that the local-density approximation (LDA) will break down for large interaction strengths, we expect it will give a good qualitative picture of the phenomena at hand.

In this section, we discuss the density profiles emerging from such an analysis. We examine the energetic signatures of this system and discuss how measurable quantities might indicate the presence of ferromagnetism.

4.2.1 The interacting Fermi gas in the local-density approximation

In analogy to the electron system of a metallic magnet, we consider a two-component Fermi gas, where the two internal states are, for instance, two hyperfine or Zeeman sublevels of the atomic state. We label these levels $|\uparrow\rangle$ and $|\downarrow\rangle$ in analogy to the electron spins these states emulate.

Uniform (untrapped) system

In the uniform (untrapped) system, the hamiltonian describing the two-component Fermi gas is

$$\hat{H}_{\text{MF, uniform}} = \mathbb{V} \sum_{\sigma} \int \frac{d^3\mathbf{K}}{(2\pi)^3} \epsilon_{\mathbf{K}} \hat{c}^{\dagger}_{\mathbf{K}\sigma} \hat{c}_{\mathbf{K}\sigma} + g \int d^3\mathbf{R} \hat{c}^{\dagger}_{\mathbf{R}\uparrow} \hat{c}^{\dagger}_{\mathbf{R}\downarrow} \hat{c}_{\mathbf{R}\downarrow} \hat{c}_{\mathbf{R}\uparrow}, \tag{4.1}$$

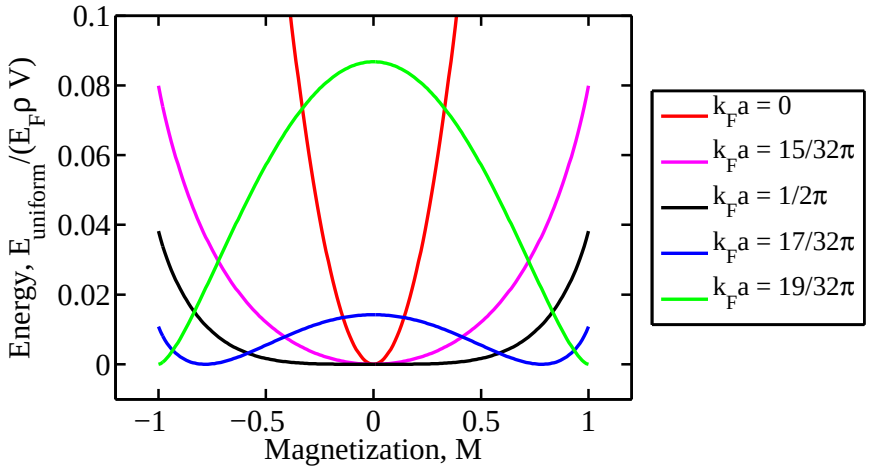

Figure 4.1: Ferromagnetic transition in uniform Fermi gas. Energy vs. magnetization is shown for various values of $k_F a$. The minimum moves from $M = 0$ for values of $k_F a < \pi/2$ to values $|M| \neq 0$ for $k_F a > \pi/2$.

where $g = 4\pi\hbar^2 a/m$ quantifies the interaction, a is the s-wave two-body scattering length, $\epsilon_{\mathbf{K}} = \hbar^2\mathbf{K}^2/2m$ is the kinetic energy, and $\mathbb{V}$ denotes the system volume. The operator $\hat{c}^\dagger_{\mathbf{K}\sigma}(\hat{c}_{\mathbf{K}\sigma})$ creates (destroys) a fermion with spin state σ and momentum $\mathbf{K}$, while the operator $\hat{c}^\dagger_{\mathbf{R}\sigma}(\hat{c}_{\mathbf{R}\sigma})$ acts in position space to create (destroy) a fermion with spin σ at position $\mathbf{R}$.

The density of each component the uniform gas is $\rho_\sigma = N_\sigma/\mathbb{V}$, where N_σ is the number of particles in each spin state, σ. The total kinetic energy of the system is

$$E_{\text{kin}} = \frac{3}{5}\mathbb{V}(E_{F\uparrow}\rho_\uparrow + E_{F\downarrow}\rho_\downarrow), \tag{4.2}$$

where $E_{F\sigma} = \beta\rho_\sigma^{2/3}$ is the Fermi energy of the σ component, and $\beta = (6\pi^2)^{2/3}\hbar^2/2m$. The total interaction energy of the system is

$$E_{\text{int}} = g\mathbb{V}\rho_\uparrow\rho_\downarrow. \tag{4.3}$$

In the uniform system, we can find an analytic solution for the critical transition strength in the crossover to a ferromagnetic state. If we assume that the system starts with locally equal densities of $\rho_\uparrow = \rho_\downarrow = \rho$, we can write the energy of the system $E_{\text{uniform}} = E_{\text{kin}} + E_{\text{int}}$

$$E_{\text{uniform}} = E_F\rho\mathbb{V}\left(\frac{6}{5} + \frac{4k_F a}{3\pi}\right), \tag{4.4}$$

where $k_F = (6\pi^2\rho)^{1/3}$, and $E_F = E_{F,\uparrow} = E_{F,\downarrow}$. If we imagine increasing the scattering length, a, there may come a point at which the system would segregate into two or more domains in which the magnetization, $M = (\rho_\uparrow - \rho_\downarrow)/(\rho_\uparrow + \rho_\downarrow)$ is non-zero. The total energy would become

$$E_{\text{uniform}}(M) = E_F \rho \mathbb{V} \left(\frac{3}{5} \left[(1+M)^{5/3} + (1-M)^{5/3} \right] + \frac{4 k_F a}{3\pi} (1+M)(1-M) \right). \quad (4.5)$$

We can minimize this energy with respect to the magnetization by studying the first and second derivatives of Eq. (4.5), $\partial E_{\text{uniform}}(M)/\partial M$ and $\partial^2 E_{\text{uniform}}(M)/\partial M^2$. Visually, we can see the change in the minimum energy configuration by plotting $E_{\text{uniform}}(M)$, as in Fig. 4.1. For values of $k_F a < \pi/2$, the energetic minimum is always at $M = 0$, and the system remains unmagnetized. For $M = \pi/2$, the second derivative is zero at $M = 0$, and there is an inflection in the curve, indicating a transition to a magnetized state. For $k_F a > \pi/2$, there exist energetic minima at $|M| \neq 0$, indicating the system's preference for a magnetized state.

Trapped system

To extend this treatment beyond the uniform gas, the LDA is employed. At each point, the gas is treated as locally-uniform, with an extra potential energy $V(\mathbf{R})$. Rewriting the hamiltonian Eq. (4.1) with the potential energy term gives

$$\hat{H}_{\text{MF, trap}} = \sum_\sigma \left[\int \frac{d^3\mathbf{K}}{(2\pi)^3} \epsilon_{\mathbf{K}} \hat{c}^\dagger_{\mathbf{K}\sigma} \hat{c}_{\mathbf{K}\sigma} + \int d^3\mathbf{R}\; V(\mathbf{R}) \hat{c}^\dagger_{\mathbf{R}\sigma} \hat{c}_{\mathbf{R}\sigma} \right] + g \int d^3\mathbf{R}\; \hat{c}^\dagger_{\mathbf{R}\uparrow} \hat{c}^\dagger_{\mathbf{R}\downarrow} \hat{c}_{\mathbf{R}\downarrow} \hat{c}_{\mathbf{R}\uparrow}. \quad (4.6)$$

To determine the position-dependent density of each component, and the energetics associated with each, the ground state energy can be found by minimizing the energy functional

$$E[\{\rho_\sigma(\mathbf{R})\}] = \int \mathrm{d}^3\mathbf{R} \left[\frac{3}{5} \beta \sum_\sigma \rho_\sigma^{5/3}(\mathbf{R}) + g \rho_\uparrow(\mathbf{R}) \rho_\downarrow(\mathbf{R}) + V(\mathbf{R}) \sum_\sigma \rho_\sigma(\mathbf{R}) - \sum_\sigma E_{\mathrm{F},\sigma} \rho_\sigma(\mathbf{R}) \right], \quad (4.7)$$

where $\{\rho_\sigma(\mathbf{R})\} = \{\rho_\uparrow(\mathbf{R}), \rho_\downarrow(\mathbf{R})\}$ is the set of density profiles of spin species $\sigma = \uparrow, \downarrow$, and $E_{\mathrm{F},\sigma}$ are Lagrange multipliers for each spin component, and are, as the nomenclature suggests, equivalent to the Fermi energy of that spin species in this zero-temperature formulation. These Lagrange multipliers impose the conservation of atom number of each spin such that $\int d^3\mathbf{R} \rho_\sigma(\mathbf{R}) = N_\sigma$. This separate constraint on each spin state is specific to the

atomic system, where the two components are far-separated in energy and spins cannot spontaneously flip. In an analogous condensed matter system, the spin would not similarly be conserved.

Scaling for an anisotropic harmonic trap

In this work, we consider the case of a harmonic trapping potential, which may be anisotropic. The potential takes the form $V(\mathbf{R}) = \frac{1}{2}m\sum_i \omega_i^2 \mathbf{R}_i^2$, where i runs over the three dimensions and ω_i characterises the trapping frequency in each dimension. The harmonic trap can be be rescaled to an isotropic one by setting $\widetilde{\mathbf{R}}_i = \mathbf{R}_i(\omega_i/\overline{\omega})$, where $\overline{\omega} = (\omega_1\omega_2\omega_3)^{1/3}$ is the geometric mean of the trap frequencies. The energy functional 4.7 becomes

$$E[\{\rho_\sigma(\widetilde{\mathbf{R}})\}] = \int d^3\widetilde{\mathbf{R}}\Bigg[\frac{3}{5}\beta\sum_\sigma \rho_\sigma^{5/3}(\widetilde{\mathbf{R}}) + g\rho_\uparrow(\widetilde{\mathbf{R}})\rho_\downarrow(\widetilde{\mathbf{R}}) + \frac{1}{2}m\overline{\omega}^2\widetilde{\mathbf{R}}^2\sum_\sigma \rho_\sigma(\widetilde{\mathbf{R}}) - \sum_\sigma E_{\mathrm{F},\sigma}\rho_\sigma(\widetilde{\mathbf{R}})\Bigg]. \tag{4.8}$$

Noninteracting unmagnetized gas

The average magnetization of the system is $m \equiv (N_\uparrow - N_\downarrow)/(N_\uparrow + N_\downarrow)$. We consider the case of equal populations in both spin states, $N_\uparrow = N_\downarrow = N/2$, where N is the total atom number, such that $m = 0$. To determine the appropriate scaling for this system, we consider the noninteracting case ($g = 0$). The noninteracting (NI) energy functional can be written

$$E_{N\sigma}^{\mathrm{NI}}[\rho_\sigma(\widetilde{\mathbf{R}})] = \sum_\sigma \int d^3\widetilde{\mathbf{R}}\left[\frac{3}{5}\beta\rho_\sigma^{5/3}(\widetilde{\mathbf{R}}) + \frac{1}{2}m\overline{\omega}^2\widetilde{\mathbf{R}}^2\rho_\sigma(\widetilde{\mathbf{R}}) - E_{\mathrm{F},\sigma}\rho_\sigma(\widetilde{\mathbf{R}})\right]. \tag{4.9}$$

The condition of zero magnetization lends a symmetry to the problem and sets $E_{\mathrm{F},\uparrow} = E_{\mathrm{F},\downarrow} = E_{\mathrm{F}}^{\mathrm{NI}}$. To minimize the energy of the system, we set $\delta E_{\mathrm{F}}^{\mathrm{NI}}/\delta\rho_\sigma = 0$ and solve for the density profiles to find

$$\rho_\sigma(\widetilde{\mathbf{R}}) = \beta^{-3/2}\left[(E_{\mathrm{F}}^{\mathrm{NI}} - \frac{1}{2}m\overline{\omega}^2\widetilde{\mathbf{R}}^2)\right]^{3/2}. \tag{4.10}$$

In this LDA, there is a maximum radius of the system, beyond which the density is zero. This maximum radius,

$$R_N^{\mathrm{NI}} = \sqrt{\frac{2E_{\mathrm{F}}^{\mathrm{NI}}}{m\overline{\omega}^2}} \tag{4.11}$$

can be used as the characteristic length scale for the system. With the rescaled position variable, we use spherical symmetry to perform the integrations in Eq. (4.9) up to $R_N^{\rm NI}$ and find the characteristic variables of the noninteracting system. The new variables are:

$$E_F^{\rm NI} = \hbar\overline{\omega}(3N)^{1/3}, \tag{4.12a}$$

$$R_N^{\rm NI} = \sqrt{\frac{2E_F^{\rm NI}}{m\overline{\omega}^2}} = a_{\rm HO}(24N)^{1/6}, \tag{4.12b}$$

$$E_N^{\rm NI} = \frac{3}{4}NE_F^{\rm NI} = \frac{\hbar\overline{\omega}}{4}(3N)^{4/3}, \tag{4.12c}$$

$$\rho_N^{\rm NI}(0) = \frac{4N}{\pi^2(R_N^{\rm NI})^3} = \frac{1}{a_{\rm HO}^3}\left(\frac{2N}{3\pi^4}\right)^{1/2}, \tag{4.12d}$$

where $a_{\rm HO} = (\hbar/m\overline{\omega})^{1/2}$ is the harmonic oscillator length, $\mu_N^{\rm NI}$ is the chemical potential of the gas, $E_N^{\rm NI}$ is the total energy of the gas, and $\rho_N^{\rm NI}(0)$ is the atom density at the trap centre. The position-dependent density of the noninteracting unmagnetized Fermi gas is labelled by $\rho_N^{\rm NI}(\widetilde{\mathbf{R}})$.

Dimensionless variables for the interacting problem

For the calculations which follow, we convert our variables to dimensionless form, where the scaling is with respect to the noninteracting unmagnetised system (Eqs. (4.12)). The dimensionless variables are:

$$\mathbf{r} = \frac{\widetilde{\mathbf{R}}}{R_N^{\rm NI}}, \tag{4.13a}$$

$$n_\sigma = \frac{\rho_\sigma}{\rho_{N\sigma}^{\rm NI}(\mathbf{0})} \tag{4.13b}$$

$$\varepsilon = E/E_{\rm F}^{\rm NI}, \tag{4.13c}$$

$$\varepsilon_{{\rm F},\sigma} = E_{{\rm F},\sigma}/E_{\rm F}^{\rm NI}, \tag{4.13d}$$

$$k_{\rm F}^0 a = \left(6\pi^2\rho_N^{\rm NI}(\mathbf{0})\right)^{1/3} a \tag{4.13e}$$

where $\mathbf{r}$ is our dimensionless position variable, n_σ the density, ε the total energy, $\varepsilon_{{\rm F},\sigma}$ the chemical potential of the σ component, k_F^0 the Fermi wavevector at the trap centre for the unmagnetized noninteracting gas and $k_{\rm F}^0 a$ the dimensionless interaction parameter.

The energy functional Eq. (4.8) can be rewritten in terms of these dimensionless variables

$$\varepsilon[\{n_\sigma(\mathbf{r})\}] = \frac{16}{3\pi^2}\int d^3\mathbf{r}\left[\frac{3}{5}\left(n_\uparrow^{5/3}(\mathbf{r}) + n_\downarrow^{5/3}(\mathbf{r})\right) + \frac{4k_{\rm F}^0 a}{3\pi}n_\uparrow(\mathbf{r})n_\downarrow(\mathbf{r}) - \sum_\sigma(\varepsilon_{{\rm F},\sigma} - \mathbf{r}^2)n_\sigma(\mathbf{r})\right], \tag{4.14}$$

and assuming that the ground state solution will respect the spherical symmetry of the rescaled trap, the integral can be written in a single radial dimension

$$\varepsilon[\{n_\sigma(r)\}] = \frac{64}{3\pi}\int dr\ r^2\left[\frac{3}{5}\left(n_\uparrow^{5/3}(r)+n_\downarrow^{5/3}(r)\right)+\frac{4k_{\mathrm{F}}^0 a}{3\pi}n_\uparrow(r)n_\downarrow(r)-\sum_\sigma(\varepsilon_{\mathrm{F},\sigma}-r^2)n_\sigma(r)\right]. \tag{4.15}$$

Variational minimization sets $\delta\varepsilon/\delta n_\sigma(r)=0$ and leads to the following two equations for the two density components

$$n_\uparrow(r) = \left[\left(\varepsilon_{\mathrm{F},\uparrow}-r^2-\frac{4k_{\mathrm{F}}^0 a}{3\pi}n_\downarrow(r)\right)\right]^{3/2}, \tag{4.16a}$$

$$n_\downarrow(r) = \left[\left(\varepsilon_{\mathrm{F},\downarrow}-r^2-\frac{4k_{\mathrm{F}}^0 a}{3\pi}n_\uparrow(r)\right)\right]^{3/2}, \tag{4.16b}$$

subject to the constraints

$$4\pi\int dr\ r^2 n_\sigma(r) = \frac{\pi^2}{4}\frac{N_\sigma}{N}. \tag{4.17}$$

The coupled equations 4.16 can be solved iteratively and numerically to obtain the densities for a given interaction strength and atom number for each species. Typically, we are interested in the $m=0$ configuration. The resulting densities $n_\uparrow(r)$ and $n_\downarrow(r)$ are used to compute physical observables of the system.

Figure 4.2 shows the density profiles obtained for a variety of interaction strengths. We see that for increasing interactions, the central density is reduced and the cloud is pushed outside of its $r=1$ noninteracting radius. The system is able to minimize its energy in this way until a critical interaction strength is reached, at which point the system prefers to segregate itself into domains of spin-$\uparrow$ and spin-$\downarrow$ in the high-density regions. As we find later, this critical interaction strength is $k_{\mathrm{F}}^0 a \sim 1.84$, falling between parts (c) and (d) in Fig. 4.2. The phase-separation begins at the trap centre, at which point we can determine the local Fermi wavevector, $k_F(0) = \left(6\pi^2\rho(0)\right)^{1/3} = k_F^0 n_\sigma^{1/3}(0)$. We find at the transition point that $n_\sigma(0)\approx 0.64$, such that $k_F(0)a \approx \pi/2$, as in the uniform case. This agreement is expected in the LDA since the local properties should mimic the uniform system.

The expansion of the cloud below the critical interaction strength increases the potential energy of the system and decreases the kinetic energy as the density in the centre is reduced. For large interaction strengths, the system reduces its total energy by segregating into spin-$\uparrow$ and spin-$\downarrow$ regions and avoiding all interaction energy. The local nature of the LDA is evident in the sharp changes of the density profile, indicating shells of alternating spin. As long-range correlations are completely ignored in the LDA, the system simply adopts the

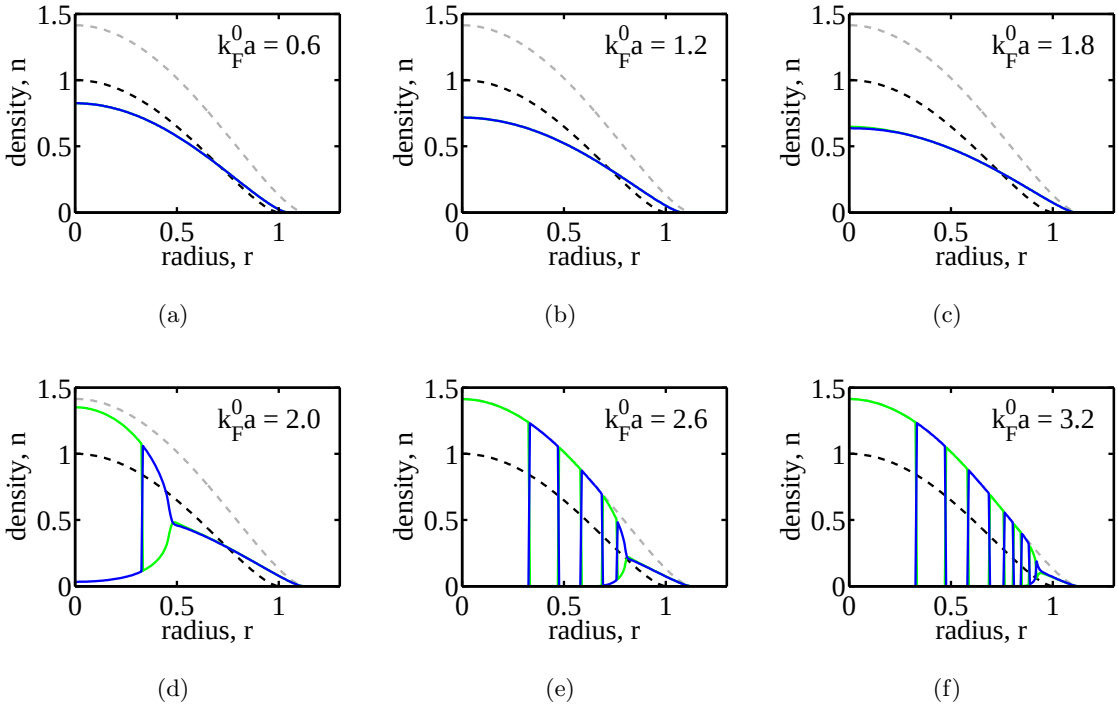

FIGURE 4.2: LDA density profiles for various interaction strengths. The numerical solutions of $n_\uparrow(r)$ (blue) and $n_\downarrow(r)$ (green) are shown for increasing interactions, with equal populations in each spin state ($N_\uparrow = N_\downarrow = N/2$; $m = 0$). Dashed black lines indicate the $k_F^0 a = 0$ noninteracting solution; grey dashed lines indicate the non-interacting solution for all particles in the same spin state ($N_\uparrow = N$; $N_\downarrow = 0$). Interaction parameters indicated in panels.

non-interacting profile for a single spin state, with each spin occupying a particular region alone. The relative widths of these shells are constrained by the conservation of each spin state, while the number of shells is an artifact of the numerical solution, and changes with initial conditions – there being no cost to the change of density, the ground state does not prefer a specific number of shells.

The sharp changes in the density profiles are unphysical. The kinetic energy cost of the density gradient must be accounted for in a proper treatment of the system (see §4.3). Regardless, the existence of a critical $k_F^0 a$ beyond which the system will tend to spin-segregate should remain.

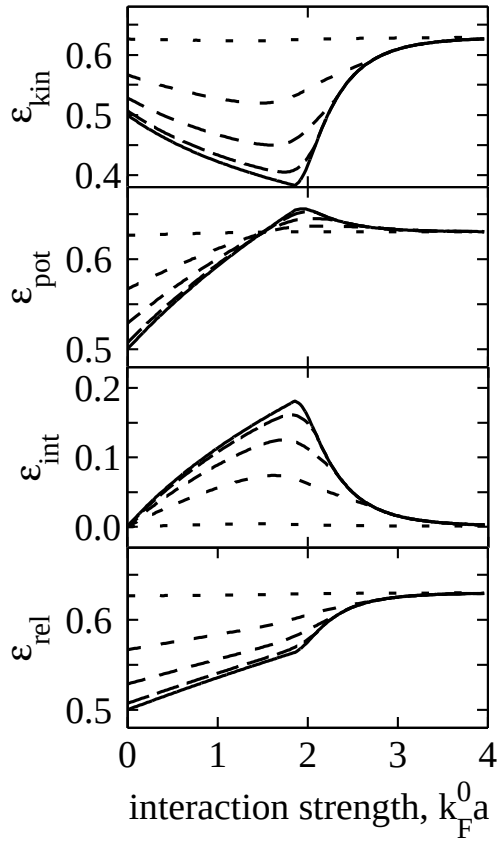

Figure 4.3: Dimensionless mean-field energies as a function of interaction strength. From top to bottom: kinetic, potential, interaction and release energies. Solid lines indicate $m = 0$, while dashed lines indicate $m = 0.25,\ 0.50,\ 0.75,\ 0.99$ with decreasing dash length. At $k_{\mathrm{F}}^0 a \approx 1.84$, there is a kink in each of the energies we calculate, which corresponds to the phase separation found in Fig. 4.2. The energy per particle in physical units may be obtained by multiplying these results by $3E_F^0/4$ where $E_F^0 = \hbar\overline{\omega}(3N)^{1/3}$. As discussed later, going beyond the LDA leads to negligible quantitative corrections to these results.

4.2.2 Characteristic energies and spin polarisation

With calculations of the density profiles in hand, the energetic characteristics of the gas can be determined. We consider the energies of the entire gas, since it is these bulk properties which might easily be measured. By identifying terms in the energy functional as either kinetic, potential, or interaction, we can write each of these contributions separately

$$\varepsilon_{\mathrm{kin}} = \frac{64}{3\pi}\int dr\ r^2\left[\frac{3}{5}\sum_{\sigma} n_\sigma^{5/3}(r)\right], \tag{4.18}$$

$$\varepsilon_{\mathrm{pot}} = \frac{64}{3\pi}\int dr\ r^2\left[r^2(n_\uparrow(r) + n_\downarrow(r))\right], \tag{4.19}$$

$$\varepsilon_{\mathrm{int}} = \frac{64}{3\pi}\int dr\ r^2\left[\frac{4k_{\mathrm{F}}^0 a}{3\pi} n_\uparrow(r) n_\downarrow(r)\right], \tag{4.20}$$

where $\varepsilon_{\mathrm{kin}}$, $\varepsilon_{\mathrm{pot}}$, and $\varepsilon_{\mathrm{int}}$ are the kinetic, potential and interaction energies, respectively.

To measure these energies experimentally, one option is to record the release energy, by rapidly switching off the trapping potential and measuring the momentum distribution of

the atoms after some time of flight. With an instantaneous switch-off process, all interaction energy is converted into kinetic energy, and the release energy $\varepsilon_{\rm kin}$ measures the sum of the interaction and kinetic components

$$\varepsilon_{\rm rel} = \frac{64}{3\pi}\int dr\ r^2\left[\frac{3}{5}\sum_\sigma n_\sigma^{5/3}(r) + \frac{4k_{\rm F}^0 a}{3\pi} n_\uparrow(r) n_\downarrow(r)\right]. \tag{4.21}$$

If interactions can be suddenly turned off (by, for example, jumping to a zero in a Feshbach resonance), the kinetic energy alone can be measured with this technique.

Figure 4.3 shows the calculations of these four energies as a function of the interaction parameter $k_{\rm F}^0 a$. Paying special attention to the solid lines, which represent the $m = 0$ scenario, there is a clear transition at $k_{\rm F}^0 a \approx 1.84$. By looking carefully at the density profiles in this region, we find this is the point of onset of phase separation. The kinetic and potential energies both account for half of the total energy at $k_{\rm F}^0 a = 0$, as expected in a harmonic trap. Likewise, for very strong interactions, the kinetic and potential energies are again equal, at the value expected for all atoms in a single spin state ($N/2 \to N$; $E_N \to 2^{1/3} E_N^0$; $\epsilon \to 2^{1/3}\varepsilon_0$). This high-interaction limit indicates that the system is completely polarised, and as discussed earlier, acts as though in a single spin state due to the lack of "communication" between domains in the LDA.

We also see that the interaction energy is maximized at this same transition point. Below the transition, an increasing interaction strength leads to an increasing interaction energy. At the transition point, the cloud begins to phase-separate, and as a result, spin-$\uparrow$ and spin-$\downarrow$ atoms avoid each other. With increasing interaction energy, the system is further polarized and the overlap of the densities $n_\uparrow(r)$ and $n_\downarrow(r)$ vanishes, leading to a decreasing $\varepsilon_{\rm int}$.

For non-zero magnetisations, Fig. 4.3 shows that the transition is less-sharp, and the differences in energy for different interaction strengths are less pronounced, but still visible.

We identify the transition to the spin-polarised state as a crossover into ferromagnetism. While these energetic signatures are an indication of the onset of ferromagnetic behaviour, direct proof of ferromagnetism requires, for example, the observation of spin-polarised domains. The actual behaviour of the gas likely depends on effects beyond the LDA, since a ferromagnetic state demonstrates long-range order, which is completely absent in the local approximation.

4.2.3 Atom loss rate

On the repulsive side of a Feshbach resonance, there is a tendency for molecular formation [84, 86, 102]. With large interaction strengths, the three-body collision rate can become quite high, where two atom molecules form as a third atom carries away the excess binding energy. All three atoms are lost from the sample – the molecule will not be detected, and may not even be trapped, and the third atom will generally have enough excess energy to escape the trap. In working with fermions, the molecular formation process is suppressed, since non-identical fermions must be the constituents of the dimer, allowing for the experiments we describe to be performed before significant loss of the sample.

Despite decreasing the time available for performing these experiments, the loss rate can act as a signature of the ferromagnetic state we seek. As the system spin polarizes, it becomes less likely that atoms of opposite spin will meet, and losses from the three-body process described above will decrease. Study of the three-fermion problem [103] leads to a model describing three-body loss,

$$\gamma_{\rm loss} = \gamma^0_{\rm loss}(k^0_{\rm F}a)^6 \int d^3\mathbf{r}\; n_\uparrow(\mathbf{r})n_\downarrow(\mathbf{r})(n_\uparrow(\mathbf{r}) + n_\downarrow(\mathbf{r})), \tag{4.22}$$

where $\gamma^0_{\rm loss}$ is an unknown prefactor.

Using the LDA density profiles calculated above, we can determine this loss rate up to the unknown $\gamma^0_{\rm loss}$, as shown in Fig. 4.4. Paying special attention to the solid $m = 0$ line, we see a rapid increase in the loss rate below the transition point due to the $(k^0_{\rm F}a)^6$ scaling. The drop-off of the loss-rate beyond the transition point comes as the system spin polarises and there is less overlap of the different spin states, suppressing the $n_\uparrow(\mathbf{r})n_\downarrow(\mathbf{r})$ term in the integrand of Eq. (4.22). The competition between these effects leads to a peak in the loss rate, which occurs slightly beyond the $k^0_{\rm F}a = 1.84$ transition point we observed in the energetic signatures, due to differences in the scaling of these quantities.

4.3 Beyond mean-field theory: gradient cost

In the preceding section, the properties of the gas were studied within the context of the LDA. The density profiles for the interacting mixture within this approximation display very large gradients at the boundaries between spin-polarized domains. The kinetic energy of these gradients is neglected within the LDA, and because this energy cost may be significant

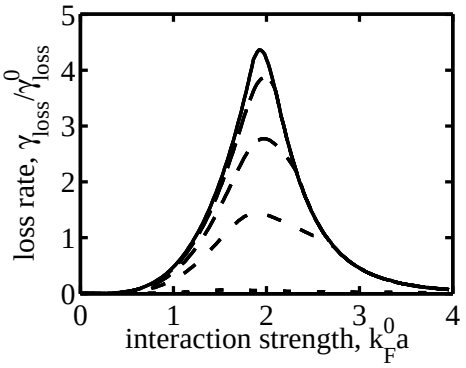

FIGURE 4.4: Dimensionless atom loss rate, Γ/Γ_0, as a function of interaction strength. Solid lines indicate $m = 0$, while dashed lines indicate $m = 0.25,\ 0.50,\ 0.75,\ 0.99$ with decreasing dash length.

in the physics of magnetism, we must consider it for a better description of the strongly-interacting system.

Another characteristic of the LDA is that the interaction energy cost comes only from atoms of different spins existing at the *same point* in space. The locality of the approximation neglects any cost of interactions between atoms of different spins at nearby locations, and so the definition of "up" and "down" at each point in the cloud may be chosen at random. In moving beyond the LDA, there exists an interaction energy for atoms at different points in space, and there is, therefore, an energetic cost when neighbouring atoms are not identical.

To extend the energy functional to account for these two effects, we promote the local magnetization to a vector quantity such that the magnetization can point in different directions on the Bloch sphere at different spatial locations, and add a surface tension term to the energy functional to account for the density gradients. With these changes, we can study various "spin textures" in this system and determine which geometry might lead to the ground state of the system.

4.3.1 Energy functional in terms of magnetization

Instead of defining the densities individually, we consider a local total density and magnetisation

$$n(\mathbf{r}) = n_\uparrow(\mathbf{r}) + n_\downarrow(\mathbf{r}) \tag{4.23}$$

$$M(\mathbf{r}) = \frac{n_\uparrow(\mathbf{r}) - n_\downarrow(\mathbf{r})}{n(\mathbf{r})}. \tag{4.24}$$

If we expand the energy functional Eq. (4.15) in powers of $M(\mathbf{r})$, keeping terms up to $M^6(\mathbf{r})$ (though terminating the expansion at $M^4(\mathbf{r})$ would not qualitatively affect our results), we find the expression can be written in two parts as

$$\varepsilon = \varepsilon_{\mathrm{a}}[n(\mathbf{r})] + \varepsilon_{\mathrm{b}}[n(\mathbf{r}), M(\mathbf{r})], \tag{4.25}$$

where

$$\varepsilon_{\mathrm{a}}[n(\mathbf{r})] = \frac{16}{3\pi^2}\int d^3\mathbf{r}\left[\frac{6}{5}\left(\frac{n(\mathbf{r})}{2}\right)^{5/3} + \frac{k_{\mathrm{F}}^0 a}{3\pi}n^2(\mathbf{r}) - (\varepsilon_{\mathrm{F}} - \mathbf{r}^2)n(\mathbf{r})\right], \tag{4.26}$$

$$\begin{aligned}\varepsilon_{\mathrm{b}}[n(\mathbf{r}), M(\mathbf{r})] = \frac{16}{3\pi^2}\int d^3\mathbf{r}[&A_2(\mathbf{r})m^2(\mathbf{r}) + A_4(\mathbf{r})M^4(\mathbf{r}) + A_6(\mathbf{r})M^6(\mathbf{r}) \\ &- H\ n(\mathbf{r})M(\mathbf{r})]\,,\end{aligned} \tag{4.27}$$

where the new Lagrange multipliers in the energy functionals are $\varepsilon_{\mathrm{F}} = (\varepsilon_{\mathrm{F},\uparrow} + \varepsilon_{\mathrm{F},\downarrow})/2$ and $H = (\varepsilon_{\mathrm{F},\uparrow} - \varepsilon_{\mathrm{F},\downarrow})/2$. The first term, ε_{a}, depends only on the density profile. We assume that this is equivalent to that calculated within the LDA, since it depends only on the interaction $k_{\mathrm{F}}^0 a$. Corrections to the LDA are small for the atom numbers we use in this work, making this approximation valid. The coefficients of the magnetization-dependent energy functional, ε_{b}, are

$$A_2(\mathbf{r}) = \frac{n^{5/3}(\mathbf{r})}{2^{2/3}3} - \frac{k_{\mathrm{F}}^0 a}{3\pi}n^2(\mathbf{r}), \tag{4.28a}$$

$$A_4(\mathbf{r}) = \frac{n^{5/3}(\mathbf{r})}{2^{2/3}81}, \tag{4.28b}$$

$$A_6(\mathbf{r}) = \frac{7n^{5/3}(\mathbf{r})}{2^{2/3}2187}. \tag{4.28c}$$

The first coefficient, $A_2(\mathbf{r})$, depends on $k_{\mathrm{F}}^0 a$ explicitly. All of the coefficients $A_{2,4,6}$ implicitly depend on $k_{\mathrm{F}}^0 a$ through the density. This dependence was ignored in earlier phenomenological work on trapped fermions in an optical lattice [104].

Vector magnetization

The magnetisation of our two-component system can be understood as a vector on a Bloch sphere (Fig. 4.5), where the poles represent the pure states of each spin component and points in between the superpositions of these. Importantly, fermions in any pure state do not interact. The vector nature of the magnetization allows for partial interactions

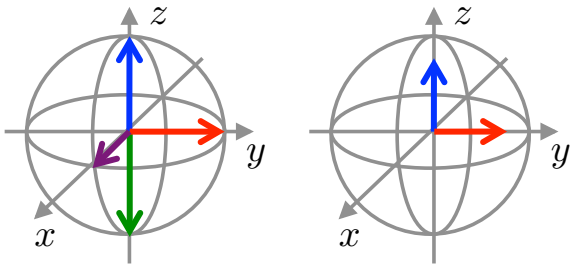

(a) (b)

Figure 4.5: Bloch sphere representation of vector magnetization of two-component Fermi gas. (a) Pure states, $|\mathbf{m}(\mathbf{r})| = 1$. Each arrow represents a different magnetization of the system, all of whose atoms are in the same state. We take $\hat{r_3}$ as the quantization axis of our two-state system. Blue: $\mathbf{m}(\mathbf{r}) = \hat{r_3}$, corresponding to $|\psi\rangle = |\uparrow\rangle$. Green: $\mathbf{m}(\mathbf{r}) = -\hat{r_3}$, corresponding to $|\psi\rangle = |\downarrow\rangle$. Purple: $\mathbf{m}(\mathbf{r}) = \hat{x}$, corresponding to $|\psi\rangle = |\uparrow\rangle + |\downarrow\rangle$. Red: $\mathbf{m}(\mathbf{r}) = \hat{y}$, corresponding to $|\psi\rangle = |\uparrow\rangle + i|\downarrow\rangle$. (b) Mixed states, $|\mathbf{m}(\mathbf{r})| < 1$. Blue: $\mathbf{m}(\mathbf{r}) = 0.5\hat{r_3}$, corresponding to 75% of the atoms in $|\psi\rangle = |\uparrow\rangle$ and 25% of the atoms in $|\psi\rangle = |\downarrow\rangle$. Red: $\mathbf{m}(\mathbf{r}) = 0.5\hat{y}$, corresponding to 75% of the atoms in $|\psi\rangle = |\uparrow\rangle + i|\downarrow\rangle$ and 25% of the atoms in $|\psi\rangle = |\uparrow\rangle - i|\downarrow\rangle$.

between two identical states on the sphere, the magnitude of which depends on the overlap of states.

To account for the vectorial nature of the magnetization in the energy functional, we promote the magnetization M and the Lagrange multiplier H to vectors $\mathbf{M}$ and $\mathbf{H}$. The value $|\mathbf{H}| = (\varepsilon_{\mathrm{F},\uparrow} - \varepsilon_{\mathrm{F},\downarrow})/2$ gives the difference in local Fermi energies, and has the same energetic form as would a local magnetic field, if the pseudospins were real.[2] We also include a surface tension term to account for gradients via a stiffness $\zeta_{\mathrm{s}}(\mathbf{r})$, and obtain the energy functional

$$\varepsilon_{\mathrm{b}}[n(\mathbf{r}), \mathbf{M}(\mathbf{r})] = \frac{16}{3\pi^2} \int d^3\mathbf{r} \left[A_2(\mathbf{r})|\mathbf{M}(\mathbf{r})|^2 + A_4(\mathbf{r})|\mathbf{M}(\mathbf{r})|^4 + A_6(\mathbf{r})|\mathbf{M}(\mathbf{r})|^6 + \frac{1}{2}\zeta_{\mathrm{s}}(\mathbf{r})\lambda_i \left(\nabla_i M_j(\mathbf{r})\right)^2 - n(\mathbf{r})\mathbf{H}(\mathbf{r}) \cdot \mathbf{M}(\mathbf{r}) \right], \tag{4.29}$$

where $\lambda_i = (\omega_i/\overline{\omega})^2$ accounts for any anisotropy in the system. The stiffness $\zeta_{\mathrm{s}}(\mathbf{r})$ depends on $\mathbf{r}$ only through the density $n(\mathbf{r})$, and it can be computed in the uniform Fermi gas

[2] In passing, we note that despite these states being merely "pseudospins," a real magnetic field would emerge in a polarized domain, since the states are defined (primarily) by their nuclear spins (see state decompositions at relevant fields for ^{40}K in Appendix A.3). Like in electron systems, the interaction energy between states is much larger than the spin energy associated with these nuclei.

assuming that the magnetization variation is slow on the scale of the interparticle spacing, but fast on the length scale over which the total density varies, so that density variations can be ignored in this computation. The Lagrange multiplier $\mathbf{H}(\mathbf{r})$ must be chosen to satisfy global constraints on the magnetization, for instance, $\int d^3\mathbf{r}\; n(\mathbf{r})M_i(\mathbf{r}) = 0$, for each component i.

Computation of the stiffness $\zeta_s(\mathbf{r})$

We determine the cost of density gradients by computing the stiffness ζ_s from the magnetic susceptibility of the uniform Fermi gas. The excess energy in an applied field $\mathbf{H}(\mathbf{q})$ (pointing in any direction) is given by $\Delta E(\mathbf{q}) = \frac{1}{2}\chi(\mathbf{q})h_i(\mathbf{q})h_i(-\mathbf{q})$ which defines the wavevector-dependent magnetic susceptibility. The magnetization $\widetilde{M}(\mathbf{q})$ in this external field is simply $\widetilde{M}(\mathbf{q}) = \chi(\mathbf{q})h(\mathbf{q})$, so that we can set $\Delta E(\mathbf{q}) = \frac{1}{2}\chi^{-1}(\mathbf{q})\widetilde{M}_i(\mathbf{q})\widetilde{M}_i(-\mathbf{q})$. Expanding $\chi^{-1}(\mathbf{q}) = \chi_0^{-1}(1 + b\mathbf{q}^2)$ then yields

$$\Delta E(\mathbf{q}) = \frac{1}{2}\chi_0^{-1}(1 + b\mathbf{q}^2)\widetilde{M}_i(\mathbf{q})\widetilde{M}_i(-\mathbf{q}). \tag{4.30}$$

The well-known result for a Fermi gas at $T = 0$ is that $b = 1/12k_F^2$, using which the energy cost becomes, in real space,

$$\Delta E = \frac{1}{2\chi_0}\int d^3\mathbf{R}\left[|\widetilde{\mathbf{M}}(\mathbf{R})|^2 + \frac{1}{12k_F^2}(\nabla\widetilde{M}_i(\mathbf{R}))^2\right], \tag{4.31}$$

where

$$\chi_0^{-1} = \frac{\pi^2\hbar^2}{mk_F} = \frac{\pi^2\hbar^2}{m}(3\pi^2\rho)^{-1/3}. \tag{4.32}$$

Rescaling distances for an isotropic harmonic trapping potential, and setting $\widetilde{M}_i = \rho^0_{N\sigma}(\mathbf{0})n(\mathbf{r})M_i(\mathbf{r})$, with $r = R/R_N^0$, we find

$$\begin{aligned}\zeta_s(\mathbf{r}) &= \frac{n^{-1/3}(\mathbf{r})}{2^{2/3}3}\frac{1}{6(3\pi^2 n(\mathbf{r}))^{2/3}}\left(\frac{1}{\rho^0_{N\sigma}(R_N^0)^3}\right)^{2/3} \\ &= \frac{1}{72n(\mathbf{r})(3N)^{2/3}}.\end{aligned} \tag{4.33}$$

For general values of the magnetization, higher order gradient terms might also become important. We will focus here on the effects of this simplest gradient term in the energy functional.

Simplified magnetization energy functional

To simplify the energy functional, we notice that $n(\mathbf{r})$ varies over the length scale of unity in our dimensionless units. The variations in magnetisation, by comparison, are

expected to change over much shorter length scales for large atom numbers, where $\zeta_{\rm s}(\mathbf{r})$ is small (Eq. (4.33)). Within this assumption, $\nabla(n(\mathbf{r})M_i(\mathbf{r})) \approx n(\mathbf{r})\nabla M_i(\mathbf{r})$, and the slightly simplified energy functional is

$$\varepsilon_{\rm b} = \frac{16}{3\pi^2}\int d^3\mathbf{r}\Big[A_2(\mathbf{r})|\mathbf{M}(\mathbf{r})|^2 + A_4(\mathbf{r})|\mathbf{M}(\mathbf{r})|^4 + A_6(\mathbf{r})|\mathbf{M}(\mathbf{r})|^6 - n(\mathbf{r})\mathbf{H}(\mathbf{r})\cdot\vec{M}(\mathbf{r}) + \frac{n(\mathbf{r})}{144(3N)^{2/3}}\lambda_i(\nabla_i M_j(\mathbf{r}))(\nabla_i M_j(\mathbf{r}))\Big], \tag{4.34}$$

where $\mathbf{H}(\mathbf{r})$ is chosen to satisfy

$$\int d^3\mathbf{r}\; n(\mathbf{r})M_i(\mathbf{r}) = 0, \tag{4.35}$$

for each component i (for zero net magnetization). Sums over all i, j are assumed throughout. Recall that $\lambda_i = (\omega_i/\overline{\omega})^2$, where $\overline{\omega} = (\omega_1\omega_2\omega_3)^{1/3}$ is the geometric mean of the trap frequencies.

4.3.2 Spin textures

As one possibility for the system to lower its energy beyond the LDA result, we consider alternate spin patterns. Using an energy functional that takes into account both the vector nature of the spin and the energy cost of spin gradients, we study various spin textures in a trapped Fermi gas.

To begin, we consider the isotropic harmonic trap and evaluate two possible spin textures: the hedgehog and domain wall configurations. Next, we study the effects of trap anisotropy by deforming the trap into a cigar shape and evaluating the energetics. In all cases, we construct an ansatz for the magnetization pattern, and numerically minimize the energy functional within the constraints imposed by this ansatz.

By ensuring that the density and magnetization satisfy the constraints that the total atom number is fixed and the total magnetization is zero, we can drop the Lagrange multipliers and express the total energy as a sum $\overline{\varepsilon} = \varepsilon_1 + \varepsilon_2$ where

$$\varepsilon_1 = \frac{16}{3\pi^2}\int d^3\mathbf{r}\left[\frac{6}{5}\left(\frac{n(\mathbf{r})}{2}\right)^{5/3} + \frac{k_{\rm F}^0 a}{3\pi}n^2(\mathbf{r}) + r^2 n(\mathbf{r})\right], \tag{4.36}$$

$$\varepsilon_2 = \frac{16}{3\pi^2}\int d^3\mathbf{r}\Big[A_2(\mathbf{r})|\mathbf{M}(\mathbf{r})|^2 + A_4(\mathbf{r})|\mathbf{M}(\mathbf{r})|^4 + A_6(\mathbf{r})|\mathbf{M}(\mathbf{r})|^6 + \frac{n(\mathbf{r})}{144(3N)^{2/3}}\lambda_i(\nabla_i\vec{m}_j(\mathbf{r}))^2\Big]. \tag{4.37}$$

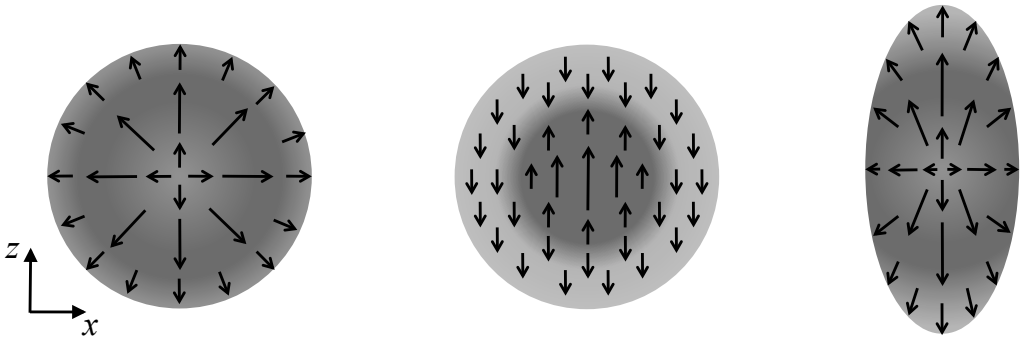

(a) (b) (c)

Figure 4.6: Spin texture ansatz schematics. Black arrows show direction and magnitude of $\mathbf{M}(r)$ throughout the trap. (a) Isotropic hedgehog, (b) isotropic domain wall, and (c) anisotropic hedgehog.

4.3.3 Isotropic trap: Hedgehog state

One of the simplest spin textures we can consider is the hedgehog state in an isotropic trap (Fig. 4.6(a)). Isotropy allows us to assume spherical symmetry, with equal trapping frequencies in all directions. The hedgehog state is one in which the spins point out from the origin at all points, in the $\hat{r}$-direction. The energetic advantage of the hedgehog geometry is that there are only ever small changes in the magnetisation point-to-point, and that neighbouring spins interact with their neighbours only very slighty. Only at the origin does the spin change drastically, and this is confined to a small volume.

Within spherical symmetry, we can write

$$\varepsilon_1^{\mathrm{HH}} = \frac{64}{3\pi}\int \mathrm{d}r\; r^2 \left[\frac{6}{5}\left(\frac{n(r)}{2}\right)^{5/3} + \frac{k_{\mathrm{F}}^0 a}{3\pi} n^2(r) + r^2 n(r)\right]. \tag{4.38}$$

In the magnetization-dependent energy functional, we set $\lambda_i = 1$ for the isotropic trap. The hedgehog geometry dictates that we choose $\mathbf{M}(\mathbf{r}) = M(r)\hat{r}$. This leads to

$$\begin{aligned}\varepsilon_2^{\mathrm{HH}} = \frac{64}{3\pi}\int dr\; r^2 \Bigg[& A_2(r)M^2(r) + A_4(r)M^4(r) + A_6(r)M^6(r) \\ & + \frac{n(r)}{144(3N)^{2/3}}\left\{2\frac{M^2(r)}{r^2} + \left(\frac{dM(r)}{dr}\right)^2\right\}\Bigg].\end{aligned} \tag{4.39}$$

We need not keep track of the zero magnetization constraint, as it is guaranteed for any choice of $M(r)$ by the hedgehog ansatz symmetry. For particle numbers typical in experiments, $N \sim 10^4 - 10^6$, and ζ_{s} is small. Therefore, we assume that the average density

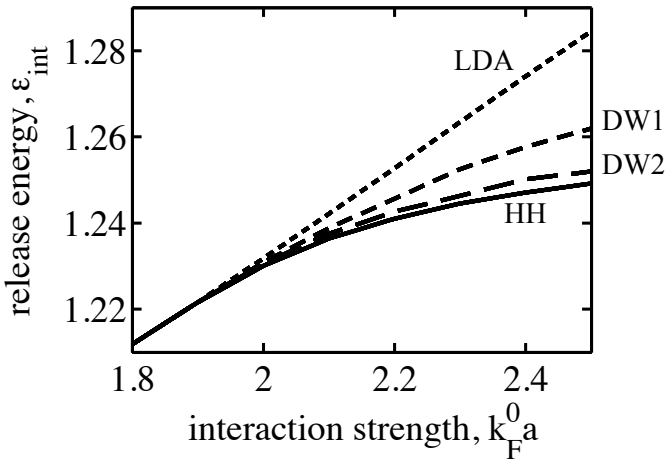

Figure 4.7: Dimensionless total energy, $\varepsilon_1 + \varepsilon_2$, shown as a function of interaction strength, $k_F^0 a$, for an isotropic harmonic trap. Solid line indicates the hedgehog solution, long dashes are for the domain wall state at 10^6 atoms and short dashes for 10^4 atoms. Shortest dashes are the non-optimized solution.

profile $n(r)$ obtained from the LDA calculation remains unchanged. We need only consider changes due to the gradient term.

Starting with some initial magnetization profile, we numerically vary $M(r)$ through an "annealing" process to find the profile that minimizes ε_2. Figure 4.7 shows the total energy $\bar{\varepsilon}^{\rm HH}$ of the hedgehog state as a function of the interaction parameter. We find that above the transition point, the energy can be made smaller than that found in the LDA by allowing for the spin texture to emerge.

Figure 4.8(a) shows the calculated magnetization profile of the hedgehog state at two interaction strengths. We find that the magnetization is suppressed in a small region around the trap centre and vanishes at $r = 0$. The form of the magnetization profile near the trap centre is understood by considering the last two terms in Eq. (4.39). By taking the functional derivative with respect to $M(r)$ and setting it to zero, one finds that $M(r) \sim r^2$ at small r. Far from the centre, we expect the magnetization to be small, as is consistent with the magnetization profiles shown in Fig. 4.8(a).

4.3.4 Isotropic trap: Domain wall state

Again considering the case of spherical symmetry, we are able to write down an alternate ansatz. The domain wall ansatz is one in which there are two regions of the system – one

with all of the atoms in one spin state, the second region with atoms in the opposite state (Fig. 4.6(b)). The symmetry of the system implies a core and an outer shell, with some shell-shaped domain wall between them. The advantage of the domain wall in terms of energy is that there exist large volumes in which the interaction energy is strictly zero, with all effects of the interactions localized to the domain wall.

As in the hedgehog ansatz, ε_1 does not depend on the magnetization, so we find the same expression as $\varepsilon_1^{\rm DW} = \varepsilon_1^{\rm HH}$. For the magnetization dependent energy functional, $\lambda_i = 1$ in the isotropic trap and we choose $\mathbf{M}(\mathbf{r}) = M(r)\hat{r_3}$ for the domain wall geometry, meaning and atoms are either in $\mathbf{M}(\mathbf{r}) = \hat{r_3}$ or $\mathbf{M}(\mathbf{r}) = -\hat{r_3}$, and $M(r)$ tracks the local population difference between these states. We find

$$\varepsilon_2^{\rm DW} = \frac{64}{3\pi}\int {\rm d}r\ r^2\Bigg[A_2(r)M^2(r)+A_4(r)M^4(r) + A_6(r)M^6(r) + \frac{n(r)}{144(3N)^{2/3}}\left(\frac{dM(r)}{dr}\right)^2\Bigg], \tag{4.40}$$

where, for $N_\uparrow = N_\downarrow$, we must satisfy the constraint $\int {\rm d}r\ r^2 n(r)M(r) = 0$.

Similar to the solution for the hedgehog ansatz, we minimize $\varepsilon^{\rm DW}$ by simulating an anneal of the magnetization profile (§4.4.2) to find the optimal $M(r)$, subject to the zero magnetization constraint. Figure 4.7 shows the energy $\bar{\varepsilon}^{\rm DW}$ of the domain wall state, in comparison to the hedgehog and LDA states. Again, above the transition $k_{\rm F}^0 a$, we find the domain wall geometry is more favourable than an LDA state, though the hedgehog geometry has a lower total energy. Figure 4.8(b) shows the magnetization profile of the domain wall state. The magnetization is suppressed in a small region around the domain wall but remains nonzero at the trap centre.

4.3.5 Anisotropic trap: distorted hedgehog

To extend this analysis nearer to experimental reality, we consider the effects of anisotropy in the trapping geometry. In particular, we choose the cylindrically symmetric harmonic trap, where two trapping directions are equal and strong ($\omega_{12} = \omega_{1,2}$), and the third is weak ($\omega_3 < \omega_{12}$). As mentioned earlier, the LDA results depend only on the mean trapping frequency and are independent of the geometry – essentially, all dependence on the geometry drops out in the rescaling of the coordinates. However, the gradient term (Eq. (4.33)) used to account for the kinetic energy costs of changing magnetization retains a dependence on the shape of the trap.

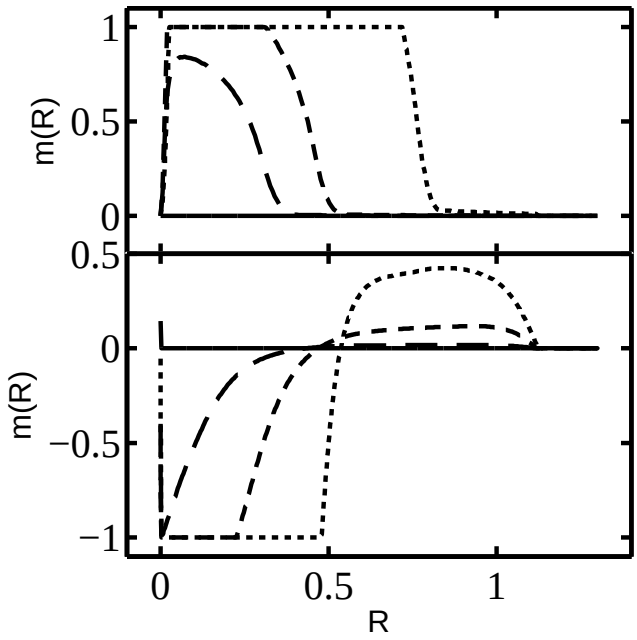

FIGURE 4.8: (a) Magnetization profiles for the hedgehog state at $k_{\rm F}^0 a = 1.8$ (solid), $k_{\rm F}^0 a = 1.9$ (very long dashes), $k_{\rm F}^0 a = 2.0$ (dashes) and $k_{\rm F}^0 a = 2.5$ (short dashes). (b) Magnetisation profiles for the domain wall state for $k_{\rm F}^0 a$ as above. The profiles have been calculated for 10^4 atoms in an isotropic trap. The hedgehog state has zero magnetization at the trap center while the domain wall state magnetization is suppressed around the domain wall but remains nonzero at the trap center.

Given that the hedgehog configuration was found to be the lower energy state, we consider this type of ansatz in the distorted geometry (Fig. 4.6(c)). We assume the magnetization adopts the cylindrical symmetry of the trap and assume an ansatz of the form

$$\mathbf{M}(\mathbf{r}) = M(\varrho_{12}, r_3) \left(\frac{x}{\varrho_{12}} \sin\varphi, \frac{y}{\varrho_{12}} \sin\varphi, \cos\varphi \right), \tag{4.41}$$

where $\varrho_{12} = \sqrt{r_1^2 + r_2^2}$ and $\varphi = \arctan(\varrho_{12}/z)$ is the polar angle. In spherical symmetry, this expression reduces to the form we found in §4.3.3, as the direction vector in Eq. (4.41) reduces to $\hat{r}$. As before, the direction of the magnetization is independent of the location in real space.

With this ansatz, we have $|\mathbf{M}(\mathbf{r})|^2 = M^2(\varrho_{12}, r_3)$, and

$$\lambda_i(\partial_i M_j)(\partial_i M_j) = \lambda_{12}(\partial_{12} M)^2 + \lambda_3(\partial_3 M)^2 + \lambda_{12}\frac{M^2}{\varrho_{12}^2}\sin^2\varphi + M^2\left[\lambda_{12}(\partial_{12}\varphi)^2 + \lambda_3(\partial_3\varphi)^2\right], \tag{4.42}$$

so the integral $\int \mathrm{d}^3\mathbf{r} \to 2\pi \int \mathrm{d}z\, \mathrm{d}\varrho_{12}\ \varrho_{12}$. We can assume that M is an even function of z and that $\varphi(\varrho_{12}, -z) = \pi - \varphi(\varrho_{12}, r_3)$ (so that $\sin^2\varphi(\varrho_{12}, -z) = \sin^2\varphi(\varrho_{12}, r_3)$) to restrict the energy integration grid to $z > 0$, ensuring that the total magnetization integrates to zero. The final expression for the energy can thus be recast, with $r \equiv \sqrt{\varrho_{12}^2 + z^2}$, as

$$\varepsilon_1 = \frac{64}{3\pi} \int \mathrm{d}r\ r^2 \left[\frac{6}{5} \left(\frac{n(r)}{2} \right)^{5/3} + \frac{k_\mathrm{F}^0 a}{3\pi} n^2(r) + r^2 n(r) \right], \tag{4.43}$$

$$\varepsilon_2 = \frac{64}{3\pi} \int_0^{R_{max}} dz \int_0^{\sqrt{r_{max}^2 - r_3^2}} \mathrm{d}\varrho_{12}\ \varrho_{12}\ \mathcal{F}(\varrho_{12}, r_3), \tag{4.44}$$

$$\mathcal{F}(\varrho_{12}, r_3) = A_2 M^2 + A_4 M^4 + A_6 M^6 + \frac{n}{144(3N)^{2/3}} \Bigg\{ \lambda_{12} \frac{M^2}{\varrho_{12}^2} \sin^2\varphi + \lambda_{12} (\partial_{12} M)^2 + \lambda_3 (\partial_3 M)^2 + M^2 \left[\lambda_{12} (\partial_{12}\varphi)^2 + \lambda_3 (\partial_3 \varphi)^2 \right] \Bigg\}, \tag{4.45}$$

with $\varphi(\varrho_{12} = 0, r_3) = 0$ and $\varphi(\varrho_{12}, r_3 = 0) = \pi/2$ by symmetry. For notational simplicity, we have suppressed the coordinate labels on n, m, φ in the above functional.

Upon performing the numerics, we find that spin textures in the elongated trap differ from the isotropic case only in the regime of very small atom numbers. In Fig. 4.9, we plot the magnetization profile as a function of ϱ_{12} and R_3 for 100 atoms, and find that the renormalized gradient of the magnetization is slightly greater in the elongated R_3 direction. Since the trapping force is less along this direction, the actual gradient in real coordinates will be weaker and thus the system chooses to configure itself to take advantage of this.

4.3.6 Summary of numerical results

In §4.2, we saw that, within the LDA, a two-component trapped ultracold Fermi gas is unstable to phase separation at an interaction strength $k_\mathrm{F}^0 a \sim 1.84$. The energetic signatures of this crossover include a minimum of kinetic energy and a maximum in potential and interaction energies near this interaction strength. We also predict a maximum loss rate from three-body loss near this phase-separation point.

In this section, we moved beyond the LDA to add a term which accounts for the energetic cost of density gradients in our system. In this system, we took into account various topologies of the magnetization profile to determine the optimum configuration to minimize these gradient costs. While the energetics of these spin textures were not significantly

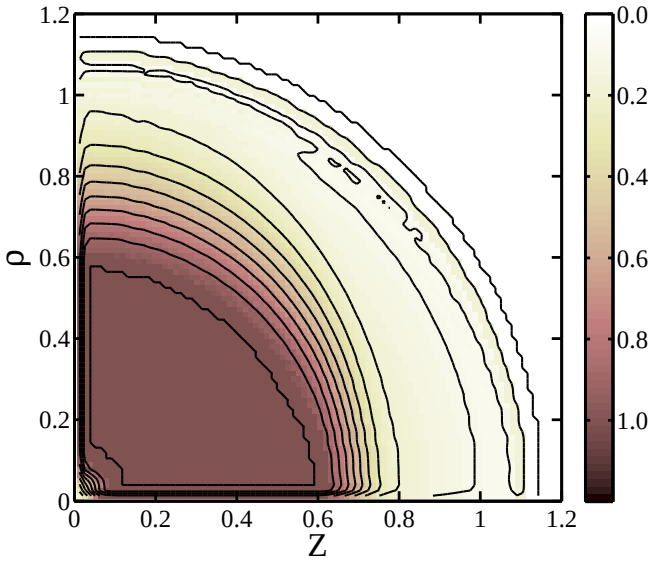

(a)

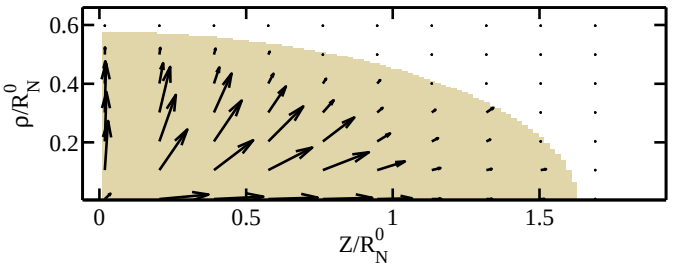

(b)

FIGURE 4.9: Two-dimensional magnetisation profile for the distorted hedgehog showing breakdown of the LDA for the magnetization density for 10^2 atoms in an anisotropic trap with $k_{\mathrm{F}}^0 a = 2.4$, and $\lambda_\perp = 2, \lambda_z = 0.25$ ($\omega_{12}/\omega_3 \approx 2.8$). (a) Plot of the magnitude of the magnetization $M(\varrho_{12}, r_3)$ and equal-magnetization contours displayed in rescaled coordinates in which the trap potential is spherically symmetric. Colorbar to the right indicates the value of $M(\varrho_{12}, r_3)$. We see that $M(\varrho_{12}, r_3)$ is larger in magnitude for larger values of ϱ_{12} than it is for z, indicating that the surface tension makes it easier to change its value in the weak trapping direction. (b) $\vec{M}$ shown as a quiver plot indicating the magnitude and direction of the magnetization (plotted in coordinates where the trap anisotropy is explicitly shown). Shaded area indicates the region of the trap where the atom density is nonzero.

different from the LDA results, there were small changes which indicate that a hedgehog-like configuration of spin directions would be favoured.

As noted in the previous section, a direct observation of the spin profile would be necessary to confirm the existence of these spin textures in such a system, especially since the energy differences between them are very small. A technique like that used to study spinor gases [105] might allow experimentalists to see these patterns.

While these results give a good qualitative understanding of the physics behind ferromagnetism in ultracold Fermi gases, there are many considerations beyond these approximations that may prove important to a better understanding of this system. Not unlike the descriptions of ferromagnetism in metals, the existence and properties of the system likely depend very strongly upon the assumptions and approximations made, and the evolution

of our understanding of this system is bound to continue as better models are constructed.

The losses inherent to this system may be one of the most important features to be brought back out from under the rug. Atoms on the repulsive side of the resonance do have the tendency to form molecules and cause loss from the atom system, on the order of tens of milliseconds for ^{40}K [102], and hundreds of milliseconds for ^{6}Li [84, 86]. This process, which limits the time available for the experiments and may prevent an equilibrium from ever being reached, is among the greatest challenges to experimental observation.

Other criticisms of the above treatment include the treatment of the interaction strength. A better description would move beyond a simple one-parameter hard-sphere scattering length to describe the interaction potential between components near the Feshbach resonance. Another improvement would be to consider the unitarity of scattering near the Feshbach resonance and how this might impose a constraint on the maximum value the scattering length may assume. These issues involve the many-body physics of the system and require sophisticated techniques, many of which are discussed in §4.5.2.

4.4 Numerical calculation details

The calculations described in the previous sections were performed numerically. While most were relatively straightforward, this section describes some of the techniques used to reach these results. All calculations were performed using the C programming language.

The optimal density and magnetization profiles for the trapped ferromagnetic Fermi gas were determinied using the energy functionals described in the above sections. In the isotropic cases (§4.3.3 and §4.3.4), the optimization is done along a one-dimensional grid (along r), generally with 200 points. In the anisotropic case, the optimization grid is taken to be 100×100 points, one dimension representing r_3 and the other ϱ_{12}.

The density profile is calculated in the LDA, and the initial magnetization profile is attained using Eq. (4.24). The optimization of the magnetization profile proceeds on a point-by-point basis, finding the value of the magnetization at each point which minimizes the total energy of the system. The routine begins with the central point, works outwards through the cloud, and repeats until convergence. The system is deemed to have converged on a magnetization profile when the energy fractionally changes by less than 10^{-6} after a full pass through the cloud.

4.4.1 Derivatives

Determining the optimal magnetization profile relies on accurate calculations of the energies of each magnetization distribution. With the greatest differences between each ansatz being the nature of the gradient of the magnetization, calculations of the derivative terms (e.g., in Eq. (4.34)) must be performed correctly.

The point-by-point nature of the optimization can lead to rapid changes in the magnetization that may or may not be accounted for in simple renderings of the derivative terms. These changes may be unphysical and simple numerical artifacts. To avoid such relics, the data is smoothed for the calculation of the derivative using a "Savitzky-Golay smoothing filter" [106].

The principle of the Savitzky-Golay smoothing filter is to approximate noisy data with a least-squares polynomial fit over some window of points before and after the point of interest. The value of the derivative of the fit at the central point is then taken as the derivative of that point. The window then slides one point down, the fit redone, and the new derivative calculated for that point. The primary advantage of this method is that the higher-order moments are retained in the smoothing process by using the fits. The method is computationally straightforward, given that least-squares fits can be performed by linear matrix inversion.

The linearity of this problem simplifies the process of fitting to the multiplication of the data by a series of pre-determined coefficients. Described at length in Ref. [106] (see §14.8 therein), these coefficients are available as a function in MATLAB[3] – one set will return the value of the data point itself, the next the value of the first derivative, the next the second derivative, and so on. The size of the window and the degree of the polynomial to which the data are fitted are the two parameters. For this work, we choose a window of 11 points - large enough that there is significant smoothing and small enough to retain local characteristics of the data. We use polynomial fits of order 4.

4.4.2 Simulated annealing

Another potential snare in these numerical calculations is the existence of local minima in energy as a function of overall magnetization profiles. We may be able to find a magnetization profile that gives the minimum energy for profiles similar to the initial state,

[3]We use the MATLAB function `sgolay(4,11)`. In the context `[b,g] = sgolay(4,11)`, we use the second column of data to determine the derivative value for the sixth point in a series of eleven: `x'(6) = [g(1,2)*x(1) + g(2,2)*x(2) + g(3,2)*x(3) + ...]`, where `x(n)` are the data points.

but there may be a condition quite different from the initial condition that gives an overall lower energy. In an attempt to allow the numerical routine to find these globally minimizing profiles, we employ an annealing procedure, in analogy to the annealing of metals where heat induces increased random motion and allows a soild to cool into its energy-minimizing cold-temperature structure.

In performing the numerical calculations described above, it was found that the annealing procedure described below was necessary for the isotropic domain wall and the anisotropic hedgehog ansatzes to reach absolute energetic minima. The parameters used in the annealing procedure were checked over a wide range of initial conditions to ensure that no further optimization could be done. For the domain wall case, the optimization procedure described above was deemed unnecessary and only the annealing was used to perform minimization. For the anisotropic hedgehog, "regular" optimization was performed first, followed by an annealing sequence.

The analogy to annealing used in this procedure comes of using a Boltzmann-type factor to determine the probability of accepting some random change to the distribution. For high temperatures, the Boltzmann distribution is broad and many energies can be accounted for with reasonable probability, while for lower temperatures, the distribution dictates that only a narrow range of energies are acceptably probable.

As with the optimization, we perform the annealing procedure point-by-point. At the initialization of the procedure, an initial artificial temperature is chosen to set the range over which the magnetization values may vary. There are two basic steps to the annealing process [107]. In the first step, the value of the magnetization profile is varied at a single point, i. In this work, we assume that the magnetization values are distributed according to a Gaussian distribution, that is the probability of finding a new magnetization value $m(r_i)^{\text{new}}$ at a given temperature T is

$$p_{\text{new}}(i) = \frac{1}{\sqrt{2\pi}\widetilde{T}} \exp\left(-\frac{(m(r_i)^{\text{new}} - m(r_i)^{\text{old}})^2}{2\widetilde{T}^2}\right) \tag{4.46}$$

when inverted, gives a value of the magnetization

$$m(r_i)^{\text{new}} = m(r_i)^{\text{old}} + \widetilde{T}\sqrt{2\ln\left(\frac{1}{\sqrt{2\pi}\widetilde{T}p_{\text{new}}(i)}\right)} \tag{4.47}$$

for some randomly chosen probability $p_{\text{new}}(i)$. To conserve magnetization, the equal and opposite change is made to another randomly-selected nearby point, j. Both changes are constrained to maintain $|m(r_{i,j})^{\text{new}}| \leq 1$.

The second step of the annealing process determines whether this new change to the magnetization should be accepted. We calculate the change in total energy ΔE of the system made by this change. If the energy is reduced, we accept the change outright. If the energy is increased, we may choose to keep the value in our quest to escape local minima. The choice to keep this new value is based upon the Boltzmann factor for the energy difference

$$p_{\text{Boltzmann}} = \frac{1}{k_{\text{B}'}T} \exp\left(-\frac{\Delta E}{k_{\text{B}'}\widetilde{T}}\right) \tag{4.48}$$

where $k_{\text{B}'}$ is an appropriately chosen constant analogous to the Boltzmann constant[4]. We then use a random number generator to find a number p_{keep} equally likely to fall between 0 and $1/k_{\text{B}'}\widetilde{T}$. If $p_{\text{Boltzmann}} > p_{\text{keep}}$, we accept the change in magnetization and proceed to the next point. If $p_{\text{Boltzmann}} < p_{\text{keep}}$, we return to the first step and attempt a different value for the magnetization.

This annealing procedure is repeated for every point in the distribution, and repeated (typically) 10 times per temperature. As this concludes, a counter variable n is advanced one unit and the temperature is then reduced according to the "schedule" $\widetilde{T}_n = \widetilde{T}_0/2^n$, where $\widetilde{T}_0$ is the initial temperature. Typical calculations used $\widetilde{T}_0 = 10$ and $n_{\max} = 100$.

4.5 Recent developments

4.5.1 Experimental evidence

In a bid to answer the question of whether a mixture of two fermionic components would undergo a transition to a ferromagnetic state in a quantum gas, Jo *et al.* subjected two hyperfine states of a ^{6}Li gas to strong repulsive interactions near a Feshbach resonance [108]. Using measurements of lifetime, kinetic energy, and chemical potential as their probes, they found signatures in these values consistent with a ferromagnetic state.

Though not in quantitative agreement with either the uniform model used in that paper [108] or this work (§4.2.2, §4.2.3), the qualitative behaviour of the measured quantities is in agreement with these models of itinerant ferromagnetism. In the measurement of the loss rate (Fig. 4.10(a)), there is an interaction strength at which the three-body loss is maximal, and a subsequent reduction in loss for yet stronger interactions, in qualitative

[4]The value of $k_{\text{B}'}$ is initially chosen to be the total energy of the system divided by the initial temperature.

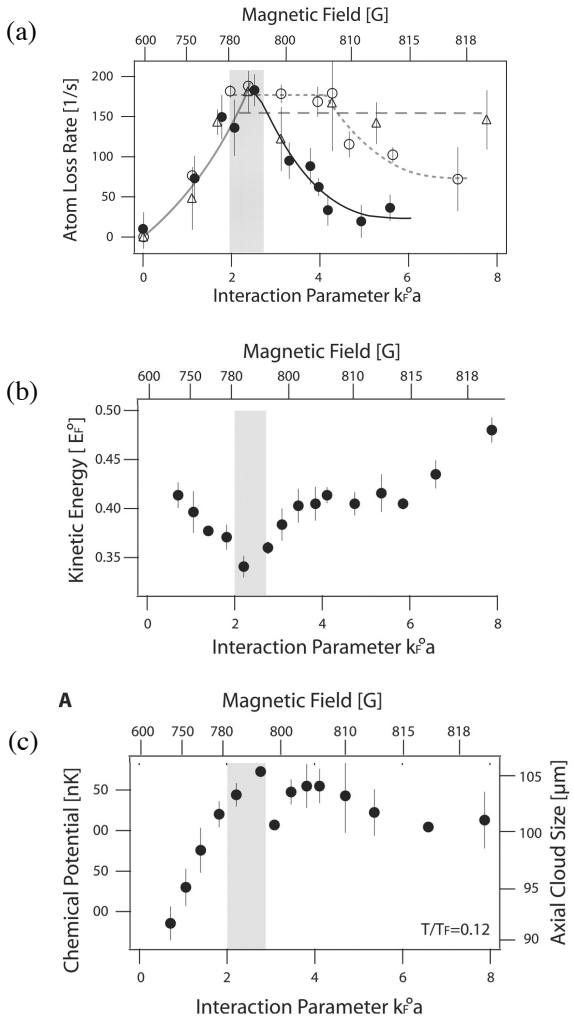

FIGURE 4.10: MIT results displaying evidence for itinerant ferromagnetism in an ultracold Fermi gas, reproduced from Jo *et al.*, [108]. The results reproduced here are for the lowest temperatures only, $T/T_F = 0.12$. The vertical grey band indicates the region of crossover to the ferromagnetic state, showing the range of possible critical interaction strengths. (a) Loss rate as a function of interaction parameter. Like Fig. 4.4, there is a peak in the loss rate, such that losses are suppressed for strong interactions. Black points show $T/T_F = 0.12$, which open circles are $T/T_F = 0.22$ and triangles are for $T/T_F = 0.55$. The curves are guides to the eye. (b) Kinetic energy vs. interaction parameter. A clear dip in the interaction energy is seen near the critical interaction strength, in qualitative agreement with results in Fig. 4.3. (c) Chemical potential and cloud size vs. interaction parameter, which is analogous to the potential energy measurement. There is a slight peak near the critical interaction strength, in qualitative agreement with results in Fig. 4.3.

agreement with Fig. 4.4. The increase in loss rate with increasing interaction strength is expected due to the dependence of the loss rate on the scattering cross-section. The decrease in loss rate for higher interaction strengths is the indicator of ferromagnetism, indicating that interactions are somehow suppressed at these large values, possibly due to a local polarization of the components. The measured peak in loss rate is found for an interaction parameter $k_F^o a$ larger than 2, and increases with temperature, while the zero temperature calculation finds the peak at $k_{\mathrm{F}}^0 a \sim 2$.

Measurements of the energies show similar qualitative agreement. The experimental kinetic energy measurements, performed by measuring the expansion energy after a rapid

turn off of both the trap and the interaction strength, display minima at particular values of the interaction parameter (Fig. 4.10(b)). The minimum exists because the large repulsive interactions existing just before the onset of ferromagnetic-like behaviour expand the cloud and reduce the kinetic energy. Beyond this transition point, the interactions have less effect as the cloud segregates and returns to its former size. The same arguments apply to the finding of a maxiumum in the chemical potential, which is directly related to the cloud size (Fig. 4.10(c)). The locations and relative changes in the energies do not fall within quantitative agreement of the results in Fig. 4.3, but the existence of the peaks and minima qualitatively corroborate these results.

One possibly obfuscating aspect of this type of experiment is the tendency for the formation of molecules on the repulsive side of the Feshbach resonance. The existence of a low-energy bound state is inherent to the mechanism of the Feshbach resonance, and the rate at which molecules form is characteristic of the atomic and molecular properties. As a result, these experiments are performed as rapidly as possible, given the constraints on magnetic field ramp times, but even so, up to 25% of the atoms exist as molecules in these samples. Though checks were made to ensure the proportion of molecules in the system did not affect the results, there may be more-complicated physics involving interactions that include the molecular component.

4.5.2 Subsequent theoretical work

In the wake of these experimental results [108], interest in ferromagnetism in cold gases has blossomed. Some of this work focusses on making better calculations of the ferromagnetic transition point, particularly through quantum Monte Carlo (QMC) calculations [101, 109]. The QMC methods allow for more complicated and possibly many-body interactions to replace the simple hard-sphere scattering approximations made in previous work. Both studies [101, 109] find that the critical interaction parameter is reduced by considering these scattering models.

The possible complications due to the presence of molecules in the sample are addressed in another work [110], where the dynamics of the experiment are considered. Using a description for the scattering that accounts for both the energy dependence near the Feshbach resonance and Pauli blocking, they study the rates of the pairing and ferromagnetic instabilities and find that the pairing instability is always dominant. Additionally, they show that a maximum in pairing rate occurs around $k_F a \sim 2$ and that there is a reduction in kinetic energy of the unpaired electrons due the shrinking Fermi sea, in qualitative agreement with

experimental results. These results suggest that pairing alone may account for some of the effects attributed to ferromagnetism.

Another vein of work inspired by this experiment considers whether there is an explanation for the non-monotonic behaviour of the energies that does not invoke ferromagnetism. Zhai asks "whether spin polarization is the only way to reduce interaction energy" [111] and answers with a calculation showing that a configuration including short-range correlations renormalizes the interaction strength and leads to the same energetic signatures as were seen in the experiment. The nature of the short-range correlations are similar to those in the Gutzwiller projected wavefunction, where the probability of two opposite-spin fermions existing at the same spatial location is suppressed without the emergence of long-range order characteristic of a ferromagnet. In particular, a variational solution to the density profile is introduced by assuming that the probability of opposite-spin fermions at the same point is reduced from ρ^2 to $(1-\widetilde{g})\rho^2$, where $\widetilde{g}$ is the variational parameter and $(1-\widetilde{g})$ reduces the interaction parameter for repulsive interactions ($\widetilde{g}>0$).

He points out that without the direct observation of ferromagnetic domains, the short-range correlated configuration cannot be distinguished from the ferromagnetic. In subsequent work [112], Zhai and Cui found that the there were regions of interaction strength in which both ferromagnetic and short-range correlation fluctuations exist, and that the ferromagnetic state was, indeed, dominant for sufficiently high interaction strengths. They point out, however, that different correlation mechanisms may be sufficient to eliminate the ferromagnetic tendencies.

In this evolution of theories, we see a trend not unlike that emerging from the original models of ferromagnetism in metals. The existence of ferromagnetism seems to depend very much on the approximations used to describe the system. Like many problems involving fermions, calculations are difficult, and the question of the existence of ferromagnetism may be best settled by an unambiguous experimental signature, such as a direct observation of spin polarization.

4.6 Observations of strongly interacting ^{40}K atoms

The original motivation for the theoretical work in ferromagnetism in trapped fermions was in preparation for experiments with strongly interacting ^{40}K. While these experiments were delayed, and some of the results of the theory confirmed by the MIT experiment [108],

plans to continue this work remain. Below is a description of the preparations made for this experiment, completed before the December 2007 apparatus renewal and the new atom chip that came with that.

The original plan for these experiments was in keeping with the suggestions put forth in Ref. [99] – we planned to prepare a ferromagnetic state and observe its subsequent decay as a function of the interaction strength between states. As such, one of the key ingredients to experiments exploring ferromagnetism is the ability to manipulate the scattering length between atoms. To do this, we plan to use an already-discovered Feshbach resonance ([113], see §4.6.2). In general, these resonances occur only for atoms in specific hyperfine and Zeeman states; in particular, high-field seeking states. These conditions stipulate that internal state manipulation is important for preparation, and optical trapping is necessary for confinement. The resonance occurs at a specific value of the magnetic field, and control of this value is important for control of the interactions between atoms. The following subsections describe the progress made in readying the apparatus for ferromagnetism experiments.

4.6.1 Internal state preparation

The experimental sequence used to gather ultracold fermions relies upon magnetic trapping, as described in §2.1.1. The sympathetic cooling done by the ^{87}Rb yields a spin-polarized DFG of ^{40}K at the end of the cooling sequence. These atoms, in the low-field seeking $|F, m_F\rangle = |9/2, 9/2\rangle$ state must be transferred to an optical trap and their internal state must be manipulated to obtain the high-field seeking states we wish to use with the Feshbach resonance. Either rf- or microwaves will induce transitions from the weak-field seeking states to the high-field seeking states; both are shown ground state manifold schematic in Fig. 4.11.

Calculating transition frequencies

The hyperfine structure of the ^{40}K atom is discussed at length in Appendix A. The frequency separations between ground states can be found from the Breit-Rabi formula, which applies to ground state atoms with ($J = \frac{1}{2}$) [62] and is an exact diagonalization of Eq. (A.11)

$$E_{\pm}/h = -\frac{A_{\rm hfs}(I+\frac{1}{2})}{2(2I+1)} + g_I\mu_{\rm B}mB \pm \frac{A_{\rm hfs}(I+\frac{1}{2})}{2}\left(1 + \frac{4m\mathcal{X}(B)}{2I+1} + \mathcal{X}^2(B)\right)^{1/2} \qquad (4.49)$$

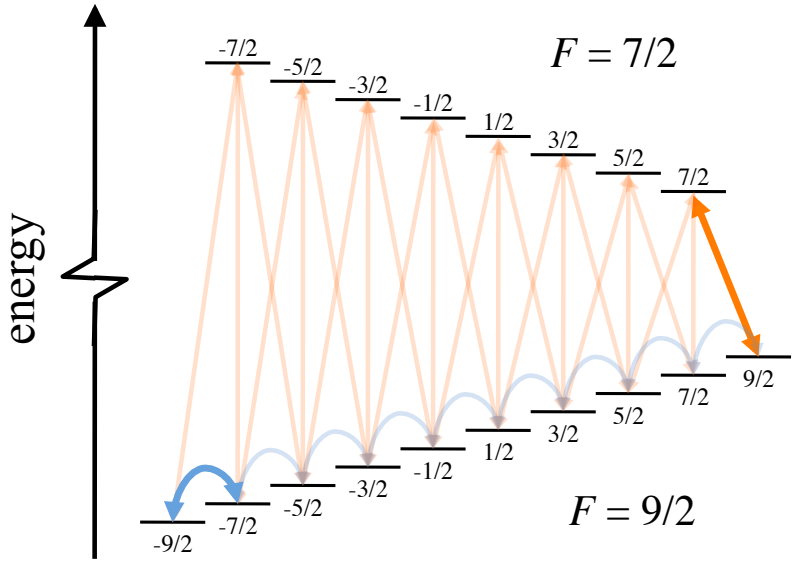

Figure 4.11: Ground state manifold of ^{40}K, in a magnetic field. Lower manifold corresponds to the $F = 9/2$ hyperfine states; upper manifold corresponds to the $F = 7/2$ manifold. Small numbers indicate m_F quantum number, good at low magnetic fields. RF transitions within the hyperfine manifold are schematically shown by blue curved arrows for the lower manifold, while the orange straight arrows correspond to the microwave transitions between hyperfine manifolds.

where

$$\mathcal{X}(B) = \frac{(g_J - g_I)\mu_B B}{A_{\rm hfs}(I + \frac{1}{2})}, \tag{4.50}$$

and $A_{\rm hfs} = -285.731$ MHz [114], $I = 4$ [61], $g_J = 2.00229421$ [61], $g_I = 0.000176490$ [61], and $m = m_I \pm \frac{1}{2}$ for all $m_I \in [-I, I]$. Additionally, this formula can be used to calculate the magnetic moments of each of the ground states as a function of magnetic field by taking the derivative of this expression,

$$\frac{\partial E_\pm}{\partial B} = g_I \mu_B m \pm \frac{(g_J - g_I)\mu_B}{4} \frac{2\mathcal{X}(B) + \frac{4m}{2I+1}}{\left(1 + \frac{4m\mathcal{X}(B)}{2I+1} + \mathcal{X}^2(B)\right)^{1/2}}. \tag{4.51}$$

The energies and magnetic moments for ^{40}K are shown in Fig. 4.12, and the transition frequencies between states for those transitions allowed in the low-field limit are tabulated in Tables 4.1 and 4.2 for the microwave and rf transitions, respectively.

In addition to determining the appropriate transition frequencies for state preparation given a magnetic field, an alternate use of these data is for calibration of a magnetic field.

			Magnetic field		
$\|F, m_F\rangle$	$\leftrightarrow$	$\|F', m'_F\rangle$	20.00 G	202.10 G	224.21 G
$\|9/2, 9/2\rangle$	$\leftrightarrow$	$\|7/2, 7/2\rangle$	1236.4	820.2	775.6
$\|9/2, 7/2\rangle$	$\leftrightarrow$	$\|7/2, 7/2\rangle$	1242.9	918.2	890.5
$\|9/2, 7/2\rangle$	$\leftrightarrow$	$\|7/2, 5/2\rangle$	1249.3	998.8	981.6
$\|9/2, 5/2\rangle$	$\leftrightarrow$	$\|7/2, 7/2\rangle$	1249.2	998.9	981.7
$\|9/2, 5/2\rangle$	$\leftrightarrow$	$\|7/2, 5/2\rangle$	1255.6	1079.6	1072.8
$\|9/2, 5/2\rangle$	$\leftrightarrow$	$\|7/2, 3/2\rangle$	1261.9	1149.7	1150.4
$\|9/2, 3/2\rangle$	$\leftrightarrow$	$\|7/2, 5/2\rangle$	1262.0	1149.7	1150.5
$\|9/2, 3/2\rangle$	$\leftrightarrow$	$\|7/2, 3/2\rangle$	1268.3	1219.8	1228.2
$\|9/2, 3/2\rangle$	$\leftrightarrow$	$\|7/2, 1/2\rangle$	1274.5	1282.6	1297.1
$\|9/2, 1/2\rangle$	$\leftrightarrow$	$\|7/2, 3/2\rangle$	1274.5	1282.7	1297.2
$\|9/2, 1/2\rangle$	$\leftrightarrow$	$\|7/2, 1/2\rangle$	1280.8	1345.5	1366.1
$\|9/2, 1/2\rangle$	$\leftrightarrow$	$\|7/2, -1/2\rangle$	1287.0	1402.9	1428.8
$\|9/2, -1/2\rangle$	$\leftrightarrow$	$\|7/2, 1/2\rangle$	1287.0	1403.0	1428.8
$\|9/2, -1/2\rangle$	$\leftrightarrow$	$\|7/2, -1/2\rangle$	1293.2	1460.4	1491.3
$\|9/2, -1/2\rangle$	$\leftrightarrow$	$\|7/2, -3/2\rangle$	1299.3	1513.6	1549.0
$\|9/2, -3/2\rangle$	$\leftrightarrow$	$\|7/2, -1/2\rangle$	1299.3	1513.7	1549.0
$\|9/2, -3/2\rangle$	$\leftrightarrow$	$\|7/2, -3/2\rangle$	1305.5	1566.9	1606.7
$\|9/2, -3/2\rangle$	$\leftrightarrow$	$\|7/2, -5/2\rangle$	1311.5	1616.8	1660.6
$\|9/2, -5/2\rangle$	$\leftrightarrow$	$\|7/2, -3/2\rangle$	1311.5	1616.9	1660.7
$\|9/2, -5/2\rangle$	$\leftrightarrow$	$\|7/2, -5/2\rangle$	1317.6	1666.7	1714.5
$\|9/2, -5/2\rangle$	$\leftrightarrow$	$\|7/2, -7/2\rangle$	1323.7	1713.7	1765.1
$\|9/2, -7/2\rangle$	$\leftrightarrow$	$\|7/2, -5/2\rangle$	1323.7	1713.8	1765.2
$\|9/2, -7/2\rangle$	$\leftrightarrow$	$\|7/2, -7/2\rangle$	1329.7	1760.7	1815.8
$\|9/2, -9/2\rangle$	$\leftrightarrow$	$\|7/2, -7/2\rangle$	1335.6	1805.1	1863.4

Table 4.1: Microwave transitions between ^{40}K ground states. All values in MHz.

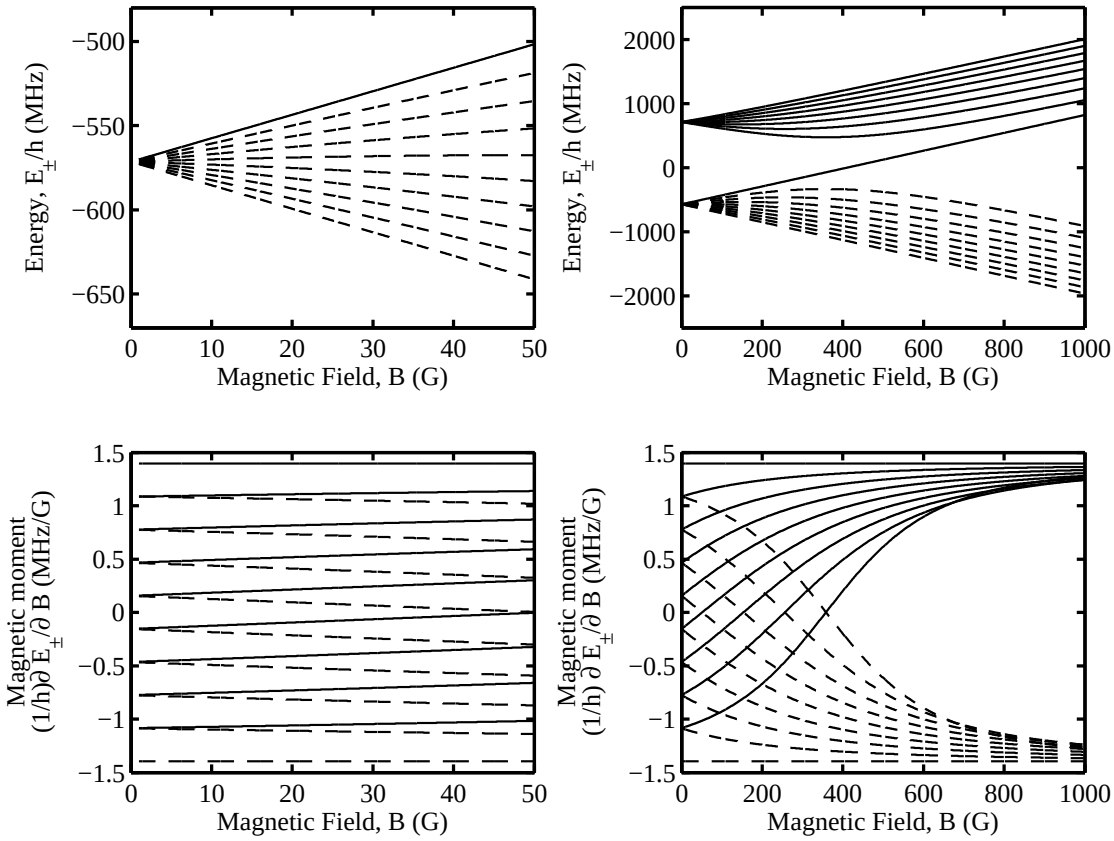

Figure 4.12: Top row: Hyperfine energies vs. magnetic field for low (left) and all (right) fields. Solid (dashed) lines indicate $E_{+(-)}$. For low fields, only the lower manifold is shown. Bottom row: magnetic moments for low (left) and all (right) magnetic field values. As above, solid (dashed) lines show $\partial E_{+(-)}/\partial B$. The quantum numbers for the states shown are (in the right panels) from top to bottom: $m_F = \{-7/2, \cdots, 7/2, 9/2, \cdots, -9/2\}$, or $m_I = \{-4, \cdots, 4, 4, \cdots, -4\}$ with $m_S = 1/2$ for the solid lines and $-1/2$ for dashed lines.

By spectroscopically determining some transition frequency between well-known states, the magnetic field can be measured precisely.

Demonstrating state control

In order to prepare atoms for the demonstration of the Feshbach resonance, we need to manipulate the internal state to prepare the appropriate combinations for the resonance we choose. In the magnetic trap, where sympathetic cooling has brought them near degeneracy, the atoms are in the magnetically trappable $|9/2, 9/2\rangle$ stretched state. These are transferred to a purely optical trap. Here, we wish to make a mixture of atoms in the $|9/2, -9/2\rangle$ and

			Magnetic field		
$\|F, m_F\rangle$	$\leftrightarrow$	$\|F', m'_F\rangle$	20.00 G	202.10 G	224.21 G
$\|9/2, 9/2\rangle$	$\leftrightarrow$	$\|9/2, 7/2\rangle$	6.4572	98.3764	115.427
$\|9/2, 7/2\rangle$	$\leftrightarrow$	$\|9/2, 5/2\rangle$	6.3909	80.7533	91.1601
$\|9/2, 5/2\rangle$	$\leftrightarrow$	$\|9/2, 3/2\rangle$	6.3266	70.1665	77.7900
$\|9/2, 3/2\rangle$	$\leftrightarrow$	$\|9/2, 1/2\rangle$	6.2642	62.8980	69.0000
$\|9/2, 1/2\rangle$	$\leftrightarrow$	$\|9/2, -1/2\rangle$	6.2036	57.5078	62.6522
$\|9/2, -1/2\rangle$	$\leftrightarrow$	$\|9/2, -3/2\rangle$	6.1447	53.3060	57.7896
$\|9/2, -3/2\rangle$	$\leftrightarrow$	$\|9/2, -5/2\rangle$	6.0875	49.9094	53.9100
$\|9/2, -5/2\rangle$	$\leftrightarrow$	$\|9/2, -7/2\rangle$	6.0319	47.0902	50.7211
$\|9/2, -7/2\rangle$	$\leftrightarrow$	$\|9/2, -9/2\rangle$	5.9383	44.3032	47.5979

Table 4.2: RF transitions in ground state ^{40}K, $F = 9/2$ manifold. All values in MHz.

$|9/2, -7/2\rangle$ states, that we might address the 202 G resonance (See §4.6.2).

First, we transfer the atoms from the weak-field seeking part of the manifold to the high-field seeking. Using adiabatic rapid passage, we can sweep an rf field through the resonances between adjacent states to complete a transfer from the weak-field seeking stretched state to the high-field seeking one. We turn on the rf field far above resonance at 11.0 MHz, so as not to induce any spurious transitions at turn on. With a quantization field of 19.8 G, we ramp the rf frequency to a value above the resonance for the first rf transition in the ladder, 6.55 MHz (See first column of Table 4.2). In 30 ms, we linearly ramp the rf frequency from 6.55 MHz to 5.70 MHz, which is below the frequency for the lowest transition on the ladder. The rf frequency is then ramped down to 1.50 MHz in 5 ms and turned off. Using Stern-Gerlach imaging, we separately image the different m_F states and optimise these parameters for transfer into the $m_F = -9/2$ state.

To create a mixture of $|9/2, -9/2\rangle$ and $|9/2, -7/2\rangle$, we add a step before ramping the frequency to 1.50 MHz. At this point, we ramp the frequency back up to the resonance position (in 5 ms) between these two states, which we experimentally determine is 5.90 MHz, by balancing the populations of the two components. The field is then suddenly turned off. That this is a mixture instead of a pure state arises due to the dephasing inherent in this experiment. Long wait times allow the atoms to sample the different magnetic fields (due to imperfect uniformity of the fields) and the phase relationship in the superposition is randomized atom-to-atom.

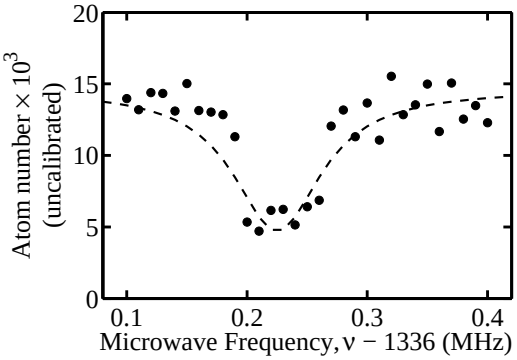

Figure 4.13: Microwave transfer in magnetic trap, with 19.8 G Ioffe field. A mixture of atoms in $|9/2, -9/2\rangle$ and $|9/2, -7/2\rangle$ is prepared. Shown is a measure of atom number in the $|9/2, -9/2\rangle$ after microwave sweep. The Lorentzian fit gives the transition centre at 1336.228 ± 0.003 MHz and width of 0.09 ± 0.01 MHz.

We also show that microwaves can manipulate the state of the atom. With a mixture created as above in a magnetic field of 19.8 G (very near the 20.00 G tabulated in Table 4.2), we transfer atoms from the $|9/2, -9/2\rangle$ to the $|7/2, -7/2\rangle$ state. We measure the atom number in the $m_F = -9/2$ state and see a loss around the expected value in Fig. 4.13.

4.6.2 Feshbach resonance in ^{40}K

The interactions between two particular internal states of an ^{40}K atom can be controlled by varying the magnetic field in the vicinity of a Feshbach resonance. Using the results of Refs. [9, 113], the scattering length between the $|9/2, -9/2\rangle$ and $|9/2, -7/2\rangle$ states as a function of magnetic field

$$a_{79}(B) = 174a_0 \left(1 - \frac{7.8}{B - 202.10\ \text{G}}\right), \tag{4.52}$$

where $174a_0$ is the background scattering length, B is the magnetic field, 202.10 ± 0.07 G is the experimentally measured centre of the resonance between these states, and 7.8 ± 0.6 G its width. A resonance between the $|9/2, -9/2\rangle$ and $|9/2, -5/2\rangle$ states has also been observed, at a magnetic field of 224.21 ± 0.05 G with a width of 9.7 ± 0.6 G [115].

To identify the position of the resonance, we rely upon the enhanced three-body loss associated with the large scattering length near the resonance. Since the loss rate is proportional to the sixth power of the scattering length [103], changes in the scattering length, a, will be mirrored by dramatic changes in the loss rate.

We create a mixture of atoms in the $|9/2, -9/2\rangle$ and $|9/2, -7/2\rangle$ states in an optical trap and turn on the magnetic field smoothly in 20 ms to values near 202.10 G. This field is held for 500 ms, after which it is smoothly turned off in 100 ms. Figure 4.14 shows the

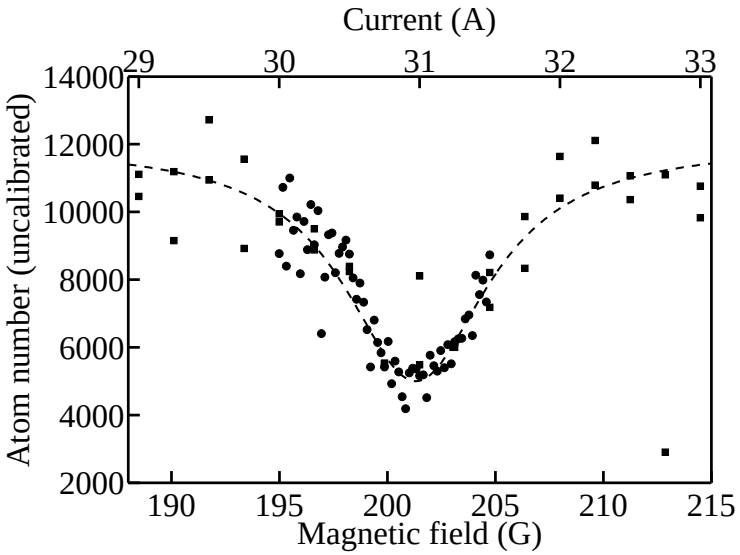

Figure 4.14: Experimental evidence of Feshbach resonance in ^{40}K. Round and square points represent two different data sets, obtained in that order within 1 hour. The magnetic field was calibrated with Zeeman transition frequencies in ^{87}Rb . The dashed line is a Lorentzian fit to all of the data, with centre at 201.3 ± 0.2 G and width 8.10 ± 0.02 G.

total atom number as a function of the final field value. There is a clear loss feature around 201.3 ± 0.2 G, with a width of 8.10 ± 0.02 G. This centre value is in good agreement with the accepted value.

4.6.3 Magnetic field stability

Stability criteria

As discussed in the theoretical sections of this chapter, the relevant control parameter is the interaction parameter, which is $k_{\mathrm{F}}^0 a = k_F^0(\mathbf{0})a$. To determine the precision with which we must control the magnetic field, we relate it to this interaction parameter. The scattering length varies with magnetic field as Eq. (4.52) and the Fermi wavevector depends on the density, and thus the number of atoms and trap parameters. As an estimate, we assume that we will use $\sim 10^4$ atoms and harmonic trap parameters $\omega = 2\pi \times (1000, 1000, 50)$ Hz, and find

$$k_F^0 = \sqrt{\frac{m\overline{\omega}}{\hbar}}(48N)^{1/6} = 1.1 \times 10^7 \mathrm{m}^{-1}. \tag{4.53}$$

The region in which the interesting physics exists is that of strong interactions, which we will define as $k_F^0 a > 1$. Using the parameters above, this amounts to a magnetic field

range from 201.22 G to 202.10 G, or a region of 880 mG width. As a comparison, if $\omega = 2\pi \times (200, 200, 50)$ Hz, the values of magnetic field at which $k_F^0 a > 1$ are 201.61 G to 202.10 G, yielding a range of 490 mG of strong repulsive interactions.

As a minimal requirement for field stability, we might assume that we need to control the magnetic field to within 10% of the field range over which interesting interaction parameters exist, meaning ~ 50 mG stability for the weaker trap. In a ~ 200 G field, this requires 1 part in 4×10^3 stability.

For a more stringent requirement on field stability, we consider a demanding measurement technique. One means of determining the existence of interactions (and thus a demagnetized state) in this system is to measure the transition frequency to an auxillary Zeeman state [115, 116]. The interactions will shift these transitions by an amount known as the clock shift, the frequency of which is

$$\Delta\nu = \frac{2\hbar}{m}\rho_7(a_{79} - a_{57}) \tag{4.54}$$

where we are considering the specific case of atoms in $|F = 9/2, m_F = -9/2\rangle$ and $|9/2, -7/2\rangle$, and an auxillary state $|9/2, -5/2\rangle$, where ρ_7 is the density of the $|9/2, -7/2\rangle$ atoms, a_{79} is the scattering length between the two states which depend on the magnetic field in the regime of this experiment, and $a_{57} = 174a_0$ is the background scattering length, since they are far from that resonance.

One possibility for the stability criterion is to demand a stability with which one can distinguish between the absence and presence of interactions to a precision equal to the background scattering length. If we assume a density $\rho_7 = 1 \times 10^{13}$ cm^{-3}, then $\Delta\nu = 913$ Hz. Translating this frequency into a magnetic field, we consider the magnetic moment differences at 202.10 G:

$$\mu_{-7/2} - \mu_{-9/2} = 154 \text{ kHz/G} \tag{4.55}$$

$$\mu_{-5/2} - \mu_{-7/2} = 170 \text{ kHz/G}, \tag{4.56}$$

where the subscripts refer to m_F. Using the first of these, this implies that a stability of 913 Hz leads to a field stability of ~ 6 mG. In fractional terms, 6 mG/202.10 G $\sim 3 \times 10^{-5}$ – a few parts in 10^4.

Comparing this number to the Jin experiment, C. Regal's thesis [117] (p112) cites a stability of 7 mG, and they can measure up to a 1 kHz precision on the $|-5/2\rangle \to |-7/2\rangle$ transition, which is similar to the demand of our estimate.

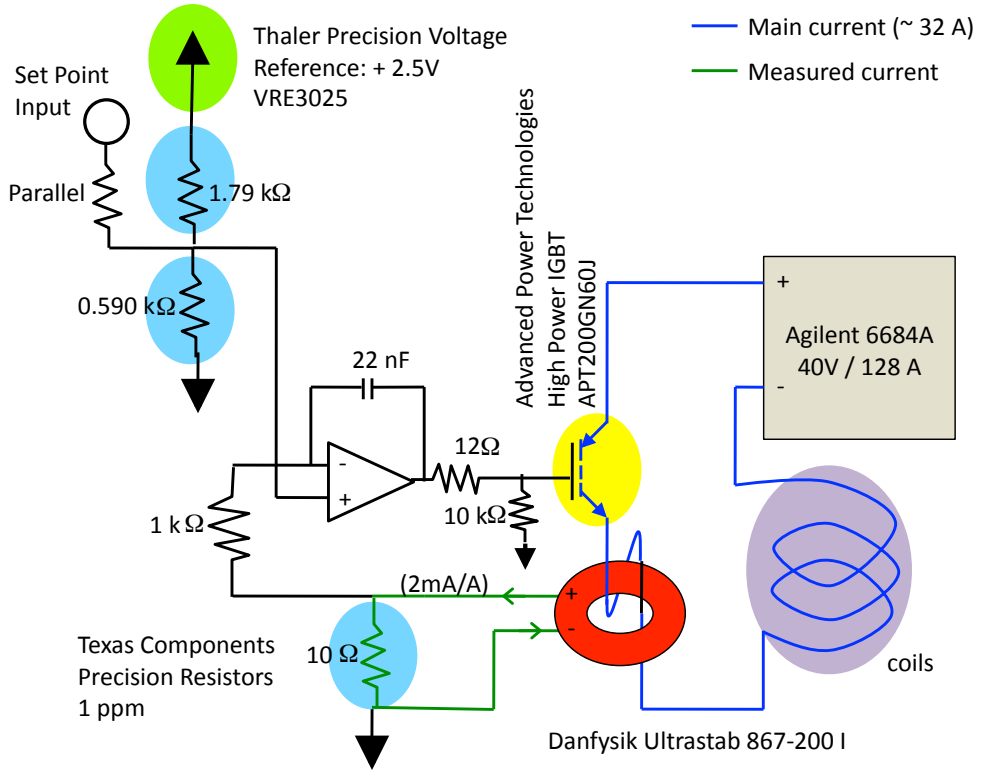

Figure 4.15: Schematic of Feshbach control circuit. Magnetic coil current (blue line) is controlled by high power IGBT (yellow), with feedback from a precision current transducer, Danfysik Ultrastab 867-200 I (red). The current output (green line) of the transducer is measured by a high-precision 10 Ω (1 ppm) resistor (blue highlight) and compared to the set voltage. The set voltage is determined by a voltage divider with similar precision resistors and powered by a precision voltage source (green highlight). The set point input allows for small changes on the set voltage.

Magnetic field stability

To gain access to the tunability of the interaction strength available at a Feshbach resonance, we must, in addition to trapping the atoms optically, stabilize the magnetic fields about the resonance feature. The precision of the magnetic field reflects that available for the interaction strength values. The same coils are used for this high magnetic field as to create the gradient for the MOT (see §2.1, [15]), but instead of anti-Helmholtz, they will be switched to a Helmholtz configuration. The existing magnetic field control was implemented via the power supply current-limit mode.

To improve upon this set up, we control the current external to a low-noise power supply using a feedback loop between a precision current probe and a high-power transistor. We use the low-noise power supply, Agilent 6684A (40 V / 128 A, noise 1.0 $\mathrm{mV_{rms}}$, 10 $\mathrm{mV_{pp}}$). We measure the current with Danfysik's Ultrastab 867-200I current sensor (temperature stability and temporal drift characteristics are $<$ 1 ppm/K, $<$ 1ppm/month). The control scheme is outlined schematically in Fig. 4.15. The basic principle is to measure the output of the current sensor across a precision resistor (Vishay VH102K series, 1 ppm) and compare this to a set point voltage, which we implement in this first version of the circuit through a precision voltage reference (Thaler VRE3025, 0.6 ppm/°C) divided down to the appropriate input value through a resistor-divider network. The resultant error signal is provided as the gate voltage on a high-power IGBT (Advanced Power Technologies APT200GN60J, 600V, 280A) such that it controls the coil current running between the collector and emitter.

To test the stability of the magnetic field control, we study the width of an atomic transition with various field control schemes. We use a transition in ^{87}Rb, loading atoms in the $|F = 2, m_F = 2\rangle$ internal state into an optical trap. We tune the magnetic field to a value we presume is near the 202 G necessary for the Feshbach control of the ^{40}K atoms. We transfer the Rb atoms to the $|2, 1\rangle$ state using an rf frequency near 128 MHz. The rf is turned on suddenly, and left on for 50 ms, and turned off suddenly. As the transform-limited width associated with this pulse is $\sim$ 20 Hz, widths greater than these would indicate an instability in the magnetic field, whose variations broaden the value of the transition. We assume the magnetic field noise is the dominant broadening mechanism in these ultracold (but not degenerate) clouds.

These transitions are shown for various configurations of field control in Fig. 4.16. Fig. 4.16(a) shows the transition for the original magnetic control scheme, and yields the widest transition. Fig. 4.16(b) shows the transition for the new magnetic control scheme, in what is called "Configuration I" – a configuration using a switching power supply in the control circuit. The transitions for "Configuration II" are shown in Figs. 4.16(c) and 4.16(d). Here, the switching power supply in the control was replaced by an HP E3611A linear power supply, which is much better at filtering line noise. With widths as small as 6 kHz on a transition of 128 000 kHz, this initial test showed a reduction of a factor of 10 in the noise, to the level of one part in 2×10^4.

Improvements to this circuit (§4.6.3) need to be made to allow fast switching over a $\sim$ 10 G range, in order to access the zero of the Feshbach resonance and turn off interactions. Changes to the input signal set-point should allow for this.

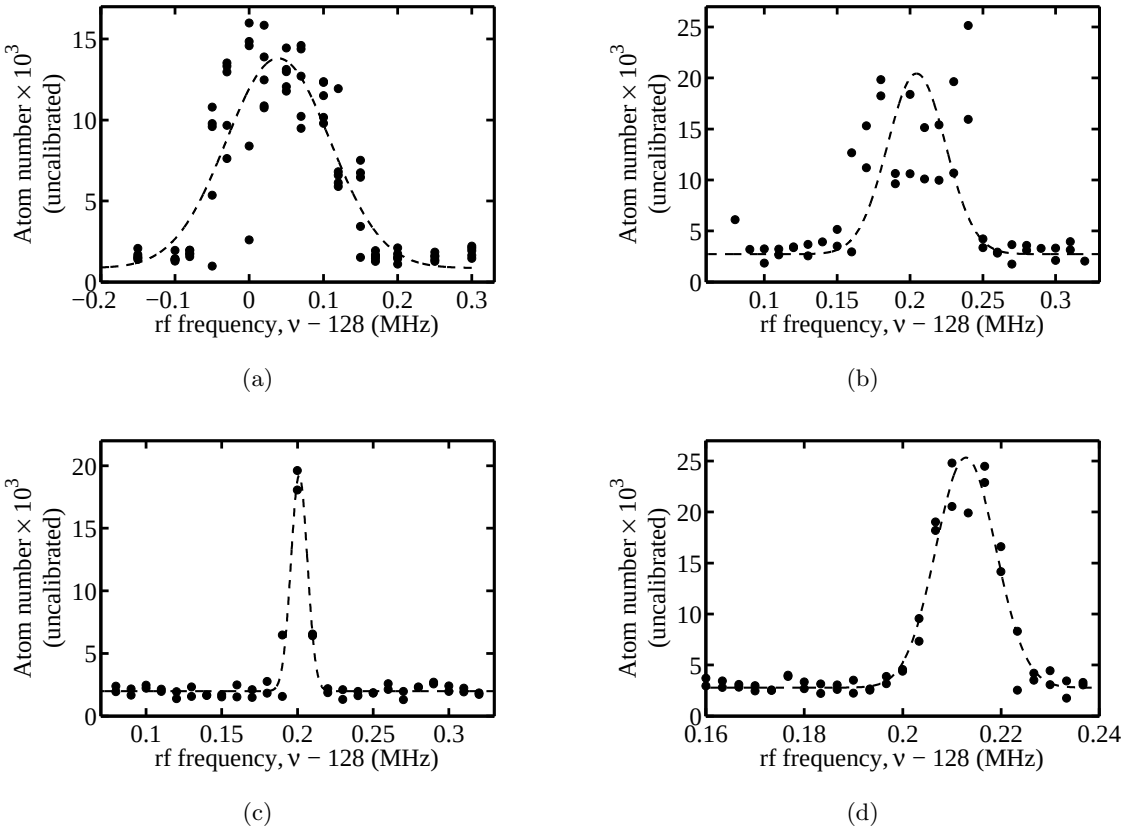

Figure 4.16: Magnetic field stability measurements, made by looking at the width of rf transitions between ^{87}Rb states $|2,2\rangle$ and $|2,1\rangle$. Horizontal scales are not equal. Dashed curves are Gaussian fits to the data, to approximate a width of the transition. (a) With original magnetic field control, $\sigma = 70 \pm 6$ kHz, (b) With new magnetic field control, Configuration I, $\sigma = 20 \pm 5$ kHz, (c) With new magnetic field control, Configuration II, $\sigma = 6.1 \pm 0.3$ kHz, (d) Same conditions as (c) with an increased sampling frequency, $\sigma = 5.4 \pm 0.2$ kHz.

4.6.4 Looking forward

Before experiments probing ferromagnetism are ready, a few challenges remain.

The fermions need to be degenerate in the optical trap, at temperatures at or below $0.2T_F$. To date in our laboratory, these temperatures have only been reached in the magnetic trap via sympathetic cooling with ^{87}Rb . The most likely route towards this is to stop the sympathetic cooling at some optimized point (before the onset of strong K-Rb losses) during the cooling process, remove all Rb from the magnetic trap, and load fermions into the optical trap. Here, a spin mixture could be made, which would then allow for thermalization during a subsequent all-optical evaporation process. A Feshbach-enhanced scattering length could

be used to optimise the procedure. At high enough magnetic fields, these states can be isolated spectroscopically and one could be removed from the trap. At this point, the desired state could be initialized through appropriate rf or microwave transitions.

Once cold fermions have been produced in the optical trap, and the magnetic field stability is deemed sufficient for the experiment, one issue facing this experiment is the loss rate to molecular production. There have been some measurements of this loss [113], but it should be measured at the densities and trap configurations we will be using. These measurements will set a time scale in which the experiments looking for ferromagnetism must to completed and may insist on more stringent requirements of timing control than are currently available.

One of the first and most straightforward experiments to perform would be that on which we originally planned – the proposal of Duine and MacDonald [99]. Using the tools developed above, atoms in an identical superposition state of the two Zeeman levels affected by the Feshbach resonance would be put in the region of strong interactions. By measuring the timescale for which the atoms remain in the ferromagnetically ordered identical states, we could observe how the preservation of a ferromagnetic state depends on the strength of the interactions. Using a trimming gradient coil, we could change the magnetic field gradients seen by the sample and measure how the dephasing induced by the different energy environment across the cloud affects the preservation of this ferromagnetism.

Chapter 5

BEC dynamics in a tunable double well

The condensation of bosons into a single ground-state wavefunction is a well understood example of individual quantum mechanical objects transitioning into a many-body state. The emergence of a single phase parameter attests to the quantum mechanical nature of this mesoscopic object. The first measurements of this phase came of probing the phase difference between two separated condensates [118], circumventing the restriction forbidding the measurement of a single phase. When there exists some wavefunction overlap between nearby condensates, the phase difference across the barrier can be well-defined and will, as first described by Josephson for superconductors [119], drive transport across the junction. Recent double well BEC experiments have exploited these properties to realize tunnelling transport [120] and to generate exotic quantum mechanical states [121].

Dynamical studies can reveal properties of the underlying hamiltonian governing the general behaviour of system. In a BEC, quantum mechanical transport is driven by spatial gradients in the phase. In the double well system, the character of the transport between the wells in particularly sensitive to the spatial phase gradients in and across the barrier region. By tuning the height of the barrier, and thus the density and healing length of the BEC at the point connecting the wells, the character of the macroscopic transport changes, revealing the many-body properties of the system.

In this chapter, a BEC is introduced to a tunable magnetic double well potential, where all barrier heights from zero to effectively-infinite are explored. This chapter studies the quantum transport of the BEC across the barrier for various out-of-equilibrium initial conditions at variable barrier heights. By studying both mass transport and phase evolution, we find the system behaves as a single "perfect" – inviscid, irrotational – fluid for low barriers and strong coupling between the wells, and as a Josephson junction for large barriers

or large initial imbalances where tunnelling is the dominant mechanism of transport.

This chapter begins in §5.1 by establishing the context for these experiments in terms of work done in similar systems both in the condensed-matter and quantum-gas worlds. A description of the underlying equations of motion in the strong and weak-coupling regimes follows in §5.2, and the experimental tools specific to this chapter are described in §5.3. For small initial imbalances, mass-transport behaviours are described in §5.4, revealing a crossover between superfluid hydrodynamics and Josephson transport. Observations of Josephson-like behaviour in the mass transport for large initial imbalances is reported in §5.5. In §5.6, the decay of population imbalance is studied. Phase signatures of quantum transport are discussed in §5.7 and the implications of this work are considered in §5.8.

5.1 Background and context for double well experiments

Long before the idea of a double well was applied to dilute-gas BECs, it was studied within the context of other many-body systems. The interesting properties of double-well physics emerged as technological advances provided better superconducting materials, and effects like tunnelling could be measured. Brian Josephson was the first to describe a set of behaviours characteristic of a tunnelling junction between two superconducting systems, each of which is described by its own wavefunction. These Josephson effects were discovered in a variety of systems, including superfluid helium. In the era of the ultracold gas, these quantum fluids have also been studied in double well environments, with motivations including precision interferometry and exotic quantum state manufacture.

Josephson junctions in condensed matter physics

In the early 1960's, fabrication techniques, especially thin-film deposition, were developed to the point where superconducting materials could be manipulated into a variety of structures. Observations of tunnelling between superconducting layers separated by an insulator [122, 123] indicated that the electron wavefunction extended beyond the classical bounds of the superconducting material.

Brian Josepshon, in thinking about the nature of the superconducting order parameter, realized that the quantum mechanical phase difference between two nearby but insulated superconducting regions would be well-defined and observable if the system could satisfy the number-phase uncertainty relationship by allowing electrons to tunnel between the

regions [124]. His calculations showed that a superconducting current would travel across the insulating barrier and predicted two effects [119]: first, for external currents less than some critical value, there would exist a supercurrent flowing across the junction with zero voltage drop; second, for external currents above the critical value, a sinusoidally varying supercurrent flows across the junction, with a frequency that depends on the potential energy difference between the regions. These stationary "dc" and oscillatory "ac" effects are defining characteristics of the Josephson junction. In the ac case, the evolution of the phase depends on the potential energy difference between the two regions in a simple way: $\dot{\phi} = \Delta E/\hbar$, where ϕ is the difference in the phase across the junction, and ΔE is a generic energy difference between them, which is this particular case takes the form $\Delta E = 2eV$, where e is the electric charge and V is the voltage difference across the junction. Evidence for these effects was seen very soon after their prediction in superconducting-insulating-superconducting sandwich geometries [125–127].

Though tunnel junctions were conceived as the original infrastructure upon which Josephson junctions were based, these devices do not hold a monopoly on Josephson-type phenomena. Similar behaviour has been found across weak links [128, 129], in which the superconducting regions are physically, but weakly, connected. The criterion establishing this weakness dictates that the effective length of the link be much smaller than the coherence length of the superconducting order parameter in the connecting region [129], such that the non-local quantum-mechanical nature of the system is important, even if tunnelling is not present. These devices typically exhibit a 2π-periodic (though not necessarily sinusoidal) current-phase relationship. The simpler manufacture and small capacitance of these weak links are two practical advantages leading to their frequent use in Josephson junction devices.

More recently, Josephson effects have been explored in superfluid helium weak-link systems. Two reservoirs of either ^{3}He [130, 131] or ^{4}He [132] are connected through the small holes in a microaperture array, in which the size of the holes was comparable to the superfluid healing length. Using a sensitive pressure detector[1] to measure small differences in pressure, superfluid flow between reservoirs was shown to exhibit both the stationary dc- and oscillatory ac-Josephson effects.

In superfluid helium, the healing length can be tuned via temperature due to its diverging behaviour near the lambda point. The nature of the current-phase relationship is explored

[1] This detector, fittingly, relies upon a SQUID, based on the Josephson effect, to sensitively measure small displacements.

in the transition between the large healing length regime, where transport between the reservoirs must rely on tunnelling, and the small healing length regime, where superfluid flow is allowed through the aperture [133]. A linear current-phase relationship is found in the small healing length regime, characteristic of hydrodynamics, while the relationship is sinusoidal for large healing lengths, consistent with Josephson-like behaviour.

Double-well BECs and Josephson junctions

Before the first dilute-gas BEC was realized, the possibility of using two of them to create a Josephson junction was discussed [134], drawing an analogy between the two superconducting reservoirs of a Josephson junction and close-but-separated condensates. The first explorations of nearby condensates demonstrated the measurable phase difference between wells through matter-wave interference [118]. These observations inspired many theoretical discussions of Josephson effects in double well BEC systems [135–139]. In general, these proposals exploit the two-mode model (TMM) to garner their results, assigning independent wavefunctions and phases to each side of the double-well junction with a well-defined phase difference between the wells.

The first experiments to observe Josephson physics with cold atoms were done in optical lattices [140, 141]. In that work, a one-dimensional lattice of many wells was used, with tunnelling between neighbouring sites determining the oscillatory behaviour measured. In the first experiment [140], analogies are made between the observed Bloch oscillations and the ac-Josephson effect, in that the frequency of oscillation depends on the potential difference between neighbouring sites. In the second experiment [141], periodic mass transport across adjacent wells is established as a consequence of the exchange between kinetic and potential (interaction) energies, establishing a "plasma-like" oscillation, in analogy to the exchange of energy between the electric field and the tunnelling energies in a solid-state Josephson junction [127].

The first direct observation of Josephson dynamics in a true double well was in Ref. [120]. With *in situ* imaging, population differences between two wells could be measured, while the phase information was obtained from matter-wave interference patterns. Plasma oscillations were observed and the current-phase relationship plotted. Some beyond-TMM characterisation of this system was required to predict the frequency of these dynamics [142]. In subsequent work [143], both the dc- and the ac-Josephson effects were observed in an atomic gas system. In the ac-effect, often called "macroscopic quantum self-trapping" (MQST), the frequency of the population oscillations depends on the chemical potential

difference between the wells.

Unique to the quantum gas implementations of the double-well system is the ability to dynamically transform the shape of the potential, from, for instance, a single to a double well. Adiabatic deformations of this type can be used to generate number squeezed states [121, 144, 145]. This squeezing manifests itself as a reduction in the fluctuations in the atom number of each well upon repetition of the splitting process, which arises due to an energetic advantage if the fluctuations are sub-Poissonian. The number-squeezing parameter $\xi_N = \sigma_N/\sigma_N^0 \approx \sqrt{k_B T/\mu}$ [121], where σ_N is the standard deviation of the number measurements, $\sigma_N^0 = \sqrt{N}$ is the standard deviation for Poissonian statistics, T is the system temperature and μ its chemical potential. Esteve *et al.* show that their results are consistent with thermal equilibrium and find $\xi_N \approx 1/\sqrt{2}$ [121]. In contrast, the work of Jo *et al.* [144, 145] cites a squeezing factor as small as $\xi_N \approx 1/25$, though the temperature is twice the chemical potential. The mystery surrounding these results may lie in the difference in geometry between these experiments, the former set in nearly spherical traps, while the latter is an elongated geometry. Phase fluctuations in the elongated trap [146–148] may suggest these experiments were out-of-equilibrium and indicate that the dynamics of the system are important to the generation of squeezed states.

Further to the initial squeezing experiments, Ref. [149] demonstrates both squeezing and antisqueezing, the former at the lowest temperatures, and the latter at intermediate temperatures, where bosonic bunching dominates. Entanglement of the two separated BECs was also demonstrated in the Ref. [121] through number and phase measurements. The use of these squeezed and entangled states is especially attractive in the context of atom interferometry [23, 150, 151], where one might be able to make use of the reduced fluctuations to improve the sensitivity of precision measurements.

The adiabatic transformation from a single to a double well used in many previous experiments traverses the crossover from the regime where hydrodynamics are valid to the regime where a TMM accurately describes the system. While previous dynamical studies of the Josephson junction [120, 143] have discussed the results in the context of a TMM, the barrier was not clearly greater than the chemical potential, and the assumption of weak coupling may not have been valid.

By characterizing the dynamics throughout the crossover in this work, the qualitative character of the transport between the wells is established and the regions in which a certain description is valid can be identified. Such an understanding of the many-body transport is required to choose appropriate rates of change for adiabatic deformation and to fully exploit

the potential for creating exotic quantum mechanical states.

5.2 Theoretical descriptions of a BEC in double well

Calculations involving BECs are greatly simplified, compared to microscopic descriptions of fermions or Boltzmann particles, by the existence of the macroscopic many-body ground state wavefunction that defines the system. In the non-interacting system, this wavefunction would simply be the many-body product of the single particle ground state wavefunctions. The existence of the s-wave contact interaction complicates this description to some degree, though the solutions to a modified Schrödinger equation, known as the Gross-Pitaevskii equation (GPE) do very well to describe the BEC in many situations. Though for complicated potentials, the GPE must be solved numerically to obtain exact results, there exist several regimes of approximation in which simpler models allow for a better intuitive understanding of the system. In the single- to double-well transition, two of these approximations are the hydrodynamic description, and the two-mode model (TMM).

5.2.1 Gross-Pitaevskii equation

The dynamics of a BEC are often well-described by the nonlinear Schrödinger equation known as the Gross-Pitaevskii equation (GPE) [152, 153], where the nonlinear mean-field term accounts for interactions between particles. This description is valid for low energies, when the interactions are local (the scattering length a is less than the interparticle spacing) and the particle number N is much greater than unity. The evolution of the condensate wavefunction, $\Psi(\mathbf{r},t)$, obeys this $T=0$ GPE

$$i\hbar\frac{\partial\Psi(\mathbf{r},t)}{\partial t} = -\frac{\hbar^2}{2m}\nabla^2\Psi(\mathbf{r},t) + \left(V_{\text{ext}}(\mathbf{r}) + g|\Psi(\mathbf{r},t)|^2\right)\Psi(\mathbf{r},t) \tag{5.1}$$

where $V_{\text{ext}}(\mathbf{r})$ describes the external potential and $g = 4\pi\hbar^2 a/m$ is the interaction parameter, and m is the particle mass. The time-independent version of this equation gives an energy eigenvalue equivalent to the chemical potential, μ, through

$$\mu\Psi(\mathbf{r}) = -\frac{\hbar^2}{2m}\nabla^2\Psi(\mathbf{r}) + \left(V_{\text{ext}}(\mathbf{r}) + g|\Psi(\mathbf{r})|^2\right)\Psi(\mathbf{r}), \tag{5.2}$$

and implies a time-dependence to the wavefunction such that $\Psi(\mathbf{r},t) \propto \exp(-i\mu t/\hbar)$.

By examining Eq. (5.2) we can evaluate the typical length scale over which the condensate wavefunction varies. Ignoring the effect of the external potential $V(\mathbf{r})$ and defining the

local density of the condensate $\rho(\mathbf{r}) = |\Psi(\mathbf{r})|^2$, we can define a local healing length, $\xi(\mathbf{r})$, as the length scale of variation where the kinetic energy term is equal to the interaction energy term, $\hbar^2/2m\xi(\mathbf{r}) = g\rho(\mathbf{r})$, such that

$$\xi(\mathbf{r}) = \sqrt{\frac{\hbar^2}{2mg\rho(\mathbf{r})}}. \tag{5.3}$$

In the context of the double well system, the value of ξ in the barrier region is important when considering transport between the two halves of the system. For low barriers, the density $\rho(\mathbf{r})$ is relatively high and ξ small, leading to hydrodynamic behaviour. When the barrier is high and depletes the density in the barrier region, ξ grows and quantum transport phenomena become important.

The GPE describes a broad range of phenomena in BECs, including studies of disorder and localization [154], soliton dynamics [155–157], vortices [158, 159], and BKT physics [160, 161]. As in these systems, we expect the GPE to capture the low-energy excitations we study. For the specific potentials used in this work, the GPE can by simplified to show limiting behaviours – on one end of our continuum, we expect hydrodynamics to rule, while at the other, a two-mode model (TMM). Both of the these simplifications are derived from the GPE, but better reveal the origins of the physics in their austerity. These limits represent two of the canonical regimes of superfluidity, and are explained in detail in the subsections to follow.

5.2.2 Hydrodynamics

An interacting BEC exhibits the properties of a superfluid. The GPE equation can be rendered to reveal these characteristics through a set of hydrodynamic equations describing perfect irrotational and inviscid fluid behaviour.

To reveal the hydrodynamics[2] of a BEC, we write the condensate wavefunction in terms of its density and phase, $\Psi(\mathbf{r},t) = \sqrt{\rho(\mathbf{r},t)}\exp(-i\phi(\mathbf{r},t))$, where $\rho(\mathbf{r},t) = |\Psi(\mathbf{r},t)|^2$ is the density and $\phi(\mathbf{r},t) = \mu(\mathbf{r})t/\hbar$ is the phase. Just as with the linear Schrödinger equation, the probability flux for the wavefunction is given by [162]

$$\mathbf{j}(\mathbf{r},t) = -\left(\frac{i\hbar}{2m}\right)\left[\Psi^*(\mathbf{r},t)\nabla\Psi(\mathbf{r},t) - \Psi(\mathbf{r},t)\nabla\Psi^*(\mathbf{r},t)\right], \tag{5.4}$$

[2]Here and throughout this chapter, we use the term "hydrodynamic" to refer to superfluid hydrodynamics, in contrast to collisional hydrodynamics which describes a different regime.

from which we can define a local superfluid velocity $\mathbf{v}_s(\mathbf{r},t) = \mathbf{j}(\mathbf{r},t)/\rho(\mathbf{r},t)$. This velocity depends on the gradient of the phase,

$$\mathbf{v}_\mathrm{s}(\mathbf{r},t) = \frac{\hbar}{m}\nabla\phi(\mathbf{r},t) \tag{5.5}$$

and because $\nabla \times \mathbf{v}_\mathrm{s} = (\hbar/m)\nabla \times \nabla\phi(\mathbf{r},t) = 0$, the condensate is irrotational, a defining characteristic of superfluidity.

Using this definition for superfluid velocity, we can rewrite the GPE in terms of the $\rho(\mathbf{r},t)$ and $\mathbf{v_s}(\mathbf{r},t)$:

$$\frac{\partial\rho(\mathbf{r},t)}{\partial t} + \nabla\cdot[\mathbf{v}_\mathrm{s}(\mathbf{r},t)\rho(\mathbf{r},t)] = 0 \tag{5.6}$$

$$m\frac{\partial\mathbf{v}_\mathrm{s}(\mathbf{r},t)}{\partial t} + \nabla\left[\tilde{\mu}(\mathbf{r}) + \tfrac{1}{2}m\mathbf{v}_\mathrm{s}^2(\mathbf{r},t)\right] = 0 \tag{5.7}$$

where

$$\tilde{\mu}(\mathbf{r},t) = V_\mathrm{ext}(\mathbf{r}) + g\rho(\mathbf{r},t) - \frac{\hbar^2}{2m\sqrt{\rho(\mathbf{r},t)}}\nabla^2\sqrt{\rho(\mathbf{r},t)}. \tag{5.8}$$

Equation 5.6 is the continuity equation, describing the local conservation of mass flow in the condensate. Equation 5.7 is the equation of motion for the velocity, and ensures conservation of momentum. The second term describes the force – the gradient of the energy – which drives fluid flow. The driving terms in the square brackets represent the local chemical potential, $\tilde{\mu}(\mathbf{r})$, and the kinetic energy of the superfluid flow.

The first two terms in the expression for the local chemical potential (Eq. (5.8)) give the contribution from the Thomas-Fermi approximation, while the last term, the only place in these formulae where $\hbar$ appears, is called the "quantum pressure" term. This kinetic energy term arises from to the zero-point motion of the particles, and does not give rise to particle currents [153]. If we define a characteristic length scale over which the condensate wavefunction and density change, d, the magnitude of the quantum pressure is $\sim \hbar^2/2md^2 = (\xi^2/d^2)g\rho(\mathbf{r},t)$. The quantum pressure can therefore be neglected in comparison to the interaction term when changes in the condensate wavefunction occur on a length scale less than the healing length, $\xi < d$. In the double-well system, d is of the order of the distance between the well minimum and the centre of the barrier. The neglect of the quantum pressure term must be justified, in particular, in the barrier region where the density is lowest.

Hydrodynamic approximation of population dynamics

To predict the character of the dynamics in the hydrodynamic regime, we take an approach which treats the system as a harmonic oscillator, whose frequency corresponds to the frequency of population transfer across the system. Using the continuity equation and equation of motion for the condensate in the hydrodynamic regime (Eqs. (5.6) and 5.7), and neglecting the quantum pressure term (by assuming $\hbar \to 0$), we can formulate the problem. In essence, we use the equation of motion to determine the force an imbalanced population exerts on the system, which we associate with a "spring force," as we expect the force to depend on the initial population difference. The spring constant associated with this force will be associated with the frequency of motion, much as a simple harmonic oscillator of mass m displaced by a distance x experiences the force $F = -kx = -m\omega^2 x$.

The oscillating variable in this system would be the population difference, $\mathcal{Z} = (N_{\mathrm{R}} - N_{\mathrm{L}})/N$, where $N_{\mathrm{R(L)}}$ is the number of atoms in the right (left) well, and $N = N_{\mathrm{R}} + N_{\mathrm{L}}$ is the total atom number. We seek a harmonic solution of the form

$$\ddot{\mathcal{Z}} = -\omega_{\mathrm{HD}}^2 \mathcal{Z} \tag{5.9}$$

where ω_{HD} is the frequency of motion in this hydrodynamic regime. The first time derivative of $\mathcal{Z}$ is

$$\dot{Z} = \frac{\dot{N_{\mathrm{R}}} - \dot{N_{\mathrm{L}}}}{N} = \frac{2\dot{N_{\mathrm{R}}}}{N} \tag{5.10}$$

where we use the fact that N is constant in time. The time dependence on one side of the well can be written

$$\begin{aligned} \dot{N_R} &= \int_{V_R} \dot{\rho}\ \mathrm{d}^3\mathbf{r} = -\int_{V_R} \nabla \cdot (\rho \mathbf{v}_s)\ \mathrm{d}^3\mathbf{r} \\ &= -\int_S \hat{n} \cdot (\rho \mathbf{v}_s)\ \mathrm{d}S \end{aligned} \tag{5.11}$$

where V_R is the volume of the right well, S is the area of the plane separating the two wells, and $\hat{n}$ is the unit normal vector for this plane. The continuity equation (Eq. (5.6)), and the Gauss's theorem are used in this expression, and ρ will be evaluated on the surface, S. Substituting this into the expression for $\mathcal{Z}$ and taking the second derivative,

$$\begin{aligned} \ddot{\mathcal{Z}} &= -\frac{2}{N}\frac{d}{dt}\int_S \hat{n} \cdot (\rho \mathbf{v}_s)\ \mathrm{d}S \\ &= -\frac{2}{N}\int_S \hat{n} \cdot (\dot{\rho}\mathbf{v}_s + \rho\dot{\mathbf{v}}_s)\ \mathrm{d}S. \end{aligned} \tag{5.12}$$

To evaluate the frequency, ω_{HD}, we assume that the system begins at rest, such that $\mathbf{v}_s(t=0)=0$, and the first term goes to zero. The time derivative of $\mathbf{v}_s$ is given by the hydrodynamic equation of motion, Eq. (5.7), and

$$\ddot{\mathcal{Z}}\Big|_{t=0} \approx \frac{2}{mN}\int_S \rho\,\hat{n}\cdot\vec{\nabla}\left(V_{\mathrm{ext}}(\mathbf{r})+g\rho\right)\,\mathrm{d}S. \tag{5.13}$$

The geometry of this double well system is such that the normal vector $\hat{n}=\hat{x}$, such that the only component of the gradient which contributes is the x-component. Assuming some initial imbalance, $\mathcal{Z}(t=0)=\mathcal{Z}_0$,

$$\omega_{\mathrm{HD}}^2 = -\frac{\ddot{\mathcal{Z}}}{\mathcal{Z}} \approx -\frac{2}{mN\mathcal{Z}_0}\iint_S \rho\,\frac{\partial}{\partial x}\left(V_{\mathrm{ext}}(\mathbf{r})+g\rho\right)\,\mathrm{d}y\,\mathrm{d}z. \tag{5.14}$$

We neglect the quantum pressure term in this analysis, such that the Thomas-Fermi solutions for the density are appropriate. For the initially imbalanced system, we consider in addition to the double well potential V_{ext} a simple linear gradient across the barrier giving a potential $V_{\mathrm{ext,grad}}=Gx$. The density profile will be found from the combined potential, $V_{\mathrm{ext}}+Gx$. At $t=0$, the gradient is removed suddenly, leaving the density profile in a non-equilibrium initial condition. We calculate this initial density profile in the tilted trap using the Thomas-Fermi approach, where

$$g\rho_{\mathrm{TF}}(\mathbf{r}) = \mu - (V_{\mathrm{ext}}(\mathbf{r})+Gx), \tag{5.15}$$

where ρ_{TF} is the density profile at $t=0$. The gradient term in Eq. (5.14) is

$$\begin{aligned}\frac{\partial}{\partial x}\left(V_{\mathrm{ext}}(\mathbf{r})+g\rho_{\mathrm{TF}}(\mathbf{r})\right) &= \frac{\partial}{\partial x}(V_{\mathrm{ext}}(\mathbf{r})+\mu-V_{\mathrm{ext}}(\mathbf{r})-Gx)\\ &= -G.\end{aligned} \tag{5.16}$$

This approximation simplifies the expression for the characteristic frequency,

$$\omega_{\mathrm{HD}}^2 = \frac{2G}{mN\mathcal{Z}_0}\iint_S \rho_{\mathrm{TF}}\,\mathrm{d}y\,\mathrm{d}z, \tag{5.17}$$

which indicates that the frequency can be found by simply evaluating the density at the surface between the two wells and integrating over the region by which the two halves are connected. From this expression, we see that the ω_{HD}^2 decreases as the area connecting the wells decreases, and falls to zero when the barrier surpasses the chemical potential.

Using the parameters for our double well potential, the hydrodynamic approximation for the frequency of population oscillation is shown in Fig. 5.1. As expected, the frequency decreases as the density in the barrier region is reduced, and it becomes strictly zero when the $\mu_{\mathrm{TF}} \leq V_{\mathrm{b}}$. This calculation is compared to the data in Fig. 5.9.

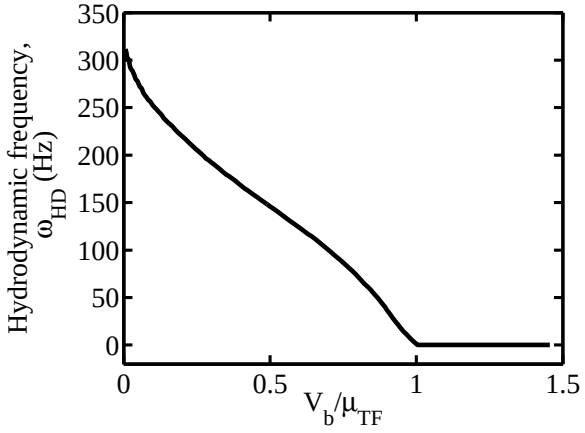

Figure 5.1: Hydrodynamic approximation for population oscillation in the double well potential, using a Thomas-Fermi density profile.

5.2.3 Two-mode model

In contrast to the low-barrier hydrodynamic regime of double well systems, the high-barrier regime is characterised by a vanishing density in the barrier region. The large healing length found here requires the inclusion of the quantum pressure term in the equations of motion, and quantum transport and tunnelling become important to the system's dynamics. When the density in the barrier region is sufficiently low, the condensate wavefunction can be described separately for each of the wells, giving rise to the two-mode model (TMM) often used to describe separated superfluid and superconducting junctions of this type.

The basic assumption of the TMM is that there are two well-defined spatially-separated wavefunctions with a perturbative tunnelling connection between them. In the time-independent GPE (Eq. (5.2)), we need only consider the two lowest eigenstates – the symmetric and antisymmetric ground states, which are nearly degenerate. The eigenvalues for the symmetric and antisymmetric eigenstates $\psi_{\rm s}(\mathbf{r})$ and $\psi_{\rm a}(\mathbf{r})$ are

$$\mu_{\rm s,a} = \int \psi^*_{\rm s,a}(\mathbf{r}) \left(-\frac{\hbar^2}{2m}\nabla^2 + V_{\rm ext}(\mathbf{r}) + gN|\psi_{\rm s,a}(\mathbf{r})|^2 \right) \psi_{\rm s,a}(\mathbf{r})\, {\rm d}\mathbf{r}, \tag{5.18}$$

where we have chosen a normalization such that $\int |\psi_{\rm s,a}(\mathbf{r})|^2\, {\rm d}\mathbf{r} = 1$, where N is the total number of atoms.

Following the formalism of Ref. [163], we begin with the many-body Hamiltonian

$$\hat{H} = \int {\rm d}\mathbf{r}\hat{\Psi} \left(-\frac{\hbar^2}{2m}\hat{\Psi}^\dagger\nabla^2\hat{\Psi} + \hat{\Psi}^\dagger V(\mathbf{r})\hat{\Psi} + \frac{g}{2}\hat{\Psi}^\dagger\hat{\Psi}^\dagger\hat{\Psi}\hat{\Psi} \right) \tag{5.19}$$

where the condensate wavefunction is written as a field operator, and using the creation operators for the two eigenstates described above, $\hat{a}^\dagger_{\mathrm{s,a}}$, is rewritten as

$$\hat{\Psi} = \psi_{\mathrm{s}}\hat{a}^\dagger_{\mathrm{s}} + \psi_{\mathrm{a}}\hat{a}^\dagger_{\mathrm{a}}. \tag{5.20}$$

With a change of basis from symmetric and antisymmetric states to states localized in the right and left wells, our two modes are then described by the right and left operators

$$\hat{a}^\dagger_{\mathrm{R}} = \tfrac{1}{\sqrt{2}}\left(\hat{a}^\dagger_{\mathrm{s}} + \hat{a}^\dagger_{\mathrm{a}}\right) \qquad \hat{a}^\dagger_{\mathrm{L}} = \tfrac{1}{\sqrt{2}}\left(\hat{a}^\dagger_{\mathrm{s}} - \hat{a}^\dagger_{\mathrm{a}}\right). \tag{5.21}$$

Using this new basis, a two-mode Hamiltonian can be written [163]

$$\hat{H}_{\mathrm{TMM,full}} = \frac{E_{\mathrm{C}}}{8}(\hat{a}^\dagger_{\mathrm{R}}\hat{a}_{\mathrm{R}} - \hat{a}^\dagger_{\mathrm{L}}\hat{a}_{\mathrm{L}})^2 - \frac{E_{\mathrm{J}}}{N}(\hat{a}^\dagger_{\mathrm{R}}\hat{a}_{\mathrm{L}} + \hat{a}^\dagger_{\mathrm{L}}\hat{a}_{\mathrm{R}}) + \frac{\delta E_{\mathrm{C}}}{4}(\hat{a}^\dagger_{\mathrm{R}}\hat{a}_{\mathrm{L}} + \hat{a}^\dagger_{\mathrm{L}}\hat{a}_{\mathrm{R}})^2 \tag{5.22}$$

where

$$E_{\mathrm{C}} = 4g\int |\psi_s|^2|\psi_a|^2\,\mathrm{d}\mathbf{r} \tag{5.23a}$$

$$E_{\mathrm{J}} = \frac{N}{2}(\mu_{\mathrm{a}} - \mu_{\mathrm{s}}) - \frac{g}{2}\frac{N(N+1)}{2}\int |\psi_a|^2|\psi_a|^2 - |\psi_s|^2|\psi_s|^2\,\mathrm{d}\mathbf{r} \tag{5.23b}$$

$$\delta E_{\mathrm{C}} = \frac{g}{8}\int |\psi_s|^2|\psi_s|^2 + |\psi_a|^2|\psi_a|^2 - 2|\psi_s|^2|\psi_a|^2\,\mathrm{d}\mathbf{r} \tag{5.23c}$$

The first term of the hamiltonian $\hat{H}_{\mathrm{TMM,full}}$ describes the charging energy of the system, which depends on the interaction parameter, g, through the charging energy E_{C}. The second term in the hamiltonian describes the tunnelling in the system, with E_{J} quantifying the energy splitting between the two lowest eigenstates, the mixing of which leads to the dynamics between the wells. The last term in Eq. (5.22) is negligible[3], and so we ignore it from this point forth.

The dynamics of this Hamiltonian can be most easily determined in the Heisenberg picture. We introduce two new operators

$$\hat{\mathcal{Z}} \equiv \frac{\hat{a}^\dagger_{\mathrm{R}}\hat{a}_{\mathrm{R}} - \hat{a}^\dagger_{\mathrm{L}}\hat{a}_{\mathrm{L}}}{N}; \qquad \hat{\alpha} \equiv \frac{\hat{a}^\dagger_{\mathrm{R}}\hat{a}_{\mathrm{L}} + \hat{a}^\dagger_{\mathrm{L}}\hat{a}_{\mathrm{R}}}{N}, \tag{5.24}$$

rewrite the Hamiltonian

$$\hat{H}_{\mathrm{TMM}} = \frac{E_{\mathrm{C}}N^2}{8}\hat{\mathcal{Z}}^2 - E_{\mathrm{J}}\hat{\alpha}, \tag{5.25}$$

[3]At $\delta_0 = 0$, the ratio $\delta E_{\mathrm{C}}/E_{\mathrm{C}} \approx 10^{-3}$, and is smaller for larger δ_0, where the validity of this TMM is better justified, as shown in §5.4.

and use the commutation relation for the operators $[\hat{\mathcal{Z}}, \hat{\alpha}] = 2(\hat{a}_{\mathrm{R}}^{\dagger}\hat{a}_{\mathrm{L}} - \hat{a}_{\mathrm{L}}^{\dagger}\hat{a}_{\mathrm{R}})/N^2$ to work out the time dependence of the operators. Using the general Heisenberg equation of motion for a generic operate $\hat{\alpha}$, $i\hbar\dot{\alpha} = [\hat{\alpha}, \hat{H}]$, the equations of motion for the operators are

$$\frac{\mathrm{d}\hat{\mathcal{Z}}}{\mathrm{d}t} = -J\left(\frac{\hat{a}_{\mathrm{R}}^{\dagger}\hat{a}_{\mathrm{L}} - \hat{a}_{\mathrm{L}}^{\dagger}\hat{a}_{\mathrm{R}}}{iN}\right) \tag{5.26a}$$

$$\frac{\mathrm{d}\hat{\alpha}}{\mathrm{d}t} = U\hat{\mathcal{Z}}\left(\frac{\hat{a}_{\mathrm{L}}^{\dagger}\hat{a}_{\mathrm{R}} - \hat{a}_{\mathrm{R}}^{\dagger}\hat{a}_{\mathrm{L}}}{iN}\right), \tag{5.26b}$$

where

$$U = \frac{E_{\mathrm{C}}N}{2\hbar} \quad \text{and} \quad J = \frac{2E_{\mathrm{J}}}{\hbar N}. \tag{5.27}$$

Replacing the quantum mechanical operators by complex numbers $\hat{c}_{\mathrm{R}}^{\dagger} \to \Psi_{\mathrm{R}}$, where

$$\Psi_{\mathrm{R(L)}} = \sqrt{N_{\mathrm{R(L)}}}e^{i\theta_{\mathrm{R(L)}}}, \tag{5.28}$$

$N_{\mathrm{R(L)}}$ is the number of atoms, and $\theta_{\mathrm{R(L)}}$ describes the macroscopic phase of the condensate on the right (left) side of the double well, the new variables can be expressed as

$$\mathcal{Z} = \frac{N_{\mathrm{R}} - N_{\mathrm{L}}}{N_{\mathrm{R}} + N_{\mathrm{L}}}; \qquad \theta = \theta_{\mathrm{L}} - \theta_{\mathrm{R}}, \tag{5.29}$$

the TMM Hamiltonian can be written as

$$H_{\mathrm{TMM}} = \frac{N\hbar}{2}\left(\frac{U}{2}\mathcal{Z}^2 - J\sqrt{1-\mathcal{Z}^2}\cos\theta\right), \tag{5.30}$$

and the equations of motion in terms of $\mathcal{Z}$ and ϕ are

$$\frac{\mathrm{d}\mathcal{Z}}{\mathrm{d}t} = -J\sqrt{1-\mathcal{Z}^2}\sin\phi \tag{5.31a}$$

$$\frac{\mathrm{d}\phi}{\mathrm{d}t} = J\frac{\mathcal{Z}}{\sqrt{1-\mathcal{Z}^2}}\cos\phi + U\mathcal{Z}. \tag{5.31b}$$

In this formalism, the variable $\mathcal{Z}$ describes the population difference between the two wells, and ϕ describes the quantum mechanical phase difference between them. The evolution of the populations depends sinusoidally on ϕ, which is characteristic of a Josephson junction. The evolution of the phase depends primarily on the second term in the right-hand-side of Eq. (5.31b), which describes the chemical potential difference between the wells. When $\mathcal{Z} \neq 0$, and the wells are well-separated such that $J \ll U$, the difference in chemical potential $\Delta\mu/\hbar = U\mathcal{Z}$ between the wells provides the energy difference ΔE that drives the evolution of ϕ.

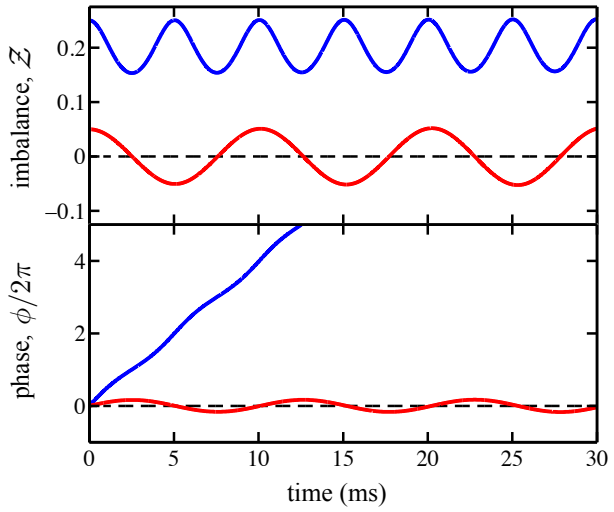

Figure 5.2: Population and phase dynamics in the TMM. Using $J = 2\pi \times 10$ Hz and $U = 2\pi \times 1000$ Hz, the evolution of the population imbalance $\mathcal{Z}$ and phase difference ϕ are calculated. Blue curve shows $\mathcal{Z}(t = 0) = 0.25$, undergoing MQST, while red curve shows $\mathcal{Z}(t = 0) = 0.05$, undergoing plasma oscillations. Both calculations use $\phi(t = 0) = 0$. In this case, $\mathcal{Z}_{\mathrm{C}} = 0.199$.

A close analogy between these equations of motion and those describing a rotating pendulum provide a picture for the dynamics. The pendulum described by Eqs. (5.31) has an angular momentum $\mathcal{Z}$, rotation angle ϕ, and length proportional to $\sqrt{1 - \mathcal{Z}^2}$. For the pendulum, a small initial momentum will result in the pendulum's swinging back and forth about the bottom of its trajectory, the momentum and phase oscillating sinusoidally. This motion is analogous to the stationary dc-Josephson effect, also known as plasma oscillations. For large initial momenta, the pendulum will swing up above its maximum and continue to swing in the same direction, its phase angle ever increasing. This motion corresponds to the oscillatory ac-Josephson effects , which in the context of cold atoms is referred to as macroscopic quantum self-trapping (MQST).

Plasma oscillations

In the limit of small amplitude perturbations about $\mathcal{Z} = 0$ and $\phi = 0$, we can rewrite Eq. (5.31) to second order in $\mathcal{Z}$ and ϕ as

$$\frac{\mathrm{d}\mathcal{Z}}{\mathrm{d}t} = -J\phi \tag{5.32a}$$

$$\frac{\mathrm{d}\phi}{\mathrm{d}t} = (J+U)\,\mathcal{Z}, \tag{5.32b}$$

such that

$$\frac{\mathrm{d}^2\mathcal{Z}}{\mathrm{d}t^2} = -J\,(J+U)\,\mathcal{Z}. \tag{5.33}$$

These equations describe harmonic motion, where $\mathcal{Z}(t) \propto \exp(i\omega_{\mathrm{p}}t)$ and the plasma frequency is

$$\omega_{\mathrm{p}} = \sqrt{J\,(J+U)}. \tag{5.34}$$

The red lines in Fig. 5.2 show the dynamics in this limit.

In this regime, the population difference $\mathcal{Z}$ and phase ϕ oscillate sinusoidally about zero. In the absence of interactions ($U \to 0$), the plasma frequency $\omega_{\mathrm{p}} \to J$, where the tunnelling rate simply corresponds to the energetic splitting between the symmetric and antisymmetric state of our ansatz. The presence of interactions increases the rate of transport between the two wells. The "plasma" nomenclature stems from the analogous effect in superconducting Josephson junctions, where energy is periodically transferred between the electric field and the junction coupling energy [127], the type of collective longitudinal oscillation of an electron gas that is called a plasmon [164].

Using the same small $\mathcal{Z}, \phi$ approximation, the Hamiltonian can be written as

$$H_{\mathrm{TMM,harmonic}} = \frac{\hbar N}{2}\left(\frac{U+J}{2}\mathcal{Z}^2 + \frac{J}{2}\phi^2\right) \tag{5.35}$$

which is recognized as a harmonic oscillator hamiltonian, where the variables $\mathcal{Z}$ and ϕ are canonically conjugate variables, with commutation relation (to the same order in $\mathcal{Z}$ and ϕ) $[\mathcal{Z}, \phi] = -2i/N$. This small amplitude approximation to the Hamiltonian is relevant in many situations where the double well system is adiabatically deformed from a single well, maintaining the ground state wavefunction.

Macroscopic quantum self-trapping

Foregoing the small $\mathcal{Z}$ and ϕ approximation, the equations of motion Eqs. (5.31) lead to ac-Josephson type effects and macroscopic quantum self-trapping (MQST). In connection to

the earlier pendulum analogy, these effects parallel the pendulum swinging around its pivot always in the same direction. For initial population imbalances $\mathcal{Z}$ or phases ϕ greater than some critical value, the population difference becomes trapped, with more atoms always on one side of the double well. Assuming zero initial phase difference between the wells, the population difference between the wells becomes trapped when the phase difference winds to $\phi(t) = \pi$ before $\mathcal{Z}$ changes sign, and the subsequent evolution of the phase drives the population $\mathcal{Z}$ back towards its initial value. This critical value is

$$\mathcal{Z}_{\mathrm{C}} = \frac{2}{U}\sqrt{J(U-J)}. \tag{5.36}$$

The "ac" terminology in this regime is due to the regular sinusoidal phase evolution. The population difference $\mathcal{Z}$ will oscillate about a non-zero value, and this establishes a mean non-zero chemical potential difference between the wells, which dictates a nearly-linear always-increasing value of the phase difference ϕ, which, modulo-2π, looks like phase-winding. The blue lines in Fig. 5.2 show these effects.

5.3 Experimental implementation

Using the adiabatic rf double well potentials described in §2.3, we can explore the dynamics of a ^{87}Rb BEC. In this section, the relevant TMM parameters for this trap are calculated, the characterization of the potential is discussed, and the experimental procedures specific to double well experiments are explained.

As described in §2.3,, the double well potential arises as the result of rf coupling between Zeeman levels of the ^{87}Rb atoms in a magnetic chip trap. The height of the barrier and the separation of the wells are varied with the frequency of the rf radiation, ω_{rf}, which we reference to the static "trap bottom" magnetic field $B_{\mathrm{S}}(\mathbf{0})$ through the detuning parameter $\delta_0 = \omega_{\mathrm{rf}} - |\mu_B g_F B_{\mathrm{S}}(\mathbf{0})/\hbar|$. As we increase the detuning, the barrier height and the well separation both increase.

5.3.1 TMM parameters

Given a description of the trapping potential and total atom number, various characteristic energies of the system can be calculated. In particular, we are interested in the value of the barrier height V_{b}, the symmetric ground state chemical potential, μ_{s}, and the TMM parameters U, J, and ω_{p}.

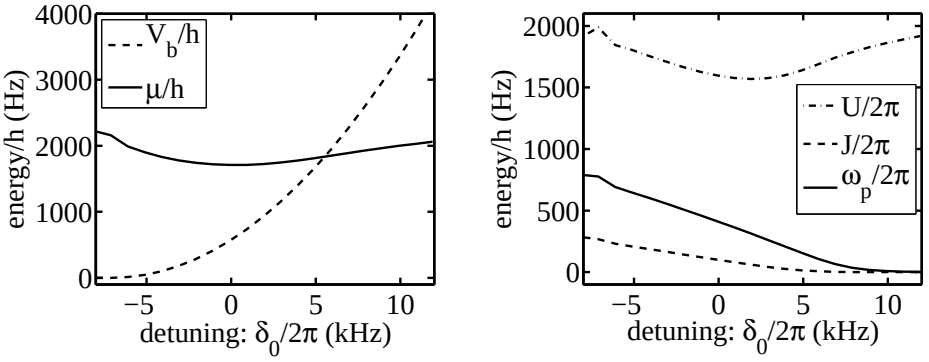

Figure 5.3: Parameters of our potential. (a) Barrier height (long dashes) and chemical potential (short dashes) for $N = 8000$. (b) TMM parameters $U/2\pi$ (short dashes), $J/2\pi$ (long dashes) and $\omega_{\rm p}/2\pi$ (solid line) for $N = 8000$ and the potential described in this section. The uniform beyond-RWA shift (see §2.3.2) has been applied in all cases.

.

To find the barrier height, only information about the geometry of the system is needed. The barrier height, $V_{\rm b}$, is defined as the difference between the minimum value of the potential along x along $y = z = 0$ and the value of the potential at $x = y = z = 0$. The remaining values depend on the atom number and require a solution to the GPE. We solve for the ground state wavefunctions, given the potential at some detuning δ_0 and atom number N. From these, the values of $\mu = \mu_{\rm s}$, U, and J are calculated using Eqs. (5.18), 5.23, and 5.27.

In general, Fig. 5.3(a) shows that the chemical potential, μ, is roughly constant for the range of detunings used, and the barrier height increases with δ_0. The TMM parameters, shown in Fig. 5.3(b), reveal that $\mu/h \sim U/2\pi$, as expected. The tunnelling parameters J decreases roughly linearly until $\mu \approx V_{\rm b}$, at which point the decrease is exponential. The plasma frequency, ω_p, falls between these two values, and because of the J dependence on δ_0, also falls off linearly, then exponentially, with δ_0.

Tunnelling parameter approximation

The calculation of the tunnelling parameter, due to its rapid decay for large barriers, is very sensitive to the form of the wavefunction used in the calculation. While we expect the GPE to provide an accurate result for this parameter, we can also use an analytic approx-

imation to confirm and interpret the results. For sufficiently high barriers, the tunnelling parameter can be found using a WKB-like approximation of the BEC wavefunction [135]. Expressions for the wavefunction and corresponding probability current in the barrier region allow for calculation of the dynamics across the junction, which can be compared to the GPE results.

To simplify the calculation, a one-dimensional approximation is used. A fit to the three-dimensional potential along x can be expressed as

$$V_{\mathrm{ext,1D}} = V_{\mathrm{b}} \left(1 - \left(\frac{x}{x_0} \right)^2 \right)^2 \tag{5.37}$$

where $\pm x_0$ are the positions of the well minima and V_b is the barrier height. Making a TMM-type approximation, we assume a total wavefunction for the system $\psi(x) = \psi_R(x) + e^{i\phi}\psi_L(x)$, where $\phi = (\mu_R - \mu_L)t/\hbar$. The WKB approximation for the wavefunction centred to the right of the barrier is [135]

$$\psi_{\mathrm{R}}(x) = \left(\frac{\hbar(x_0 - x_{\mathrm{b}})^2}{16\pi D^3 a} \right)^{1/2} \frac{A}{2m \left[V_{\mathrm{ext,1D}}(x) - \mu \right]^{1/4}} \times \exp\left(- \left(\frac{2m}{\hbar^2} \right)^{1/2} \int_{x_{\mathrm{b}}}^{x} \mathrm{d}x' 2m \left[V_{\mathrm{ext,1D}}(x') - \mu \right]^{1/2} \right) \tag{5.38}$$

where x_{b} is the half-width of the barrier (as shown in the inset of Fig. 5.4), $A = 0.397$ is found by matching solutions inside and outside the potential, and D is the boundary thickness, which sets the distance near the classical turning point over which a Thomas-Fermi wavefunction is not valid, which in this potential is $D = [(8m/\hbar^2 x_0)((\mu V_{\mathrm{b}}(1 - \sqrt{\mu/V_{\mathrm{b}}}))^{1/2}]^{-1/3}$. The wavefunction in the left well is found in a similar manner.

Assuming equal populations between the wells ($N_{\mathrm{R}} = N_{\mathrm{L}} = N/2$; $\mu_{\mathrm{R}} = \mu_{\mathrm{L}} = \mu$) and finding the probability current in the barrier, the population transport can be expressed as $\mathrm{d}N_R/\,\mathrm{d}t = -I_0 \sin\phi$ where

$$I_0 = \frac{A^2(x_0 - x_{\mathrm{b}})^2}{2\pi\hbar a x_0} \, V_{\mathrm{b}} \, \frac{x_{\mathrm{b}}}{x_0} \, \sqrt{\frac{\mu}{V_{\mathrm{b}}}} \times \exp\left(-2x_0 \left(\frac{2mV_{\mathrm{b}}}{\hbar^2} \right)^{1/2} \int_0^{x_{\mathrm{b}}/x_0} \mathrm{d}x' \left[(1 - x'^2)^2 - \left(1 - \left(\frac{x_{\mathrm{b}}}{x_0} \right)^2 \right)^2 \right]^{1/2} \right). \tag{5.39}$$

By comparing this dynamical equation with Eq. (5.31a), we find that $J_{\mathrm{WKB}} = 2I_0/N_{\mathrm{tot}}$.

In Fig. 5.4, we show the calculations for the tunnelling parameter. The result from the GPE (solid line, as calculated for Fig. 5.3) is shown along with the above calculation (dash-dotted line). Though these solutions are not identical, the scaling is similar.

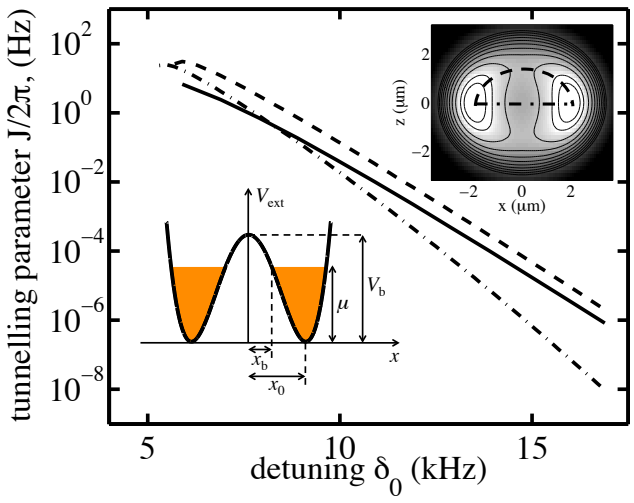

Figure 5.4: WKB approximation of tunnelling parameter. The solid line is the full GPE result, $J/2\pi$, shown in Fig. 5.3, the dash-dot line shows the tunnelling parameter $J_{\mathrm{WKB}}/2\pi$ for a 1D potential whose characteristics are those along the path in x between well centres, and the dashed line is the tunnelling parameter for a 1D system with a potential as seen along the shell of resonance in the $x-y$ plane. Upper inset shows a contour plot of the full potential at $y=0$, along with the two paths indicated. The lower inset gives a schematic of the one-dimensional double well and the parameters used in the calculation of J_{WKB}.

To better understand the tunnelling parameter in our experiments, we consider the details of our potential. As discussed in §2.3.1, there is a shell of resonance along which the minimum of the potential would fall if polarization effects were absent. When accounting for the polarization, there remains some "stretching" of the potential minima along this path, and for barriers $\delta_0 \gtrsim 4$ kHz (for our typical parameters), there is an inflection in the shape of the potential along the $x=y=0$ line, such that a pair of local minima emerge at $z \neq 0$. The path through this point provides a lower barrier connecting the two wells than the path of the shortest distance between them. The upper inset of Fig. 5.4 shows a contour plot of the potential at $y=0$ and the two paths considered: the dash-dotted line is the original path, and the dashed line is the one just described.

We repeat the same calculation of the tunnelling parameter for this second path, using a barrier height given by the height of the potential at this new minimum along the $x=y=0$ line, with x_0 being the length of the elliptical arc connecting the absolute minimum to this new point. This tunnelling parameter is shown as the dash-dotted line in Fig. 5.4. The barrier height increases less rapidly along this path than across the centre of the potential,

and results in stronger tunnelling.

If the strongest tunnelling path is chosen, the one-dimensional approximation should give an upper limit for the tunnelling parameter, since all other tunnelling pathways will be weaker. The curved path in this analysis always gives a tunnelling parameter greater than the one calculated with the full 3D GPE. Qualitatively, these results show roughly the same trend and scaling of the tunnelling parameter with respect to detuning. These results highlight the importance of using a full three-dimensional simulations to determine the tunnelling characteristics. For the low-barrier work in this thesis, the longer path is irrelevant, though the stronger connection along the shell may have implications for the high barrier work discussed in §5.6.1.

5.3.2 Characterising the double-well

In addition to calculating the dependence of the system parameters on the experimentally controlled detuning δ_0, some trap characteristics can be measured directly. While we do not have sufficient imaging resolution to measure the distance between the wells *in situ*, an interference experiment can provide information about the spacing between wells.

We begin by considering a single BEC that has been split in two, such that the halves remain phase coherent. With the centres of the split BECs separated by a distance d, the condensates are released from their traps and allowed to fall under the influence of gravity. Assuming the traps are harmonic, the condensate wavefunctions are Gaussian. For initial wavefunctions

$$\psi_{\mathrm{R(L)}} = \frac{e^{i\phi_{\mathrm{R(L)}}}}{(\pi R_0^2)^{3/4}} \exp\left[-\frac{(\mathbf{r} \pm \mathbf{d}/2)^2}{2R_0^2}\right] \tag{5.40}$$

where R_0 is the Gaussian width of the wavepacket and $\phi_{R(L)}$ is the initial phase of the right (left) condensate, the time evolution, according to the Schrödinger equation, gives [153]

$$\psi_{\mathrm{R(L)}}(t) = \frac{e^{i(\phi_{\mathrm{R(L)}}+\phi(t))}}{(\pi R_t^2)^{3/4}} \exp\left[-\frac{(\mathbf{r} \pm \mathbf{d}/2)^2(1 - i\hbar t/mR_0^2)}{2R_t^2}\right] \tag{5.41}$$

where $e^{i\phi(t)} = [R_0 - i\hbar t/mR_0]^{3/2}$, and the width after some time is

$$R_t^2 = R_0^2 + \left(\frac{\hbar t}{mR_0}\right)^2. \tag{5.42}$$

In considering the full density distribution $\rho(\mathbf{r}, t) = |\psi(\mathbf{r}, t)|^2 = |\sqrt{N_R}\psi_R(\mathbf{r}, t) + \sqrt{N_L}\psi_L(\mathbf{r}, t)|^2$, there will be an interference term

$$2\sqrt{N_R N_L}\mathrm{Re}\left[\psi_R(\mathbf{r}, t)\psi_L^*(\mathbf{r}, t)\right] \sim A\cos\left(\frac{\mathbf{r}\cdot\mathbf{d}}{R_0^2 R_t^2}\frac{ht}{m} - \phi_R + \phi_L\right) \tag{5.43}$$

where A collects all of the time-independent terms. In our geometry, $\mathbf{d} = d\hat{x}$, so the fringes we observe should be perpendicular to the x-direction. The spacing between fringes, Δx, is the distance between adjacent maxima in the density distribution, such that

$$\Delta x = 2\pi \frac{m R_t^2 R_0^2}{\hbar t d} \approx \frac{2\pi \hbar t}{m d} \tag{5.44}$$

where the long-time-of-flight approximation has been made in the last step, where $R_t \approx \hbar t / m R_0$. The density distribution is integrated along y after some time of flight t, from which Δx can be measured (see §5.3.3). Inverting Eq. (5.44) for d gives the separation between the wells.

The assumption of the absence of interactions is not valid in our system of ^{87}Rb atoms, and the wavefunctions are not Gaussian. Using a similar derivation, the initial wavefunctions and their time evolution are calculated from the GPE. In these calculations, the momentum distribution at early times gives the density distribution in long time of flight.

Figure 5.5 shows the fringe and well spacing for the double well potential as a function of rf detuning, δ_0. The inset gives an example of an averaged interference pattern at $\delta_0/2\pi =$ 14 kHz. We see good agreement between the calculation and the measurement in shape, though a shift of the theory line $\delta_0 \to \delta_0 + 2.1$ kHz is required to attain absolute agreement. The necessity of this shift is likely due to the systematic uncertainties in measuring $B_S(\mathbf{0})$, which are on the order of ± 1 kHz.

5.3.3 Initiating and measuring dynamics

To study a BEC in a double well trap, we begin by preparing a ^{87}Rb condensate in the usual way (§2.1.1). We modify the final steps of the cooling to eliminate any unwanted collective excitations by creating the BEC in a partially split trap. Dynamics are initiated by preparing an out-of-equilibrium distribution and allowing its evolution. The population distribution between the wells is measured using standard absorption imaging.

Preparing a BEC for double-well experiments

The general sequence for the preparation of a BEC in §2.1.1 is slightly modified for the following double-well experiments. In the "Evaporative cooling" step, we proceed as usual until the atoms are just above degeneracy. At this point in time, we introduce the adiabatic rf dressing to gradually deform the potential and complete the forced rf evaporation in a dressed trap.

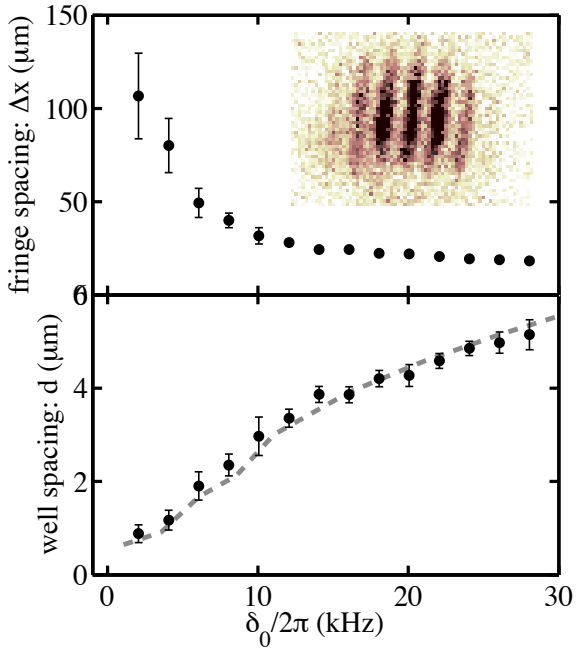

Figure 5.5: Interference pattern measurements for determination of well spacing. Top: measured fringe spacing as a function of rf detuning, δ_0. Inset: example of fringe measurement at $\delta_0/2\pi = 14$ kHz, after $t = 20.3$ ms time-of-flght, averaged over 5 images. Bottom: Calculated well-spacing from fringe spacing measurement (points), d, from Eq. (5.44), with GPE calculation prediction (dashed line). A shift in δ_0 of 2.1 kHz is applied to the theoretical data, as discussed in the text.

We choose trap parameters for the evaporative cooling such that the trap is flattened at the centre, with zero barrier. With a typical static trap bottom $\omega_{\rm TB} = 2\pi \times 787$ kHz, we linearly ramp on the rf dressing power $B_{\rm rf}$ from 0 to 240 mG at a frequency $\delta_0 = \delta_{\rm prep} = 2\pi \times (-22$ kHz) in 100 ms. Simultaneously, we raise the frequency of the rf evaporation knife, as the effective potential is now additionally separated from the adjacent $m_{\rm F}$ state by the Rabi frequency $\Omega_{\rm rf} = m'_{\rm F} g_{\rm F} \mu_{\rm B} B_{\rm rf}/\hbar$. The evaporative cooling is finished in this trap with a single 100 ms linear ramp of the rf knife to a final value that produces a quasi-pure BEC with the desired atom number, N.

Biasing and initiating dynamics

We bias the system to create out-of-equilibrium population distributions by introducing an optical force to the system, as described in §2.2. By weakly focussing a 1064 nm "bias beam," (which is a misaligned and expanded ODT1) with beam waist $w \approx 65$μm and power $P_{\rm bias}$ propagating in the the y-direction at a point in the x-z plane off-centre from the barrier, we can provide a roughly linear optical potential across the junction. When we choose to prepare a biased sample, we ramp on the power of this beam in 100 ms before the BEC is created (see Fig. 5.6(a)).

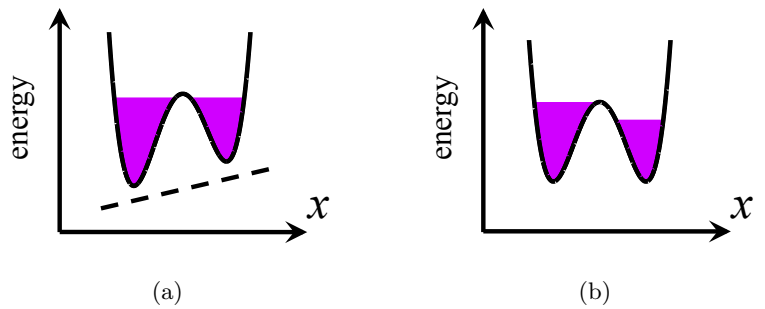

(a) (b)

Figure 5.6: Biasing the double well. (a) The BEC is prepared in a biased double well, where the tilt potential originates from an ODT focussed off-centre from the double well (in this case, at large x.) The focus is much larger than the size of the system, such that the potential is roughly linear across the wells. (b) The bias potential is removed to initiate the dynamics. By suddenly removing it, the systems is left in an out-of-equilibrium distribution, with a higher chemical potential (and more atoms) on one side than the other.

To split the clouds, we leave the bias beam on and increase ω_{rf} (and thus δ_0) to the desired value $\delta_0 = \delta_{\mathrm{hold}}$ in 20 ms. We have checked that this ramp is adiabatic – slow enough so as not to change the final results. The bias beam power, P_{bias}, is ramped off in 0.5 ms, which leaves a population imbalance in a symmetric potential (Fig. 5.6(b)). We allow for dynamical evolution of the system for a time t, after which we freeze dynamics by rapidly increasing both B_{rf} and ω_{rf} to separate the clouds and raise the barrier. The steps listed in this paragraph are illustrated in Fig. 5.7.

Measuring double-well populations

To determine the changing population imbalance, we use absorption imaging to count the numbers of atoms in the right and left wells, N_{R} and N_{L}, respectively. The dynamics are frozen after t_{hold} by raising the barrier and separating the well minima diabatically via rapid changes in both rf frequency and amplitude. The initial stage of this ramp eliminates the tunnelling between wells, leaving two completely separated samples. Because only the relative atom number between these samples is important, the heating associated with the rapid changes in the potential after separation is inconsequential, so long as the atom number does not change in the process. The clouds are then separated to ~ 70 µm, at which point the imaging resolution is more than sufficient to image the left and right clouds independently.

All magnetic and rf traps are turned off suddenly. After 1.3 ms time-of-flight (TOF)

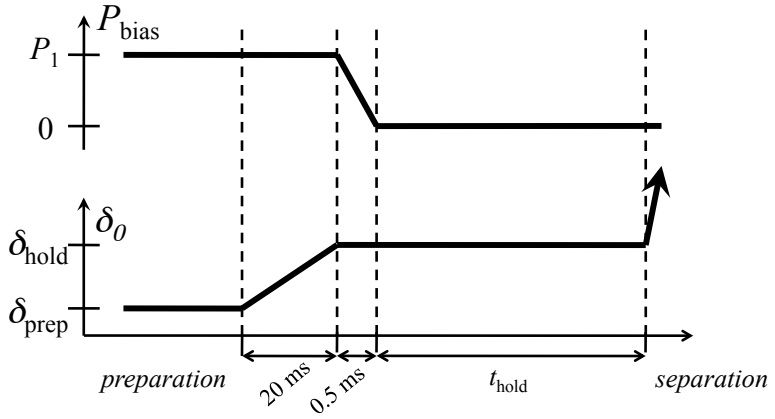

FIGURE 5.7: Timing sequence for double-well dynamics. Top: power in bias beam, where P_1 is adjusted to create the desired imbalance at $t = 0$. Bottom: detuning, δ_0, of rf frequency. BEC is prepared with $\delta_{\text{prep}} < 0$, then ramped up adiabatically in 20 ms to the desired value δ_{hold}. At the completion of t_{hold}, δ_0 is rapidly increased.

.

(for all magnetic fields to off completely), an absorption image is recorded. The absorption probe is directed along the y-axis so that the image is taken along the long axes of the clouds and two round clouds are seen. A detailed discussion of the imaging system and techniques can be found in Ref. [15].

Phase analysis

As previously discussed, the phase difference between opposite sides of the double well is determined from the interference of the matter waves after release from the trap and long time-of-flight. Reference [15] (§7.1.1) discusses in depth the fitting procedure used to extract the phase of the fringe pattern. In short, the two-dimensional absorption images of momentum space distributions are summed along a direction perpendicular to the line connecting the centres of the original two clouds. A Gaussian envelope encloses the sinusoidal fringe pattern, and we fit to the function

$$f(x) = \exp\left(-\frac{(x-x_0)^2}{2\sigma_x^2}\right)\left[1 + \mathcal{V}\cos\left(\frac{2\pi(x-x_0)}{\Delta x} + \phi_{\text{fr}}\right)\right], \tag{5.45}$$

where x is the distance along the direction connecting the cloud centres, σ_x and x_0 are the size and centre of the Gaussian envelope, $\mathcal{V}$ is the visibility of the fringes, Δx is the fringe spacing, and ϕ_{fr} is the phase we wish to measure.

To find the average of a large number of measurements of phase, as is needed in the repeated measurements made in the following experiments, we must take care in describing the phase because of its being measured *modulo* 2π. To find the average phase angle, phasors are constructed $\mathcal{F}(\phi_{\rm fr}) = \exp(i\phi_{\rm fr})$ and averaged in the vector sense, to give a mean phasor length, $\mathcal{R} = 1/N \times |\sum_n \mathcal{F}_n(\phi_{\rm fr})|$. The angle of this averaged phasor then extracted, $\overline{\phi}_{\rm fr} = \angle(\sum_n \mathcal{F}_n(\phi_{\rm fr}))$. For a well-defined phase, the phasors will add in the same direction and $\mathcal{R}$ will fall close to unity. For random phases, the phasors will add destructively and $\mathcal{R}$ will tend to zero.

5.4 Hydrodynamic to Josephson transition: small imbalance population dynamics

The study of transport across a barrier reveals important properties about the many-body physics governing the system. When the healing length in a superfluid is small, the local velocity and density are well-defined and the flow is hydrodynamic. The introduction of a barrier in this superfluid creates a region of low density and large healing length, such that the transport through the this region will depend on long-range properties of the system. When the density in the barrier region classically vanishes, phenomena like tunnelling are significant and Josephson effects emerge.

Using the tunability of the barrier height, we study the system's dynamical response to small population imbalances as a function of the barrier height, and characterize the transport as a function of the coupling between the wells. GPE calculations are compared with these results, and facilitate an interpretation of the transport. In the low-barrier strong-coupling regime, a hydrodynamic description of the system is valid, while when the barrier is higher than the chemical potential, a TMM is sufficient and Josephson behaviours emerge. In this work, we see a gradual crossover between these behaviours through intermediate barrier heights.

5.4.1 Population oscillation measurements

We use the population difference between the wells as a function of time, $\mathcal{Z}(t)$, to characterize the dynamics of the system.

The system is prepared as described in §5.3.3 with initial imbalances $\mathcal{Z}(0) = 0.05$ to

0.10, and allowed to evolve as described in §5.3.3. The population distribution $\mathcal{Z}(t)$ is measured after a hold time t. A new sample is prepared for each measurement, with 4 to 6 measurements made per hold time. In general, we sample dynamics for hold times between 15 and 30 ms with sampling rates ranging between 100 and 400 Hz.

An example time series is shown in Fig. 5.8(a). We see a clear indication of the population oscillating back and forth between the wells, in the presence of a decay bringing the population towards $\mathcal{Z} = 0$ over a longer time scale. This decay will ignored for the present analyses and further discussed in §5.6. A close examination of the data reveals that the behaviour is more than a simple damped sinusoid: a Fourier transform (FT) of these data reveal two distinct frequencies rising above the noise floor (Fig. 5.8(b)).

We repeat these measurements at many values of δ_0. In the data presented here, the total atom number is $N_R + N_L = 6800 \pm 400 \ \pm 1700$ where the first error bar is statistical (variations in $N_R + N_L$ run-to-run) and the second systematic (absolute atom number calibration uncertainty, see Appendix C). Using our description of the potential and the atom number, we use the Thomas-Fermi approximation to determine the chemical potential μ at each δ_0, and Eq. (2.13) (in addition to the corrections as described in §2.3.2) to determine V_b.

Frequency analysis

To prepare the data for Fourier analysis, we eliminate any small offset from the asymptotic value of $\mathcal{Z}$ by subtracting from each point the mean value of $Z(t)$ across the entire time series, where the mean might be non-zero due to a small equilibrium imbalance in the system. To smooth the transformed data, the time series is padded with zeros to a total of 1024 points. When identifying peaks in Fourier space, we ignore points below the frequency given by $1/t_\mathrm{tot}$, where t_tot is the longest hold time, which would be artifacts of the windowing introduced by the finite period of measurement. The two peaks with the greatest heights are identified and used as the data points in Fig. 5.9. The colour map behind these data is an interpolation between the Fourier spectra (which run along vertical lines) at each data point.

The uncertainty in the frequency measurement is found by simulating data with the same level of noise as the original time series. The quantity of noise is determined by fitting the time series to a 2-frequency decaying exponential function

$$\mathcal{Z}(t) = e^{-t/\tau} \left[a_1 \sin(2\pi\nu_1(t - t_{01})) + a_2 \sin(2\pi\nu_2(t - t_{02})) \right], \tag{5.46}$$

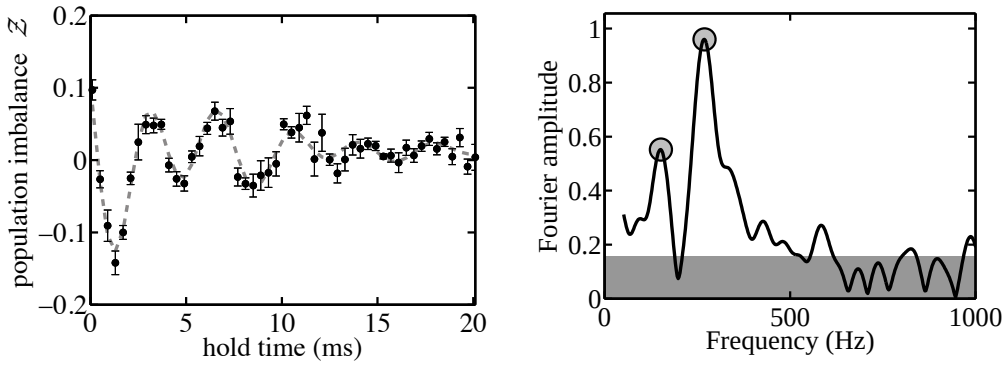

(a) (b)

FIGURE 5.8: (a) Population imbalance, z, vs. time for $\delta_0 = 2\pi \times 0.1$ kHz, $N_{tot} = 5900$. The dashed line is a decaying two-frequency sinusoidal fit to the data, using fixed frequencies from (b). Each point represents 6 BECs, error bars statistical. (b) Fourier transform amplitude spectrum of data showing two distinct peaks at 268 ± 6 and 151 ± 13 Hz rising above the noise floor (grey).

.

where τ is a time constant for decay, $a_{1(2)}$ is the amplitude of the first (second) frequency component, and $\nu_{1(2)}$ is the first (second) frequency component, and $t_{01(02)}$ is the constant accounting for the phase shift of the first (second) component. The standard deviation of the residuals from this fit gives the noise level. We simulate 100 sets of data with the same parameters as those given by the fit, with the same total time and density of points, but with different randomized instances of Gaussian noise whose standard deviation is the same as that measured. Taking the frequency measurements from each of these trials, we determine the smallest range inside of which 68% of the measurements lie. This confidence interval is used as the uncertainty in the frequency measurement.

The noise floor in the Fourier transform is established in a similar fashion. Using the result for the noise level from the time series, we simulate Gaussian noise and take the Fourier transform of this. The noise floor shown in Fig. 5.8(b) is the mean plus one standard deviation of the maximum peak amplitudes found in 100 such simulations.

Figure 5.9 shows the population oscillation frequencies as a function of $V_{\rm b}/\mu$ and δ_0. For small values of barrier height, two frequency components are evident in the data, and both are plotted. For higher barriers, only one frequency component can reliably be extracted from the Fourier spectrum, and this alone is plotted.

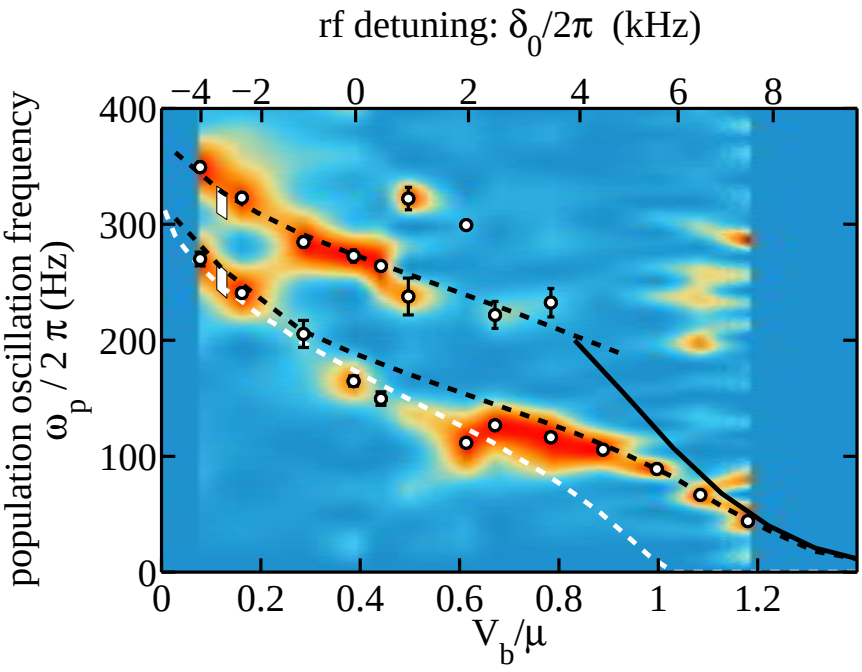

Figure 5.9: Frequencies of small-imbalance double well population dynamics vs. rf detuning (measured) and barrier height (calculated). Experimental points (white circles) represent the two highest Fourier components at each detuning; error bars are statistical. Dashed lines represent calculated (3D GPE) frequencies for N = 8000 and $\mathcal{Z}(0) = 0.075$. The solid line indicates the plasma oscillation frequency predicted by the TMM. The white dashed line is the hydrodynamic frequency, $\omega_{\rm HD}/2\pi$, as calculated and discussed in §5.2.2. The colour map is map of the spectral weight of each of the measurements shown, interpolated numerically between points, as a guide to the eye of the strength of each component. White bars at $V_b/\mu \sim 0.1$ indicate the bounds of the GPE simulation corresponding to the systematic plus statistical uncertainty in atom number. The statistical uncertainty in δ_0 is $\pm(2\pi \times 0.5)$ kHz (not shown).

Amplitude analysis

In addition to information about the frequencies of population oscillation, data such as that in Fig. 5.8 yields information about the relative amplitudes of the modes excited by the initial population imbalance. From the fits to the data (Eq. (5.46)), the amplitudes the two analyzed modes are given by a_1 and a_2. The fractional dominance of the lower mode can be quantified as $\mathscr{R}_1 = a_1/(a_1 + a_2)$. The uncertainties in these values are determined in a similar way to those in the frequencies; we use the noise level in the residuals of the fit, simulate and fit 100 sets of data with similar parameters, and use the 68% confidence interval of these results to represent our uncertainty.

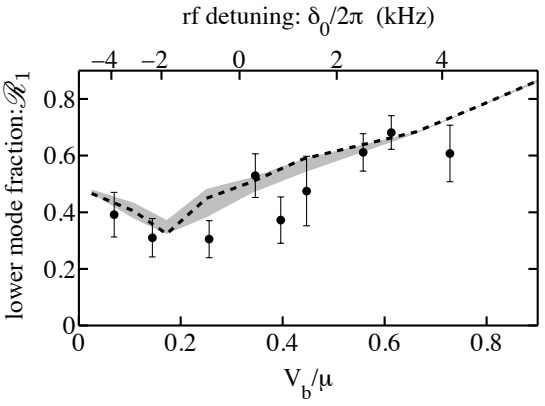

Figure 5.10: Fraction of low-frequency mode in population dynamics. Dashed line shows the GPE simulation for 8000 atoms with initial imbalance $\mathcal{Z}(0) = 0.075$. The grey shaded area represents the variation of the GPE calculations over the range of $\mathcal{Z}(0) = 0.05$ to 0.10. The vertical error bars are statistical; the statistical uncertainty in δ_0 is $2\pi \times 0.5$ kHz (not shown). The GPE calculation gives $\mathscr{R}_1 = 1$ when $V_b/\mu \simeq 1.1$.

This fraction is plotted as a function of δ_0 and V_b/μ in Fig. 5.10 for barrier heights at which two frequencies could be reliably measured.

5.4.2 GPE calculations

Given the broad applicability of the GPE to BEC systems, we sought to use the fully time-dependent three-dimensional GPE to simulate the dynamics we observe in our tunable double well. We compare our experimental results to these simulations to determine the origin and explain the changing amplitude of the frequency components in the population oscillations.

The calculations presented here use Eq. (5.1) to determine the condensate wavefunction in the RWA potential (Eq. (2.13)). Corrections to account for beyond-RWA effects accounted for, as discussed in §2.3.2, with a shift of the detuning, δ_0. All GPE calculations in this work were performed with $N = 8000$, which is the atom number for which the best agreement was found in the results shown in Fig. 5.10. The initial imbalance for the calculations is $\mathcal{Z}(0) = 0.075$, which is turned off suddenly. As in the experiment, we extract a value of $\mathcal{Z}(t)$, counting the number of atoms on each side of the well after a variable hold time, t. Unlike in the experiments, the full density distribution is available and can be studied to determine the nature of the motion in all dimensions.

Figure 5.11 shows one time series simulation, with experimental data superimposed. The

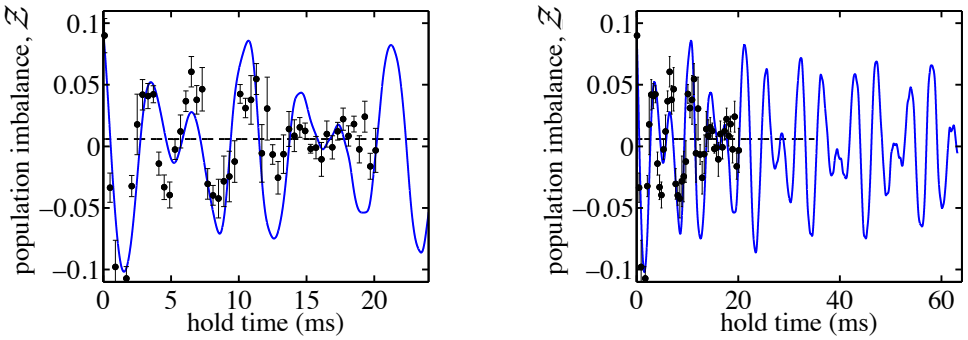

Figure 5.11: Direct comparison of data to the GPE calculation, for $\delta_0 = 2\pi \times 0$ kHz. Blue line represents the GPE calculation result, black points are the experimental data from Fig. 5.8(a). The two panels show the same data for (a) 24 ms and (b) 64 ms. Calculation data were shifted back in time by 0.5 ms to account for the experimental ramp-down time of the bias field.

dynamics which emerge from the GPE calculation are similar to those in the experiment in that two frequency components are evident, though the experimentally observed decay is absent. We extract frequency and amplitude information from the GPE calculations using the same FT and fit methods as are used on the experimental data.

Healing length calculation

From the density distributions found in the GPE calculations, the trap-centre healing length can be found by calculating $\xi(\mathbf{r} = \mathbf{0})$ (Eq. (5.3)). Assigning a characteristic length scale of the system, d, to be the distance from the minimum of the well to the middle of the barrier, the ratio of healing length to system size can be determined. As noted in §5.2.2, the size of healing length relative to the system size dictates whether the neglect of the quantum pressure term is valid. Figure 5.12 shows that the trap-centre healing length is smaller than the system size until the barrier surpasses the chemical potential ($V_\mathrm{b} > \mu$), indicating a hydrodynamic description of the system is not longer valid in this high barrier regime.

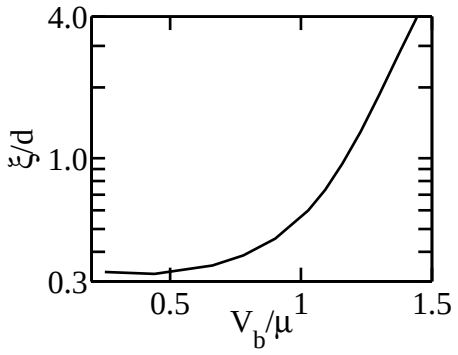

Figure 5.12: Healing length as a function of double-well coupling. The characteristic system size, d, is the distance between the well minimum and the barrier maximum. Courtesy of F. Piazza.

5.4.3 Interpretations of small amplitude transport

Frequency characteristics

The experimental frequency data are compared to the GPE simulations (solid lines) in Fig. 5.9, with very good agreement in the shape and slope of the frequency vs. detuning characteristic. As in the experimental data, multiple frequency components are evident in the simulation for low barriers. To compensate for a systematic unknown in $B_{\rm S}(\mathbf{0})$, we perform a single-parameter fit of the data to the GPE results and find that a shift of $\delta^{\rm TB}_{\rm shift} = 2\pi \times (5.1 \pm 0.1)$ kHz aligns the data to the theory (Fig. 5.9).

Also plotted in Fig. 5.9 is the prediction of the TMM for the system parameters. Though it drastically diverges from the data in the low-barrier limit, it lies close to both the experimental points and the GPE simulation in the high barrier limit, indicating that this lower mode transforms into the plasma mode as the barrier is raised.

In the opposite limit, the healing length is much smaller than the characteristic system size and hydrodynamics dominate the system behaviour. Rich dynamics are observed in this regime, where $V_{\rm b} < \mu$. The appearance of more than one population oscillation mode arises as a consequence of trap anharmonicity, interactions, and trap anisotropy. If our trap were harmonic, a linear bias would excite only a single dipole mode. The barrier breaks harmonicity along the splitting direction and allows the linear perturbation ($\ell = 1, m = 0$, where x is the azimuthal axis) to excite multiple modes [165]. These x excitations are coupled to transverse (y,z) motion through the nonlinear atom-atom interaction term in the GPE.

In axial symmetry, only the $m = 0$ mode would result in population differences between the wells. The anisotropy of the trap in the y-z plane leads to the mixing of this mode with higher order modes which contain transverse (y,z) character, and the resulting mixed modes, with some $m = 0$ character, both result in population transfer.

The leading character of the two modes we measure can be identified through an analysis of the time-dependent density distributions. If our trap were smoothly deformed to a spherical harmonic potential, the two lowest modes connect to odd-parity modes [166, 167]: the lower mode connects to the lowest $m = 0$ mode (coming from the $\ell = 1$ mode at spherical symmetry), while the higher mode originates from the lowest $m = 2$ mode ($\ell = 3$ at spherical symmetry). This was checked numerically with the GPE by deforming the trap into a fully harmonic axially symmetric trap, and following the mode frequencies throughout this process.

Away from the hydrodynamic regime, the predicted frequency of the plasma mode from the TMM is also plotted in Fig. 5.9. While the dynamics we observe at weak couplings fall outside of the TMM, the lower frequency mode approaches the TMM value for barriers $V_b \gtrsim 1.1\mu$. In keeping with the behaviour of the healing length, the TMM, which relies on quantum transport, is valid only in the regime where the quantum pressure term in the GPE cannot be neglected.

Amplitude characteristics

The amplitudes of the population oscillations from the simulations are compared with experimental measurements in Fig. 5.10. As the barrier height increases, the lower frequency dipole-like mode increasingly dominates. The fractional contribution of this mode nears unity as the frequency of this mode approaches that predicted by the TMM, indicating that this lower mode attains the character of the Josephson plasma mode as the barrier is raised.

When the barrier is raised from zero, the higher mode is at first more easily excited due to an increased anharmonicity along x as the trap bottom becomes flatter. By further increasing the barrier, the higher frequency mode disappears from the population oscillation spectrum due to the vanishing excitation of transverse modes. As the wavefunctions in each individual well are increasingly localized to the effectively harmonic minima, the linear bias no longer excites intra-well transverse motion. Furthermore, in the linear perturbation regime, the inter-well Josephson plasma oscillation, like all Bogoliubov modes, cannot itself trigger any other collective mode.

5.4.4 Implications of small-amplitude population oscillation results

In the experiments described in this section, we describe the first measurements exploring the transition from hydrodynamic to Josephson tunnelling regimes in a double well system. We find rich dynamics in the strongly-coupled low-barrier hydrodynamic regime, where the calculated healing length in the barrier region is small. These dynamics transition towards a single low-frequency mode of population transfer between the wells, consistent with a dc-Josephson-type effect and a healing length in the barrier region larger than the system size.

Experiments using an adiabatic deformation of a trap from a single to a double well cross through this transition on their way to the creation of various interesting quantum states [121, 144, 149–151]. An understanding of the dynamics throughout this regime is important if the criteria for adiabaticity are to be maintained throughout. In the high-barrier regime, this criterion can be calculated with the TMM [168], but as we observe, the lowest frequency mode falls below the TMM prediction for barrier heights just less than the chemical potential.

These results highlight the importance of a quantitative understanding of the double well system. Though we observe population oscillations that, at first glance, resemble the plasma oscillations of a Josephson junction, the system may be in the hydrodynamic limit and the TMM will not apply. If the physics in question rely on a tunnelling connection, as in experiments that purport squeezed states, this distinction is important. However, the observation that "Josephson-like" behaviour exists outside the TMM, as it does in the weak-link condensed matter systems, demonstrates the generality of these phenomena and the continuity of the many-body behaviour throughout the crossover into a tunnelling regime.

5.5 Population dynamics of large imbalances

As discussed in §5.2.3, a BEC in a double well will become self-trapped for sufficiently large initial population imbalances. The phase difference between the wells, driven by the large chemical potential difference between them, winds quickly. The direction of population transport between the wells depends on the value of the phase, and its speed by the tunnelling parameter. If the population transfer is slow enough, it does not cross the $\mathcal{Z} = 0$ point before the change in phase implores the atoms to repopulate the side of the potential

with more atoms in it. In the TMM, the dynamics cross over into this MQST regime when the tunnelling parameter J is small, restricting the flow of population across the wells, and the chemical potential, μ, is large, driving the rapid phase winding. We find this behaviour emerging for barrier heights slightly below the chemical potential, where the TMM was unable to predict the plasma oscillation frequency in §5.4 and cannot be an accurate model for the system.

5.5.1 Onset of MQST

Given a set of trap parameters, and thus a value of J, the onset of MQST can be measured by observing the initial at which the population difference Z no longer crosses through $Z = 0$. Systems with large initial imbalances are prepared by increasing the power of the biasing beam P_{bias}, to values that give imbalances up to $\mathcal{Z}(t = 0) = 0.4$, using the techniques described in §5.3.3 and §5.3.3. A series of $\mathcal{Z}(t)$ values is obtained for many hold times at several values of the initial imbalance, over times much longer than the characteristic dynamics of the system and on the order of typical decay times. For each initial imbalance, all measurements of $\mathcal{Z}(t)$ are averaged. If the system remains in the regime of plasma oscillations, the averaged imbalance $\langle \mathcal{Z} \rangle$ is expected to be zero, while for a system undergoing MQST, $\langle \mathcal{Z} \rangle \neq 0$

Figure 5.13(a) shows that the average imbalance $\langle \mathcal{Z} \rangle$ remains near zero for small initial imbalances, and becomes non-zero above some larger initial imbalance. We are able to determine a point of onset of MQST with a simple two-piece linear fit, where the first fit has zero-slope, the second slope is free, and the meeting of these lines indicates the transition to non-zero population imbalances for long hold times and the onset of MQST.

These measurements are somewhat obscured by the presence of decay in this system. While both a TMM and the GPE predict the self-trapping will exist forever, we find that the population imbalance exhibits some decay and tends towards $\mathcal{Z}(0) = 0$ after a characteristic time that depends on the barrier height (see §5.6). For this reason, the slope of the second piece of the line is not unity, as might be expected. In addition, the decay inherent to this system erases the jump in $\langle \mathcal{Z} \rangle$ that would be expected at $\mathcal{Z}(0) = \mathcal{Z}_{\text{C}}$. This effect of the decay can be simulated by adding to the equation of motion Eq. (5.31a) an Ohmic damping term (§5.6.1, [171]), and is shown in Fig. 5.13(b). The effect of the decay on both the slope and the absence of the jump are confirmed. Despite the obfuscating properties of the decay, we are able to conclude that there is a qualitative change in dynamics as a function of initial imbalance in these measurements which corresponds to the observation of the onset

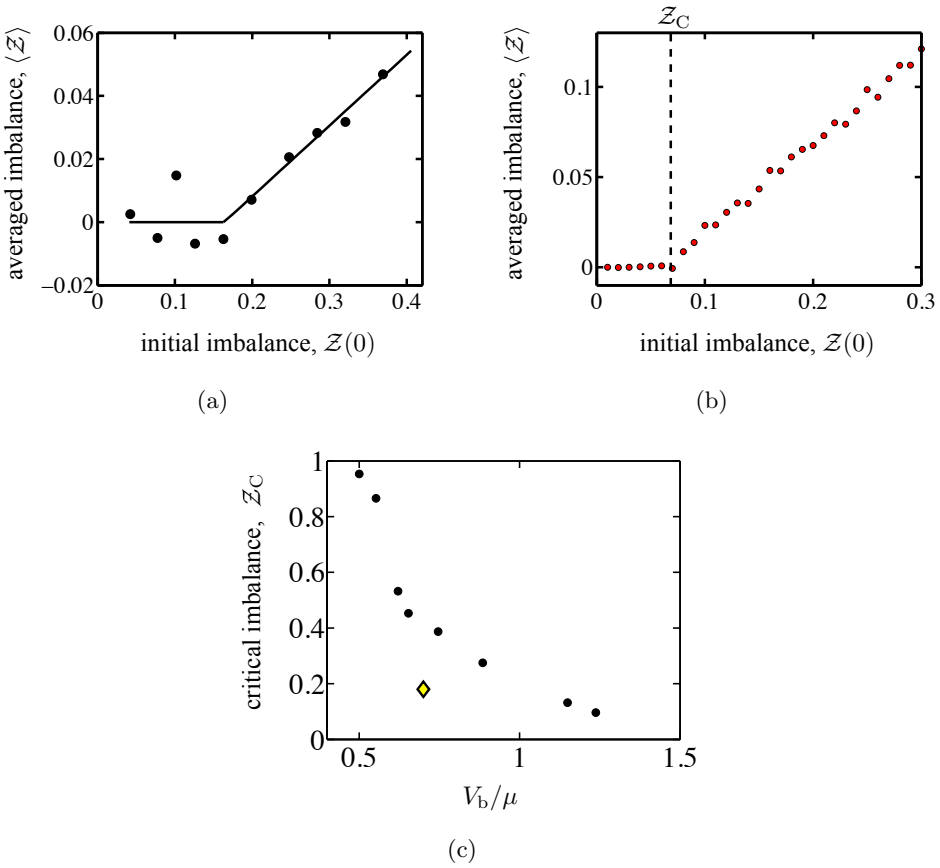

Figure 5.13: Onset of MQST. (a) Average value of imbalance vs. initial imbalance, $V_b/\mu = 0.75$ ($\delta = 2\pi \times 3.1$ kHz, N = 5500). As initial imbalance is increased, the average value of $\mathcal{Z}$ crosses over from its equilibrium value near 0.03 to some larger value. The relationship is not one-to-one due to decay of the self-trapped state for low-barriers. The solid line is a guide to the eye, showing the transition to the self-trapped state beginning at $\mathcal{Z}(t = 0) = 0.18$. (b) Calculated average imbalance vs. initial imbalance in the presence of decay. Parameters used are $N = 5000$, $U = 2\pi \times 750$ Hz, $J = 2\pi \times 0.88$ Hz, with a decay time $\tau \approx 75$ ms. (c) Calculated $\mathcal{Z}_C$ vs. barrier height (black circles, courtesy of F. Piazza) and value extracted from data in (a) (diamond).

of self-trapping.

GPE calculations similar to those done for the small-amplitude oscillations, show that self-trapping emerges within the GPE, even in the strong-coupling regime. Fig. 5.13(c) shows the results of these calculations, as well as the result from Fig. 5.13(a). Clearly, the calculation does not adequately describe these dynamics, and it is likely that the decay of the population imbalance contributes to the discrepancy. However, it should be noted that the example we show here demonstrates that MQST occurs for $\mu > V_b$, where there remains

a significant coupling between the wells.

5.5.2 MQST population oscillations

The population dynamics of MQST can be directly observed by measuring the time dependence of $\mathcal{Z}(t)$. Using the same preparation method as described in §5.5.1, the population dynamics are measured with a finer time resolution. Figure 5.14 shows an oscillating population imbalance about a non-zero and decaying value of $\mathcal{Z}$. In the TMM, these oscillations are attributed to the sinusoidal current-phase relationship characteristic of the Josephson junction (Eq. (5.31b)), and indicate that the phase difference across the wells is well-defined and drives the population across the junction as it evolves. In this case, where $V_\mathrm{b}/\mu = 0.8$ and the TMM is not expected to apply, there exist indications of a phase-driven population in the oscillatory behaviour of $\mathcal{Z}(t)$.

These observations of Josephson-like behaviour in the intermediate coupling regime, where the results of §5.4 would indicate that the TMM is not a valid description of the system, indicate that "Josephson"-like effects exist in regimes where there remains a direct connection between wells. As demonstrated by the calculation of the healing length (Fig. 5.12), the system's properties are increasingly non-local as the barrier is raised, and extend across the barrier region even before the physical connection between the wells is classically broken when $\mu = V_\mathrm{b}$. The Josephson behaviour is associated with the non-locality of the relevant quantities describing the system – as the local hydrodynamic description fails, the long-range parameters like phase and number difference across the wells become good parameters of the system. Like the condensed matter weak-link junctions described in §5.1, Josephson effects emerge when the long-range properties are important, even if tunnelling transport is not yet the only connection between the regions.

5.6 Decay of population imbalance

Throughout our exploration of the tunable double well, we find an unavoidable decay in the population imbalance, as displayed in both Figs. 5.8(a) and 5.14. The origin of this decay remains an open question. In attempts to understand its origin, we have measured the characteristic times for the population imbalance to reach zero as a function of various system parameters, including barrier height and temperature.

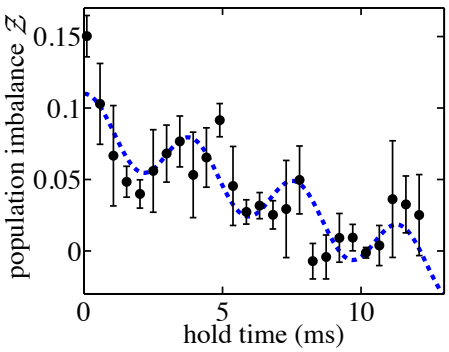

Figure 5.14: MQST population oscillations for $V_b/\mu = 0.8$, $N = 8300 \pm 200$. Dashed line is intended as a guide to the eye; using a sinusoidal + linear fit, we find the frequency of population oscillations is $\nu = 266 \pm 4$ Hz.

5.6.1 Theoretical treatment of decay

The phenomenon of population decay, whether of the plasma oscillations or MQST, is not often treated in theoretical descriptions of BEC double-well dynamics. Though the zero-temperature GPE model described in §5.4.2 very well describes the frequencies and amplitudes of the dynamics we observe, it does not display any indication of the decay of the population oscillation signal over its 64 ms time span, as seen in Fig. 5.11. The absence of decay in the GPE calculations eliminates the possibility that this is due to some dephasing from higher-frequency modes that might have been excited alongside those we measured.

One theoretical treatment considering decay in the double well system attributes it to finite temperature. Zapata, Leggett and Sols [169] consider the transfer of the non-condensed atoms across the barrier in both high and low barrier configurations. They find within their assumptions that the dissipation is "Ohmic," that is, it the current $\mathrm{d}\mathcal{Z}/\,\mathrm{d}t \propto -G\mathcal{Z}$. They find that in both the high-barrier limit that $G \sim T^2 \exp\left(-V_b/k_B T\right)$ while in the low-barrier limit $G \sim T^2$. Other theoretical treatments [170, 171], in reference to [169] add a "phenomenological" decay term with an Ohmic dependence.

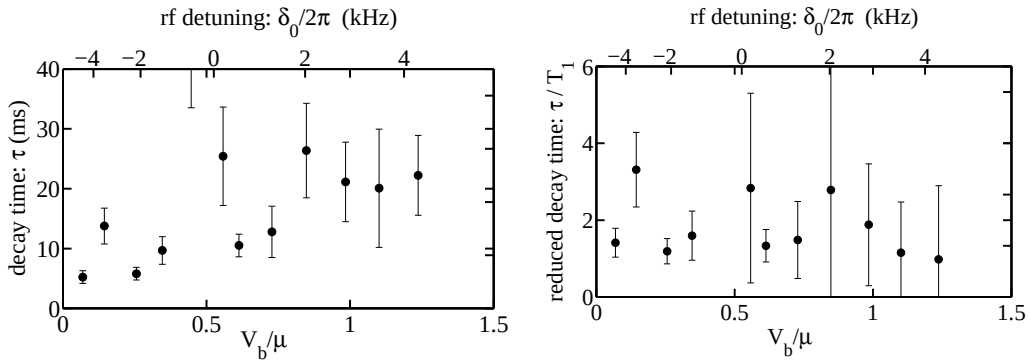

Figure 5.15: Decay of small amplitude population oscillations. (a) Decay time, τ, for small imbalance population oscillation data. (b) Reduced decay time τ/T_1, or small imbalance population oscillation data, where we normalize by the period of the low-frequency oscillation. For both (a) and (b), two points fall above the top edge of this plot, likely the result of fitting difficulties.

5.6.2 Observations of decay

Decay of plasma oscillations

The analysis in §5.4 ignored the presence of decay in the system. To quantify this damping for the small-amplitude perturbations, we use the decaying two-frequency fit (Eq. (5.46)) to determine the characteristic time for decay. Figure 5.15(a) shows the value of τ as a function of the detuning δ_0, and Fig. 5.15(b) shows the same data normalized by the period of the lower frequency oscillation, $T_1 = 1/\nu_1$. We find that the decay time is roughly two oscillation periods, for the data discussed in §5.4. The error bars obtained for this data are quite large, due to the difficulty of extracting a characteristic decay time from a time series whose total length is approximately equal to the decay time.

We can evaluate the effect that this decay will have on the frequency of population oscillation by assuming the system is a simple harmonic oscillator. In the presence of decay, the frequency of motion $\omega_\mathrm{d} = 2\pi\nu$ (Eq. (5.46)) is modified as $\omega_\mathrm{d} = \sqrt{\omega_0^2 - \gamma^2}$, where ω_0 is the natural frequency of the system, and $\gamma = 1/\tau$ is the decay constant. To estimate this frequency shift in our system, we use $\gamma = 1/2T_1 = \omega_\mathrm{decay}/4\pi$. In this case, $\omega_\mathrm{d} \approx 0.997\omega_0$, which is much smaller than the uncertainties in the measurement.

Decay of MQST

The decay of $\mathcal{Z}$ is also evident in experiments with larger initial population imbalances, where the system undergoes MQST. In this case, we measure the decay by fitting the data $\mathcal{Z}(t)$ to a simple exponential decay and extracting the $1/e$ decay time, τ. Figure 5.16(a) displays two such curves for different values of barrier height. The rate of decay is slower for the higher barrier, as might be expected. To further quantify this, we calculate the tunnelling parameter J (§5.2.3) for each set of experimental parameters, and plot the rate of decay, $1/\tau$ as a function of J. There is a weak power-law dependence, which we extract by fitting the data to a linear function on a log-log plot (Fig. 5.16(b)). We find that the decay rate depends on the tunnelling parameter as $1/\tau \propto J^{0.22}$.

Temperature dependence

As a means to better understand the origin of this population decay, we also study the decay rate as a function of the system temperature. To quantify temperature, the condensate fraction is used as a measure. The experiments are performed by alternately measuring the characteristic time for decay, τ (as in Fig. 5.16(a)) and condensate fraction, N_C/N, for identical preparations. The condensate fraction measurements are performed immediately before the splitting process (after the "preparation" step in Fig. 5.7), by releasing the atoms from the trap and recording a momentum distribution along the y axis after 13 ms time of flight (see Appendix C for details of the fitting procedure that determines condensate fraction).

Because the change in temperature is effected through evaporation, the number, N, is not constant. To account for the change in tunnelling parameter J caused by the change in number, we normalize the decay rate to the tunnelling rate, through the power-law fit found at constant temperature in Fig. 5.16(b). Using the condensate fraction as the parameter indicating temperature, we plot the normalized decay rate to find no significant dependence of the decay rate on temperature.

The non-dependence of the decay time upon temperature is surprising, and may indicate that the origin of the decay is technical. A more expansive study of the decay, over broader ranges of tunnelling parameters and temperatures, is needed to better understand the phenomenon. In addition, the finite-temperature modelling of this system may lend insight into the source of this dissipation, using, for example, "ZNG" [172] techniques to simulate the dynamics of the system.

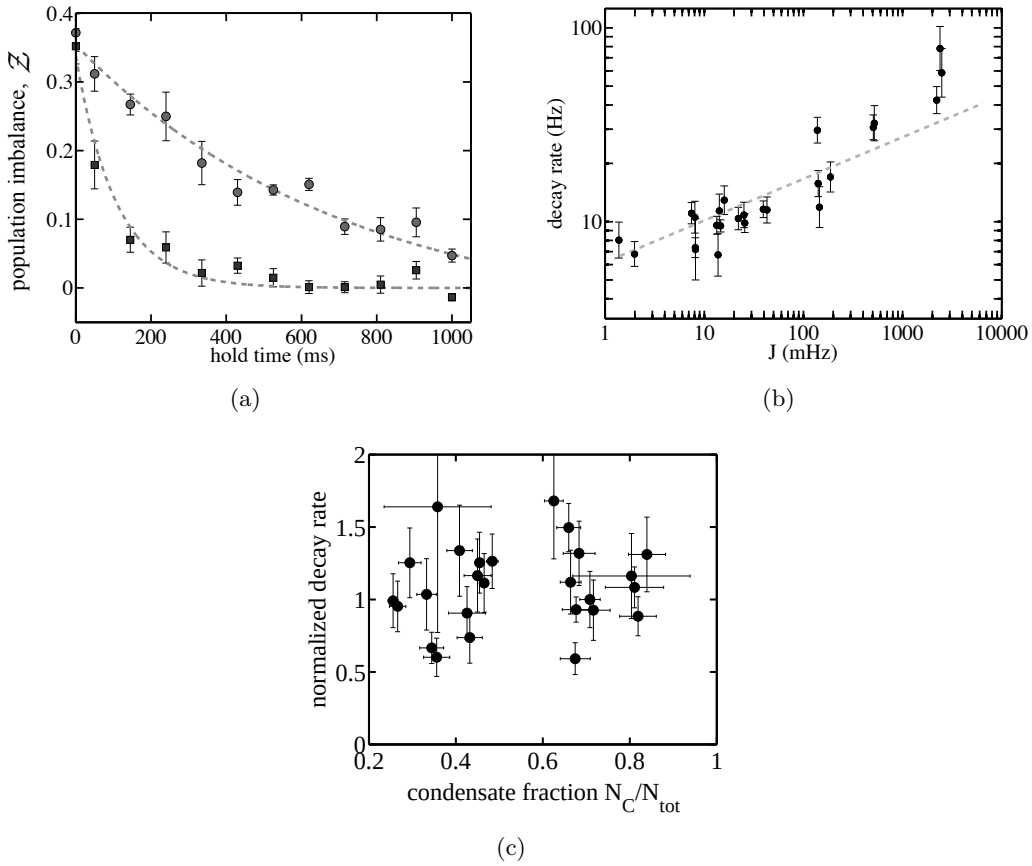

FIGURE 5.16: Decay of large amplitude population oscillations. (a) With large initial imbalances, decay curves for $\widetilde{\delta_0} = 2\pi \times 12$ kHz (squares) and $\widetilde{\delta_0} = 2\pi \times 27$ kHz (circles) with $1/e$ decay times $\tau = 110$ and 720 ms, respectively. (b) Rate of decay ($1/\tau$) vs. tunnelling parameter, J at constant temperature and $N = 9100 \pm 700$. The dashed line is a fit giving a power law relationship that gives the relationship $1/\tau \propto J^{0.215\pm0.008}$. The tunnelling rate is varied by changing the height of the barrier, with detunings ranging from $\delta_0 \approx 5$ to 13 kHz. (c) We measure the decay rate as a function of condensate fraction by varying the condensed fraction and number. The decay rate is normalized to the tunnelling parameter for each set of experimental conditions using the power-law relationship found in (b). Given a value of J for each experimental point, the normalized decay rate is the measured rate divided by the rate given by the fit in (b) at this value of J.

5.7 PHASE SIGNATURES

While the experimental work discussed to this point interrogates the population differences between wells, the phase difference between the condensates in each well can also be measured. As discussed in §5.3.2, if the clouds from the two wells are allowed to overlap after some time of flight, interference fringes will be visible along the direction connect-

ing the centres of the clouds. The phase of these fringes, with respect to the envelope, is representative of the quantum mechanical phase difference between the clouds. Using this information, we have an additional tool for probing the understanding of the double-well system.

A direct comparison of these data to that presented in previous sections is hampered by a change in the apparatus between the taking of the data in this section to those in previous sections. The phase data presented here were collected before a "proper" technique was developed for compensating gravitational forces, and so there existed in these double well traps the "banana" deformation that changes the tunnelling pathways ([15], §2.3.3). As a result, though every attempt has been made to match the calibrations from this older configuration with the newer results of previous sections, the correspondence between values of δ_0 between sections is not direct. To emphasize this difference to the reader, the detuning values in this section will be denoted as $\widetilde{\delta_0}$.

5.7.1 Coherence time measurements

To establish the feasibility of using phase dynamics to reveal the behaviour of the double well system, we studied the repeatability of phase measurements over many realizations of a BEC in the double well potential. Starting with a single well, the trap is deformed into a double well configuration. If the BEC is subject to the same process for each repetition of the experiment, the phase difference between the wells should evolve in the same way, and the phase measured in the momentum distribution should remain constant. If these phase measurement are repeatable, we know that the experiment is well controlled, and that reliable measurements of the phase can be obtained.

Early results are discussed in Ref. [15] (§7.1.2). In the present work, the coherence of the relative phase between the wells is measured as a function of a hold time after the splitting process. Many phase measurements are repeated at each hold time, and the degree of repeatabiity is quantified as the degree of coherence as measured by the quantity $\mathcal{R}$, which is defined in §5.3.3.

Figure 5.17 shows one such measurement. The usual splitting procedure is performed with no initial imbalance, and the atoms are held in the split trap for some variable time. We see that the mean phasor length decreases with time, though the fall off is quite slow in this well-connected configuration. Also shown are three examples of the individual measurement results in Fig. 5.17(b,c,d) and the measure of $\mathcal{R}$ and $\overline{\phi}_{\mathrm{fr}}$.

These results are encouraging, suggesting that well-resolved phase measurements can be

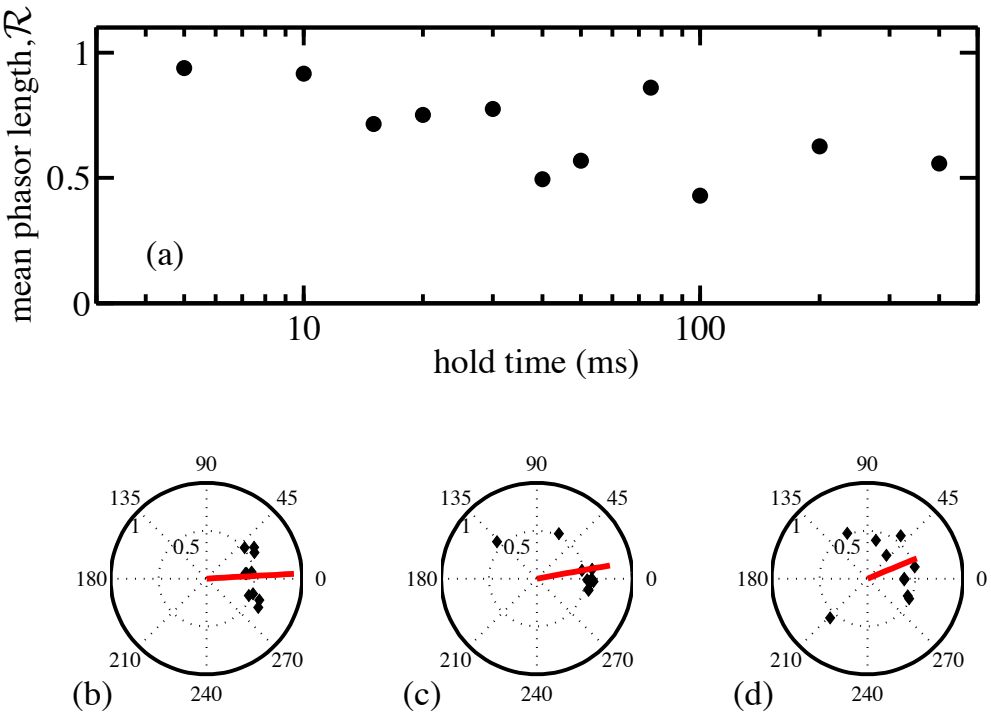

Figure 5.17: Coherence time measurements, $\tilde{\delta_0} = 6.5$ kHz (a) Mean phasor length, $\mathcal{R}$, vs time. (b,c,d) Individual phase measurements (black diamonds) plotted at angle $\phi_{\rm fr}$ and radius corresponding to the visibility, $\mathcal{V}$. Red line indicates the calculated value of length $\mathcal{R}$ at angle $\overline{\phi}_{\rm fr}$. Phases measured at (b) 10 ms, (c) 75 ms, and (d) 400 ms hold time.

made even after relatively long hold times.

5.7.2 Josephson dynamics

In earlier sections, the population dynamics of both small (§5.4) and large imbalances (§5.5) were studied in detail. In compliment to these measurements, the phase signatures of these dynamics can also be measured. Though these were not studied in the same detail, this section presents proof-of-principle demonstrations of both dc- and ac-Josephson effect behaviour.

Plasma oscillations in phase

For small initial population imbalances, §5.2.3 describes a harmonic oscillator hamiltonian (Eq. (5.35)), in which $\mathcal{Z}$ and ϕ are conjugate variables. In this description, as in a

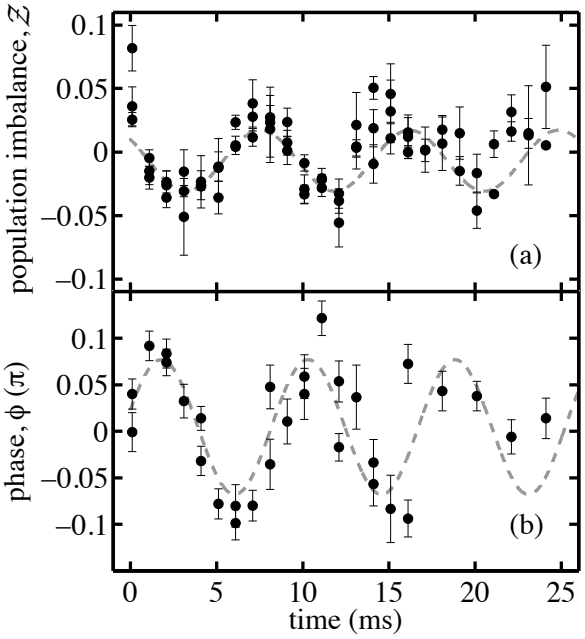

FIGURE 5.18: Plasma oscillations in population and phase. System parameters are $\tilde{\delta}_0 \approx 2\pi \times 16$ kHz and $N = 6000$. Data are fit with single-frequency undamped sinusoids to determine the frequencies of oscillation (dashed lines) (a) Population imbalance vs. time, $\omega_{\rm p} = 2\pi \times (115 \pm 1)$ Hz, (b) Phase vs. time, $\omega_{\rm p} = 2\pi \times (117 \pm 2)$ Hz. The phase relationship between the population and phase oscillations is obscured by the measurement method (see text).

simple harmonic oscillator, energy is periodically transferred between the interaction and the tunnelling energies, in analogy to the transfer between potential and kinetic energy of the oscillating pendulum.

Using the same techniques described in §5.3.3 to initiate population dynamics in the small amplitude regime, we measure both the population imbalance oscillations and the conjugate oscillations in phase. Figure 5.19 demonstrates the oscillatory behaviour of both $\mathcal{Z}$ and ϕ for identical experimental conditions. The measured oscillation frequencies from these sets of data agree with one another at $\omega_{\rm p} = 2\pi \times (115 \pm 1)$ Hz for the population oscillations and $\omega_{\rm p} = 2\pi \times (117 \pm 2)$ Hz for the phase.

Phase winding in MQST

The phase evolution for the large population imbalances, as suggested by the oscillating population dynamics observed in §5.5.2, is responsible for MQST. As shown in Fig. 5.2, the phase should always increase in this regime, unlike the oscillatory behaviour observed for plasma oscillations. In the limit of small change in populations ($J \ll U$; $\mathcal{Z}(t) = \text{const}$), the Josephson equation holds, and the phase evolves linearly in time, as $\phi(t) = U\mathcal{Z}t$. The frequency of these phase oscillations is $\omega_{\rm MQST} = U\mathcal{Z}$, which is just the chemical potential

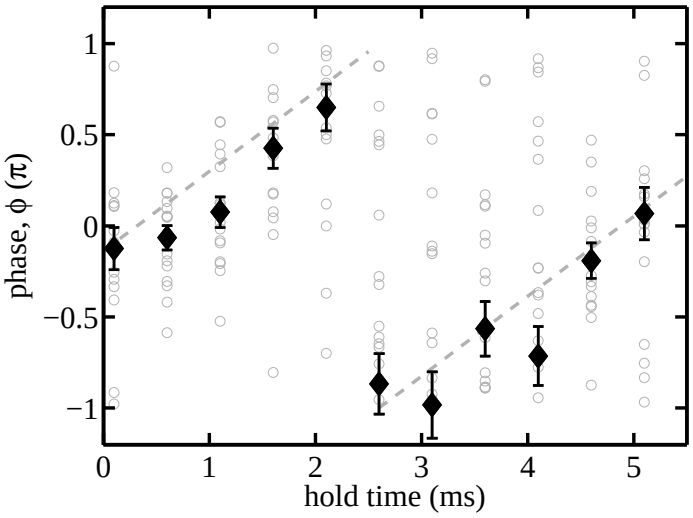

Figure 5.19: Phase winding and MQST. After preparing an initial imbalance of $\mathcal{Z}(0) = 0.06 \pm 0.01$ at $\tilde{\delta_0} \approx 2\pi \times 24$ kHz with $N = 7000$, the system is allowed to evolve for some hold time, after which the phase is measured. Solid black points show the average phase as a function of hold time, where the open points represent the results of individual measurements. Dashed grey line indicates a fit to the data assuming 2π-periodic linear phase winding, giving a frequency $\omega_{\mathrm{MQST}} \approx 2\pi \times 220$ Hz.

difference between the wells.

While we were never able to capture both the population oscillations for the same parameters (and on the same day) as the phase winding dynamics, they have been observed separately. By creating a large initial population imbalance as described in §5.5, the MQST dynamics were initiated. Fig. 5.19 shows the evolution of the phase over across one period. The fit to these data yields a frequency of $\omega_{\mathrm{MQST}} \approx 2\pi \times 220$ Hz, where the approximate equality is because of the uncertainty in fitting to only one period of oscillation.

The method of phase imprinting could be used as an alternate means to engineer an out-of-equilibrium initial condition, with which the dynamics could be initiated.

5.7.3 Phase imprinting

Just as the when there exists a number difference $\mathcal{Z} \neq 0$, the phase difference between the wells will evolve if a chemical potential difference is established with an external potential. Through precise control of such an external potential, the phase difference between the wells could be controlled and the method could be used as a tool to "write" a specific phase difference into the system.

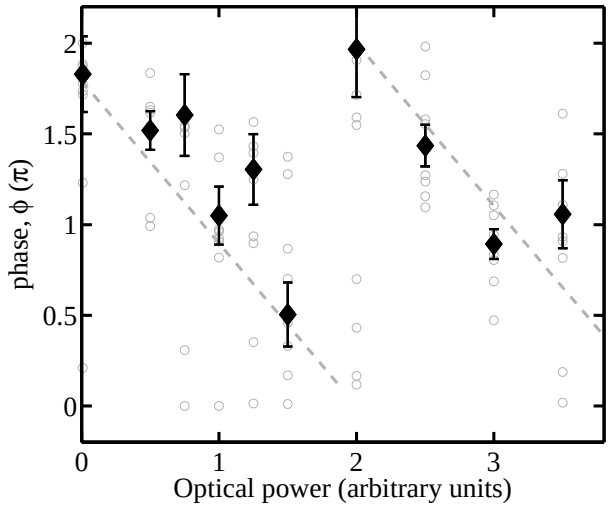

Figure 5.20: Phase imprinting with $\tilde{\delta_0} = 2\pi \times 8$ kHz, $N = 8000$, and balanced populations. Optical power, in arbitrary units, was applied for 0.5 ms and the phase observed. The solid points are the average of 10 measurements, which are shown individually as the open circles. The rate of phase difference accumulation is determine from the dashed grey line fit and gives $\mathrm{d}\phi/\,\mathrm{d}t = -0.90\pi$ rad per unit optical power.

Using the same laser beam (ODT1) that biases the wells for initiating population dynamics, a potential energy difference is established for the $\mathcal{Z} = 0$ populations. The BEC is released from the double well potential and the momentum distribution is analyzed to determine the relative phase between the wells as a function of the strength of this potential difference.

Figure 5.20 shows a measurement of the phase imprinting. Unlike in previous sections, we prepare a balanced population in the double well system. For 0.5 ms, we apply a pulse of light whose focus is to the outside of both wells, such that the intensity incident on one well is greater than the other. As a function of the power of this beam, we measure the phase difference between the wells and find that it has a roughly linear dependence on this power. A linear-modulo-2π fit shows that the phase winds with a rate $\mathrm{d}\phi/\,\mathrm{d}t = -0.90\pi$ rad per unit optical power[4]. Assuming the atom number is perfectly balanced, the chemical potential difference will be entirely due to the potential energy difference between the two wells, the difference between the two wells is $V_{\mathrm{bias}}/\hbar = 2\pi \times 450$ Hz.

[4]The optical power for this experiment was not calibrated, though it is known that this scale is linear in real optical power.

5.8 Lessons from a tunable double well

One of the great advantages of studying many-body problems with a quantum gas is the ability to precisely control an atomic system's parameters. Through the combination of magnetic trapping and rf-induced internal state manipulation, we exploit this advantage to create a tunable double well potential for a BEC, where we can transform the environment from a single to a double well. The particular focus of the work presented in this chapter is the study of dynamical properties as a function of the barrier height.

The major result of this work is the observation of the transition between a hydrodynamic regime of superfluid dynamics at low barrier heights and a Josephson tunnelling regime at barriers higher than the BEC chemical potential. We see a low-lying mode of the hydrodynamic system transform into the Josephson plasma mode as the barrier is raised, indicating the continuity of the physics between these regimes. The presence of an unavoidable higher-lying mode in the hydrodynamic regime indicates that the geometry of the system is an important consideration in the design of devices that require a transition between these regimes to perform the splitting of a condensate.

While the TMM describes the frequencies of these dynamics for high barriers, its divergence from the experimental results at barrier heights lower than the chemical potential warns against using this model too freely when establishing criteria for adiabaticity in splitting processes. However, in our measurements of MQST, we find that this TMM-derived Josephson-effect remains in the intermediate regime of barrier heights and is predicted by the GPE. These results establish that the domain of Josephson-type effects in this BEC system extends beyond the regime of validity of the TMM.

These results both indicate the regimes in which the hydrodynamic and TMM approximations of the GPE are valid, and confirm that the full GPE is an accurate predictor of the frequencies and amplitudes of the dynamics in all regimes we consider. The observation not accounted for by the GPE is the damping of the population dynamics, which remains the most striking open question in this system. Our measurements seem to indicate that the damping of these dynamics is independent of temperature, and that the time for damping depends only very weakly on the tunnelling parameter, J. While further work may be required to eliminate the possibility that the source of this noise is technical, calculations that include temperature and other non-GPE excitations may shed insight into this problem.

This work, which began in an attempt to understand the parameters U and J and their role in the dynamical splitting process on the path to squeezed state generation [15], has

demonstrated that the geometry of the system is important, and that the full three dimensions of the system must be included in any analysis. We have found that though dynamical signatures qualitatively resemble those predicted by the TMM, the parameters of these dynamics do not necessarily provide a direct measure of the TMM parameters. Instead, we see a continuous transformation of the dynamics from a regime where hydrodynamics are valid to one where a TMM is valid. These results should better inform future experiments employing dynamical splitting processes to perform interferometry [23, 150, 151] or to create unconventional quantum states [121, 149].

Chapter 6

Conclusions and outlook

The foundation on which this thesis is built is an experimental apparatus designed and built to produce ultracold ^{87}Rb BECs and ^{40}K DFGs, atomic ensembles in which thermal motion is negligible and interactions between particles dominate the energetics. The availability of these quantum degenerate samples inspired theoretical and experimental studies of ultracold Bose and Fermi gases in configurations designed to expose particular many-body effects, including ferromagnetism, hydrodynamics, and Josephson tunnelling.

Three principal contributions are presented in this thesis. First, a technique using the spectroscopic distinguishability between atomic species to selectively manipulate one species in a mixture is developed, and the applications of this tool are discussed. Second, the signatures of a ferromagnetic state in a trapped two-component Fermi gas are predicted and the foundations for the experimental realization of this transition in an ultracold gas of ^{40}K are laid. Third, the many-body dynamics of a ^{87}Rb BEC in a tunable double well system are explored, with a focus on the crossover behaviour between hydrodynamic and tunnelling transport between the wells. These topics are summarized below, with reflections on the prospects for further study.

Species selectivity

Chapter 3 describes a new technique for manipulating a species mixture of ultracold alkali atoms. Using the differences in the spectroscopic character between atomic species, the effect of an optical field on each species can be tailored through choice of wavelength. We show that when this wavelength is chosen to fall between the two strong transitions in the alkali atom, there will be zero potential energy shift for a reservoir species, while there remains a shift for a target species. Similarly, the wavelength can be chosen near

the strong transition for the target species, rendering negligible, by comparison, the shift on the reservoir. Upon evaluating the potential energies and losses associated with these schemes in mixtures of alkali atoms, we find that both are experimentally feasible: the tune-in scheme is better suited to heavier elements while the tune-out scheme should work well for mixtures of the lighter elements.

With an increasing number of ultracold gas experiments using two or more atomic species [35, 56, 58–60, 173, 174], techniques like this species selectivity make possible the exploration new many-body systems. As a tool to reach colder temperatures, selective addressability has been used to transfer entropy from a target species to a reservoir species [32], providing additional cooling to reach lower energy scales and new regimes of many-body physics. If the optical field is established as a standing wave, a lattice potential can be imposed upon one species, leaving the other delocalized from the lattice sites. For shallow lattices, this technique could tune the effective mass of the target species [77] to create a more favourable ratio of masses between species. In mixtures of fermions and bosons, a bosonic background species could mediate interactions between identical fermions on separated lattice sites, through, for example, phonon excitations [51–53, 175]. In general, species specificity provides access to at least one additional degree of freedom in the system, which can be used to implement an increasingly detailed environment for the atoms, which might prompt the discovery of new many-body phenomena.

Ultracold ferromagnetism

Chapter 4 discusses the signatures of itinerant ferromagnetism in trapped ultracold fermions subject to strong repulsive interactions. At the crossover to the ferromagnetic state, mean-field, local-density calculations predict observable discontinuous features in the bulk energies of the system, which were confirmed by an experiment [108]. Further calculations show that the energetic costs associated with magnetization gradients give a preference to the three-dimensional magnetization configuration that distributes the gradients across the entire system, in a hedgehog geometry.

To access the regime of strong interactions with ^{40}K , the experimental apparatus was adapted to include optical traps and stabilized magnetic fields. Using a two-state mixture of ^{40}K , strong interactions were observed as a loss feature near the Feshbach resonance. While questions remain regarding its three-body loss rates in the repulsively interacting regime, ^{40}K offers advantages over ^{6}Li: its greater mass allows for quieter imaging, and its narrower Feshbach resonance implies that smaller, and therefore faster, magnetic field

changes are required to change the interaction strength.

The apparatus is well-poised to continue exploring ferromagnetism in a trapped Fermi gas, both to confirm the results observed in ^{6}Li [108] and to complement these results by distinguishing between the ferromagnetic state discussed here and other possible effects displaying similar energetic signatures [110, 111]. To determine unambiguously if the system is ferromagnetic, a direct measure of magnetic properties is required – the observation of domains or a measurement of the magenetic susceptibility [176] may help to clarify the state or the system.

Exact calculations for strongly interacting fermion systems are beyond the capabilities of modern computational methods. A thorough experimental understanding of the ground state of this system would constitute one of the first realizations of a cold-atom quantum simulator, and could answer questions about the minimal set of conditions required for a system to undergo a magnetic transition. By establishing the experimental techniques in this system and demonstrating the feasibility of using ultracold gases as quantum simulators, increasingly complicated simulations could be performed by, for example, adding a lattice potential to the trapping geometry [13, 177–179].

Double well BEC dynamics

Chapter 5 explores the many-body dynamics of a double-well BEC system over a wide range of barrier heights. A crossover between two standard paradigms of superfluidity is observed as the system crosses over from hydrodynamic to tunnelling behaviour as the barrier is varied and the BEC density in the region connecting the wells disappears. For $V_\mathrm{b} \gtrsim 1.1\mu$, we make the first direct observation of tunnelling transport through a magnetic barrier and find that the dynamics here are predicted by the two-mode model. Further experiments show that the macroscopic quantum self-trapping behaviour expected in the regime of tunnelling dynamics is found at some barrier heights less than the chemical potentials, as low as $V_\mathrm{b} \approx 0.8\mu$.

An awareness of the appropriate description of a double-well BEC system is important when determining the parameters of an experiment. Transformations from a single to a double-well are often required [23, 121, 149–151], and the hydrodynamic to tunnelling crossover is traversed. For the split BEC to remain in the many-body ground state, this transformation must be adiabatic. The lowest excitation energies of the system in the hydrodynamic regime are smaller than in the tunnelling model, indicating that a more-stringent limitation is placed on the limits of adiabaticity than might be assumed in by

two-mode model [168]. Our observations that qualitative Josephson-style behaviour exists outside the regime of validity of the TMM indicate that the observation of such effects is not a sufficient condition for the application of the TMM. We show that a thorough study of the system's dynamics can be used to characterize the regimes of validity of various models.

Double well BEC systems, especially as implemented with an atom chip technology as described in this thesis, may prove useful as interferometers [23, 150, 151]. By further developing the understanding of the many-body physics in this system, squeezing [121, 149] could be improved to increase the precision of these measurements.

Closing remarks

The relationships between the interaction properties of individual quantum mechanical objects and the many-body effects they encourage provide insight into the connection between the quantum mechanical and classical worlds. Using what are distinctly individual quantum objects – ^{87}Rb and ^{40}K atoms – we find that we are able to measure the collective parameters of system composed of these objects, such as, for example, their phase, mass transport or magnetization. Though the specific origins of the many-body effects discussed in this thesis depend on the details of the constituent particles and their environments, a common property emerges: a system can often lower its energy by having its constituent particles act communally.

In the context of ultracold atoms, the diversity of many-body phenomena predicted in the literature is vast. By continuing to reduce the energetic scales characterizing these systems, the dominant interactions driving the collective response may expose new classes of behaviour. Exploring this variety of many-body phenomena will lead to new questions about the quantum mechanical world, while simultaneously increasing our understanding of its manifestations in the classical world with which we are more familiar.

Appendix A

^{40}K hyperfine structure and transition matrix elements

The contents of this appendix are largely the reproduction of a report prepared as a final project for PHY2206S (Atomic and Molecular Physics) in the spring semester of 2006, with the more detailed derivations omitted. In the spirit of similar reports prepared by Daniel Steck for some of the other alkali metals [62–64, 180], this collection of data is intended to be a useful resource for those working with ^{40}K.

This appendix includes a brief discussion of the fine structure splitting in ^{40}K in §A.1. The hyperfine structure is discussed for the ground and first excited states in §A.2, and is calculated over a wide range of magnetic fields in §A.3, in extension of the Breit-Rabi calculations done in §4.6.1. The transition matrix elements for the electric dipole transition are found and tabulated in §A.4.

A.1 Fine structure

To good approximation, the alkali metals are "hydrogen-like" in that they have a single electron in the s-state orbitting a charged core. For hydrogen, the core is just the nucleus, while for the higher atomic numbers it is the nucleus surrounded by closed shell electron orbitals. The Coulomb interaction of this electron with the core, together with the interaction between the angular momenta of the electron's orbit and its spin, gives rise to the discretization of energy levels for the electron known as the fine structure.

For an electron orbitting a charged core, we consider an angular momentum, $\mathbf{L}$, associ-

Property	Value	Ref.
Atomic number (Z)	19	
Total nucleons ($Z+N$)	40	
Relative natural abundance	0.011 7(1) %	[181]
Atomic mass (m)	39.963 998 48(21) amu	[181]
Nuclear spin (I)	4	[181]
D1 Transition Wavelength ($^2S_{1/2} \rightarrow {}^2P_{1/2}$)	770.10929 nm 12 985.170 cm^{-1}	[182]
D2 Transition Wavelength ($^2S_{1/2} \rightarrow {}^2P_{3/2}$)	766.70207 nm 13 042.876 cm^{-1}	[182]

Table A.1: General properties of ^{40}K

ated with the orbital angular momentum, **S**, due to the spin of the electron. These are coupled through the *spin-orbit* interaction [162]. Adding these contributions, we obtain a value for the total angular momentum of the electron, $\mathbf{J} = \mathbf{L} + \mathbf{S}$. The value of J follows the triangle rule (i.e., $|L - S| \leq J \leq L + S$).

In this work, we consider the two lowest lying transitions. Since, by selection rules, L must change by one, the lowest lying transition is from the $L = 0$ ground state is to the $L = 1$ state. This level is doubly-degenerate, due to the two possible values of the spin, $S = \pm 1/2$. These two lines are known as the D_1 and the D_2 lines, and have total angular momenta $J = \frac{1}{2}$ and $J = \frac{3}{2}$ respectively.

The fine structure splitting is most accurately determined experimentally, and measured values will be used. Table A.1 gives the transition wavelengths for the D1 and D2 lines, which are separated by 3 nm in ^{40}K.

A.2 Hyperfine structure

The next degree of precision in determining the energy levels of an alkali atom is to consider the effect of the nucleus. There will be two main contributions to the Hamiltonian which describes the energy of the atom: one due to the effective magnetic field arising from the spin of the nucleus, **I**, the other from the finite extent of the charge distribution of the nucleus and the associated higher-order electric multipole moments.

A.2.1 Effects of nuclear spin

In the fine structure calculations, nuclear spin is neglected because of the large mass of the nucleus in comparison to the electron. Moving beyond these approximations, it is one of the primary considerations. The energy shifts arise due to the interaction of the nuclear spin with the effective magnetic field of either the orbital electron or an external magnetic field.

Internal effects

As with the electron spin, **S**, we can associate with the nucleus an intrinsic angular momentum, or spin, called **I**. This spin is the result of the addition of the spins of each of the constituent particles in the nucleus, and is determined experimentally. The spin of the ^{40}K nucleus is $I = 4$ [181].

In the absence of an external magnetic field, the term in the Hamiltonian that accounts for the energy of the nuclear spin in the magnetic field of the orbitting electron is

$$H_{\mathrm{B,el}} = -\frac{\boldsymbol{\mu}_I}{\hbar} \cdot \mathbf{B_J}, \tag{A.1}$$

where $\boldsymbol{\mu}_I$ is the magnetic moment of the nucleus, $\mathbf{B_J}$ is the effective magnetic field due to the orbitting electron, defined by its angular momentum and **J**. Whereas with the fine structure, we considered LS coupling, here, we consider IJ coupling. Separate electron energy levels are well-defined by the angular momentum **J**, and are much more closely-spaced than the fine structure energy levels. In this approximation I and J are both good quantum numbers. We can then assume the nuclear magnetic moment is proportional to its angular momentum

$$\boldsymbol{\mu_I} = g_I \mu_N \mathbf{I}, \tag{A.2}$$

where g_I is the effective g-factor for the nucleus, $\mu_N = (m_e/m_N)\mu_B$, is the nuclear magneton, $\mu_B = \hbar e/2m_e$ is the Bohr magneton, and m_e and m_N are the electronic and nuclear masses.

In writing Eq. (A.1), we assume that B_J acts only in the electronic (and not the nuclear) subspace and can it is proportional to **J**. In this case, the hamiltonian can be written as a product of two operators, each acting on their own subspace

$$H_{\mathrm{B,el}} = A_{\mathrm{hfs}} \mathbf{I} \cdot \mathbf{J}, \tag{A.3}$$

where A_{hfs} depends on details of the atomic structure and can be calculated (see, for example, Ref. [183]). For the purposes of this Appendix, we use an experimentally determined value, which is more accurate than the calculations (See Table A.2).

External effects

In addition to the effects within the atom, the nuclear and electronic spins can also interact with external magnetic fields, which is known as the Zeeman effect. The term in the hamiltonian arising from the external magnetic field is

$$H_{\mathrm{B,ext}} = \frac{1}{\hbar}\left(\boldsymbol{\mu}_J \cdot \mathbf{B} + \boldsymbol{\mu}_I \cdot \mathbf{B}\right) \tag{A.4}$$

where the terms $\boldsymbol{\mu}_J = g_J \mu_B \mathbf{J}$ and $\boldsymbol{\mu}_I = g_I \mu_B \mathbf{I}$ define the g-factors. By invoking the projection theorem, expressions for the g_J factors can be obtained:

$$g_J = g_L \frac{J(J+1) - S(S+1) + L(L+1)}{2J(J+1)} + g_S \frac{J(J+1) + S(S+1) - L(L+1)}{2J(J+1)} \tag{A.5}$$

where g_L and g_S are experimentally determined values (the Landé g-factors) for the magnetic dipole moments of the electron orbital angular momentum and electron spin, quoted in Table A.2, along with the measured values of g_J, where available.

Expressions for the strong and the weak field limits of H_B are common in quantum mechanics or atomic physics textbooks (see, e.g. [184]). In the weak field, the sum of electron and nuclear angular momentum $\mathbf{F} = \mathbf{I} + \mathbf{J}$ provides a new set of good quantum numbers F and m_F. The $|F, m_F\rangle$ states are the eigenstates of the system and the external field Hamiltonian can be written

$$H_{\mathrm{B,ext}}^{\mathrm{weak}} = \frac{\mu_B}{\hbar} g_F \mathbf{F} \cdot \mathbf{B}. \tag{A.6}$$

where

$$g_F = g_J \frac{F(F+1) - I(I+1) + J(J+1)}{2F(F+1)} + g_I \frac{F(F+1) + I(I+1) - J(J+1)}{2F(F+1)}. \tag{A.7}$$

In the high field limit, the effects of the magnetic field on the electron are far greater than those on the nucleus, rendering the coupling between them negligible. Here (and, indeed, everywhere), the eigenstates can be defined by $|J, m_J, I, m_I\rangle$ and the hamiltonian becomes

$$H_{\mathrm{B,ext}}^{\mathrm{strong}} = \frac{\mu_B}{\hbar}\left(g_J \mathbf{J} + g_I \mathbf{I}\right) \cdot \mathbf{B}. \tag{A.8}$$

In this work, all magnetic fields are considered and the $|J, m_J, I, m_I\rangle$ states are used throughout to calculate the energy of the hyperfine interactions, due to the magnetic fields being diagonal in this basis. Taking into account all effects due to the nuclear spin, we find a hamiltonian

$$H_B = A_{\mathrm{hfs}} \mathbf{I} \cdot \mathbf{J} + \frac{\mu_B}{\hbar}\left(g_J \mathbf{J} + g_I \mathbf{I}\right) \cdot \mathbf{B}. \tag{A.9}$$

A.2.2 The electric quadrupole moment

For a complete description of the interaction between the angular momenta of the electron and the nucleus, a multipole expansion of the charge distributions of both the nucleus and the electron is required. The derivation of Eq. A.3, in which we assume both that the magnetic moment of the nucleus and the field created by the orbiting electron are proportional to their angular momenta, is equivalent to using only the monopole moments for both distributions. For electron spins $J > 1/2$, higher order moments may be important. Parity considerations restrict the nucleus from having odd multipole moments, and so the quadrupole moment is the next correction to these results [185].

Details of this calculation can be found, for example, in Refs. [185, 186]. The hamiltonian containing the quadrupole contribution to the hyperfine splitting is

$$H_Q = \frac{B_{\text{hfs}}}{2I(2I-1)J(2J-1)}\left[3(\mathbf{I}\cdot\mathbf{J})^2 + \frac{3}{2}(\mathbf{I}\cdot\mathbf{J}) - \mathbf{I}^2\mathbf{J}^2\right]. \tag{A.10}$$

The coefficient B_{hfs} has been measured for the D2 line in ^{40}K (see Table A.2). This quadrupole term is relevant only to the D2 line as both the ground state and D1 lines have $J = 1/2$, whose symmetry prevents a quadrupole term from entering the expansion.

A.3 Calculating the hyperfine splitting for all magnetic fields

Taking into account both the effects of the nuclear spin and the electric quadrupole moment (the latter only for the D2 line), the hyperfine Hamiltonian can be written,

$$H_{\text{hfs}} = A_{\text{hfs}}\mathbf{I}\cdot\mathbf{J} + B_{\text{hfs}}\frac{3(\mathbf{I}\cdot\mathbf{J})^2 + \frac{3}{2}\mathbf{I}\cdot\mathbf{J} - \mathbf{I}^2\cdot\mathbf{J}^2}{2I(2I-1)J(J-1)} + \frac{\mu_B}{\hbar}(g_J m_J + g_I m_I)B \tag{A.11}$$

where all terms have been defined in §A.2. Experimental values for A_{hfs}, B_{hfs}, and the g-factors are given in Table A.2.

The hyperfine splitting can be easily calculated in either the low magnetic field or the high magnetic field situations. In the first, the magnetic field dependent effects are treated as a perturbation and the good quantum numbers are given by $|F, m_F\rangle$. In the latter, the electric quadrupole term is treated perturbatively, and the states $|J, m_J, I, m_I\rangle$ define the good eigenstates. However, neither approach gives a complete description of the magnetic

	Ground ($^2S_{1/2}$)	D1 ($^2P_{1/2}$)	D2 ($^2P_{3/2}$)
$A_{\rm hfs}$ (MHz)	-285.731(16) [187]	-34.49(11) [188]	-7.48(6) [188]
$B_{\rm hfs}$ (MHz)	n/a	n/a	-3.23(50) [188]
Isotope shift, $\Delta\nu$ (MHz) (relative to ^{39}K)	125.58(26) [188]	n/a	n/a
g_J	2.00229421(24) [61]	0.665885†	1.334102228†
g_I	0.000176490(34) [61]		
g_S	-2.002 319 304 3622(15) [189]		
g_L	0.99998627(25)* (from [189])		

Table A.2: Electronic and magnetic parameters for ^{40}K. All values are determined experimentally unless otherwise noted. † Calculated using g_S, g_L with Eq. (A.5); * Calculated using $g_L = 1 - m_e/m_{nuc}$.

field dependence of the hyperfine splitting. To determine the energies at all values of the magnetic field, Eq. (A.11) must be numerically diagonalised[1].

To perform such a calculation, it is necessary to choose a set of states under which to write the original Hamiltonian. The $|J, m_J, I, m_I\rangle$ states are a good choice, as expressions for the matrix elements necessary for the calculation can be found. In particular, if we can determine the matrix elements with respect to the nuclear spin term of the Hamiltonian by considering the operator

$$\mathbf{I}\cdot\mathbf{J} = \mathbf{I}_z\mathbf{J}_z + \frac{1}{2}(\mathbf{I}_+\mathbf{J}_- + \mathbf{I}_-\mathbf{J}_+), \tag{A.12}$$

using

$$\langle I, m_I \pm 1|I_\pm|I, m_I\rangle = \sqrt{(I \mp m_I)(I \pm m_I + 1)}, \tag{A.13}$$

and writing down the non-zero matrix elements for the operator (A.12). The relevant matrix

[1] An analytic solution does exist for the $J = 1/2$ case, and is known as the Breit-Rabi formula. This is the description for the ground state hyperfine characteristics used in §4.6.1. In this Appendix, all values are calculated using the numerical method, though, of course, this gives the same results as the Breit-Rabi formula for $J = 1/2$.

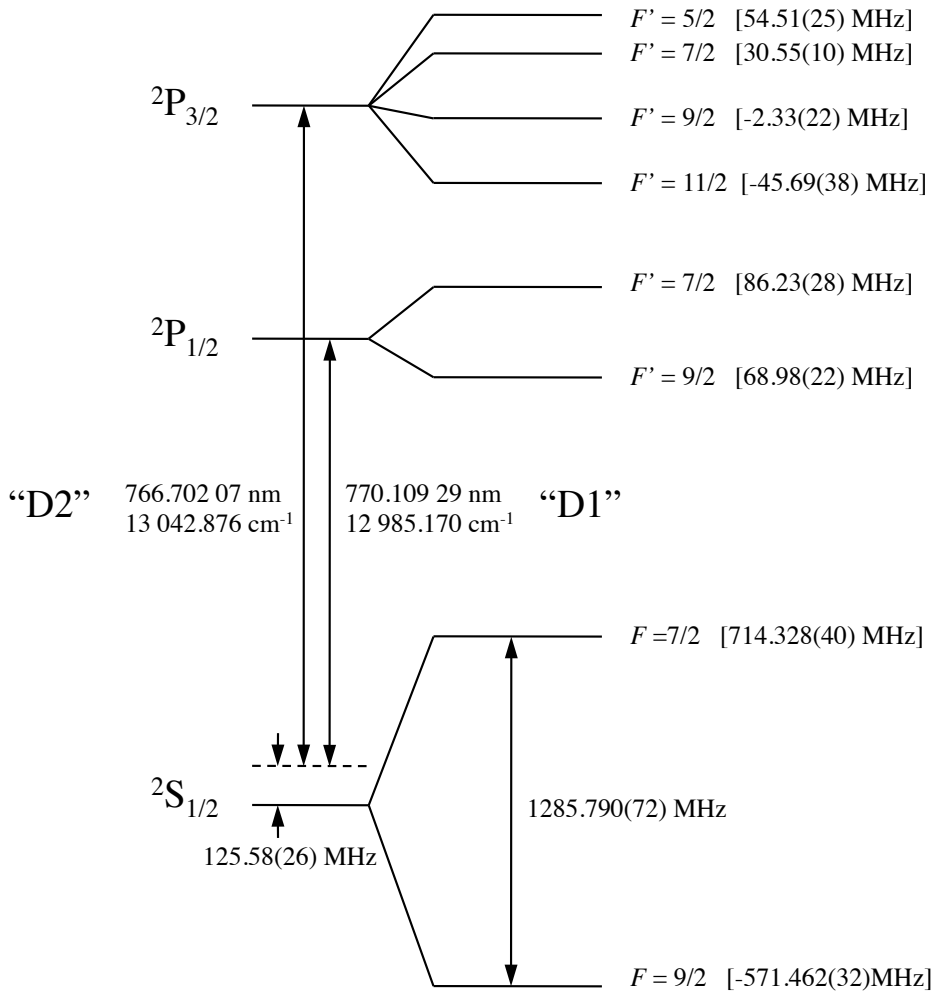

FIGURE A.1: Level diagram for ^{40}K; calculated at zero magnetic field. All values derived from constants in Table A.2.

elements can be expressed:

$$\begin{aligned}
\langle J, m_J, I, m_I | \mathbf{I}\cdot\mathbf{J} | J, m_J, I, m_I\rangle &= m_J m_I \\
\langle J, m_J, I, m_I | \mathbf{I}\cdot\mathbf{J} | J, m_J+1, I, m_I-1\rangle &= \frac{1}{2}\sqrt{(J+m_J)(J-m_J+1)} \\
&\quad \times \sqrt{(I-m_I)(I+m_I+1)} \\
\langle J, m_J, I, m_I | \mathbf{I}\cdot\mathbf{J} | J, m_J-1, I, m_I+1\rangle &= \frac{1}{2}\sqrt{(J-m_J)(J+m_J+1)} \\
&\quad \times \sqrt{(I+m_I)(I-m_I+1)}.
\end{aligned} \tag{A.14}$$

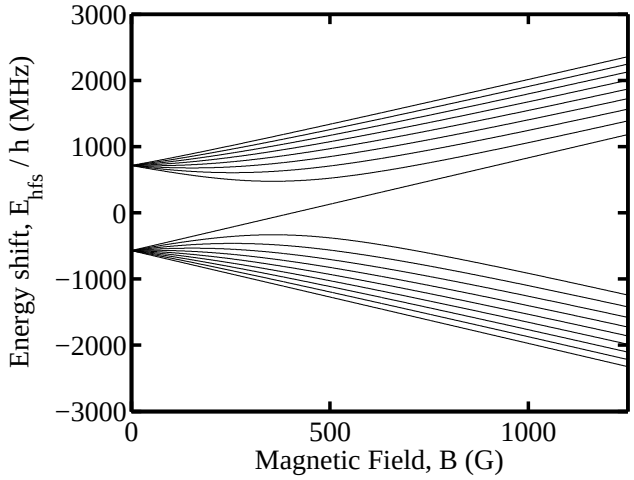

Figure A.2: Hyperfine energy shift for the ground state ($^2S_{1/2}$) of ^{40}K as a function of magnetic field. The highlighted curve is used in the calculation in §.

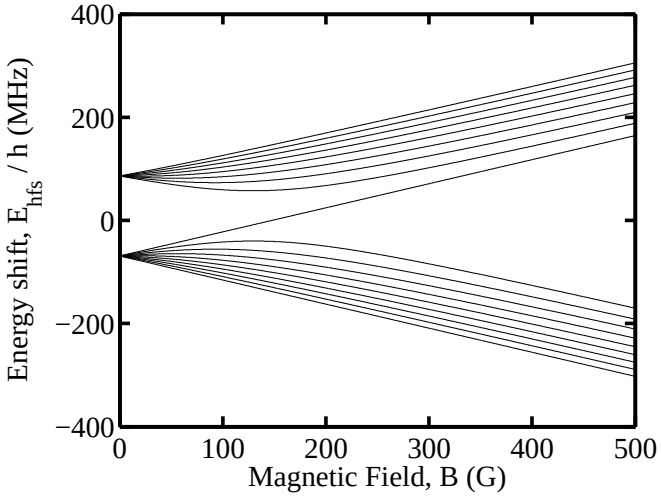

Figure A.3: Hyperfine energy shift for the D1 manifold ($^2P_{1/2}$) of ^{40}K as a function of magnetic field

Similarly, for the electric quadrupole term, it is useful to consider the operator

$$f = 3(\mathbf{I}\cdot\mathbf{J})^2 + \frac{3}{2}\mathbf{I}\cdot\mathbf{J} - \mathbf{I}^2\cdot\mathbf{J}^2 \tag{A.15}$$

and determine the matrix elements with respect to it. These can be found in Appendix C

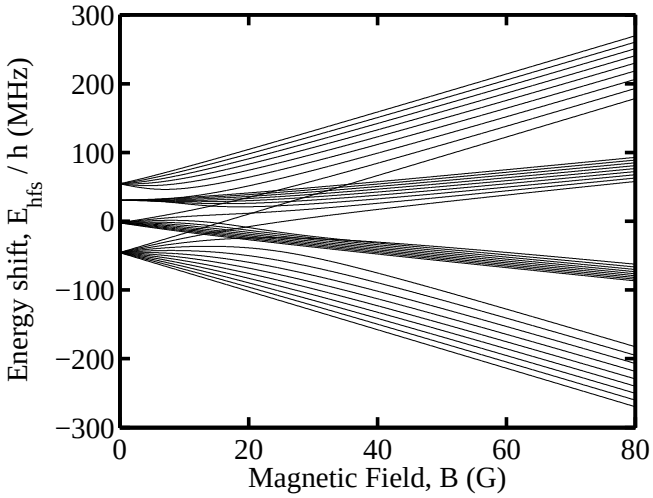

Figure A.4: Hyperfine energy shift for the D2 manifold ($^2P_{3/2}$) of ^{40}K as a function of magnetic field. The highlighted curve is used in the calculation in §.

of Ref. [185] are are expressed:

$$\langle m_J, m_I|f|m_J, m_I\rangle = \frac{1}{2}\left[3m_I^2 - I(I+1)\right]\left[3m_J^2 - J(J+1)\right]$$

$$\langle m_J, m_I|f|m_J-1, m_I+1\rangle = \frac{3}{4}(2m_J-1)(2m_I+1) \times \left[(J+m_J)(J-m_J+1)(I-m_I)(I+m_I+1)\right]^{\frac{1}{2}}$$

$$\langle m_J, m_I|f|m_J+1, m_I-1\rangle = \frac{3}{4}(2m_J+1)(2m_I-1) \times \left[(J-m_J)(J+m_J+1)(I+m_I)(I-m_I+1)\right]^{\frac{1}{2}}$$

$$\langle m_J, m_I|f|m_J-2, m_I+2\rangle = \frac{3}{4}\big[(J+m_J)(J+m_J+1)(J-m_J+1)(J-m_J+2) \times (I-m_I)(I-m_I-1)(I+m_I+1)(I+m_I+2)\big]^{\frac{1}{2}}$$

$$\langle m_J, m_I|f|m_J+2, m_I-2\rangle = \frac{3}{4}\big[(J-m_J)(J-m_J-1)(J+m_J+1)(J+m_J+2) \times (I+m_I)(I+m_I-1)(I-m_I+1)(I-m_I+2)\big]^{\frac{1}{2}} \quad \text{(A.16)}$$

Finally, the term involving the magnetic field is diagonal in the $|J, m_J, I, m_I\rangle$ basis, which makes the calculation of the relevant matrix elements relatively simple.

The actual calculation of the energies can be performed numerically, and was done using MATLAB. For each of the three manifolds considered, a vector containing each of the possible states was created, i.e. for the $^2\mathrm{S}_{1/2}$ (ground) state, there are 18 substates defined all possible combinations of m_J and m_I where $-\frac{1}{2} \leq m_J \leq \frac{1}{2}$ and $-4 \leq m_I \leq 4$. The Hamiltonian matrix is constructed by calculating each element individually. For example, if the state vector is defined as (using an $|m_J, m_I\rangle$ notation)

$$\Psi_{m_J,m_I} = \begin{bmatrix} |1/2,4\rangle \\ |1/2,3\rangle \\ |1/2,2\rangle \\ \vdots \end{bmatrix}$$

then we may define an 18×18 Hamiltonian matrix as

$$H_{\mathrm{hfs}} = \begin{bmatrix} \langle 1/2,4|H_{\mathrm{hfs}}|1/2,4\rangle & \langle 1/2,4|H_{\mathrm{hfs}}|1/2,3\rangle & \langle 1/2,4|H_{\mathrm{hfs}}|1/2,2\rangle \cdots \\ \langle 1/2,3|H_{\mathrm{hfs}}|1/2,4\rangle & \langle 1/2,3|H_{\mathrm{hfs}}|1/2,3\rangle & \langle 1/2,3|H_{\mathrm{hfs}}|1/2,2\rangle \cdots \\ \langle 1/2,2|H_{\mathrm{hfs}}|1/2,4\rangle & \langle 1/2,2|H_{\mathrm{hfs}}|1/2,3\rangle & \langle 1/2,2|H_{\mathrm{hfs}}|1/2,2\rangle \cdots \\ \vdots & \vdots & \vdots \quad \ddots \end{bmatrix}.$$

This matrix is then calculated for a value of magnetic field, B, and numerically diagonalised. The energy eigenvalues are stored, and this process is repeated for 10 000 small increments in magnetic field. By plotting the energy eigenvalues for all magnetic field values, we find that the low field eigenstates gradually merge into the high-field eigenstates. A schematic of the zero-field structure is shown in Fig. (A.1). The results of the full calculations, shown in Figs. (A.2), (A.3), and (A.4) for the ground ($^2\mathrm{S}_{1/2}$), D1 ($^2\mathrm{P}_{1/2}$), and D2 ($^2\mathrm{P}_{3/2}$) levels, demonstrate the gradual transformation from $|F, m_F\rangle$ states to the $|m_J, m_I\rangle$ states.

State selectivity

In the high field, the ground state splitting can be larger than the natural linewidth of a transition between the ground and excited states. This allows for the selective imaging of one ground state, since the other will be far off-resonance.

As a practical example, consider the the states that connect to low-field $|9/2, \text{-}9/2\rangle$ and $|9/2, \text{-}7/2\rangle$ states, which have a Feshbach resonance at 202.10 G. Assuming σ^- imaging on

the D_2 line, we consider the energetics of three transitions: (1) $|F = 9/2, m_F = -9/2\rangle \rightarrow |F = 9/2, m_F = -11/2\rangle$, and (2) $|F = 9/2, m_F = -9/2\rangle \rightarrow |F = 9/2, m_F = -11/2\rangle$.

The energetic difference between these transitions is shown in Fig. A.5. At 202.10 G, the difference in energy between transitions is $\Delta E = 2\pi \times 34$ MHz, which, with a linewidth of $\Gamma_{D2} = 2\pi \times 6.01$ MHz, are ensure that one can image on one transition while remaining several linewidths away from the other.

At this magnetic field, the ground states used in the Feshbach resonance are, written in terms of the $|m_I, m_J\rangle$ basis, can be found from the numerical diagonalization, and are ($|F, m_F\rangle \rightarrow |m_I, m_J\rangle$):

$$|9/2, -9/2\rangle \rightarrow |-4, -1/2\rangle \tag{A.17}$$

$$|9/2, -7/2\rangle \rightarrow -0.2359|-4, 1/2\rangle - 0.9718|-3, -1/2\rangle. \tag{A.18}$$

Likewise, for the excited states ($|F', m'_F\rangle \rightarrow |m'_I, m'_J\rangle$),

$$|11/2, -11/2\rangle \rightarrow |-4, -3/2\rangle \tag{A.19}$$

$$|11/2, -9/2\rangle \rightarrow -0.0485|-4, -1/2\rangle - 0.9988|-3, -3/2\rangle. \tag{A.20}$$

A.4 Transition matrix elements

The charged particles that make up an atom can be manipulated with electromagnetic fields. Light at optical frequencies strongly couples energy levels with adjacent values orbital angular momentum, L.

A.4.1 The reduced matrix element

When considering the interaction of atoms and electromagnetic fields, the electric dipole term is the largest perturbation to the atomic energy levels [190]. This operator, defined by

$$H_{E1} = \mathbf{d} \cdot \mathbf{E}(\mathbf{0}, \mathbf{t}) = -e\mathbf{r} \cdot \mathbf{E}(\mathbf{0}, \mathbf{t}) \tag{A.21}$$

where $\mathbf{E}(\mathbf{0}, \mathbf{t})$ is the time-dependent electric field at the origin, $\mathbf{r}$ is the position operator at the origin, and $\mathbf{d}$ is dipole operator, can be treated using time-dependent perturbation theory. Assuming that all transitions will be made with near-resonant light, the rotating

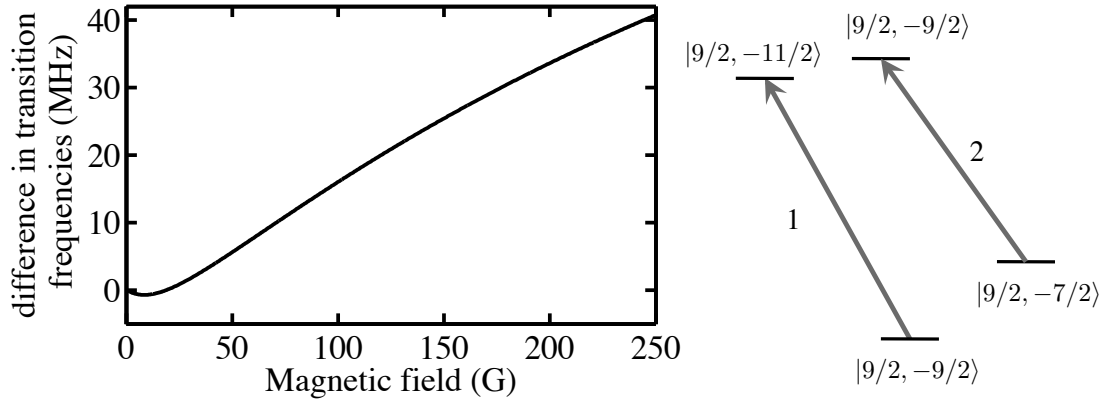

Figure A.5: State selectivity for imaging ^{40}K at various magnetic fields. The transitions considered are indicated to the right, for the D_2 transition. The differences in these transiton frequencies are plotted as a function of magnetic field: the solid line indicates the *difference* between the transitions $|F = 9/2, m_F = -9/2\rangle \rightarrow |F = 9/2, m_F = -11/2\rangle$ (1) and $|F = 9/2, m_F = -7/2\rangle \rightarrow |F = 9/2, m_F = -9/2\rangle$ (2). The natural linewidth of this transition is $\Gamma_{D2} = 2\pi \times 6.01$ MHz. Near the Feshbach resonance, the transitions are both well distinguished: at 202 G, the difference between (1) and (2) is 34 MHz.

wave approximation (RWA) is justified, and the dipole matrix elements can be expressed in terms of the dipole matrix elements, (see, for example, Ref. [191])

$$A_{if} = \frac{1}{\tau_{\text{life}}} = \frac{\omega_0^2 |\langle i|\mathbf{d}|f\rangle|^2}{3\pi\epsilon_0\hbar c^3}, \tag{A.22}$$

where τ_{life} is the radiative lifetime, ω_0 is the angular frequency of the electromagnetic field, i and f stand for the initial and final states, respectively, and A_{if} is the rate of decay between these states.

To evaluate the matrix element in Eq. A.22, we begin by expressing the dipole operator as

$$\mathbf{d} = -e \sum_{q=-1}^{1} r_q^{(1)} \mathbf{e}_q \tag{A.23}$$

where the e is the electric charge, $r_q^{(1)}$ are first-rank spherical tensors, and the $\mathbf{e}_q$ are the unit direction vectors for each $r_q^{(1)}$. Each of these vectors represents a specific polarization of the light field: $\mathbf{e}_{\pm 1}$ represent circularly polarized light ($\sigma^{\pm}$), while $\mathbf{e}_0$ is π-polarized; these vectors form a complete basis in polarization space. The dipole matrix element between an initial state (defined by the angular momentum P_i and projection m_i) and a final state

(with P_f and projection m_f) can be expressed using the Wigner-Eckart theorem[2]

$$\langle i|\mathbf{d}|f\rangle = (-1)^{2P_f - m_f + P_i + 1}\langle i||er^{(1)}||f\rangle \sum_q \begin{pmatrix} P_i & 1 & P_f \\ m_i & q & -m_f \end{pmatrix} \mathbf{e}_q \tag{A.24}$$

where $\langle i||er^{(1)}||f\rangle$ is the reduced matrix element, which is independent of $m_{i.f}$ and q and the term in round brackets is the Wigner 3-j symbol, which is related to the Clebsch-Gordan coefficient and provides the sum of the three angular momenta. The rate of this transition, from Eq. A.22 is

$$A_{if} = \frac{\omega_0^3}{3\pi\epsilon_0\hbar c^3}|\langle i||er^{(1)}||f\rangle|^2 \left[\sum_q \begin{pmatrix} P_i & 1 & P_f \\ m_i & q & -m_f \end{pmatrix}^2\right] \tag{A.25}$$

where the orthogonality of the $\mathbf{e}_q$ gives only the elements diagonal in q.

In general, the lifetime between specific initial and final states is not resolved; instead, a total decay from one excited level to the ground level, $A_{if}^{\text{tot}} = \sum_{m_i} A_{if}$ is measured. By summing A_{if} over all possible initial states,

$$\sum_{m_i} A_{if} = \frac{\omega_0^3}{3\pi\epsilon_0\hbar c^3}|\langle i||er^{(1)}||f\rangle|^2 \left[\sum_{q,m_i} \begin{pmatrix} P_i & 1 & P_f \\ m_i & q & -m_f \end{pmatrix}^2\right] = \frac{\omega_0^3}{3\pi\epsilon_0\hbar c^3}\frac{|\langle i||er^{(1)}||f\rangle|^2}{(2P_f+1)}, \tag{A.26}$$

where we have used the normalization condition for the 3-j symbols to obtain the $(2P_f+1)$ factor.

The reduced matrix element can be expressed in terms of $A_{if}^{\text{tot}} = 1/\tau_{\text{life}}^{\text{tot}}$,

$$|\langle i||er^{(1)}||f\rangle| = \left[\frac{3\pi\epsilon_0\hbar c^3(2P_f+1)A_{if}^{\text{tot}}}{\omega_0^3}\right]^{1/2} = \sqrt{2P_f+1}\;\mu_{if} \tag{A.27}$$

where μ_{if} is the dipole matrix element described for a two-level system. Using this expression with Eq. A.24, the amplitude of any transition can be expressed in terms of the reduced matrix element and a 3-j symbol. Using the lifetimes for transitions between J manifolds, the $|\langle J||er^{(1)}||J'\rangle|$ can be found, and are shown in Table A.3.

A.4.2 Reducing the dipole operator

In small magnetic fields, where many atomic physics experiments are performed, the eigenstates $|F, m_F\rangle$ are good. To express the dipole matrix elements between states in this basis, Eq. (A.24) is used

$$\langle F, m_F|er_q^{(1)}|F', m_F'\rangle = (-1)^{2F' - m_F + F + 1}\langle F||er_q^{(1)}||F'\rangle \begin{pmatrix} F & 1 & F' \\ m_F & q & -m_F' \end{pmatrix}. \tag{A.28}$$

[2]All sign and normalization conventions follow Ref. [192], which are also followed by Mathematica.

	D1 ($^2P_{1/2}$)	D2 ($^2P_{3/2}$)	Ref.
$\tau_{\text{life}}^{\text{tot}}$	26.79(7) ns	26.45(7) ns	[193]
$\langle J\|\|er^{(1)}\|\|J'\rangle$	4.102(5) $e \cdot a_0$	5.811(7) $e \cdot a_0$	-
$\mu_{J,J'}$	2.906(4) $e \cdot a_0$	2.901(4) $e \cdot a_0$	-

Table A.3: Lifetimes of D1 and D2 levels and associated reduced matrix elements for ^{40}K, where e is the elementary charge and a_0 is the Bohr radius.

The selection rules in the low-field regime dictate $\Delta F = 0, \pm 1$, $\Delta M_F = 0, \pm 1$, and $F = 0 \rightarrow F' = 0$ transitions are not allowed [194]. The reduced matrix element in this basis is not directly accessible. To connect this basis to the J basis, in which the reduced matrix element is known, we consider the addition of angular momenta defining the states in the F basis. Since $\mathbf{F} = \mathbf{I} + \mathbf{J}$, we can use the Wigner 6-j symbols to write $\langle F||er_q^{(1)}||F'\rangle$ in terms of $\langle J||er_q^{(1)}||J'\rangle$ [192]. The reduced matrix elements is found to be

$$\langle F||er^{(1)}||F'\rangle = (-1)^{F'+I+J+1}\sqrt{(2F+1)(2F'+1)}\begin{Bmatrix} J' & J & 1 \\ F & F' & I \end{Bmatrix}\langle J||er_q^{(1)}||J'\rangle \tag{A.29}$$

where the term in the curly brackets is the 6-j symbol.

To determine the overall transition matrix element for the $|F, m_F\rangle$ states, we substitute Eq. (A.29) into Eq. (A.28) and by collect all coefficients (including 3-j and 6-j symbols) into one, to obtain the expressions, using two different conventions

$$\langle F, m_F|er_q^{(1)}|F', m_F'\rangle = C_1(J, J\prime, F, m_F, F', m_F', q)\ \langle J'||er^{(1)}||J\rangle \tag{A.30}$$

$$= C_2(J, J\prime, F, m_F, F', m_F', q)\ \mu_{J,J'} \tag{A.31}$$

where $\mu_{J,J'} = C_1(J, J\prime, F, m_F, F', m_F', q)/\sqrt{2J'+1}$ and the coefficients are

$$C_1(J, J', F, m_F, F', m_F', q) = (-1)^{3F'+J+F}\sqrt{(2F+1)(2F'+1)}\begin{Bmatrix} J' & J & 1 \\ F & F' & I \end{Bmatrix}\begin{pmatrix} F & 1 & F' \\ m_F & q & -m_F' \end{pmatrix} \tag{A.32}$$

$$C_2(J, J', F, m_F, F', m_F', q) = \sqrt{(2J'+1)}\ C_1(J, J', F, m_F, F', m_F') \tag{A.33}$$

depending on total angular momentum, F, hyperfine substate, m_F, total orbital angular momentum, J, and the polarization of the excitation, q. These coefficients were calculated with the help of Mathematica with the functions "ThreeJSymbol" and "SixJSymbol." The coefficients C_2 are calculated in Mathematica using

```
C2[F_, mF_, Fp_, mFp_, J_, Jp_,q_] :=
```

```
(-1)^(3 Fp + J + F - mFp) Sqrt[(2 Jp + 1) (2 F + 1) (2 Fp + 1)]
ThreeJSymbol[{F, mF}, {1, q}, {Fp , -mFp}]
SixJSymbol[{J, 1 , Jp}, {Fp, 4, F}];
```

where the variables with "p" stand for the primed equivalents. These coefficients are listed for the $F = 9/2 \rightarrow J' = 3/2$ transition (D_2 line) in Table A.4.; the remaining three transitions can be calculated in a similar fashion.

A.4.3 High-field transition matrix elements

In strong magnetic fields, the states defined by quantum numbers $|J, m_J, I, m_I\rangle$ are good eigenstates, as was seen in earlier discussion. The selection rules are $\Delta J = 0, \pm 1$, $\Delta L = \pm 1$, $\Delta m_J = 0, \pm 1$ and $\Delta m_I = 0$ [194]. We can see this by writing the Wigner-Eckhart equation for these states, Eq. (A.24)

$$\langle J, m_J, I, m_I | er_q^{(1)} | J', m'_J, I, m'_I \rangle = (-1)^{2J' - m_J + J + 1} \langle J || er_q^{(1)} || J' \rangle \begin{pmatrix} J & 1 & J' \\ m_J & q & -m'_J \end{pmatrix} \langle I, m_I | I', m'_I \rangle \tag{A.34}$$

where the final matrix element enforces the selection rule $m_I = m'_I$, since the nuclear part is unaffected by the dipole field. The 3-j coefficients give the m_J selection rule.

	m_F	9/2	7/2	5/2	3/2	1/2	-1/2	-3/2	-ha5	-7/2	-9/2
σ^+	$F'=7/2$	1	$\frac{3}{\sqrt{11}}$	$\frac{6}{\sqrt{55}}$	$\frac{2\sqrt{7}}{\sqrt{55}}$	$\frac{\sqrt{21}}{\sqrt{55}}$	$\frac{\sqrt{3}}{\sqrt{11}}$	$\frac{\sqrt{2}}{\sqrt{11}}$	$\frac{\sqrt{6}}{\sqrt{55}}$	$\frac{3}{\sqrt{55}}$	$\frac{1}{\sqrt{55}}$
	$F'=9/2$	0	$-\frac{4\sqrt{2}}{3\sqrt{33}}$	$-\frac{16\sqrt{2}}{9\sqrt{33}}$	$-\frac{4\sqrt{14}}{9\sqrt{11}}$	$-\frac{16}{9\sqrt{11}}$	$-\frac{20\sqrt{2}}{9\sqrt{11}}$	$-\frac{16}{9\sqrt{11}}$	$-\frac{4\sqrt{14}}{9\sqrt{11}}$	$-\frac{16\sqrt{2}}{9\sqrt{33}}$	$-\frac{4\sqrt{2}}{3\sqrt{33}}$
	$F'=9/2$	0	0	$\frac{\sqrt{7}}{9\sqrt{15}}$	$\frac{\sqrt{7}}{9\sqrt{5}}$	$\frac{\sqrt{14}}{9\sqrt{5}}$	$\frac{\sqrt{14}}{9\sqrt{3}}$	$\frac{\sqrt{7}}{9}$	$\frac{7}{9\sqrt{5}}$	$\frac{14}{9\sqrt{15}}$	$\frac{2\sqrt{7}}{3\sqrt{15}}$
π	$F'=11/2$	$\frac{\sqrt{2}}{\sqrt{11}}$	$-\frac{3\sqrt{2}}{\sqrt{55}}$	$-\frac{2\sqrt{6}}{\sqrt{55}}$	$-\frac{2\sqrt{7}}{\sqrt{55}}$	$-\frac{\sqrt{6}}{\sqrt{11}}$	$-\frac{\sqrt{6}}{\sqrt{11}}$	$-\frac{2\sqrt{7}}{\sqrt{55}}$	$-\frac{2\sqrt{6}}{\sqrt{55}}$	$-\frac{3\sqrt{2}}{\sqrt{55}}$	$\frac{\sqrt{2}}{\sqrt{11}}$
	$F'=9/2$	$\frac{4}{\sqrt{33}}$	$\frac{28}{9\sqrt{33}}$	$\frac{20}{9\sqrt{33}}$	$\frac{4}{3\sqrt{33}}$	$\frac{4}{9\sqrt{33}}$	$-\frac{4}{9\sqrt{33}}$	$-\frac{4}{3\sqrt{33}}$	$-\frac{20}{9\sqrt{33}}$	$-\frac{28}{9\sqrt{33}}$	$-\frac{4}{\sqrt{33}}$
	$F'=7/2$	0	$-\frac{2\sqrt{14}}{9\sqrt{15}}$	$-\frac{7\sqrt{2}}{9\sqrt{15}}$	$-\frac{\sqrt{14}}{3\sqrt{15}}$	$-\frac{2\sqrt{7}}{9\sqrt{3}}$	$-\frac{2\sqrt{7}}{9\sqrt{3}}$	$-\frac{\sqrt{14}}{3\sqrt{15}}$	$-\frac{7\sqrt{2}}{9\sqrt{15}}$	$-\frac{2\sqrt{14}}{9\sqrt{15}}$	0
σ^-	$F'=11/2$	$-\frac{\sqrt{1}}{\sqrt{55}}$	$-\frac{\sqrt{3}}{\sqrt{55}}$	$-\frac{\sqrt{6}}{\sqrt{55}}$	$-\frac{\sqrt{2}}{\sqrt{11}}$	$-\frac{\sqrt{3}}{\sqrt{11}}$	$-\frac{\sqrt{21}}{\sqrt{55}}$	$-\frac{2\sqrt{7}}{\sqrt{55}}$	$-\frac{\sqrt{6}}{\sqrt{55}}$	$-\frac{3}{\sqrt{11}}$	1
	$F'=9/2$	$\frac{4\sqrt{2}}{3\sqrt{33}}$	$\frac{16\sqrt{2}}{9\sqrt{33}}$	$\frac{4\sqrt{14}}{9\sqrt{11}}$	$\frac{16}{9\sqrt{11}}$	$\frac{20\sqrt{2}}{9\sqrt{33}}$	$\frac{16}{9\sqrt{11}}$	$\frac{4\sqrt{14}}{9\sqrt{11}}$	$\frac{16\sqrt{2}}{9\sqrt{33}}$	$\frac{4\sqrt{2}}{3\sqrt{33}}$	0
	$F'=7/2$	$\frac{2\sqrt{7}}{3\sqrt{15}}$	$\frac{14}{9\sqrt{15}}$	$\frac{7}{9\sqrt{5}}$	$\frac{\sqrt{7}}{\sqrt{9}}$	$\frac{\sqrt{14}}{9\sqrt{3}}$	$\frac{\sqrt{14}}{9\sqrt{5}}$	$\frac{\sqrt{7}}{9\sqrt{5}}$	$\frac{\sqrt{7}}{9\sqrt{15}}$	0	0

Table A.4: Coefficients $(J, J\prime, F, m_F, F', m'_F)$ for hyperfine dipole matrix elements for EM transitions to the D_2 ($^2P_{3/2}$) manifold for $|F = {}^9/_2, m_F\rangle \rightarrow |F', m'_F\rangle$, where $m'_F = m_F + 1$ for σ^+, $m'_F = m_F$ for π, and $m'_F = m_F - 1$ for σ^-.

Appendix B

Intensity dependence of optical density

B.1 Optical density for resonant light: calculations

B.1.1 Atoms at rest

To obtain quantitative results from absorption imaging, we measure the amount and spatial distribution of light scattered from an incoming near-resonant beam. We compare the intensity for beams with and without atoms and define the quantity, "optical density" (OD) for a beam travelling in the r_3 direction

$$\mathrm{OD}(r_1, r_2) = -\ln\left(\frac{I(r_1, r_2)}{I_0(r_1, r_2)}\right), \tag{B.1}$$

where $I_0(r_1, r_2)$ is the intensity of the incident beam recorded when no atoms are present, and $I(r_1, r_2)$ is the intensity measured after the light has been scattered by the atoms.

The rate at which the atoms scatter light from the incoming beam depends on the natural linewidth and the excited state fraction, which can be expressed as

$$\gamma_{\mathrm{sc}} = \frac{\Gamma}{2}\,\frac{I/I_{\mathrm{sat}}}{1 + I/I_{\mathrm{sat}}}, \tag{B.2}$$

where I is the intensity of the incoming light, $I_{\mathrm{sat}} = \pi h c \Gamma / 3\lambda^3$ is the saturation intensity, λ is the resonant wavelength and Γ is the natural linewidth of the transition.

As a beam travels in the r_3 direction, the loss in its intensity as a function of distance is equivalent to the power scattered from the beam, given by

$$\frac{\mathrm{d}I}{\mathrm{d}r_3} = \hbar\omega_L \gamma_{\mathrm{sc}} \rho = -\sigma_{\mathrm{sc}}\ \rho \left(\frac{I}{1 + I/I_{\mathrm{sat}}}\right), \tag{B.3}$$

where ω_L is the transition frequency of the transition used for imaging, ρ is the density of the atoms, and $\sigma_{\rm sc} = 3\lambda^2/2\pi$ is the resonant scattering cross section. Integrating this equation we find the implicit expression for I (because $\mathrm{OD}(r_1, r_2)$ depends on I and I_0)

$$\mathrm{OD}(r_1, r_2) = \mathrm{OD}_0(r_1, r_2) + \frac{I(r_1, r_2) - I_0(r_1, r_2)}{I_{\rm sat}}, \tag{B.4}$$

where $\mathrm{OD}_0(r_1, r_2) = -\sigma_{\rm sc} \int \rho(r_1, r_2, r_3)\, \mathrm{d}r_3$ is the zero-intensity limit of the OD. When the absorption is small, $|I - I_0| \ll I_{\rm sat}$ and the second term can be neglected. The lines in Figs B.1 (a,b) show the solutions to this equation for three values of OD_0.

B.1.2 Recoil-induced Doppler shift

A second consideration in quantifying the optical density is the recoil of the atoms caused by the absorption and reemission of photons in the imaging process. The Doppler shift associated with this motion will put the atoms out of resonance, modifying the absorption characteristics. If we assume that the atom's velocity increases, on average, by one recoil velocity, v_r, every scattering lifetime, $1/\gamma_{\rm sc}$, then the velocity as a function of time is $v(t) = v_r \gamma_{sc} t$. The Doppler shift from the resonance frequency is $\omega_D(t) = kv(t)$, where k is the wavevector of the incident light. Assuming that laser is set to being on resonance, $\omega_D(t)$ is the time-dependent detuning for these recoiling atoms. The Doppler-modified, time-dependent scattering rate is

$$\gamma_{\rm sc,D}(t) = \frac{\Gamma}{2} \frac{I/I_{\rm sat}}{1 + I/I_{\rm sat} + \left[\frac{2\pi}{\lambda} \frac{I/I_{\rm sat}}{(1+I/I_{\rm sat})} v_r t\right]^2}. \tag{B.5}$$

Using the same method of integrating the expression for the scattered power Eq. B.3, this time replacing $\gamma_{\rm sc}$ by $\gamma_{\rm sc,D}$, we come to

$$\mathrm{OD}(t) = \mathrm{OD}_0 + \frac{I - I_0}{I_{\rm sat}} + (kv_r t)^2 \left[\frac{I_{\rm sat}}{I + I_{\rm sat}} - \frac{I_{\rm sat}}{I_0 + I_{\rm sat}} + \ln\left(\frac{I + I_{\rm sat}}{I_0 + I_{\rm sat}}\right)\right] \tag{B.6}$$

where, for clarity, we suppress the (r_1, r_2) dependence of I and I_0. Taking the time average of this expression, $\langle \mathrm{OD} \rangle = \frac{1}{t_{\rm tot}} \int_{t_{\rm tot}} \mathrm{OD}\, \mathrm{d}t$, where $t_{\rm tot}$ is the total imaging time,

$$\langle \mathrm{OD} \rangle = \mathrm{OD}_0 + \frac{I - I_0}{I_{\rm sat}} + \frac{(kv_r t_{\rm tot})^2}{3} \left[\frac{I_{\rm sat}}{I + I_{\rm sat}} - \frac{I_{\rm sat}}{I_0 + I_{\rm sat}} + \ln\left(\frac{I + I_{\rm sat}}{I_0 + I_{\rm sat}}\right)\right]. \tag{B.7}$$

The lines in Figs. B.1(c,d) show the solutions to this equation for three OD_0.

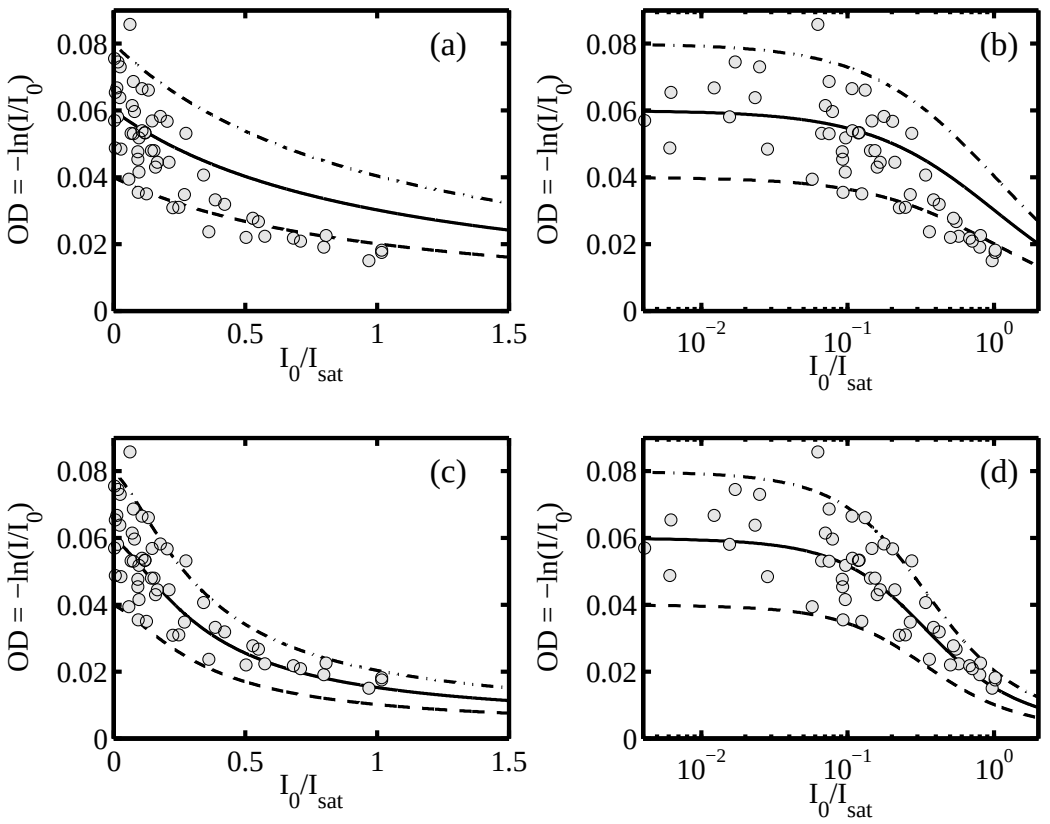

Figure B.1: Optical density intensity dependence. Measured optical density OD vs. normalized intensity, $I_0/I_{\rm sat}$. Data is identical in all plots, theory lines neglect Doppler shift, as in from Eq. for (a) and (b); theory lines include Doppler shift for (c) and (d). Theory lines are for $\mathrm{OD}_0 = 0.08$ (dash-dot), 0.06 (solid) and 0.04 (dashed). Left plots are on a linear scale, right plots have a logarithmic $I_0/I_{\rm sat}$ scale.

B.2 Optical density measurements

We measured the intensity dependence of the optical density by taking repeated images of an ultracold cloud of ^{87}Rb atoms. We assume that all clouds are prepared with the same density characteristics, and thus a constant OD_0. We use $t_{\rm tot} = 100$ µs pulses, vary the incident intensity I_0, and measure OD as a function of I_0. The results are plotted with the curves that both neglect (Figs. B.1(a,b)) and include (Figs. B.1(c,d)) the Doppler shift. We see the data clearly requires the consideration of the Doppler shift to account for the reduction in OD observed as a function of intensity.

To avoid the effects of the Doppler shift, we perform all of our experiments in the

small I_0/I_{sat} regime, specifically, $I_0/I_{\text{sat}} \approx 0.1$, which as can be seen in the logarithmic plot Fig. B.1(d), the point after which the intensity dependence of the imaging becomes important.

Appendix C

Atom number calibration

It is often important to know as precisely as possible the number of atoms in various experiments. While the use of absorption imaging on the cycling transition *should* properly account for the number, magnetic fields may slightly point in the wrong direction, and the polarization of the imaging light may be imperfect. To calibrate the atom number, we use the transition point for BEC and its dependence upon N. Both temperature and this transition point can be determined with better accuracy than N.

C.1 Condensate fraction measurements

As part of the method to calibrate the atom number, we must determine the condensate fraction as a function of temperature, in order to find the temperature at which the condensate appears. In a partially condensed cloud, there is both a thermal and condensate component. Because the condensate occupies only the ground state, its momentum distribution is much narrower than that of the thermal cloud, which occupies many higher momentum states.

We prepare ^{87}Rb BECs in a well defined trapping potential, and measure their momentum distributions by turning off the potential and observing the expanding cloud after some time of flight. The momentum distribution is bimodal – there is a broad thermal distribution with a narrow peak in the centre corresponding to the BEC. Two pieces of information are available from this measurement: the number of atoms in each component, and the temperature of the thermal cloud.

To analyze the data, we fit a Bose-Einstein distribution function to the thermal wings

of the momentum distribution. The optical density distribution gives yields the two-dimensional integrated-density profile, $\mathrm{OD} = -\ln(I/I_0) = \sigma_{\mathrm{res}} \int \rho(\mathbf{r})\, \mathrm{d}r_3$, where σ_{res} is the scattering cross-section. Figure C.1(a) shows an optical density profile for a cloud of ^{87}Rb after 8 ms time of flight. The bimodal structure is evident in the left image. To analyze the thermal part of the distribution, the central region, containing the information about the condensate, is masked out, as in the right image.

A two-dimenstional function describing the thermal Bose cloud is fit to thermal part of the OD distribution, the fitting function for which is

$$\mathrm{OD}_{\mathrm{th}}(r_1, r_2) = \mathrm{OD}_{\mathrm{th}}^{\mathrm{pk}} \times g_2 \left(\mathsf{z} \exp\left(-\frac{(r_1 - r_{2,c})^2}{2\sigma_1^2} - \frac{(r_2 - r_{2,c})^2}{2\sigma_2^2} \right) \right) + m_1 r_1 + m_2 r_2 + \mathrm{OD}_{\mathrm{bkgd}} \tag{C.1}$$

where $\mathrm{OD}_{\mathrm{th}}^{\mathrm{pk}} \times g_2(\mathsf{z})$ is the peak OD, $\mathsf{z} = \exp(\mu/k_{\mathrm{B}}T)$ is the fugacity, $(r_{1,c}, r_{2,c})$ is the centre of the cloud, (m_1, m_2) account for any slope in the background, and $\mathrm{OD}_{\mathrm{bkgd}}$ is the background OD value. The function, g_2 is the Bose-Einstein function, which we approximate near the transition point as

$$g_2(\mathsf{z}) = (1 - \mathsf{z}) \log(1 - \mathsf{z}) + 1.98\mathsf{z} - 0.16\mathsf{z}^2 - 0.17\mathsf{z}^3. \tag{C.2}$$

Profiles of this two-dimensional fit are shown in Figs. C.1(b) and (c), where the image and fits have been summed along the perpendicular direction. The red curves show the function $\mathrm{OD}_{\mathrm{th}}(r_1, r_2)$, while the blue fit is to the entire bimodal distribution. The area under the red curves indicate the thermal atom number and their widths give the temperature.

The temperature of the cloud can be determined from the widths as $k_B T_i = m\omega_i^2 \sigma_i^2/(1 + \omega_i^2 t^2)$, where ω_i is the trapping frequency in the $\hat{r}_i$ direction. The number of thermal atoms can be found by integrating over the part of the $\mathrm{OD}_{\mathrm{th}}$ distribution that is due to the atomic signal

$$N_{\mathrm{th}} = \frac{1}{\sigma_{\mathrm{res}}} \int\int \mathrm{d}r_1\, \mathrm{d}r_2\ \mathrm{OD}_{\mathrm{th}}^{\mathrm{pk}} \times g_2 \left(\mathsf{z} \exp\left(-\frac{(r_1 - r_{2,c})^2}{2\sigma_1^2} - \frac{(r_2 - r_{2,c})^2}{2\sigma_2^2} \right) \right). \tag{C.3}$$

The total atom number, N, is obtained by numerically integrating over the entire OD profile, after subtracting from the data the background slopes and offset from the fit. Using this, the condensate fraction N_C/N and temperature are both available.

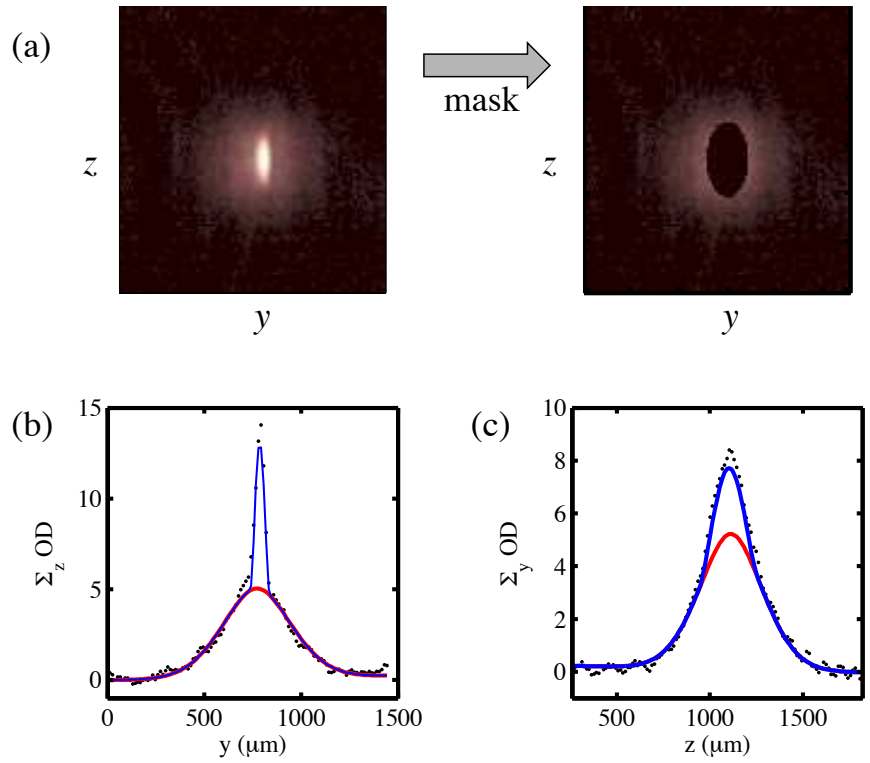

Figure C.1: Condensate fraction measurement.

C.2 Finding the transition temperature

To determine the transition temperature to BEC, we make BECs at a number of temperatures above and below the transition point, which we can find roughly by looking for the visual onset of bimodality in the cloud. The condensate fraction N_C/N, temperature, T, and total number N are extracted from each image as described above. Figure C.2 (top panel) shows the condensate fraction as a function of temperature. The bottom panel shows the total number of atoms at each temperature point, corresponding to the above data.

We determine the condensation temperature by finding the onset of BEC using the intersection of two linear fits near the transition. Taking into account both finite-size and interaction effects [195], the condensate temperature, T_C for a gas of bosons in a harmonic

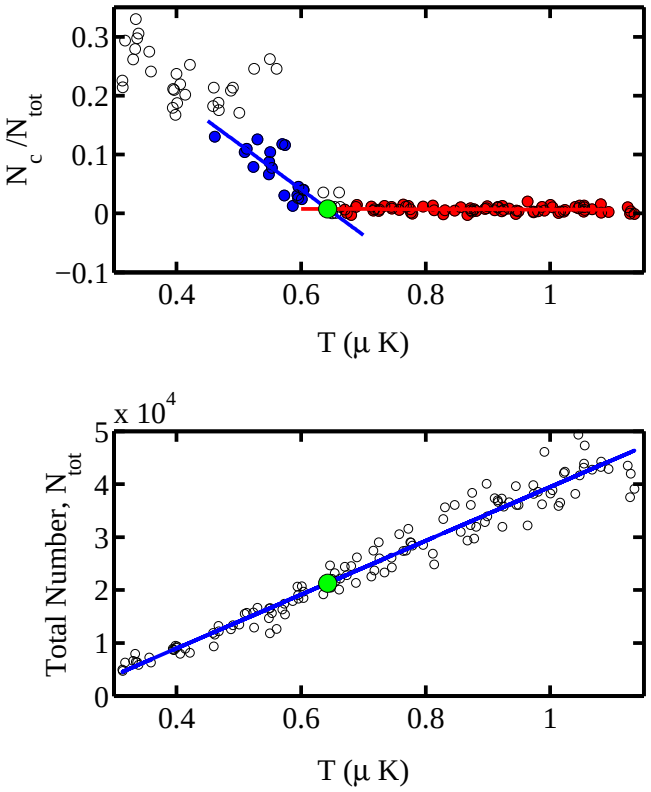

FIGURE C.2: Number calibration using BEC transition temperature. Top: Condensate fraction vs. temperature. Linear fits to the coloured points (red above T_C, blue below) cross at T_C. Large green point indicates the location of the crossing of the fits, $T_C = 640 \pm 40$ nK. Bottom: Atom number as a function of temperature (due to evaporation). Large green point indicates T_C, where $N = 21000 \pm 3000$ atoms.

trap is

$$T_C = T_C^0 \left(1 - 1.326 \frac{a}{a_{HO}} N^{1/6}\right) - 0.6842 \frac{\hbar \omega_{ar}}{k_B} \tag{C.4}$$

$$T_C^0 = \frac{\hbar \bar{\omega}}{k_B} \left(\frac{N}{\zeta(3)}\right)^{1/3}, \tag{C.5}$$

where T_C^0 is the critical temperature in the ideal case, $\bar{\omega}$ is the geometric mean of the trap frequencies and $\omega_{ar} = (\omega_x + \omega_y + \omega_z)/3$ is the arithmetic mean, k_B is Boltzmann's constant, $\zeta(n)$ is the Riemann-zeta function, a is the s-wave scattering length, $a_{HO} = (\hbar/m\bar{\omega})^{1/2}$ is the harmonic oscillator length of the trap, and N is the number of atoms.

Given this relationship between temperature and number, we translate the measured condensation temperature ($T_C = 640 \pm 40$ nK) into a corresponding atom number and compare that to the one measured (in the bottom panel). Propagating these numbers and their uncertainties, we arrive at a calibration factor $N_{actual} = N_{measured} \times (1.3 \pm 0.3)$, which accounts for the systematic uncertainty in our atom number, which is, for example, $N = 6600 \pm 1700$ in §5.4.

Bibliography

[1] J. P. Gordon and A. Ashkin, *Motion of atoms in a radiation trap*, Phys. Rev. A **21**, 1606 (1980). vii, 26

[2] F. Gerbier and Y. Castin, *Heating rates for an atom in a far-detuned optical lattice*, arxiv:1002:5018 (2010). vii, 26, 40

[3] E. L. Raab, M. Prentiss, A. Cable, S. Chu, and D. E. Pritchard, *Trapping of Neutral Sodium Atoms with Radiation Pressure*, Phys. Rev. Lett. **59**, 2631 (1987). 1

[4] N. Masuhara, J. M. Doyle, J. C. Sandberg, D. Kleppner, T. J. Greytak, H. F. Hess, and G. P. Kochanski, *Evaporative Cooling of Spin-Polarized Atomic Hydrogen*, Phys. Rev. Lett. **61**, 935 (1988). 1

[5] M. H. Anderson, J. R. Ensher, M. R. Matthews, C. E. Wieman, and E. A. Cornell, *Observation of Bose-Einstein Condensation in a Dilute Atomic Vapor*, Science **269**, 198 (1995). 1

[6] B. DeMarco and D. S. Jin, *Onset of Fermi Degeneracy in a Trapped Atomic Gas*, Science **285**, 1703 (1999). 1, 41

[7] M. Greiner, O. Mandel, T. Esslinger, T. Hansch, and I. Bloch, *Quantum phase transition from a superfluid to a Mott insulator in a gas of ultracold atoms*, Nature **415**, 39 (2002). 2, 23, 37

[8] T. Kinoshita, T. Wenger, and D. S. Weiss, *Observation of a One-Dimensional Tonks-Girardeau Gas*, Science **305**, 1125 (2004). 2

[9] C. A. Regal, M. Greiner, and D. S. Jin, *Observation of Resonance Condensation of Fermionic Atom Pairs*, Phys. Rev. Lett. **92**, 040403 (2004). 2, 79

[10] M. W. Zwierlein, J. R. Abo-Shaeer, A. Schirotzek, C. H. Schunck, and W. Ketterle, *Vortices and superfluidity in a strongly interacting Fermi gas*, Nature **435**, 1047 (2005). 2, 41

[11] J. Billy, V. Josse, Z. Zuo, A. Bernard, B. Hambrecht, P. Lugan, D. Clement, L. Sanchez-Palencia, P. Bouyer, and A. Aspect, *Direct observation of Anderson localization of matter waves in a controlled disorder*, Nature **453**, 891 (2008). 2

[12] R. Feynman, *Simulating physics with computers*, Int. J. Th. Phys. **21**, 467 (1982). 3

[13] W. Hofstetter, J. I. Cirac, P. Zoller, E. Demler, and M. D. Lukin, *High-Temperature Superfluidity of Fermionic Atoms in Optical Lattices*, Phys. Rev. Lett. **89**, 220407 (2002). 3, 23, 135

[14] A. V. Gorshkov, M. Hermele, V. Gurarie, C. Xu, P. S. Julienne, J. Ye, P. Zoller, E. Demler, M. D. Lukin, and A. M. Rey, *Two-orbital SU(N) magnetism with ultracold alkaline-earth atoms*, Nat Phys **6**, 289 (2010). 3

[15] M. H. T. Extavour, Ph.D. thesis, University of Toronto, 2009. 5, 6, 14, 18, 20, 82, 109, 126, 131

[16] S. Aubin *et al.*, *Trapping Fermionic* ^{40}K *and Bosonic* ^{87}Rb *on a Chip*, J. Low Temp. Phys. **140**, 377 (2005). 6

[17] S. Aubin, S. Myrskog, M. Extavour, L. LeBlanc, D. McKay, A. Stummer, and J. Thywissen, *Rapid sympathetic cooling to Fermi degeneracy on a chip*, Nat. Phys. **2**, 384 (2006). 6, 24

[18] M. H. T. Extavour, L. J. LeBlanc, T. Schumm, B. Cieslak, S. Myrskog, A. Stummer, S. Aubin, and J. H. Thywissen, *Dual-species quantum degeneracy of* ^{40}K *and* ^{87}Rb *on an atom chip*, At. Phys. **20**, 241 (2006). 6, 23

[19] R. Grimm, M. Weidemller, and Y. B. Ovchinnikov, *Optical dipole traps for neutral atoms*, Adv. At., Mol., Opt. Phys. **42**, 95 (2000). 9, 10, 25

[20] C. Chin, R. Grimm, P. Julienne, and E. Tiesinga, *Feshbach resonances in ultracold gases*, Rev. Mod. Phys. **82**, 1225 (2010). 9

[21] Y. Colombe, E. Knyazchyan, O. Morizot, B. Mercier, V. Lorent, and H. Perrin, *Ultracold atoms confined in rf-induced two-dimensional trapping potentials*, Europhys. Lett. **67**, 593 (2004). 13

[22] M. White, H. Gao, M. Pasienski, and B. DeMarco, *Bose-Einstein condensates in rf-dressed adiabatic potentials*, Phys. Rev. A **74**, 023616 (2006). 13

[23] T. Schumm, S. Hofferberth, L. Andersson, S. Wildermuth, S. Groth, I. Bar-Joseph, J. Schmiedmayer, and P. Kruger, *Matter-wave interferometry in a double well on an atom chip*, Nature Phys. **1**, 57 (2005). 13, 90, 132, 135, 136

[24] I. Lesanovsky, T. Schumm, S. Hofferberth, L. M. Andersson, P. Krüger, and J. Schmiedmayer, *Adiabatic radio-frequency potentials for the coherent manipulation of matter waves*, Phys. Rev. A **73**, 033619 (2006). 13, 15

[25] S. Hofferberth, B. Fischer, T. Schumm, J. Schmiedmayer, and I. Lesanovsky, *Ultracold atoms in radio-frequency dressed potentials beyond the rotating-wave approximation*, Phys. Rev. A **76**, 013401 (2007). 13, 17

[26] W. Ketterle, D. S. Durfee, and D. M. Stamper-Kurn, *Making, probing and understanding Bose-Einstein condensates*edited by M. Inguscio, S. Stringari, and C.E. Wieman (IOS Press, Amsterdam, 1999), Vol. 140, pp. 67–176. 15

[27] T. Ido and H. Katori, *Recoil-Free Spectroscopy of Neutral Sr Atoms in the Lamb-Dicke Regime*, Phys. Rev. Lett. **91**, 053001 (2003). 22

[28] O. Mandel, M. Greiner, A. Widera, T. Rom, T. W. Hänsch, and I. Bloch, *Coherent Transport of Neutral Atoms in Spin-Dependent Optical Lattice Potentials*, Phys. Rev. Lett. **91**, 010407 (2003). 22

[29] P. J. Lee, M. Anderlini, B. L. Brown, J. Sebby-Strabley, W. D. Phillips, and J. V. Porto, *Sublattice Addressing and Spin-Dependent Motion of Atoms in a Double-Well Lattice*, Phys. Rev. Lett. **99**, 020402 (2007). 22

[30] D. Pertot, B. Gadway, and D. Schneble, *Collinear Four-Wave Mixing of Two-Component Matter Waves*, Phys. Rev. Lett. **104**, 200402 (2010). 22

[31] D. McKay and B. DeMarco, *Thermometry with spin-dependent lattices*, New Journal of Physics **12**, 055013 (2010). 22, 35, 40

[32] J. Catani, G. Barontini, G. Lamporesi, F. Rabatti, G. Thalhammer, F. Minardi, S. Stringari, and M. Inguscio, *Entropy Exchange in a Mixture of Ultracold Atoms*, Phys. Rev. Lett. **103**, 140401 (2009). 22, 134

[33] J. Doyle, B. Friedrich, R. V. Krems, and F. Masnou-Seeuws, *Editorial: Quo vadis, cold molecules?*, Euro. Phys. J. D - At., Mol., Opt. and Plas. Phys. **31**, 149 (2004), see also references therein and the special issue which follows. 23

[34] C. J. Myatt, E. A. Burt, R. W. Ghrist, E. A. Cornell, and C. E. Wieman, *Production of Two Overlapping Bose-Einstein Condensates by Sympathetic Cooling*, Phys. Rev. Lett. **78**, 586 (1997). 23

[35] F. Schreck, G. Ferrari, K. L. Corwin, J. Cubizolles, L. Khaykovich, M.-O. Mewes, and C. Salomon, *Sympathetic cooling of bosonic and fermionic lithium gases towards quantum degeneracy*, Phys. Rev. A **64**, 011402 (2001). 23, 134

[36] A. G. Truscott, K. E. Strecker, W. I. McAlexander, G. B. Partridge, and R. G. Hulet, *Observation of Fermi Pressure in a Gas of Trapped Atoms*, Science **291**, 2570 (2001). 23

[37] G. Modugno, G. Ferrari, G. Roati, R. J. Brecha, A. Simoni, and M. Inguscio, *Bose-Einstein Condensation of Potassium Atoms by Sympathetic Cooling*, Science **294**, 1320 (2001). 23

[38] K. Mølmer, *Bose Condensates and Fermi Gases at Zero Temperature*, Phys. Rev. Lett. **80**, 1804 (1998). 23

[39] H. Heiselberg, C. J. Pethick, H. Smith, and L. Viverit, *Influence of Induced Interactions on the Superfluid Transition in Dilute Fermi Gases*, Phys. Rev. Lett. **85**, 2418 (2000). 23, 24, 37

[40] M. J. Bijlsma, B. A. Heringa, and H. T. C. Stoof, *Phonon exchange in dilute Fermi-Bose mixtures: Tailoring the Fermi-Fermi interaction*, Phys. Rev. A **61**, 053601 (2000). 23, 24, 37

[41] M. Taglieber, A.-C. Voigt, F. Henkel, S. Fray, T. W. Hänsch, and K. Dieckmann, *Simultaneous magneto-optical trapping of three atomic species*, Phys. Rev. A **73**, 011402 (2006). 23

[42] E. Wille *et al.*, *Exploring an Ultracold Fermi-Fermi Mixture: Interspecies Feshbach Resonances and Scattering Properties of ^6Li and ^{40}K*, Phys. Rev. Lett. **100**, 053201 (2008). 23

[43] C. Presilla and R. Onofrio, *Cooling Dynamics of Ultracold Two-Species Fermi-Bose Mixtures*, Phys. Rev. Lett. **90**, 030404 (2003). 23

[44] P. W. Courteille, B. Deh, J. Fortgh, A. Gnther, S. Kraft, C. Marzok, S. Slama, and C. Zimmermann, *Highly versatile atomic micro traps generated by multifrequency magnetic field modulation*, Journal of Physics B: Atomic, Molecular and Optical Physics **39**, 1055 (2006). 23

[45] R. Onofrio and C. Presilla, *Reaching Fermi Degeneracy in Two-Species Optical Dipole Traps*, Phys. Rev. Lett. **89**, 100401 (2002). 23

[46] W. S. Bakr, J. I. Gillen, A. Peng, S. Folling, and M. Greiner, *A quantum gas microscope for detecting single atoms in a Hubbard-regime optical lattice*, Nature **462**, 74 (2009). 23

[47] A. Klinger, S. Degenkolb, N. Gemelke, K.-A. B. Soderberg, and C. Chin, *Optical lattices for atom-based quantum microscopy*, Rev. Sci. Instr. **81**, 013109 (2010). 23

[48] D. Jaksch, C. Bruder, J. I. Cirac, C. W. Gardiner, and P. Zoller, *Cold Bosonic Atoms in Optical Lattices*, Phys. Rev. Lett. **81**, 3108 (1998). 23

[49] M. Köhl, H. Moritz, T. Stöferle, K. Günter, and T. Esslinger, *Fermionic Atoms in a Three Dimensional Optical Lattice: Observing Fermi Surfaces, Dynamics, and Interactions*, Phys. Rev. Lett. **94**, 080403 (2005). 23, 24

[50] J. K. Chin, D. E. Miller, Y. Liu, C. Stan, W. Setiawan, C. Sanner, K. Xu, and W. Ketterle, *Evidence for superfluidity of ultracold fermions in an optical lattice*, Nature **443**, 961 (2006). 23

[51] L. Viverit, *Boson-induced s-wave pairing in dilute boson-fermion mixtures*, Phys. Rev. A **66**, 023605 (2002). 24, 37, 134

[52] D. H. Santamore, S. Gaudio, and E. Timmermans, *Zero Sound in a Mixture of a Single-Component Fermion Gas and a Bose-Einstein Condensate*, Phys. Rev. Lett. **93**, 250402 (2004). 24, 37, 134

[53] K. Günter, T. Stöferle, H. Moritz, M. Köhl, and T. Esslinger, *Bose-Fermi Mixtures in a Three-Dimensional Optical Lattice*, Phys. Rev. Lett. **96**, 180402 (2006). 24, 134

[54] S. Ospelkaus, C. Ospelkaus, O. Wille, M. Succo, P. Ernst, K. Sengstock, and K. Bongs, *Localization of Bosonic Atoms by Fermionic Impurities in a Three-Dimensional Optical Lattice*, Phys. Rev. Lett. **96**, 180403 (2006). 24

[55] D.-W. Wang, M. D. Lukin, and E. Demler, *Engineering superfluidity in Bose-Fermi mixtures of ultracold atoms*, Phys. Rev. A **72**, 051604 (2005). 24, 37

[56] G. Roati, F. Riboli, G. Modugno, and M. Inguscio, *Fermi-Bose Quantum Degenerate $K40-R87b$ Mixture with Attractive Interaction*, Phys. Rev. Lett. **89**, 150403 (2002). 24, 134

[57] J. Goldwin, S. Inouye, M. L. Olsen, B. Newman, B. D. DePaola, and D. S. Jin, *Measurement of the interaction strength in a Bose-Fermi mixture with Rb87 and K40*, Phys. Rev. A **70**, 021601 (2004). 24

[58] C. Ospelkaus, S. Ospelkaus, K. Sengstock, and K. Bongs, *Interaction-Driven Dynamics of $K40-Rb87$ Fermion-Boson Gas Mixtures in the Large-Particle-Number Limit*, Phys. Rev. Lett. **96**, 020401 (2006). 24, 134

[59] M. Anderlini, E. Courtade, M. Cristiani, D. Cossart, D. Ciampini, C. Sias, O. Morsch, and E. Arimondo, *Sympathetic cooling and collisional properties of a Rb−Cs mixture*, Phys. Rev. A **71**, 061401 (2005). 24, 134

[60] C. Silber, S. Günther, C. Marzok, B. Deh, P. W. Courteille, and C. Zimmermann, *Quantum-Degenerate Mixture of Fermionic Lithium and Bosonic Rubidium Gases*, Phys. Rev. Lett. **95**, 170408 (2005). 24, 33, 134

[61] E. Arimondo, M. Inguscio, and P. Violino, *Experimental determinations of the hyperfine structure in the alkali atoms*, Rev. Mod. Phys. **49**, 31 (1977), and references therein. 25, 75, 142

[62] D. A. Steck, Rubidium 87 D Line Data, available online at http://steck.us/alkalidata (revision 2.1.2, 12 August 2009). 25, 74, 137

[63] D. A. Steck, Sodium D Line Data, available online at http://steck.us/alkalidata (revision 2.1.3, 12 August 2009). 25, 137

[64] D. A. Steck, Cesium D Line Data, available online at http://steck.us/alkalidata (revision 2.1.2, 12 August 2009). 25, 137

[65] M. E. Gehm, Properties of ^{6}Li, available online at http://www.phy.duke.edu/research/photon/qoptics/techdocs/ (version 1.1, 26 September 2003). 25

[66] M. Zucker, A. Kishore, R. Sukumar, and R. Dragoset, *Elemental Data Index* (version 2.2), [Online]. http://physics.nist.gov/Handbook, [2006], National Institute of Standards and Technology, Gaithersburg, MD. 25

[67] S. Inouye, J. Goldwin, M. L. Olsen, C. Ticknor, J. L. Bohn, and D. S. Jin, *Observation of Heteronuclear Feshbach Resonances in a Mixture of Bosons and Fermions*, Phys. Rev. Lett. **93**, 183201 (2004). 33

[68] C. R. Monroe, E. A. Cornell, C. A. Sackett, C. J. Myatt, and C. E. Wieman, *Measurement of Cs-Cs elastic scattering at T=30 μK*, Phys. Rev. Lett. **70**, 414 (1993). 34

[69] B. DeMarco, S. B. Papp, and D. S. Jin, *Pauli Blocking of Collisions in a Quantum Degenerate Atomic Fermi Gas*, Phys. Rev. Lett. **86**, 5409 (2001). 34

[70] T. Kinoshita, T. Wenger, and D. S. Weiss, *A quantum Newton's cradle*, Nature **440**, 900 (2006). 34

[71] L. D. Carr, T. Bourdel, and Y. Castin, *Limits of sympathetic cooling of fermions by zero-temperature bosons due to particle losses*, Phys. Rev. A **69**, 033603 (2004). 34

[72] A. Griessner, A. J. Daley, S. R. Clark, D. Jaksch, and P. Zoller, *Dark-State Cooling of Atoms by Superfluid Immersion*, Phys. Rev. Lett. **97**, 220403 (2006). 35

[73] P. B. Blakie and A. Bezett, *Adiabatic cooling of fermions in an optical lattice*, Phys. Rev. A **71**, 033616 (2005). 37, 40

[74] M. Lewenstein, L. Santos, M. A. Baranov, and H. Fehrmann, *Atomic Bose-Fermi Mixtures in an Optical Lattice*, Phys. Rev. Lett. **92**, 050401 (2004). 37

[75] R. Roth and K. Burnett, *Quantum phases of atomic boson-fermion mixtures in optical lattices*, Phys. Rev. A **69**, 021601 (2004). 37

[76] A. Klein, M. Bruderer, S. R. Clark, and D. Jaksch, *Dynamics, dephasing and clustering of impurity atoms in Bose-Einstein condensates*, New Journal of Physics **9**, 411 (2007). 37

[77] B. Paredes, A. Widera, V. Murg, O. Mandel, S. Folling, I. Cirac, G. Shlyapnikov, T. Hansch, and I. Bloch, *Tonks-Girardeau gas of ultracold atoms in an optical lattice*, Nature **429**, 277 (2004). 38, 134

[78] H. Pu, L. O. Baksmaty, W. Zhang, N. P. Bigelow, and P. Meystre, *Effective-mass analysis of Bose-Einstein condensates in optical lattices: Stabilization and levitation*, Phys. Rev. A **67**, 043605 (2003). 38

[79] M. Krämer, L. Pitaevskii, and S. Stringari, *Macroscopic Dynamics of a Trapped Bose-Einstein Condensate in the Presence of 1D and 2D Optical Lattices*, Phys. Rev. Lett. **88**, 180404 (2002). 38

[80] W. Zwerger, *MottHubbard transition of cold atoms in optical lattices*, J. Opt. B: Quantum Semiclassical Opt. **5**, S9 (2003). 38

[81] M. Köhl, *Thermometry of fermionic atoms in an optical lattice*, Phys. Rev. A **73**, 031601(R) (2006). 40

[82] S. Trotzky, L. Pollet, F. Gerbier, U. Schnorrberger, I. Bloch, N. Prokof'ev, B. Svistunov, and M. Troyer, *Suppression of the critical temperature for superfluidity near the Mott transition: validating a quantum simulator*, arxiv:0905.4882 (2010). 40

[83] T. Loftus, C. A. Regal, C. Ticknor, J. L. Bohn, and D. S. Jin, *Resonant Control of Elastic Collisions in an Optically Trapped Fermi Gas of Atoms*, Phys. Rev. Lett. **88**, 173201 (2002). 41

[84] K. Dieckmann, C. A. Stan, S. Gupta, Z. Hadzibabic, C. H. Schunck, and W. Ketterle, *Decay of an Ultracold Fermionic Lithium Gas near a Feshbach Resonance*, Phys. Rev. Lett. **89**, 203201 (2002). 41, 55, 67

[85] K. M. O'Hara, S. L. Hemmer, S. R. Granade, M. E. Gehm, J. E. Thomas, V. Venturi, E. Tiesinga, and C. J. Williams, *Measurement of the zero crossing in a Feshbach resonance of fermionic* ^6Li, Phys. Rev. A **66**, 041401 (2002). 41

[86] T. Bourdel, J. Cubizolles, L. Khaykovich, K. M. F. Magalhães, S. J. J. M. F. Kokkelmans, G. V. Shlyapnikov, and C. Salomon, *Measurement of the Interaction Energy near a Feshbach Resonance in a Li*6 *Fermi Gas*, Phys. Rev. Lett. **91**, 020402 (2003). 41, 55, 67

[87] C. A. Regal, M. Greiner, and D. S. Jin, *Observation of Resonance Condensation of Fermionic Atom Pairs*, Phys. Rev. Lett. **92**, 040403 (2004). 41

[88] N. W. Ashcroft and N. D. Mermin, *Solid state physics* (Holt, New York, 1976). 42

[89] W. Heisenberg, *Zur Theorie des Ferromagnetismus*, Z. Phys. **49**, 619 (1928). 43

[90] F. Bloch, *Bemerkung zer Elektronentheorie des Ferromagnetismus und der elektrischen Leitfähigkeit*, Z. Phys. **57**, 545 (1929). 43

[91] C. Herring, *Magnetism,* edited by G. T. Rado and H. Suhl (Academic Press Inc., New York, 1966), Vol. 4, subtitled: *Exchange interactions among itinerant electrons*, and references therein. 43

[92] E. C. Stoner, *Atomic moments in ferromagnetic metals and alloys with non-ferromagnetic elements*, Phil. Mag. **15**, (1933). 43

[93] J. Hubbard, *Electron Correlations in Narrow Energy Bands*, Proc. R. Soc. A. **276**, 238 (1963). 43

[94] M. C. Gutzwiller, *Effect of Correlation on the Ferromagnetism of Transition Metals*, Phys. Rev. Lett. **10**, 159 (1963). 43

[95] L. Salasnich, B. Pozzi, A. Parola, and L. Reatto, *Thermodynamics of multi-component Fermi vapours*, J. Phys. B: At., Mol. Opt. Phys. **33**, 3943 (2000). 44

[96] M. Amoruso, I. Meccoli, A. Minguzzi, and M. P. Tosi, *Density profiles and collective excitations of a trapped two-component Fermi vapour*, Euro. Phys. J. D - At. Mol. Opt. Plasma Phys. **8**, 361 (2000). 44

[97] R. Roth and H. Feldmeier, *Phase diagram of trapped degenerate Fermi gases including effective s- and p-wave interactions*, Journal of Physics B: Atomic, Molecular and Optical Physics **34**, 4629 (2001). 44

[98] T. Sogo and H. Yabu, *Collective ferromagnetism in two-component Fermi-degenerate gas trapped in a finite potential*, Phys. Rev. A **66**, 043611 (2002). 44, 46

[99] R. A. Duine and A. H. MacDonald, *Itinerant Ferromagnetism in an Ultracold Atom Fermi Gas*, Phys. Rev. Lett. **95**, 230403 (2005). 45, 74, 85

[100] I. Berdnikov, P. Coleman, and S. H. Simon, *Itinerant ferromagnetism in an atom trap*, Phys. Rev. B **79**, 224403 (2009). 45

[101] S. Pilati, G. Bertaina, S. Giorgini, and M. Troyer, *Itinerant Ferromagnetism of a Repulsive Atomic Fermi Gas: A Quantum Monte Carlo Study*, Phys. Rev. Lett. **105**, 030405 (2010). 45, 72

[102] C. A. Regal, M. Greiner, and D. S. Jin, *Lifetime of Molecule-Atom Mixtures near a Feshbach Resonance in $K40$*, Phys. Rev. Lett. **92**, 083201 (2004). 55, 67

[103] D. S. Petrov, *Three-body problem in Fermi gases with short-range interparticle interaction*, Phys. Rev. A **67**, 010703 (2003). 55, 79

[104] I. Berdnikov, P. Coleman, and S. H. Simon, *Itinerant ferromagnetism in an atom trap*, Phys. Rev. B **79**, 224403 (2009). 57

[105] L. E. Sadler, J. M. Higbie, S. R. Leslie, M. Vengalattore, and D. M. Stamper-Kurn, *Spontaneous symmetry breaking in a quenched ferromagnetic spinor Bose-Einstein condensate*, Nature (London) **443**, 312 (2006). 66

[106] W. H. Press, S. A. Teukolsky, W. T. Vetterling, and B. P. Flannery, *Numerical recipes in C: the art of scientific computing*, 2^{nd} ed. (Cambridge University Press, Cambridge, 1992). 68

[107] R. J. Schilling and S. L. Harris, *Applied numerical methods for engineers using MATLAB and C* (Brooks/Cole Publishing Company, Pacific Grove, CA, 2000). 69

[108] G.-B. Jo, Y.-R. Lee, J.-H. Choi, C. A. Christensen, T. H. Kim, J. H. Thywissen, D. E. Pritchard, and W. Ketterle, *Itinerant Ferromagnetism in a Fermi Gas of Ultracold Atoms*, Science **325**, 1521 (2009). 70, 71, 72, 73, 134, 135

[109] S.-Y. Chang, M. Randeria, and N. Trivedi, *Ferromagnetism in repulsive Fermi gases: upper branch of Feshbach resonance versus hard spheres*, arXiv.org:1004.2680 (2010). 72

[110] D. Pekker, M. Babadi, R. Sensarma, N. Zinner, L. Pollet, M. W. Zwierlein, and E. Demler, *Competition between pairing and ferromagnetic instabilities in ultracold Fermi gases near Feshbach resonances*, arXiv.org:1005.2366 (2010). 72, 135

[111] H. Zhai, *Correlated versus ferromagnetic state in repulsively interacting two-component Fermi gases*, Phys. Rev. A **80**, 051605 (2009). 73, 135

[112] X. Cui and H. Zhai, *Stability of a fully magnetized ferromagnetic state in repulsively interacting ultracold Fermi gases*, Phys. Rev. A **81**, 041602 (2010). 73

[113] C. A. Regal, C. Ticknor, J. L. Bohn, and D. S. Jin, *Tuning p-Wave Interactions in an Ultracold Fermi Gas of Atoms*, Phys. Rev. Lett. **90**, 053201 (2003). 74, 79, 85

[114] J. T. Eisinger, B. Bederson, and B. T. Feld, *The Magnetic Moment of K^{40} and the Hyperfine Structure Anomaly of the Potassium Isotopes*, Phys. Rev. **86**, 73 (1952). 75

[115] C. A. Regal and D. S. Jin, *Measurement of Positive and Negative Scattering Lengths in a Fermi Gas of Atoms*, Phys. Rev. Lett. **90**, 230404 (2003). 79, 81

[116] S. Gupta, Z. Hadzibabic, M. W. Zwierlein, C. A. Stan, K. Dieckmann, C. H. Schunck, E. G. M. van Kempen, B. J. Verhaar, and W. Ketterle, *Radio-Frequency Spectroscopy of Ultracold Fermions*, Science **300**, 1723 (2003). 81

[117] C. Regal, Ph.D. thesis, University of Colorado, 2006. 81

[118] M. Andrews, C. Townsend, H. Miesner, D. Durfee, D. Kurn, and W. Ketterle, *Observation of interference between two Bose condensates*, Science **275**, 637 (1997). 86, 89

[119] B. D. Josephson, *Possible new effects in superconductive tunnelling*, Physics Letters **1**, 251 (1962). 86, 88

[120] M. Albiez, R. Gati, J. Fölling, S. Hunsmann, M. Cristiani, and M. K. Oberthaler, *Direct Observation of Tunneling and Nonlinear Self-Trapping in a Single Bosonic Josephson Junction*, Phys. Rev. Lett. **95**, 010402 (2005). 86, 89, 90

[121] J. Esteve, C. Gross, A. Weller, S. Giovanazzi, and M. K. Oberthaler, *Squeezing and entanglement in a Bose-Einstein condensate*, Nature **455**, 1216 (2008). 86, 90, 118, 132, 135, 136

[122] I. Giaever, *Electron Tunneling Between Two Superconductors*, Phys. Rev. Lett. **5**, 464 (1960). 87

[123] J. Nicol, S. Shapiro, and P. H. Smith, *Direct Measurement of the Superconducting Energy Gap*, Phys. Rev. Lett. **5**, 461 (1960). 87

[124] B. D. Josephson, *The discovery of tunnelling supercurrents*, Rev. Mod. Phys. **46**, 251 (1974). 88

[125] P. W. Anderson and J. M. Rowell, *Probable Observation of the Josephson Superconducting Tunneling Effect*, Phys. Rev. Lett. **10**, 230 (1963). 88

[126] I. Giaever, *Detection of the ac Josephson Effect*, Phys. Rev. Lett. **14**, 904 (1965). 88

[127] A. J. Dahm, A. Denenstein, T. F. Finnegan, D. N. Langenberg, and D. J. Scalapino, *Study of the Josephson Plasma Resonance*, Phys. Rev. Lett. **20**, 859 (1968). 88, 89, 100

[128] P. W. Anderson and A. H. Dayem, *Radio-Frequency Effects in Superconducting Thin Film Bridges*, Phys. Rev. Lett. **13**, 195 (1964). 88

[129] K. K. Likharev, *Superconducting weak links*, Rev. Mod. Phys. **51**, 101 (1979), and references therein. 88

[130] S. Pereverzev, A. Loshak, S. Backhaus, J. Davis, and R. Packard, *Quantum oscillations between two weakly coupled reservoirs of superfluid He-3*, Nature (London) **388**, 449 (1997). 88

[131] S. Backhaus, S. Pereverzev, A. Loshak, J. Davis, and R. Packard, *Direct measurement of the current-phase relation of a superfluid He-3-B weak link*, Science **278**, 1435 (1997). 88

[132] K. Sukhatme, Y. Mukharsky, T. Chui, and D. Pearson, *Observation of the ideal Josephson effect in superfluid 4He*, Nature **411**, 280 (2001). 88

[133] E. Hoskinson, Y. Sato, I. Hahn, and R. E. Packard, *Transition from phase slips to the Josephson effect in a superfluid ^{4}He weak link*, Nature Physics **2**, 23 (2005). 89

[134] J. Javanainen, *Oscillatory exchange of atoms between traps containing Bose condensates*, Phys. Rev. Lett. **57**, 3164 (1986). 89

[135] F. Dalfovo, L. Pitaevskii, and S. Stringari, *Order parameter at the boundary of a trapped Bose gas*, Phys. Rev. A **54**, 4213 (1996). 89, 103

[136] M. W. Jack, M. J. Collett, and D. F. Walls, *Coherent quantum tunneling between two Bose-Einstein condensates*, Phys. Rev. A **54**, R4625 (1996). 89

[137] A. Smerzi, S. Fantoni, S. Giovanazzi, and S. R. Shenoy, *Quantum Coherent Atomic Tunneling between Two Trapped Bose-Einstein Condensates*, Phys. Rev. Lett. **79**, 4950 (1997). 89

[138] S. Raghavan, A. Smerzi, S. Fantoni, and S. R. Shenoy, *Coherent oscillations between two weakly coupled Bose-Einstein condensates: Josephson effects, π oscillations, and macroscopic quantum self-trapping*, Phys. Rev. A **59**, 620 (1999). 89

[139] C. Menotti, J. R. Anglin, J. I. Cirac, and P. Zoller, *Dynamic splitting of a Bose-Einstein condensate*, Phys. Rev. A **63**, 023601 (2001). 89

[140] B. P. Anderson and M. A. Kasevich, *Macroscopic Quantum Interference from Atomic Tunnel Arrays*, Science **282**, 1686 (1998). 89

[141] F. S. Cataliotti, S. Burger, C. Fort, P. Maddaloni, F. Minardi, A. Trombettoni, A. Smerzi, and M. Inguscio, *Josephson Junction Arrays with Bose-Einstein Condensates*, Science **293**, 843 (2001). 89

[142] D. Ananikian and T. Bergeman, *Gross-Pitaevskii equation for Bose particles in a double-well potential: Two-mode models and beyond*, Phys. Rev. A **73**, 013604 (2006). 89

[143] S. Levy, E. Lahoud, I. Shomroni, and J. Steinhauer, *The a.c. and d.c. Josephson effects in a Bose-Einstein condensate*, Nature (London) **449**, 579 (2007). 89, 90

[144] G. B. Jo, Y. Shin, S. Will, T. A. Pasquini, M. Saba, W. Ketterle, D. E. Pritchard, M. Vengalattore, and M. Prentiss, *Long phase coherence time and number squeezing of two Bose-Einstein condensates on an atom chip*, Phys. Rev. Lett. **98**, 030407 (2007). 90, 118

[145] G.-B. Jo, J.-H. Choi, C. A. Christensen, Y.-R. Lee, T. A. Pasquini, W. Ketterle, and D. E. Pritchard, *Matter-Wave Interferometry with Phase Fluctuating Bose-Einstein Condensates*, Phys. Rev. Lett. **99**, 240406 (2007). 90

[146] S. Dettmer *et al.*, *Observation of Phase Fluctuations in Elongated Bose-Einstein Condensates*, Phys. Rev. Lett. **87**, 160406 (2001). 90

[147] R. Gati, B. Hemmerling, J. Fölling, M. Albiez, and M. K. Oberthaler, *Noise Thermometry with Two Weakly Coupled Bose-Einstein Condensates*, Phys. Rev. Lett. **96**, 130404 (2006). 90

[148] S. Hofferberth, I. Lesanovsky, B. Fischer, T. Schumm, and J. Schmiedmayer, *Non-equilibrium coherence dynamics in one-dimensional Bose gases*, Nature **449**, 324 (2007). 90

[149] K. Maussang, G. E. Marti, T. Schneider, P. Treutlein, Y. Li, A. Sinatra, R. Long, J. Esteve, and J. Reichel, *Enhanced and reduced atom number fluctuations in a BEC splitter*, arxiv:1005:1922 (2010). 90, 118, 132, 135, 136

[150] Y.-J. Wang, D. Z. Anderson, V. M. Bright, E. A. Cornell, Q. Diot, T. Kishimoto, M. Prentiss, R. A. Saravanan, S. R. Segal, and S. Wu, *Atom Michelson Interferometer on a Chip Using a Bose-Einstein Condensate*, Phys. Rev. Lett. **94**, 090405 (2005). 90, 118, 132, 135, 136

[151] G.-B. Jo, J.-H. Choi, C. A. Christensen, T. A. Pasquini, Y.-R. Lee, W. Ketterle, and D. E. Pritchard, *Phase-Sensitive Recombination of Two Bose-Einstein Condensates on an Atom Chip*, Phys. Rev. Lett. **98**, 180401 (2007). 90, 118, 132, 135, 136

[152] F. Dalfovo, S. Giorgini, L. P. Pitaevskii, and S. Stringari, *Theory of Bose-Einstein condensation in trapped gases*, Rev. Mod. Phys. **71**, 463 (1999). 91

[153] C. J. Pethick and H. Smith, *Bose-Einstein condensation in dilute gases* (Cambridge University Press, Cambridge, 2002). 91, 93, 105

[154] E. E. Edwards, M. Beeler, T. Hong, and S. L. Rolston, *Adiabaticity and Localization in One-Dimensional Incommensurate Lattices*, Phys. Rev. Lett. **101**, 260402 (2008). 92

[155] J. Denschlag *et al.*, *Generating Solitons by Phase Engineering of a Bose-Einstein Condensate*, Science **287**, 97 (2000). 92

[156] C. Becker, S. Stellmer, P. Soltan-Panahi, S. Dorscher, M. Baumert, E.-M. Richter, J. Kronjager, K. Bongs, and K. Sengstock, *Oscillations and interactions of dark and dark-bright solitons in Bose-Einstein condensates*, Nature Phys. **4**, 496 (2008). 92

[157] A. Weller, J. P. Ronzheimer, C. Gross, J. Esteve, M. K. Oberthaler, D. J. Frantzeskakis, G. Theocharis, and P. G. Kevrekidis, *Experimental Observation of Oscillating and Interacting Matter Wave Dark Solitons*, Phys. Rev. Lett. **101**, 130401 (2008). 92

[158] K. W. Madison, F. Chevy, V. Bretin, and J. Dalibard, *Stationary States of a Rotating Bose-Einstein Condensate: Routes to Vortex Nucleation*, Phys. Rev. Lett. **86**, 4443 (2001). 92

[159] M. Tsubota, K. Kasamatsu, and M. Ueda, *Vortex lattice formation in a rotating Bose-Einstein condensate*, Phys. Rev. A **65**, 023603 (2002). 92

[160] T. P. Simula, M. D. Lee, and D. A. W. Hutchinson, *Transition from the Bose-Einstein condensate to the Berezinskii-Kosterlitz-Thouless phase*, Phil. Mag. Lett. **85**, 395 (2005). 92

[161] Z. Hadzibabic, P. Kruger, M. Cheneau, B. Battelier, and J. Dalibard, *Berezinskii-Kosterlitz-Thouless crossover in a trapped atomic gas*, Nature **441**, 1118 (2006). 92

[162] J. J. Sakurai, *Modern Quantum Mechanics* (Addison-Wesley, Reading, MA, 1994). 92, 138

[163] R. Gati, J. Esteve, B. Hemmerling, T. B. Ottenstein, J. Appmeier, A. Weller, and M. K. Oberthaler, *A primary noise thermometer for ultracold Bose gases*, N. J. Phys. **8**, 189 (2006). 96, 97

[164] C. Kittel, *Introduction to solid state physics* (Wiley, New York, 1996), p. 98. 100

[165] H. Ott, J. Fortágh, S. Kraft, A. Günther, D. Komma, and C. Zimmermann, *Nonlinear Dynamics of a Bose-Einstein Condensate in a Magnetic Waveguide*, Phys. Rev. Lett. **91**, 040402 (2003). 116

[166] D. A. W. Hutchinson and E. Zaremba, Phys. Rev. A **57**, 1280 (1998). 117

[167] S. Stringari, *Collective Excitations of a Trapped Bose-Condensed Gas*, Phys. Rev. Lett. **77**, 2360 (1996). 117

[168] A. J. Leggett and F. Sols, *Comment on "Phase and Phase Diffusion of a Split Bose-Einstein Condensate"*, Phys. Rev. Lett. **81**, 1344 (1998). 118, 136

[169] I. Zapata, F. Sols, and A. J. Leggett, *Josephson effect between trapped Bose-Einstein condensates*, Phys. Rev. A **57**, R28 (1998). 122

[170] F. Meier and W. Zwerger, *Josephson tunneling between weakly interacting Bose-Einstein condensates*, Phys. Rev. A **64**, 033610 (2001). 122

[171] S. Kohler and F. Sols, *Chemical potential standard for atomic Bose-Einstein condensates*, N. J. Phys. **5**, 94 (2003). 119, 122

[172] A. Griffin, T. Nikuni, and E. Zaremba, *Bose-condensed gases at finite temperatures* (Cambridge University Press, Cambridge, 2009). 124

[173] F. M. Spiegelhalder, A. Trenkwalder, D. Naik, G. Kerner, E. Wille, G. Hendl, F. Schreck, and R. Grimm, *All-optical production of a degenerate mixture of ^6Li and ^{40}K and creation of heteronuclear molecules*, Phys. Rev. A **81**, 043637 (2010). 134

[174] K. K. Ni, S. Ospelkaus, D. Wang, G. Quemener, B. Neyenhuis, M. H. G. de Miranda, J. L. Bohn, J. Ye, and D. S. Jin, *Dipolar collisions of polar molecules in the quantum regime*, Nature **464**, 1324 (2010). 134

[175] A. Klein and D. Jaksch, *Phonon-induced artificial magnetic fields in optical lattices*, Europhys. Lett.) **85**, 13001 (2009). 134

[176] A. Recati and S. Stringari, *Spin fluctuations, susceptibility and the dipole oscillation of a nearly ferromagnetic Fermi gas*, arxiv:0909.2475 (2010). 135

[177] L. Santos, M. A. Baranov, J. I. Cirac, H.-U. Everts, H. Fehrmann, and M. Lewenstein, *Atomic Quantum Gases in Kagomé Lattices*, Phys. Rev. Lett. **93**, 030601 (2004). 135

[178] F. Werner, O. Parcollet, A. Georges, and S. R. Hassan, *Interaction-Induced Adiabatic Cooling and Antiferromagnetism of Cold Fermions in Optical Lattices*, Phys. Rev. Lett. **95**, 056401 (2005). 135

[179] J. von Stecher, E. Demler, M. D. Lukin, and A. M. Rey, *Probing interaction-induced ferromagnetism in optical superlattices*, New Journal of Physics **12**, 055009 (2010). 135

[180] D. A. Steck, Rubidium 85 D Line Data, available online at http://steck.us/alkalidata (revision 2.1.2, 12 August 2009). 137

[181] J. E. Sansonetti, W. C. Martin, and S. Young, *NIST Handbook of Basic Atomic Spectroscopic Data* (version 1.1.2), [Online]. http://physics.nist.gov/Handbook, 2005, [2010, August 25]. National Institute of Standards and Technology, Gaithersburg, MD. 138, 139

[182] Y. Ralchenko, A. Kramida, J. Reader, and NIST ASD Team , *NIST Atomic Spectra Database* (version 3.1.5), [Online]. Available: http://physics.nist.gov/asd3, 2008, [2010, August 25]. National Institute of Standards and Technology, Gaithersburg, MD. 138

[183] G. K. Woodgate, *Elementary Atomic Structure*3rd ed. (Oxford University Press, Oxford, 1980). 139

[184] C. Cohen-Tannoudji, B. Diu, and F. Laloë, *Quantum Mechanics* (John Wiley & Sons, New York, 1977). 140

[185] N. Ramsey, *Molecular Beams* (Oxford University Press, New York, 1956). 141, 145

[186] N. Ramsey, *Nuclear Moments* (John Wiley & Sons, New York, 1953). 141

[187] F. Touchard *et al.*, *Isotope shifts and hyperfine structure of 38-47K by laser spectroscopy*, Phys. Lett. B **108**, 169 (1982). 142

[188] N. Bendali, H. T. Duong, and J. L. Vialle, *High-resolution laser spectroscopy on the D 1 and D 2 lines of 39, 40, 44 K using RF modulated laser light*, J. Phys. B: At. Mol. Phys. **14**, 4231 (1981). 142

[189] P. Mohr, B. Taylor, and D. Newell, *The 2006 CODATA Recommended Values of the Fundamental Physical Constants* (Web Version 5.2). This database was developed by J. Baker, M. Douma, and S. Kotochigova., 2007, available: http://physics.nist.gov/constants [2010, August 25]. National Institute of Standards and Technology, Gaithersburg, MD. 142

[190] D. F. V. James, PHY2206S lecture notes, University of Toronto, Spring 2006. 147

[191] R. Loudon, *The Quantum Theory of Light,* 3rd ed. (Oxford University Press, Oxford, 2000). 148

[192] A. Messiah, *Quantum Mechanics* (North Holland Publishing Co., Amsterdam, 1962). 149, 150

[193] U. Volz and H. Schmoranzer, *Precision lifetime measurements on alkali atoms and on helium by beamgaslaser spectroscopy*, Physica Scripta **1996**, 48 (1996). 150

[194] L. Bergmann and C. Schaeffer, *Constituents of Matter: Atoms, Molecules, Nuclei and Particles* (Walter de Gruyter, Berlin, 1997). 150, 151

[195] S. Giorgini, L. P. Pitaevskii, and S. Stringari, *Condensate fraction and critical temperature of a trapped interacting Bose gas*, Phys. Rev. A **54**, R4633 (1996). 159